A FUNDAMENTAL STUDY TO ENABLE ULTRASONIC STRUCTURAL HEALTH MONITORING OF A THICK-WALLED, COMPOSITE, OVER-WRAPPED PRESSURE VESSEL

A Dissertation
Presented to
The Academic Faculty

By

Peter McKeon

In Partial Fulfillment
Of the Requirements for the Degree
Doctor of Philosophy in the
Woodruff School of Mechanical Engineering

Georgia Institute of Technology
December, 2014

A FUNDAMENTAL STUDY TO ENABLE ULTRASONIC STRUCTURAL HEALTH MONITORING OF A THICK-WALLED, COMPOSITE, OVER-WRAPPED PRESSURE VESSEL

Approved by:

Nico F. Declercq, co-adviser
George W. Woodruff School of Mechanical Engineering
Georgia Institute of Technology

Slah Yaacoubi, co-adviser
Research and Development
Institut de Soudure

Jennifer E. Michaels
School of Electrical and Computer Engineering
Georgia Institute of Technology

Yves Berthelot
George W. Woodruff School of Mechanical Engineering
Georgia Institute of Technology

Laurence J. Jacobs
School of Civil and Environmental Engineering
Georgia Institute of Technology

Laurent Capolungo
George W. Woodruff School of Mechanical Engineering
Georgia Institute of Technology

Date Approved: October 8th, 2014

ACKNOWLEDGEMENTS

First and foremost, I would like to thank my advisors, Dr. Slah Yaacoubi and Dr. Nico F. Declercq. You have provided me with invaluable guidance during the last four years -- not just in structural health monitoring and ultrasonic wave propagation, but personal and career advice as well. My time at Georgia Tech Lorraine has certainly been a changing point in my life and I am grateful for your support. I would also like to thank my Ph.D. committee for their constructive criticism, effort and time: Dr. Yves Berthelot, Dr. Laurence J. Jacobs, Dr. Jennifer E. Michaels, and Dr. Laurent Capolungo.

I am of course indebted to the financial support supplied by the Institut de Soudure as well as the other industrial partners involved in the Horizon Hydrogen Energy project. However, I would be amiss not to thank the Institut de Soudure not just for their financial contribution to this work (and supply of samples), but also for the entire team's intellectual help during the past few years, most notably Dr. Weina Ke Yaccoubi.

I would also like to thank my fellow Ph.D. students for their help and support throughout the years, especially Chris Bishop and Kareem Khoury for their editing expertise on this manuscript.

TABLE OF CONTENTS

CHAPTER 1: INTRODUCTION

CHAPTER 2: INVESTIGATIONS ON MODES, DISPERSION AND ATTENUATION

CHAPTER 3: FINITE ELEMENT METHOD, MODELS AND VALIDATIONS

CHAPTER 4: SIMULATION OF SELECT DAMAGE TYPES IN THE FINTE ELEMENT ENVIRONMENT

CHAPTER 5: OPTIMIZATION STUDIES AND GUIDELINES

CHAPTER 6: EXPERIMENTAL STUDIES

CHAPTER 7: CONCLUSION

LIST OF TABLES

LIST OF FIGURES

LIST OF SYMBOLS

Γ	Baseline Subtraction Algorithm Output
λ	Wavelength
v	Poission's Ratio
δ	Characteristic Mesh Dimension
ρ	Density
ω	Frequency (radians)
A	Amplitude (arbitrary units)
B_{Noise}	Noise Bandwidth
C *or* C_{ijkl}	Stress Tensor
c_g	Group Velocity
c_{Long}	Longitudinal Bulk Wave Velocity
c_p	Phase Velocity
c_{Shear}	Shear Bulk Wave Velocity
d	Thickness or Depth
E	Young's Modulus
f	Frequency
F_c	Central Frequency
H	Window Function
k	Wavenumber
L_a	Length of ABR
P_{AV}	Time-Average Poynting Vector
$R_{j,i}$	Ratio of Modal Amplitude *j* to *i* in Reflected Field

$s(t)$	Signal as a Function of Time
t	Time
$T_{j,i}$	Ratio of Modal Amplitude j to i in Transmitted Field
u	Displacement (x-direction)
u_{AV}	Time-Average Stored Energy Density
v	Displacement (y-direction)
V_e	Energy Velocity
w	Displacement (z-direction) or width
x or x_i	Material Coordinate

2DFFT	Two-Dimensional Fourier Transform
ABR	Absorbing Boundary Region
AE	Acoustic Emission
COPV	Composite Over-wrapped Pressure Vessel
CPU	Central Processing Unit
CWT	Continuous Wavelet Transform
FBG	Fiber Bragg Grating
FEM	Finite Element Method
H2E	Horizon Hydrogen Energy
MBPE	Model Based Parameter Estimation
NDE	Non-Destructive Evaluation
NDT	Non-Destructive Testing
PZT	Piezo-Electric Transducer(s)

SH	Shear Horizontal
SHM	Structural Health Monitoring
SNR	Signal-to-Noise Ratio
STFT	Short-Time Fourier Transform
TFR	Time-Frequency Representation(s)
TOF	Time of Flight
UGW	Ultrasonic Guided Wave(s)

SUMMARY

A European project involving 19 industrial and academic partners called the Horizon Hydrogen Energy (H2E) progam is currently underway with the goal of building sustainable hydrogen-energy solutions. Composite Over-Wrapped Pressure Vessels (COPV) are envisioned to store hydrogen at high-pressures for hydrogen vehicles. Structural failure of the COPV is unacceptable, and thus Structural Health Monitoring (SHM) techniques are needed to give real-time updates on the structural integrity of the reservoirs. Ultrasonic techniques are one of the methods being investigated due to their non-destructive and cost-efficient attributes.

This work focuses on addressing some of the fundamental concerns with implementing a SHM system based on the excitation and detection of Ultrasonic Guided Waves (UGW) in this novel environment. Most notably, this study uses experimental, analytical and numerical modeling techniques to consider the modal shapes and dispersive properties in this novel environment in order to make key decisions concerning frequency range, modal selection and emitter/receiver type and placement. UGW can be excited by permanently attached transducers on the exterior of the structure and signal analysis techniques can be used to determine if an excited wave packet has interacted with a defect within its propagation path. Wave packet interaction with damage can be quantified by mode conversion and/or mode reflection/transmission coefficients. These interactions are studied in a numerical environment via the finite element method for three specific damage types which were identified by our industrial partners as being critical. Some experimental results are presented as well to corroborate the findings of the numerical simulations.

CHAPTER 1

INTRODUCTION

1.1 Motivation

The world today is faced with a dual-edged problem concerning our growing energy needs and our environmental obligations to future generations. Specifically, transportational technologies currently using natural gas are one of the largest contributors to pollution, especially the accumulation of greenhouse gases [1]. Hydrogen, used as an energy carrier, may be a viable solution to both sides of this problem, i.e. fulfilling our large transportational energy and environmental needs. The Horizon Hydrogen Energy (H2E) program is a European project involving 19 industrial and academic partners with the single goal of “building sustainable and competitive hydrogen-energy solutions” [2]. With respect to automobiles and other transportation technologies, this endeavor has many components, with the storage system being one of the most complex [3].

The complexity of hydrogen storage is due to its molecular attributes; being a smaller, light-weight molecule, it is difficult to store in both its liquid and gas forms [4]. The storage of liquid hydrogen is complicated due to its susceptibility to evaporation. Even with the use of complex multi-layer vessels (typically with vacuum sealing), the interior absorbs heat form the environment, converting to the gas phase and pressurizing the vessel. Reportedly, proposed hydrogen cryogenic vessels for automobiles must be vented every 3-5 days of inactivity to equalize this pressure [4]. If stored as a gas, it is possible to increase molecule density using the favorable solid-gas interaction qualities of adsorptive super-carbons or similar materials [5]. However complete reverse sorption can only occur at very high temperatures, and the super-carbons add weight, cost and increased complexity to the storage system [4]. Otherwise, as a gas in an initially empty vessel, hydrogen needs to be stored at extremely high pressures, upwards of 700 bar, to be of any practical use. For high pressure storage vessels, there are several different design types.

Metal cylindrical vessels are well-documented and understood [6]. However, for the walls of the reservoir to be thick enough to withstand the maximum storage pressure (including a healthy factor of safety) they tend to be bulky and heavy. Therefore, reservoirs reinforced with composite fibers are more attractive for transportational technologies, where any method of weight reduction is a benefit. The popularity of composite fiber materials has increased in recent years, with this trend being especially noticeable in the aerospace and automotive industries [7, 8], due mostly to their high strength-to-weight ratio.

Naturally, one of the first iterations of the design process involved metal pressure vessels reinforced cylindrically by a fiber composite layer [6]. This design allowed for the walls of the tank to be slightly reduced, lowering the overall weight. A third design used a composite wrap in both cylindrical and transverse directions, thus even further reducing the wall thickness. The fourth and current design iteration uses a plastic (or otherwise non-metal) material as the liner which acts as a barrier for molecule diffusion, and gives the reservoir its shape. However, almost all of the structural strength comes from the composite fiber layer, which needs to be over-wrapped with sufficient thickness. This reservoir design type is called a Composite Over-wrapped Pressure Vessel (COPV), and is the type of reservoir that has been deemed as the most promising for answering the hydrogen energy storage problem within the framework of the H2E project.

However, if these COPV's are to be successfully implemented in such a pivotal (not to mention proximate to the general public) use, their structural health will have to be monitored and ensured at all times. Since these reservoirs house hydrogen gas at such high pressures, the failure of a COPV could be catastrophic. Therefore, Non-

Destructive Testing and Evaluation (NDT/NDE) will need to be applied to ensure public safety, similar to other high-risk technologies, such as the nuclear, oil transport and railway industries [9]. More specifically, a permanently installed NDT method that acts as a continuous Structural Health Monitoring (SHM) system would be ideal, so as to give up-to-date, real-time diagnostic information on the health of the given reservoir.

This study intends to answer some fundamental questions concerning the development of an SHM system for the monitoring of COPVs, specifically for hydrogen storage. First, the relevant failure mechanisms and critical damage types need to be identified and understood. These mechanisms inform the eventual development of a SHM system, as well as supply an appropriate rubric with which to assess the system's success. This chapter is thus organized: common defect types will be discussed followed by a brief discussion of the defect types of most interest for this study. Then, common NDT methods and competing technologies will be presented. Finally, the specific purpose of this study will be stated, and a general methodology will be introduced.

1.2 Defect Types in COPV

1.2.1 Range of Defects Expected in COPV

The thick, composite fiber, overwrapping layer can be considered to be almost 100% of the load bearing element of the COPV structure, while the thinner polyamide layer is responsible for the prevention of molecule diffusion and provides the vessel with its shape. A vessel will be considered to have failed if the liner ruptures, since this will result in the release of hydrogen at any pressure. However, liner rupture will most likely occur at high pressures when the composite fiber layer is damaged and unable to adequately bear the load. Consequently, a vessel's ability to withstand high

Table 1.1 : List of defects, causes and their level of criticality to the overall integrity of a COPV

Defect types	Causes	Critical?
Fiber rupture	Cyclical stress, static shocks, cuts, nicks, abrasions	Yes
Delamination	Cyclical stress, static shocks, cuts, nicks, abrasions	Yes
Fibers coming unglued from the matrix	Cyclical stress, static shocks, cuts, nicks, abrasions	Yes
Unraveling of fibers	Shocks, water absorption, UV light exposure, exposure to oxygen, cyclical stress	Yes
Cracks in the matrix	Shocks, water absorption, UV light exposure, exposure to oxygen, cyclical stress	Yes
Holes/indentations	Shocks, falls, compression	Yes
Nicks or abrasions	Wear and tear, shocks, grinding, friction	Yes
Burns	Exposure to heat or open flame	Yes
Porosity / dislocations	Fabrication problems	No
Wrinkles	Fabrication problems	No
Excess resin	Fabrication problems	No
Foreign object inclusion	Fabrication problems	No
Global deformation	Internal pressure, rupture of the liner, defects already present	Yes
Local Deformation	Poor design, where one part of the bottle is weaker than the rest	Yes
Liner Deformation	Degradation of the composite making up the liner	Yes
Cracks in the liner	Cyclical loading or pressure and/or temperature	Yes

pressures can be rendered ineffective if the composite layer undergoes certain damage types, especially ones that weaken its principal strength, namely the fibers themselves. However, since the composite fiber layer is formed by wrapping over the polyamide liner, an alteration to the geometry of the liner is necessarily harmful to the structural integrity of the over-wrapped layer.

The industrial partners for the H2E project have compiled a list of the most probable defect types, which is shown below in Table 1.1. This table should not be considered all inclusive, but it does encompass a large majority of the defect types that are to be expected during the regular life cycle of a COPV. Note that a large majority of the defect types affect primarily the composite fiber layer and, in particular, the outer extremity of the vessel. Specifically, critical issues dealing with fiber failings such as ruptures or delaminations can often stem from (or be attributed to) cuts and abrasions, which necessarily occur on the outside of the vessel.

Whereas the metal-based pressure vessels mentioned in section 1.1 have failure modes that are fairly well understood (for example, analytical solutions for homogenous, isotropic cylinders exist) the complexity of COPV's warrants an experimental validation of their performance [10]. The pressure vessels in the H2E project have thus undergone several different performance evaluating tests. Cyclical pressure loading, for instance, at 1.5 times the intended pressure allows the engineers to evaluate the performance of such tanks if they happen to be exerted to extreme conditions. These tests can help ensure that the intended design will not fail during normal intended use.

Other common failure tests include:

a) Cut and gouge testing

b) Impact damage tests

c) Heat damage tests

d) Fatigue testing through pressure cycling

e) Stress rupture testing

f) Environmental Testing

This study intends to answer some fundamental questions concerning the implementation of an SHM system in a COPV. To that end, specific damage types need to be chosen that are deemed elementary and critical. Furthermore, it would be beneficial at this early stage of the H2E project to investigate damage types that can be experimentally replicated, so damaged specimens could be taken from routine testing. This is to say that the defects to be studied are ideally those being experimentally inflicted on the samples by our industrial partners.

1.2.2 Defects to be studied

This study is an essential primary step toward the ultimate goal of the design of a complete SHM system implemented in a COPV. However, to limit the scope of this study, three specific damage types will be investigated. This is not to belittle the importance of all the damage types in Table 1.1, but rather to ensure that a few fundamental damage types are investigated thoroughly. (Furthermore, it is worthy of note that this project is being carried out in terms of a much larger project; other partners have been assigned to look at some of the other damage types.)

Consequently this study aims to investigate a few of the causes of critical failure due to fiber rupture:

- Surface originating cracks or cut-type defects caused either from the further propagation of micro-cracking (due to surface impacts) or gauges / cuts

- Abrasions (defined as the decrease in carbon-epoxy layer thickness due to rubbing or grinding against external structures)

Furthermore, since changes in liner geometry can also be considered critical, a third defect type will be examined; it is caused by either rapid depressurization, or the cyclical loading and unloading of high pressures:

- Disbonding or `collapse defect' (defined specifically as the detachment of the polyamide liner from the over-wrapped carbon epoxy matrix. As thus defined, disbonding is specifically and explicitly different from delaminations, which is defined rather as separation of fibers within the carbon epoxy matrix.)

There are several tanks sizes used in the H2E program, but the specific application for this study is a 2.5 L COPV. Nevertheless, the defects investigated here (surface-originating cracks or cuts, disbonds, and abrasions) are general enough that they occur in many different materials and applications. As a result, the work produced in this study, although immediately beneficial to the H2E program, has implications in a much larger range of SHM problems.

1.3 Monitoring Technique Selection

Ultimately, the NDT method that will eventually be developed must allow the manufacturer (in our case: Air Liquide) to examine if the pressure vessels can remain in service or must be replaced because a defect has occurred and has the possibility to grow to critical level. Accordingly, early detection is key, and although identification of damage is important, sizing of the damage will testify to its criticality. At this stage of the project, localization, although certainly helpful, is less important, whereas identification and sizing give more information as to the necessity of replacing the vessel.

1.3.1 Existing Monitoring Techniques and Methods

The requirement to find NDT methods modified to fit SHM needs is apparent and obvious for this endeavor. Storage tanks that will eventually be used in transportation available to the general public must be safe, and the tolerance for failure is zero. With this in mind several NDT methods are being evaluated by our industrial partners to assess their potential success in an eventual SHM system, including: visual inspection, hydraulic testing, acoustic emission, fiber-optics, and ultrasonic methods (guided waves, and bulk waves). Each technique is evaluated based on cost, reliability, technical complexity, and sensitivity.

Visual inspection, although simple, has unfortunately many drawbacks. First of all, a SHM technique based on visual inspection is practically impossible, since it would require having a user physically watch the tank at all times [11]. Additionally, periodic inspection is also unfeasible, since the tanks are refillable, and are intended to stay *in situ*. As a final nail in the proverbial coffin, visual inspection has known to be unreliable for COPV’s due to the difficult-to-see critical damage types.

Hydraulic Testing, although informative, is not strictly non-destructive, since it involves the cyclical pressurization of the COPV to 150% its intended pressure maximum. Therefore if a defect is present, the vessel will almost certainly rupture, and at best its condition will worsen at such extreme conditions. This however, is a testing process that our industrial partners perform on the tanks to ensure that they are ready for field use.

Another technique involves the embedding of optical fibers in the COPV itself. Previously, other researchers [12] have shown that optical fibers show promise for the detection of some properties such as internal pressure and temperature. However, these optical fiber sensors such as Fiber Bragg Grating optical sensors

(FBG) are known to be extremely delicate and hard to implement. Furthermore, their implication would have to be incorporated into the design/manufacturing stages, since they are most decidedly embedded in the structure itself. Nevertheless, another partner in the H2E program has been charged with the task of evaluating an optical fiber solution to our SHM on COPV problem.

Ultrasonic C-scans have many positive attributes, and are generally well documented and understood [13, 14]. One such attribute is that they are fairly thorough and can detect extremely small damage, depending on the frequency used [15]. A range of post-processing techniques in both the temporal domain and frequency domain have been shown to be able to detect changes in layer thickness, the presence of internal cracks, and changes to material properties such as Young's modulus, which can be an indication of moisture content (for example) [16, 17, 18]. However, the implementation of such a scan dictates a scanning apparatus; this in turn means a robotic or movable portion. Such a configuration would not only be costly to develop, but impractical *in situ*.

Acoustic Emission (AE) is an NDT method that works under the principle that the formation (or eventual evolution) of damage sites can act as a source for structurally borne sound waves [19, 20]. Therefore, if a system of permanently placed PZTs is available to witness and record their initial formation, these damage sites can be immediately identified, or at least detected [21, 22]. An advantage of this solution method is that it fulfills the goal of being a real-time, continuous monitoring system. In fact, if the investigation does not happen in real-time, which is to say when the defect initially occurs, then detection may not even be possible, since its formation is what acts as the initial source. Eventually if the sensors are rendered temporarily ineffective, then the formation of the defect will go unnoticed. Furthermore, the inspection cannot be conducted statistically, so this method is more susceptible to the effects of environmental noise. Nevertheless, the H2E program plans on eventually having a SHM system that incorporates both UGW and AE, and accordingly have assigned another industrial partner to work on determining the best course of action for detecting elementary defect types based on their emitted structurally borne sound.

Ultimately, a non-destructive technique that makes use of structure-borne sound as in AE, but inspects the structural integrity of the structure independent of the damage formation time (thus capable of making statistically thorough measurements) would be an optimal solution. An inspection method utilizing Ultrasonic Guided Waves (UGW) and permanently attached PZT's that act as both emitters and receivers fits those criteria. Consequently, this study aims at investigating the propagation of UGW in the novel environment, as well as said waves interaction with the defects identified in section 1.2.2. The following section will present some of the advantages and limitations associated with UGW SHM systems, as well as provide a brief and broad literature review, covering a few of the major and pertinent advances in the use of UGW in NDT and SHM. The list of references discussed is by no means all-inclusive. For a complete list of references, see the reference section.

1.3.2 Ultrasonic Guided Waves Technique

Ultrasonic Guided Waves (UGW) have many properties ideal for NDT endeavors. Intrinsically, UGW travel along wave guides such as plates, pipes, rods, etc., covering larger distances than traditional tools, such as C-scans which inspect these structures point by point [23]. Furthermore, unlike C-scans, UGW techniques have the potential of being permanently attached to the structure in question, which make them ideal for SHM systems. The application range of UGW NDT systems has been expanded to more complex materials and geometries, with considerable effort being directed at implementing these systems for the purpose of damage detection in anisotropic composites [24, 25].

Worlton [26] is often attributed for being the first to identify the potential usefulness of Lamb waves in NDT. Worlton successfully demonstrated implementing Snell's Law for the purpose of exciting and detecting certain modes at a given frequency-thickness. Furthermore, he displayed mathematically that the first few modes were essentially Rayleigh waves for large values of frequency-thickness and his verification of this demonstrated the importance of mode selection in terms of modal shape. Mode and frequency range selection have continued to be important aspects of the successful implementation of UGW in NDT. This was extended to the case of composites by Percival and Birt [27]. By examining the stress distributions, it became clear that mode selection would play an important role in determining what type of damage could be identified and localized.

The dispersive nature of Lamb waves has also been a point of interest concerning their application in NDT. Alleyne and Cawley [28] determined that waveforms could be simplified by intelligently choosing a frequency range below the higher mode cut-off frequency, and in a range of relatively low dispersion. Wilcox *et al.* [29, 30, 31] attacked the problem of dispersion differently, claiming that it is not always necessary to avoid operating in dispersive frequency regions as long as the dispersive nature is well understood. These regions can be characterized in terms of their limiting impact on resolution [29] which may furthermore be temperature dependent [31], or the effects of dispersion may be dealt with in a post-processing environment given certain a priori information, such as analytically or experimentally determined dispersion curves [30]. This latter technique is more generally referred to as dispersion compensation, and has been employed by a host of other researchers in some form or another.

The ability to determine the amplitude of individual overlapping modes is critical. As has been previously mentioned, each mode corresponds to a different modal shape and correspondingly interacts with defects uniquely. Furthermore, the dispersive nature of Lamb waves leads to the temporal spreading of wave packets which complicates the separation of modes in the time domain [32]. Alleyne and Cawley used the idea of a two-dimensional fast Fourier transform (2DFFT) applied to equally spaced waveforms in order to resolve the modes in the frequency-wavenumber space [33]. Hall and Michaels presented a Model Based Parameter Estimation (MBPE) algorithm that assumes a theoretical description of a wave's propagation and uses the waveforms collected from a sparse array of transducers to determine the amplitude of various modes. The algorithm as presented in reference [34] was limited by the necessity of temporal modal separation. The Short-Time Fourier Transform (STFT) method has also been used to determine modal amplitudes and dispersion curves, but only in terms of group velocity [35]. However, one advantage of the STFT method that is particularly enticing is the prospect of measuring dispersion curves using only two recorded signals. Unfortunately, Zhao *et al.* first noticed that there is a noticeable difference between actual dispersion curves and those measured directly by the STFT [36].

More recently, a group at the University of Bordeaux has been investigating NDT of composite reinforced metal cylinders using UGW. Levels of humidity and microcracks caused by very low temperatures were monitored by comparing semi-analytical models to actual measured values [24, 37]. These studies showed that specific parameters, e.g. attenuation or change in wavenumber, can be targeted to help keep track of a specific type of change in material health. Disbonding between an anisotropic composite tank and its isotropic liner was investigated by comparing an actual experimental case with a non-cylindrical, planar finite element model assessed in the frequency domain via a formulation of the Helmholtz equation [38].

To summarize, systems utilizing UGW's have significant potential for SHM and NDT. Techniques involving UGW are expanding rapidly to many different areas of manufacturing and in-service inspection [23, 39, 40, 41, 42, 43, 44]. This is mainly due to their:

- relatively long propagation distance,
- propagation in the whole wall thickness of the structure to be tested/monitored, which allows to detected inner (volumetric) defects,
- sensitivity to anomalies along the propagation path,
- ability to be used to detect defect from one side (useful to detect defects in inaccessible areas).

These benefits make it a serious candidate for resolving our problem, which concerns the monitoring of COPVs. Despite the well-known advantages of UGW techniques, it is often complicated by the existence of a multitude of propagating modes, wave dispersion, attenuation, etc. [45]

1.4 Problem Statement and Methodology

1.4.1 Research Purpose and Objectives

The purpose of this study is to investigate the propagation of ultrasonic guided waves in a thick-walled composite over-wrapped pressure vessel intended for hydrogen storage, for the purpose of structural health monitoring. The objectives of this study are to verify that a system based on UGW is capable of identifying and sizing the isolated occurrence of three damage types, namely, surface-originating cracks (or cuts), abrasions, and disbonds in the central, cylindrical portion of the given COPV.

Figure 1.1: Example of a multi-layer composite vessel intended for housing Hydrogen gas at high pressures: overview (left) and sectional view (right).

To this end, this fundamental study will determine appropriate methods of excitation and reception, an optimal operational frequency range, and propose post-processing techniques for damage detection and sizing.

1.4.2 Methodology

In order to fulfill the purpose and complete the objectives determined in section 1.4.1, a methodology was developed. In accordance with section 1.3.2, the method of defect detection employed utilizes UGW propagation. The methodology is presented here.

Piezo-electric transducers (PZTs) can be permanently attached to a structure to act as the emitters and receivers of UGW in a SHM system [46]. Eventually, the adhesive used to permanently attach the PZTs has the dual purpose of holding the PZTs in place and acting as a coupling medium. Furthermore, the PZTs can be attached to the outer surface of the COPV, meaning that their inclusion will not alter the design process, they will not undergo drastic ambient pressure changes, and they can be easily reached for maintenance.

The underlying principle that will be employed in this study for the purpose of defect detection consists of monitoring the modal amplitudes of UGW in the reflection and transmission fields of a defect. That is to say, when a UGW mode interacts with a damage site, its energy is converted into several different modes in both the reflection and transmission fields. This set of new modal amplitudes can be compared with what would exist in a healthy specimen, i.e. those that were initially sent by the emitting transducer. In other words, we assume each defect type (and size) has a modal amplitude “fingerprint” by which it can be identified.

The thicknesses of the various layers are considered constant in the principal cylindrical portion of the vessel (in the absence of damage) along the axial and circumferential directions: roughly 2 mm for the polyamide liner, and 8 mm for the carbon-epoxy layer (see figure 1.1). Due to the fundamental nature of this study, the endcaps of the reservoir will be ignored for the remainder of this work (see figure 1.2). Although the spherical end caps may also undergo damage, this present work will focus on the cylindrical central portion of the reservoir that makes up the majority of its surface area. Furthermore, it will be assumed that the wave excitation and reception is sufficiently far away from the endcaps that any reflection/mode conversion due to such an interaction can be ignored. This is not to say that the endcaps are not susceptible to damage, but rather that the complication of their respective geometry renders their simulation and investigation outside of the scope of this fundamental study. Nevertheless, it can be said that the work done here informs the eventual inspection of the endcaps. For more on the eventual effect of the endcaps, see Chapter 7.

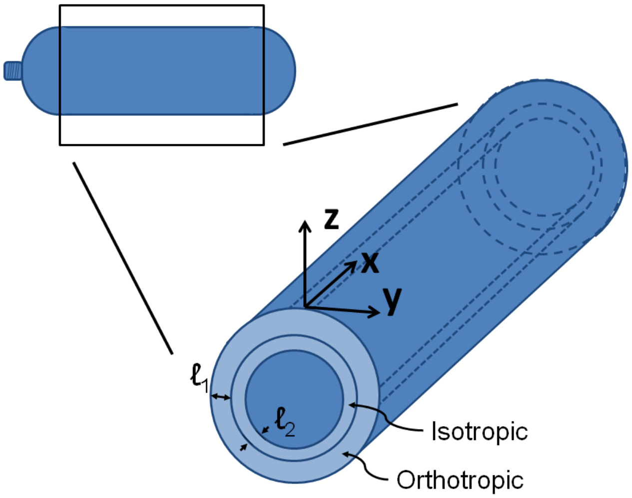

Figure 1.2: Present study focuses on the annular cylindrical portion of the COPV, the portion that makes up the vast majority of the surface area. A Cartesian coordinate system has been superimposed where x is along the axial direction and y is tangential to the cylindrical surface. The principal directions of the orthotropic layer are aligned with the Cartesian coordinate frame.

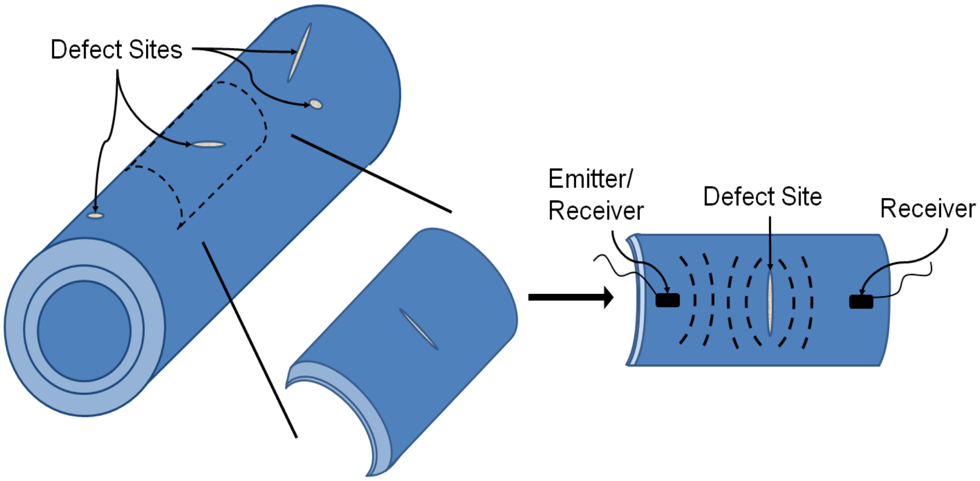

Figure 1.3 : Fundamental study presents the interaction of UGW with an isolated defect

Thus, the work presented in this study investigates not only UGW propagation in the thick, multi-layer COPV, but also said guided waves' interaction with the three defect types specified in section 1.2.2. These interactions will be studied in an ideal and isolated manner, which is to say each defect will be studied individually without the presence of other defects, as shown in figure 1.3. In this way, this study will present the essential building-blocks necessary to the engineers who will eventually design the SHM system.

A Cartesian coordinate system has been assigned in figure 1.2, where the 'x' direction is parallel to the axis of the cylinder, the 'y' axis is tangent to the surface and 'z' is perpendicular to the surface. This basis orientation facilitates the description of UGW propagating in a direction parallel to the cylindrical axis, which is a natural choice for non-destructive inspection.

It is of relevance to address the limitations of this methodology. This methodology is limited in the sense that it precludes the possibility of several damage sites in the zone being monitored. It also is limited in its scope in that:

- It covers only the cylindrical portion
- It does not cover the whole cylindrical portion but just a section since normally there would be a whole network of transducers, and we are only looking at one emitter/receiver pair. See figure 1.3.

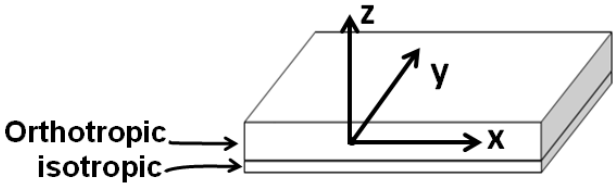

Figure 1.4: Planar Approximation

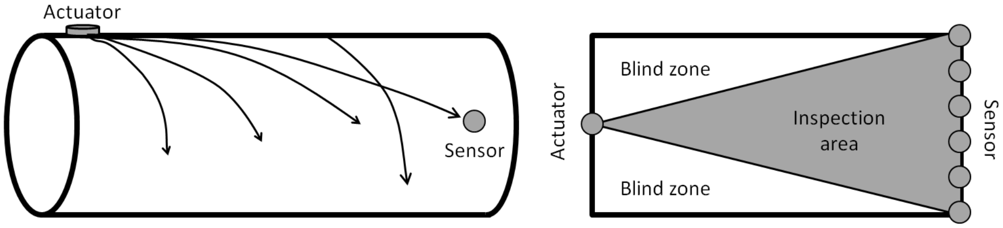

Figure 1.5: (left) There are an infinite number of paths, but only one direct path between the emitting actuator and the receiving sensor. (right) Inspection coverage and blind zones of a pipeline using only one actuator and several sensors in a pitch-catch configuration [47]

Certain assumptions can be made to further simplify the mathematical models. The following subsections will address those assumptions.

1.4.2.1 Influence of Cylindrical Curvature (Planar Approximation)

It is immediately evident that a cylindrical environment is inherently more complicated that its planar counterpart [48, 49]. However, it was verified by Wilcox *et al.* [37] that if the ratio of the radius of an annular cylinder to its layer thickness is greater than or equal to 8, the waves propagating in the cylindrical structure will do so in the same manner as they would a plate of equal thickness. For our structure, the reservoir radius to wall thickness ratio is roughly 8, and is therefore right at the limit of plate-approximation proposed by Wilcox *et al.*

Consequently the wave fields are assumed to propagate as they would in a plate of equal thickness (see figure 1.4). In general, one can imagine the possibility of an infinite number of ray paths propagating away from the actuating PZT along the cylindrical wave guide as shown in figure 1.5. However, only one of those rays can be considered a direct arrival between the actuator and the sensor. The direct ray is the usual inspection path in the planar case for UGW. If a series of sensors is placed in the circumferential direction, an inspection area can be determined as being the triangular area between the emitter and the two extreme end sensors, as shown in the right hand side of figure 1.5, effectively broadening the inspected area from a 2D ray to a 3D area. Using an intelligently placed array of transducers, eventually the entire cylindrical portion of the reservoir can be inspected in this manner.

It is noteworthy that of the three Cartesian coordinate directions, one is aligned with the axial direction of the cylinder, and one is aligned with the surface vector, i.e. perpendicular to the surface of the cylinder. Previously other researchers have worked on vessels with similar yet less complicated geometry, and have made similar assumptions [37, 24].

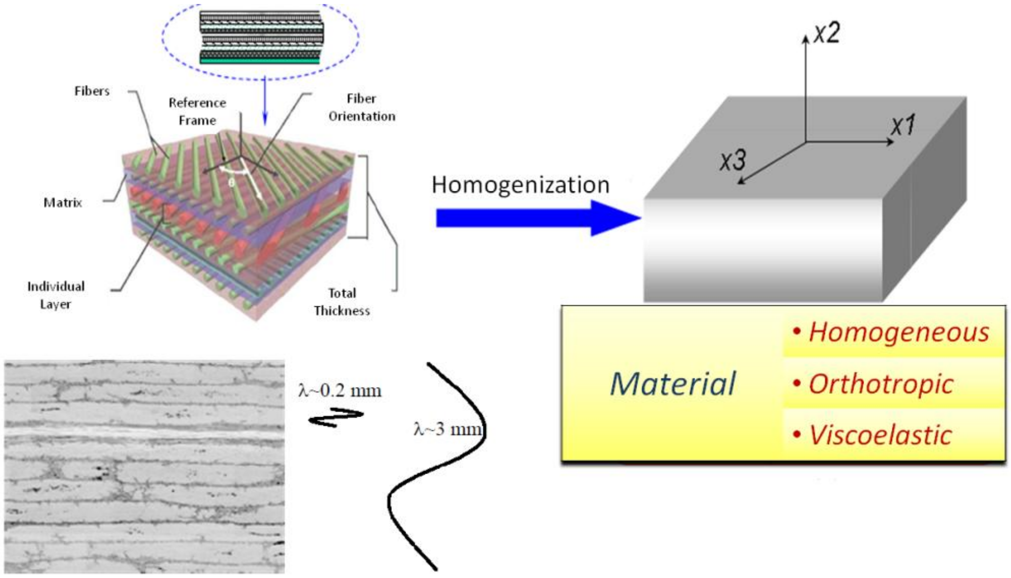

Figure 1.6: Homogenization, and other bulk material properties of a multi-layer composite plate [37, 50]

1.4.2.2 Material Behavior

The complexity of multi-layer composite epoxy materials is due to their heterogenic and anisotropic nature [50]. Wave propagation in such materials is, in general, strongly affected by these two material qualities. It is well known that a mismatch in acoustic impedance causes reflection and transmission phenomena [51]. In a composite, reflection and transmission phenomena occur constantly since structural-borne waves are propagating in a medium where acoustic impedance is essentially a three-dimensional function of position. Even if the change in acoustic impedance is slight, recorded signals are characterized by structural noise dependant on the nature of the composite [50].

Materials can be assumed to be anisotropically homogeneous with respect to the propagating wavelengths. The carbon fibers (and glass fibers) in the composite epoxy layers have diameters approximately equal to 7 μm, whereas the propagating ultrasonic waves have wavelengths on the order of mm (see Chapter 2 for a discussion on frequency range). Considering the relative size of the fiber diameter to the range of wavelengths, it is possible to consider the material to be macroscopically homogeneous, i.e. its heterogeneous nature is not relevant on this scale [50, 52].

Our industrial partners have been able to supply a C-matrix for the thick, load-bearing, carbon-epoxy layer, and according to their measurements, it macroscopically behaves orthotropically. This has significant implications for the study of the structure, specifically in the finite element analysis, which will be further discussed in later chapters (see section 1.5).

A common method of accounting for viscoelastic effects in mathematical models involves using complex values instead of purely real values in the C-matrix. The real part therefore corresponds to the directionally dependent elasticity constant, and the imaginary portion causes an exponential decrease in amplitude with respect to propagation distance [53]. In this work, the material elasticity constants have been obtained by our industrial partners, assuming a purely elastic material that is macroscopically orthotropic (see section 4.2.2.2). To account for viscoelastic effects, an imaginary portion is added to the non-zero C-matrix values. The viscoelastic effect is, however, assumed to behave isotropically and thus the imaginary portion is the same for every non-zero C-matrix value in the propagation domain. The perfectly matched boundary layers will use a cubically increasing imaginary portion to effectively dampen unwanted edge reflections.

1.4.3 Practical Restrictions

Certain practical restrictions are often imposed on real-world experimental setups. It is often the case that only one side of a bilayer structure is accessible to ultrasonic transducers (be it contact, or non-contact inspection). As a matter of practicality, the work here is limited to excitation and detection solely on the carbon-epoxy surface. This has direct implications in choosing the optimal frequency and modes of interest, since transducers will favor modeshapes with greater displacements occurring at that surface.

Several other restrictions are self-imposed to help limit the scope of the present work. Only out-of plane displacement on the top surface of the structure will be monitored as a means of reception, since out-of-plane motion on the surface of the plate is not only accessible, but a common parameter monitored by already existing SHM methods [54]. Damage detection will be accomplished via the appearance (or change in amplitude) of modes in the transmission and reflection field after the incident wave interacts with the damage site. Propagating modes can be distinguished by the receiving method, and can be accomplished via a variety of means, for example, through intelligent angling of air-coupled transducers according to Snell's law [26], applying a short-time Fourier transform (STFT) to a single waveform [35], or a spatial Fourier transform to a series of evenly spaced waveforms, which coincidently is how modes are distinguished in this work.

1.4.4 Finite Element as an Optimization Tool

1.4.4.1 Benefits of FEM (Numerical Modeling)

Predictions made via numerical simulations are highly beneficial for the optimization of experimental procedures [55, 56]. Numerical simulations can offer insight into the nature of wave propagation phenomena and help explain experimental results. Furthermore if the simulations accurately reflect physical trials, then they can help save time and money; the number of expensive and time consuming experimental setups can be reduced. As a final point, numerical analysis carried out in the temporal domain can be used directly to demonstrate post-processing techniques on experimentally collected data in a best case scenario with regards to the Signal-to-Noise Ratio (SNR). That is to say, the lower limits of a method can be determined in the absence of noise due to instruments or heterogeneity.

The Finite Element Method (FEM) is a tool commonly used to investigate Lamb waves' interaction with various damage types [57, 58, 59, 60]. In essence, the FEM numerically solves a governing partial differential equation over a discretized domain, using an interpolation function between discrete points. In our present study, the assumption has been made that the wave motion in the novel environment can be described by the well understood wave equation, altered to allow for general material anisotropy. Currently there are several commercially available FEM software packages such as Ansys[61], Abaqus [62], Comsol[63], etc.

In summary, the FEM allows for:

- an understanding of waves' behavior even in complex waveguides [64, 65, 66]
- the simulation of interactions between waves and realistic defects (with arbitrary forms and sizes) [67, 59, 68, 69]
- the simulation of the generation of a pure mode [70],
- the optimization of the size and sensitivity of sensors and actuators [71, 72]

As for the impact of the experimental findings on the modeling, the results can be used to change parameters to induce the same sort of effects on wave-number or primary frequency attenuation to imitate damage. For instance, an increase in the imaginary component of the Young's modulus can be used to affect attenuation of the fundamental antisymmetric mode only without significantly changing the wave-numbers just as how moisture content affected the sample in the experiments.

Similarly, reducing the real parts of elements of the stress matrix can affect wave-numbers, just as micro-cracking demonstrated experimentally.

1.4.4.2 Choice of Software

Of the FEM softwares commercially available, COMSOL Multiphsyics^{TM} has the advantage of being readily available at Georgia Tech Lorraine, has a script feature similar and compatible to MATLAB, allows for flexibility in solving systems with multiple governing equations of several forms, and has already been verified by other researchers at successfully simulating the propagation of UGW. However, the acoustics module only supports the propagation of pressure waves, so the general multi-physics module will be used in the structural mechanics mode, which is governed by a more general vector equation. Of note, the time-dependent solver in COMSOL is implicit.

1.5 Outline of the Dissertation

The remainder of this thesis is organized as follows:

> Chapter 2: an analytical study is presented on UGW characteristics, especially dispersive properties. Material properties are defined. The effects of layer thickness, number of layers, attenuation, and anisotropy are discussed
>
> Chapter 3: the numerical environment is introduced and the governing equations needed in the temporal and frequency domains are discussed. Wave propagation is presented for the case of a healthy (defect free) specimen.
>
> Chapter 4: the necessary boundary conditions and/or geometrical changes needed to simulate the defects of interest are defined. A post-processing

technique is proposed to help identify small amounts of modal conversion and consequently small defects.

Chapter 5: an optimization study is conducted based on the finite element simulations discussed in chapters 3 and 4. Key investigated parameters include frequency range, transducer type, receiver placement and modal selection.

Chapter 6: Experimental work that informs and validates the finite element simulations is presented. An experimental setup is defined for future researchers.

Chapter 7: Conclusions and suggestions for future work are presented.

1.6 Summary

The current use of natural gas to power the majority of the world's transportational means is unsustainable. Hydrogen is potentially a more environmentally friendly energy carrier, however implementation of hydrogen in transportational technologies is complicated by the complexity of its storage system. Composite over-wrapped high-pressure vessels are an attractive solution to the storage problem due to their high strength-to-weight ratio, but their structural integrity must be ensured at all times through non-destructive testing methods. The Institut de Soudure has tabulated a list of common defects and evaluated them with respect to their critical nature. The goals of this study are to verify that a system based on UGW is capable of identifying and sizing the isolated occurrence of three damage types, namely, surface-originating cracks (or cuts), abrasions, and disbonds in the central, cylindrical portion of the given COPV. Methods of excitation and reception, an optimal operational frequency range, and post-processing techniques for damage detection and sizing will be investigated.

Certain assumptions will be made concerning material properties and geometry to simplify the problem, such as homogeneity, orthotropicity, planarity, etc. The problem will be investigated numerically via the commercially available finite element software, COMSOL. This numerical investigation will be used to optimize eventual SHM systems and explain experimental findings.

1.7 References

[1] S. Sunita, J. Petrovic, C. Read and G. Thomas, "The U.S. Department of Energy's National Hydrogen Storage Project: Progress towards meeting hydrogen-powered vehicle requirements," *Catalysis Today,* vol. 120, pp. 246-256, 2007.

[2] Air Liquide, [Online]. Available: http://www.airliquide.com/en/air-liquide-launches-the-horizon-hydrogen-energy-h2e-program.html .

[3] A. Dillon and M. Heben, "Hydrogen storage using carbon adsorbents: past, present and future," *Applied Physics A,* vol. 72, pp. 133-142, 2001.

[4] S. M. Aceves, F. Espinosa-Loza, E. Ledesma-Orozco, T. O. Ross, A. H. Weisberg, T. C. Brunner and O. Kircher, "High-density automotive hydrogen storage with cryogenic capable pressure vessels," *International Journal of Hydrogen Energy,* vol. 35, pp. 1219-1226, 2010.

[5] J. M. Zielinski, P. McKeon and M. F. Kimak, "A Simple Technique for the Measurement of H2 Sorption Capacities," *I&EC,* vol. 46, 2007.

[6] B. C. Lung, "A structural health monitoring system for composite pressure vessels," Saskatoon, 2005.

[7] P. D. Mangalgiri, "Composite materials for aerospace applications," *Bulletin of Material Science,* vol. 22, no. 3, pp. 657-664, 1999.

[8] U. Sundararaj and O. Breuer, "Big returns from small fibers: a review of

polymer/carbon nanotube composites," *Polymer Composites,* pp. 630-645, 2004.

[9] C. L. Davis, M. Papaelias and C. Roberts, "A review on non-destructive evaluation of rails: state-of-the-art and future developments," *Prod. I Mech E,* vol. 222, pp. 367-384, 2008.

[10] B. Su and G. S. Bhuyan, "Effect of composite wrapping on the fracture behavior of the steel-lined hoop-wrapped cylinders," *International Journal of Pressure Vessels and Piping,* vol. 75, pp. 931-937, 1998.

[11] Y. Zou, L. Tong and G. P. Steven, "Vibration-based model-dependent damage (delamination) identification and health monitoring for composite structures - a review," *Journal of Sound and Vibration,* vol. 230, no. 2, pp. 357-378, 2000.

[12] C. Frias, H. Faria, O. Farzao, P. Vieira and A. Marques, "Manufacturing and testing composite overwrapped pressure vessels with embedded sensors," *Materials and Design,* vol. 31, pp. 4016-4022, 2010.

[13] Lemistre, "Structural health monitoring system based on diffracted Lamb wave analysis by multiresolutional processing," *Smart Material Structures,* pp. 504-511, 2001.

[14] P. Cawley, "The rapid non-destructive inspection of large composite structures," *Composites,* vol. 25, no. 5, pp. 351-357, 1993.

[15] C. Miyasaka, B. R. Tittmann and S.-I. Tanaka, "Characterization of stress at a ceramic/metal joined interface by the V(z) technique of scanning acoustic microscopy," *Journal of Pressure Vessel Technology,* vol. 124, pp. 336-342,

2002.

[16] H. Sakai, A. Minamisawa and K. Takagi, "Effect of moisture content on ultrasonic velocity and attenuation in woods," *Ultrasonics,* vol. 28, pp. 382-385, 1990.

[17] E. Blomme, D. Bulcaen and F. Declercq, "Air-coupled ultrasonic NDE: experiments in the frequency range 750 kHz - 2 MHz," *NDT&E International,* vol. 35, pp. 417-426, 2002.

[18] J.-K. K. Shang-Lin Gao, "Scanning acoustic microscopy as a tool for quantitative characterisation of damage in CFRPs," *Composites Science and Technology,* vol. 59, pp. 345-354, 1999.

[19] T. Holroyd and N. Randall, "USE OF ACOUSTIC-EMISSION FOR MACHINE CONDITION MONITORING," *BRITISH JOURNAL OF NON-DESTRUCTIVE TESTING,* vol. 35, no. 2, pp. 75-83, 1993.

[20] W. Staszewski, S. Mahzan and R. Traynor, "Health monitoring of aerospace composite structures – Active and passive approach," *Composites Science and Technology ,* vol. 69 , p. 1678–1685, 2009.

[21] T. Toutountzakis and D. Mba, "Observations of acoustic emission activity during gear defect diagnosis," *NDT&E International,* vol. 36, no. 7, pp. 471-477, 2003.

[22] X. P. Qing, H.-L. Chana, S. J. Bearda, T. K. Ooib and S. A. Marotta, "Effect of adhesive on the performance of piezoelectric elements used to monitor structural health," *International Journal of Adhesion & Adhesives,* vol. 26, pp. 622-628,

2006.

[23] J. L. Rose, "Ultrasonic Guided Waves in Structural Health Monitoring," *Key Engineering Materials,* pp. 270-273, 2004.

[24] M. Castaings and B. Hosten, "Ultrasonic guided waves for health monitoring of high-pressure composite tanks," *NDT&E International,* no. 41, pp. 648-655, 2008.

[25] S. Grondel, C. Paget, C. Delebarre and J. Assaad, "Design of optimal configuration for generating A0 Lamb mode in a composite plate using piezoceramic transducers," *Journal of the acoustical society of America,* vol. 112, no. 1, pp. 84-90, 2002.

[26] D. Worlton, "Experimental confirmation of Lamb waves at megacycle frequencies," *Journal of Applied Physics,* vol. 32, no. 6, pp. 967-971, 1961.

[27] E. A. Birt and W. J. Percival, "A study of Lamb wave propagation in carbon-fibre composites," *INSIGHT,* vol. 39, no. 10, pp. 728-735, 1997.

[28] P. Cawley and D. N. Alleyne, "Optimization of Lamb wave inspection techniques," *NDT&E International,* vol. 25, no. 1, pp. 11-22, 1992.

[29] P. Cawley, P. Wilcox and M. Lowe, "The effect of dispersion on long-range inspection using ultrasonic guided waves," *NDT&E International,* vol. 34, pp. 1-9, 2001.

[30] P. D. Wilcox, "A rapid signal processing technique to remove the effect of

dispersion from guided wave signals," *IEEE,* vol. 50, pp. 419-427, 2003.

[31] G. Konstantinidis, A. J. Croxford, P. D. Wilcox and B. W. Drinkwater, "Strategies for guided-wave structural health monitoring," *Proceedings of the Royal Society A,* vol. 463, pp. 2961-2981, 2007.

[32] W. Sachse and Y.-H. Pao, "On the determination of phase and group velocities of dispersive waves in solids," *Journal of Applied Physics,* vol. 49, no. 8, pp. 4320-4327, 1978.

[33] P. Cawley and D. N. Alleyne, "A two-dimensional Fourier transform method for the meausrement of propagating multimode signals," *Journal of the Acoustical Society of America,* vol. 89, no. 3, pp. 1159-1168, 1991.

[34] J. E. Michaels and J. S. Hall, "A model-based approach to dispersion and parameter estimation for ultrasonic guided waves," *Journal of the Acoustical Society of America,* vol. 127, no. 2, pp. 920-930, 2009.

[35] L. J. Jacobs and M. Niethammer, "Time-frequency representation of Lamb waves using the reassigned spectrogram," *Journal of the Acoustical Society of America,* vol. 107, no. 5, pp. 19-24, 2000.

[36] G. Mittal, B. Zhao and O. Basir, "Estimation of ultrasound attenuation and dispersion using short time Fourier transform," *Ultrasonics,* vol. 43, pp. 375-381, 2005.

[37] M. Cinquin, "Suivi par Ondes Guidees de l'Etat de Sante de Reservoirs

Composites," Universite de Bordeaux, Bordeaux, 2004.

[38] W. Ke, "Simulations 3D de la Generation et de la Reception d'Ondes Guidees - Application a la Detection de Defauts dans des Structures Composites," University of Bordeaux, Bordeaux, 2009.

[39] A. Demma, P. Cawley, M. Lowe, A. Roosenbrand and B. Pavlakovic, "The reflection of guided waves form notches in pipes: a guide for interpreting corrosion measurements"," *NDT&E International,* vol. 37, pp. 167-180, 2004.

[40] S. Lebsack, "Guided wave ultrasonic inspection and verification studies of buried pipelines," January 2014. [Online]. Available: www.ndt.net/article/wcndt2004/pdf/guided_waves/818_lebsack.pdf.

[41] M. Lowe, D. Alleyne and P. Cawely, "Defect detection in pipes using guided waves," *Ultrasonics,* pp. 147-154,, 1996.

[42] Y. Cho, J. Jung and J. Kim, "A study of guided ultrasonic wave application for heat exchanger performance improvement," *Advanced Non-Destructive Evaluation,* pp. 443-449, 2007.

[43] S. Sharma and A. Mukherjee, "Longitudinal Guided Waves for Monitoring Chloride Corrosion in Reinforcing Bars in Concrete," *Structural Health Monitoring,* no. 9, p. 555–567, 2010.

[44] C. Doherty and W. Chiu, "Scattering of ultrasonic-guided waves for health monitoring of fuel weep holes," *Structural Health Monitoring,* vol. 11, pp. 27-42,

2012.

[45] W. Staszewski, B. C. Le and a. R. Traynor, "Fatigue crack detection in metallic structures with Lamb waves and 3D laser vibrometry," *Measurement Science and Technology,* vol. 18 , p. 727–739, 2007.

[46] J. Hall, P. McKeon, L. Satyanarayan, J. E. Michaels, N. F. Declercq and Y. Berthelot, "Minimum variance guided wave imaging in a quasi-isotropic composite plate," *Smart Materials and Structures,* vol. 20, 2011.

[47] Z. Su and L. Ye, Identification of Damage Using Lamb Waves: From Fundamentals to Application, Berlin: Springer-Verlag, 2009.

[48] M. Kley, C. Valle, L. J. Jacobs, J. Qu and J. Jarzynski, "Development of dispersion curves for two-layered cylinders using laser ultrasonics," *Journal of the Acoustical Society of America,* vol. 106, no. 2, pp. 582-588, 1999.

[49] C. Valle, J. Qu and L. J. Jacobs, "Guided circumferential waves in layered cylinders," *International Journal of Engineering Science,* vol. 37, pp. 1369-1387, 1999.

[50] N. Dominguez, O. Grellou and S. Van-der-Veen, "Simulation of ultrasonic NDT in composite radius," in *European Conference on NDT*, Moscow, 2010.

[51] D. T. Blackstock, Fundamentals of Physical Acoustics, Canada: John Wiley and Sons, 2000.

[52] S. H. D. Valdes and C. Soutis, "Real-time nondestructive evaluation of fiber

composite laminates using low-frequency Lamb waves," *Journal of the Acoustical Society of America,* vol. 111, no. 5, pp. 2026-2033, 2002.

[53] M. Castaings and B. Hosten, "Guided waves propagating in sandwich structures made of anisotropic, viscoelastic, composite materials," *Journal of the Acoustical Society of America,* vol. 113, no. 5, p. 2622, 2003.

[54] T. E. Michaels, J. E. Michaels and M. Ruzzene, "Frequency-wavenumber domain analysis of guided wavefields," *Ultrasonics,* vol. 51, pp. 452-466, 2011.

[55] Y. Lin and H. A. Sodano, "Concept and model of a piezoelectric structural fiber for multifunctional composites," *Composites Science and Technology,* vol. 68, pp. 1911-1918, 2008.

[56] T. Hayashi and S. Endoh, "Calculation and visualization of Lamb wave motion," *Ultrasonics,* vol. 38, p. 770–773, 2000.

[57] P. Cawley and D. N. Alleyne, "The interaction of Lamb waves with defects," *IEEE Transaction on Ultrasonics, Ferroelectrics and Frequency Control,* vol. 39, no. 3, pp. 381-396, 1992.

[58] C. Bacon, D. Singh and M. Castaings, "Sizing strip-like defects in plates using guided waves," *NDT~\&~E International,* vol. 44, pp. 394-404, 2011.

[59] L. Moreau and M. Castaings, "The use of an orthogonality relation for reducing the size of finite element models for 3D guided waves scattering problems," *Ultrasonics,* vol. 48, pp. 357- 366, 2008.

[60] L. Moreau, M. Caleap, A. Velichko and P. Wilcox, "Scattering of guided waves by flat-bottomed cavities with irregular shapes," *Wave Motion,* vol. 49, pp. 375-387, 2012.

[61] Ansys, [Online]. Available: http://www.ansys.com/, .

[62] Abaqus, "Home," 2013. [Online]. Available: www.abaqus.com.

[63] Comsol, [Online]. Available: http://www.comsol.com/.

[64] W. Ke, M. Castaings and C. Bacon, "3D Finite Element simulations of an air-coupled ultrasonic NDT system," *NDT&E International,* vol. 42, pp. 524-533, 2009.

[65] T. Hayashi, W.-J. Song and J. L. Rose, "Guided wave dispersion curves for a bar with an arbitrary cross-section, a rod and rail example," *Ultrasonics,* vol. 41, no. 3, pp. 175-183, 2003.

[66] Y. Lu, L. Ye, Z. Su and C. Yanga, "Quantitative assessment of through-thickness crack size based on Lamb wave scattering in aluminum plates," *NDT&E International,* vol. 41, pp. 59-68, 2008.

[67] P. McKeon, S. Yaacoubi, N. Declercq and S. Ramadan, "Issues concerning using mode conversion of guided waves to size defects in plates," in *Issues concerning using mode conversion of guided waves to size defects in plates", Acoustics 2012 : The 11th Acoustical French Congress and the 2012 Annual IOA Meeting*, Nantes, France, 2012.

[68] N. Terrien, D. Royer, F. Lepoutre and A. Dom, "Numerical predictions and experiments for optimizing hidden corrosion detection in aircraft structures using Lamb modes," *Ultrasonics,* vol. 46, no. 3, pp. 251-265, 2007.

[69] S. K. Datta, A. H. Shah and W. Karunasena, "Ultrasonic Waves and Material and Defect Characterization in Composite Plates," *Mechanics of Composite Materials and Structures,* vol. 6, no. 4, pp. 285-300, 1999.

[70] M. Castaings, C. Bacon, B. Hosten and M. V. Predoi, "Finite element predictions for the dynamic response of thermo-viscoelastic material structures," *Journal of the Acoustical Society of America,* vol. 115, no. 3, pp. 1125-1133, 2004.

[71] J. H. Nieuwenhuis, J. J. Neumann, D. W. Greve and I. J. Oppenheim, "Simulation and Testing of Transducers for Lamb Wave Generation," *http://users.ece.cmu.edu/~dwg/research/216_opp.pdf.*

[72] L. Duquenne, E. Moulin, J. Assaad and S. Grondel, "Transient modelingmodelling of Lamb waves generated in viscoelastic materials by surface bonded piezoelectric transducers," *JASA,* vol. 116, pp. 133-141, 2004.

[73] N. Terrien, D. Osmont, D. Royer, F. Lepoutre and A. Deom, "A combined finite element and modal decomposition method to study the interaction of Lamb modes with micro-defects," *Ultrasonics,* vol. 46, pp. 74-88, 2007.

[74] S. Kessler, S. Spearing and C. Soutis, "Damage detection in composite materials using Lamb wave methods," *Smart Materials and Structures,* vol. 11, pp. 269-278, 2002.

[75] S. Valdes and C. Soutis, "Real-time nondestructive evaluation of fiber composite laminates using low-frequency Lamb waves," *Journal of the Acoustical Society of America,* vol. 111, pp. 2026-2033, 2002.

[76] J. Rose, "Guided Wave Nuances for Ultrasonic Nondestructive Evaluation," *IEEE Transactions on Ultrasonics, Ferroelectrics, and Frequency Control,* vol. 47, no. 3, pp. 575-583, 2000.

[77] M. Lowe and O. Diligent, "Low-frequency reflection characteristics of the S0 Lamb wave from a rectangular notch in a plate," *Journal of the Acoustical Society of America,* vol. 111, no. 1, pp. 64-74, 2001.

[78] M. Lowe, P. Cawley, J.-Y. Kao and O. Diligent, "The low-frequency reflection characteristics of the fundamental antisymmetric Lamb wave a0 from a rectangular notch in a plate," *Journal of the Acoustical Society of America,* vol. 112, no. 6, pp. 2612-2622, 2002.

[79] F. Benmeddour, S. Grondel, J. Assaad and E. Moulin, "Experimental study of the A0 and S0 Lamb waves interaction with symmetrical notches," *Ultrasonics,* vol. 49, pp. 202-205, 2009.

[80] B. Kim and Y. Roh, "Simple expressions of the reflection and transmission coefficients of fundamental lamb waves by a rectangular notch," *Ultrasonics,* vol. 51, pp. 734-744, 2011.

[81] D. N. Alleyne and P. Cawley, "Optimization of lamb wave inspection techniques," *NDT&E International,* vol. 25, no. 1, pp. 11-22, 1992.

[82] P. McKeon, S. Yaacoubi, N. Declercq, S. Ramadan and W. Y. Yaacoubi, "Baseline subtraction technique in the frequency–wavenumber domain for high sensitivity damage detection," *Ultrasonics,* vol. 54, pp. 592-603, 2014.

[83] L. Moreau, M. Caleap, A. Velichko and P. D. Wilcox, "Scattering of guided waves by through-thickness cavities with irregular shapes," *Wave Motion,* vol. 48, pp. 586-602, 2011.

[84] P. S. Tua, S. TQuek and Q. Wang, "Detection of cracks in plates using piezo-actuated Lamb waves," *Smart Materials and Structures,* vol. 13, pp. 643-660, 2004.

CHAPTER 2

INVESTIGATIONS ON MODES, DISPERSION AND ATTENUATION

2.1 Introduction

It was established in chapter 1 that UGW techniques will be adapted for the purpose of creating a SHM system for the COPV in question. For the approach to be most effectively employed, some fundamental issues associated with UGW damage detection need to be studied and/or clarified. This chapter intends on presenting some of the defining characteristics of Lamb waves, especially their dispersive and multi-modal nature.

Dispersion can be predicted for a given structure based on analytical dispersion curves. In many cases, solutions are achieved numerically based on matrix methods [1, 2] or by semi-analytical finite element (SAFE) methods [3]. These curves can be extremely useful, since, in general, the frequency range of operation is chosen to achieve some combination of the following criteria:

- Low number of propagating modes
- Low level of dispersion
- Propagating modes have low levels of attenuation
- Modes are easy to excite/detect from the attainable surface of the structure
- Modes have a high `visibility' to critical damage

The first two points concern the ability to properly interpret the received signal. UGW signals become quickly convoluted by the simultaneous propagation of many modes [4]. Additionally, the temporal and spatial spreading of wave packets due to dispersion also greatly complicates signal interpretation [4].

It has been noted in preliminary studies of the COPV that attenuation is significantly higher in this structure than in thinner or metallic structures, and increases drastically with frequency. Therefore, attenuation may eventually limit the frequency range and even play a role in modal selection. For example, larger sections of the COPV can be inspected if modes with minimal energy attenuation are exploited [5].

The final two points concern excitation, detection and visibility to damage. For the COPV, sensors will necessarily need to be attached to the exterior of the vessel, and therefore will only come in contact with the composite, traction-free surface. These final points are the primary focus of this thesis work and are addressed in chapters 3, 4 and 5.

This chapter is organized as follows: UGW properties and characteristics will be further presented with a brief history of their use in SHM and NDT&E, focusing on previous advancements in simpler structures. Materials of primary interest in this study will then be presented based on work done by industrial partners in the H2E project. The subject of sections 2.4 and 2.5 is perfectly-elastic materials, where it will be shown why multi-layer thick composite structures are so complex and how the operating frequency range was chosen for this present work. Section 2.6 will introduce the concept of attenuation (and consequently amplitude loss), and section 2.7 will discuss the effects of the anisotropic nature of the present working environment.

2.2 Defining Characteristics of UGW

Classic UGW propagation examples include Lamb, Rayleigh, and Scholte-stonely waves [1]. The Lamb wave problem is reserved, strictly speaking, for wave propagation in a traction-free homogeneous isotropic plate, although the terminology has been expanded to propagation in a variety of double-sided structures including multi-layer plates, rods, tubes, etc. This section purports to define and describe some of the defining characteristics of Lamb wave propagation, according to its larger, more encompassing definition.

2.2.1 Dispersion

One of the defining characteristics of Lamb Waves is their dispersive nature, i.e. that the corresponding wave velocities can be theoretically described as a function of the product of frequency and plate thickness. A brief background on previous work done concerning UGW dispersion and dispersive characteristics is presented here followed by a description of graphical dispersion representations.

2.2.1.1 Background

The analytical solution for dispersion curves in isotropic media was described by Sir Horace Lamb in his work published in 1916 [6], and subsequently investigated numerically by I. A. Viktorov in 1967 [7]. A fundamental theoretical description of Lamb waves, is available in this seminal work by Viktorov, and is included in Appendix A.

Recently, Lamb waves are finding use in NDT/NDE in an increasing range of materials and geometries, and therefore methods of analytically and numerically determining dispersion curves have continued to be documented [8, 9]. In terms of SHM, information levied from the dispersion curves has been shown to be useful in many ways. Cut-off frequencies can be ascertained in order to ensure the excitation of only lower order modes, which can decrease the complexity of received signals [4]. Another example of potential use of dispersion curves is the determination of regions of relatively low dispersion, since time-of-flight measurements are complicated by pulse spreading caused by dispersive behavior. More recently, Hall *et al*. have investigated the use of incorporating dispersion curve data to increase the accuracy of the back-propagation of waves in minimum variance ultrasonic imaging [10, 11].

Wilcox *et al*. [12, 13] performed a study that was fundamentally concerned with characterizing and minimizing the effects of dispersion. In order to model how dispersion affects wave propagation, phase velocity information from the available dispersion curves in conjunction with a Fourier decomposition technique was leveraged. However, it was quickly ascertained that the envelope of the wave is the only information needed to determine the wave-packet's boundaries, and therefore a convenient reference level for calculating the envelope was determined, which turned out to be the peak amplitude at each distance. Wilcox *et al.* found that the duration increased linearly with propagation distance, and coincidently is a function of the dispersion of the frequencies present and the number of cycles in the original excitation signal.

Birt *et al*. furthered the understanding of the propagation of Lamb waves in composites by developing a one-dimensional finite-element model that specializes in anisotropic layered structures [14]. Using numerical simulations, dispersion curves were obtained for the first few modes for various layups, showing the dependency of different modeshapes not only on the bulk materials of the composite, but also on the directionality of each layer, and the degree of difference between layers. However, one of the interesting conclusions that was reached was that different modes have varying degrees of sensitivity to the lay-up of the composite structure. For example, the S_0 mode was shown to have increasing phase velocity associated with increasing the number of plies in the propagation direction, whereas the A_0 mode seemed to be relatively independent of the laminate lay-up structure.

Unlike the work done by Birt *et al*., Kessler *et al*. compared their numerical predictions with two sets of experiments, one on narrow strips of composite structures, and the other on sandwich structures with four different types of cores: low and high density aluminium honeycomb configuration, Nomex and Rohacell [15]. Kessler *et al*. varied tensile modulus, Poisson ratio, density and thickness independently and documented the effects on the dispersion curves. Actuator and sensor geometry were also briefly explored (albeit admittedly inexhaustively) to see if different propagation patterns could be generated.

Recently, commercial software, Disperse, is available that makes use of the Global transfer matrix method [2]. Although well established for simple geometries and material properties, the software has self-proclaimed faults when calculating complicated lay-ups, specifically anisotropic materials off the principal material directions.

2.2.1.2 Dispersion Curves

There exist at least three common ways of displaying dispersion information, commonly referred to as ‘dispersion curves’. Two of the three methods use the same independent variable, namely the product of frequency and plate thickness, *fd*. The dependent variables are phase velocity c_p, and group velocity c_g. Inspection of the Lamb equations given in the work by Viktorov [7] quickly reveals why the product of frequency and thickness is used instead of pure frequency, and will be further discussed in section 2.4.1. The third method displays wavenumber *k* as a function of frequency. Alternatively, the product of wavenumber and thickness, *kd*, can be plotted as a function of the product of frequency and thickness to keep the same independent variable, *fd*. Examples of these three dispersion curve manifestations for the simple case of an aluminum plate ($E = 70.76$ GPa , $\rho = 2700$ kg/m^3 , $v = 0.3375$) are shown in figure 2.1.

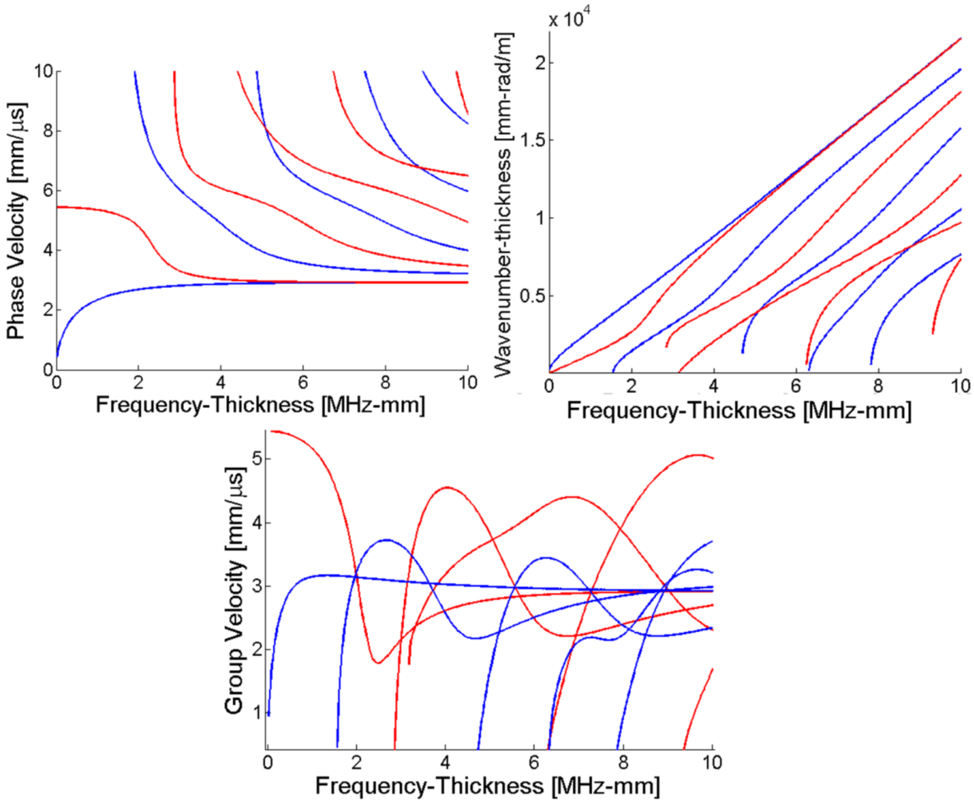

Figure 2.1: Dispersion curves for an aluminum plate as a function of the product of frequency-thickness, in terms of phase velocity (top left), wavenumber (top right) and group velocity (bottom)

Since c_g and c_p are so commonly displayed on an *fd* scale, many researchers [5, 16, 17] also display wavenumber *k* as a function of *fd*. However, phase velocity and wavenumber are inversely proportional as given by the expression:

$$k = \frac{2\pi f}{c_p} \tag{2.1}$$

where *f* is given in Hz. Therefore, even though c_p can be shown as a function of the product of *fd*, *k* is a function of *f*. To keep the same independent variable (*fd*), it is necessary to multiply eq. 2.1 by *d* as well, resulting in a plot of *fd* vs. *kd*.

The equation relating group velocity to phase velocity and wavenumber is slightly more complex.

$$c_p = 2\pi \frac{df}{dk} = c_p + k \frac{dc_p}{dk} \tag{2.2}$$

As can be seen in eq. 2.2, given c_p *(f)* or *k (f)*, it is possible to calculate c_g, but the same is not true for the inverse. There exists a constant of integration required to obtain c_p dispersion curves from a dispersion curve originally manifested in terms of c_g. Rose has included a discussion concerning the relationship between phase and group velocity in his text `Ultrasonic Waves in Solid Media' [18].

2.2.2 Mode Shapes

Another tremendously important consideration in the selection of guided wave modes for a particular experiment is associated with particle displacement across the through-thickness of the structure. The in-plane and out-of-plane displacements, and consequently stress distribution, vary across the thickness of the structure, often significantly. The stress distribution is not only dependent on the lay-up of multi-layered structures but also on the frequencies present in the mode [14]. By examining the stress distributions, it is clear that mode selection plays an important part in determining what type of damage could be detected.

2.3 Material Definition

As outlined in chapter 1, section 1.1, the structure in question is a COPV. In general the reservoirs of interest follow the basic structure outlined in chapter 1, figure 1.2, consisting of a thin inner polyamide layer and a thicker carbon-epoxy overlap. Our industrial partners are also considering having a third, thin layer consisting of a glass-epoxy that is used to protect the load-bearing CE layer from impact damage.

Material properties are referenced directly in the wave equation / Helmholtz equation, and thus proper simulation, dispersion curve calculation, and thickness measurements hinge upon their accuracy. Thickness values can be chosen based on specifications provided, or rather by time of flight measurements taken from bulk

Table 2.1: Pertinent material properties for polyamide layer, based on common values for such materials (not sample specific)

Density	1140 kg/m^3
Young's Modulus	2.3e9 GPa
Poisson's Ratio	0.3

wave excitation and using material properties. The following subsections define the materials as used in this work.

2.3.1 Polyamide Liner

The polyamide liner was neither identified by our industrial partner, nor were any material properties specified. Moreover, even an ASME publication concerning COPV failed to list material properties for common liners, since it is deemed "non-structural" [19]. Consequently, common values for a nylon-type material are used in this work. It is assumed that both the order of magnitude difference and the noticeable size discrepancy between the polyamide layer and the carbon-epoxy overlap layer sanction the use of generic material properties that do not have to be sample specific to be relevant. The pertinent material properties are shown in table 2.1.

2.3.2 Carbon-Fiber Reinforced Polymer Overwrap

In general, composites exhibit high strength-to-weight ratios making them ideal for transportation technologies. Several categories of composites exist including carbon-epoxy and glass-epoxy structures. These structures are made from many layers of fibers embedded in an adhesive epoxy; each layer's orientation is rotated with respect to the previous layer, which in turn affects the directionality of the macroscopic material properties. Depending on the intended load-bearing needs, layers can be continually overwrapped to create structures having a large variety of total thickness, with common dimensions lying between 1 to 40 mm [19].

Table 2.2: Structural properties (C-matrix) for Carbon-Epoxy layer as supplied by our industrial partner (EADS, Composite Acquitaine), units given in Pa

64.628e9	13.140e9	3.530e9	0	0	0
13.140e9	82.389e9	3.585e9	0	0	0
3.530e9	3.585e9	8.165e9	0	0	0
0	0	0	2.887e9	0	0
0	0	0	0	2.786e9	0
0	0	0	0	0	12.606e9

The carbon-epoxy is being treated in this work as having macroscopic orthotropic material properties. Material properties were supplied by our H2E industrial partners, however it should be noted that the C-matrix shown in table 2.2 is assuming orthotropic plate-like behavior, not cylindrical. Therefore, it is understood that the principal directions (which normally are Cartesian) are aligned with the axial (x), tangential (y) and radial (z) cylindrical directions. Density is given as 1600 kg/m^3.

2.3.3 Glass Fiber Reinforced Polymer Shell

A third layer consisting of a glass-epoxy overwrap may be present on the COPV used in the H2E project. This layer’s principal purpose is to act as a protective shell, and can also be considered to be non-load bearing. It should be noted that it is not of primary interest at this stage of the development of an SHM system, but is included here since one damaged sample investigated in chapter 6 includes this shell.

Fortunately, the glass-epoxy layer can also be considered to be macroscopically orthotropic, with the relevant material properties shown in table 2.3, again supplied by our industrial partner. Its principal directions are also aligned with the much thicker carbon-epoxy overwrap layer. Density is given as 1900 kg/m^3.

Table 2.3: Structural properties (C-matrix) for Glass-Epoxy layer as supplied by our industrial partner (EADS, Composite Acquitaine), units given in Pa

25.219e9	3.942e9	3.487e9	0	0	0
3.942e9	25.913e9	3.492e9	0	0	0
3.487e9	3.492e9	7.987e9	0	0	0
0	0	0	2.314e9	0	0
0	0	0	0	2.314e9	0
0	0	0	0	0	2.657e9

2.4 Effect of Thickness

The effect that thickness has on the calculation of dispersion curves is strongly dependent on the number of layers in the structure. The next two sections will address the role of thickness under the assumption that for a given layer, the thickness of that layer is constant throughout the structure. Single layer and multi-layer structures are presented.

2.4.1 Single Layer Structures

It is generally accepted that wavenumber, phase and group velocity of UGW are functions of the product of frequency and plate-thickness (see Appendix A). A single set of plotted dispersion curves thus fully describes the Lamb wave dispersive qualities for a given material independent of thickness. A change in thickness can be compensated by scaling the frequency to maintain the same frequency-thickness product. As an example case consider figure 2.1, where the dispersion curves of aluminum are displayed as a function of frequency-thickness. One can easily imagine that to operate, for example, below the A_1 cut-off frequency for a 1 mm plate, it suffices to excite frequencies inferior to 1.5 MHz. Likewise, a 5 mm plate would necessitate frequencies inferior to 300 kHz to operate below the A_1 cut-off frequency. It is worthy of note that for both of these cases, the relevant modeshapes are also functions of the product of frequency-thickness.

2.4.2 Multi-layer Structures

It was seen in single layer structures that a change in thickness can be easily accommodated by scaling operating frequencies. However, in multi-layer structures, the direct scaling of dispersion curves based on changes of thickness is only appropriate when the number of layers is constant, and furthermore that the ratio of thicknesses of the layers is also maintained.

Table 2.4: Nominative High-Pressure Hydrogen Reservoir Specifications

Volume	Polyamide	C.E.	G.E.	Ratio C.E./Polyamide	Total
2.5 L	2 mm	8 mm	X	4	10 mm
2.5 L	2 mm	8 mm	2 mm	4	12 mm
150 L	4 mm	36	X	9	40 mm

2.4.2.1 Number of Layers

A number of the COPV samples in this work consist of two layers, namely an inner polyamide liner and a thick carbon-epoxy overlap. However, it has been proposed to

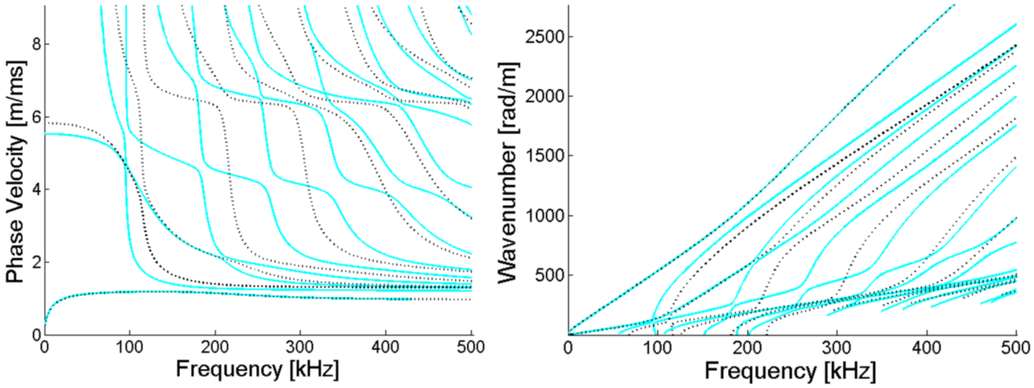

Figure 2.2: Dispersion curve comparison between tri-layer (blue solid) and the bilayer (black dashed) lay-up for a 2.5 L reservoir (see table 2.4) along axial direction.

also include a protective thin outer glass-epoxy layer. The change in the number of layers will change the dispersivity of the sample, as seen in figure 2.2.

In figure 2.2 it is clear that only Mode 1 has similar dispersive qualities for the two cases. Every other mode is affected by the addition of the glass-epoxy layer. Of note, the function describing the higher order modes for the trilayer case is not simply shifted to the right due to the increase of thickness when adding the third layer. It is however interesting that there is a correlation between certain modes over certain frequency regions. For example, Mode 3 is largely left unchanged between 120 and 200 kHz. Despite these correlations, dispersion curves should be recalculated for the case of an additional layer.

2.4.2.2 Thickness Ratio

The H2E project involves many different sizes of COPV intended for a range of internal pressures. Since the strength of the COPV is inherently defined by the overwrapped composite layer, and the inner layer is used only to prevent gas particle diffusion, the thickness ratios are not necessarily scaled with different size COPV. The pertinent COPV dimensions are given in table 2.4. Significantly, the thickness ratios for the bilayer reservoirs for various volumes are vastly different.

Ultimately, this results in the requirement to look at sample specific dispersion curves, and it is consequently more rational to plot said dispersion curves as a function of frequency only, instead of the product of frequency-thickness. Figure 2.3 depicts two sets of dispersion curves in terms of phase velocity and wavenumber for both the 150 L and the 2.5 L bilayer COPV as a function of frequency-thickness. Specifically, regions of high dispersion (easily seen in the phase velocity representation as regions with large slopes) are shifted, and the amount of shift on the frequency axis is not constant but rather mode specific. This has obvious consequences for selecting an operating frequency range. If regions of high

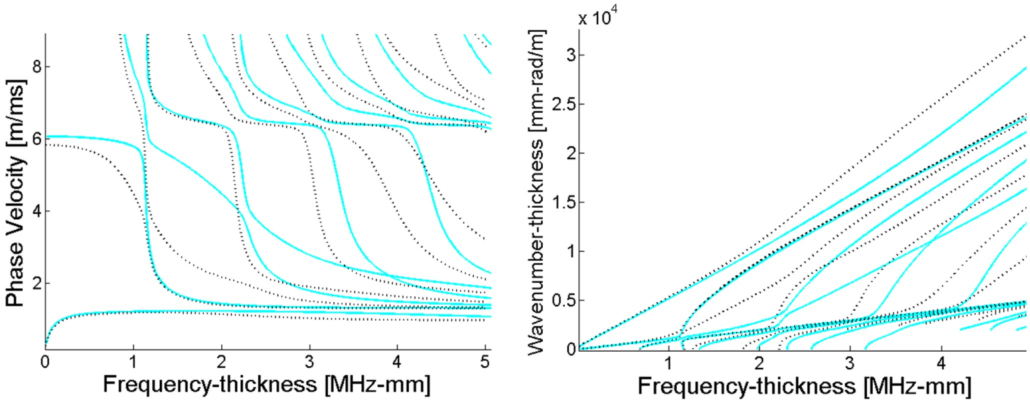

Figure 2.3: Phase velocity (left) and wavenumber (right) dispersion curves for the 150 L bilayer tank (blue solid) and the 2.5 L bilayer (black dotted) COPV as a function of frequency-thickness

dispersion are to be avoided to evade the effects of wave packet spreading, work done in one size reservoir is not easily translatable to another.

2.5 Dispersive Qualities

As previously discussed (section 2.2), dispersion curves are extremely useful for predicting the number of propagating modes at a given frequency, and the level of dispersion of each of those said modes. These two qualities can, in turn, be used to fix an operating frequency range. The operating frequency range should aim to cover a range of wavelengths that are on the same order of magnitude as the characteristic dimensions of the damage that the SHM system is intended to detect. For the purpose of signal clarity, it is better to operate in a frequency range with limited possible propagating modes, and low levels of dispersion [4, 12].

2.5.1 Number of Modes

As was seen in section 2.4, thickness has an obvious effect on the number of possible propagating modes for a given operating frequency. In figure 2.4 and in figure 2.5, the relevant dispersion curves have been plotted for the 2.5 L and 150 L COPV respectively. Of note, they are on different frequency scales. The 2.5 L tank

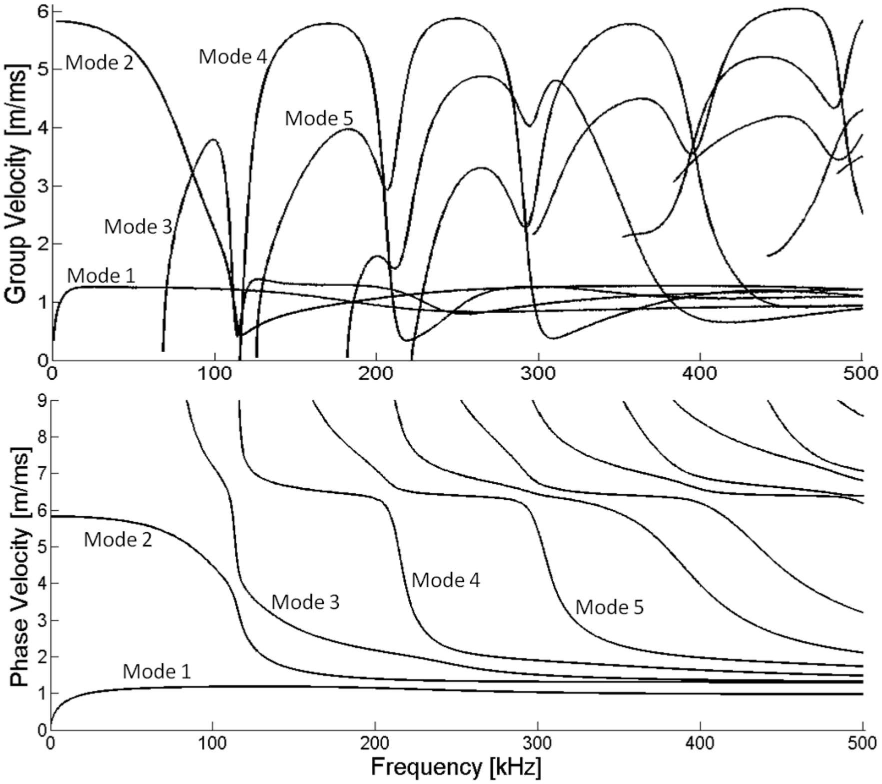

Figure 2.4: Group velocity (top) and phase velocity (bottom) dispersion curves for the 2.5 L bilayer reservoir. The first five modes are labeled since they are of highest interest in this work.

has 12 possible modes under 500kHz, whereas the 150 L tank has 19 possible propagating modes under 200 kHz. It should be noted that only modes with displacement in the x-z plane are considered. Modes with displacement in the y-direction (SH modes) are ignored.

2.5.2 Frequency Range

Traditionally, dispersion curves can help inform decisions concerning the design of SHM systems [12]. If frequency range selection is made solely based on semi-analytical dispersion curves, two major points to be considered are: the level of dispersion, and the appearances of higher order modes which occur at cut-off frequencies.

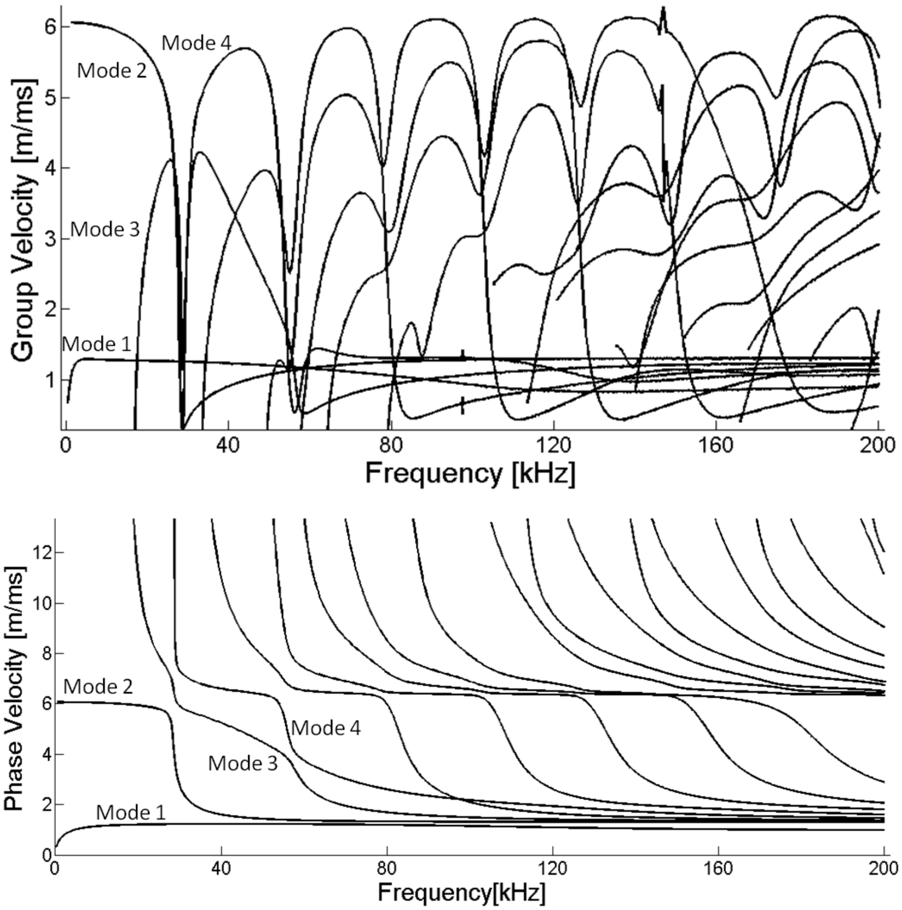

Figure 2.5: Group velocity (top) and phase velocity (bottom) dispersion curves for the 150 L bilayer reservoir. The first four modes have been labeled.

2.5.2.1 Level of Dispersion

When taking into account phase velocity dispersion curves, modes that are weak functions of frequency are considered non-dispersive, whereas modes that are strong functions of frequency are considered highly dispersive. Consider again figure 2.4 and figure 2.5. For the 2.5 L reservoir, the first mode is highly dispersive until about 25 kHz. Mode 2 has a range of high dispersivity from 25 kHz to 150 kHz. For the 150 L reservoir, Mode 1 is highly dispersive until 10 kHz, whereas Mode 2's range of high dispersion is from 30 kHz to 40 kHz. Most of the higher order modes

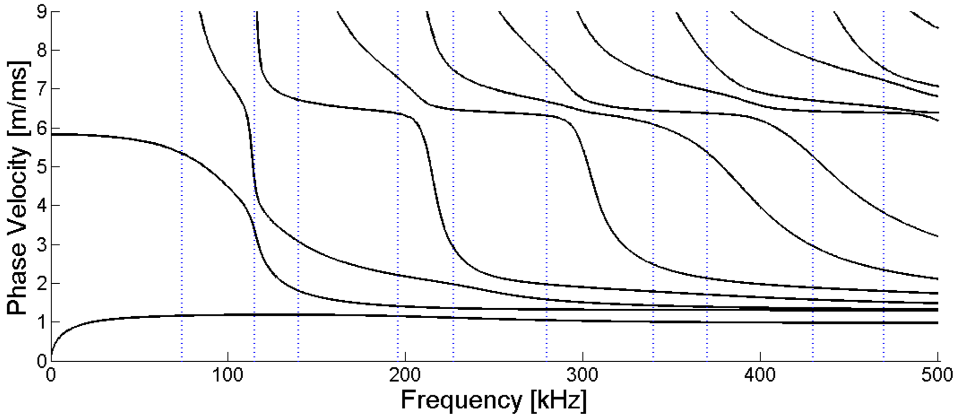

Figure 2.6: Cut-off frequencies for the 2.5 L tank

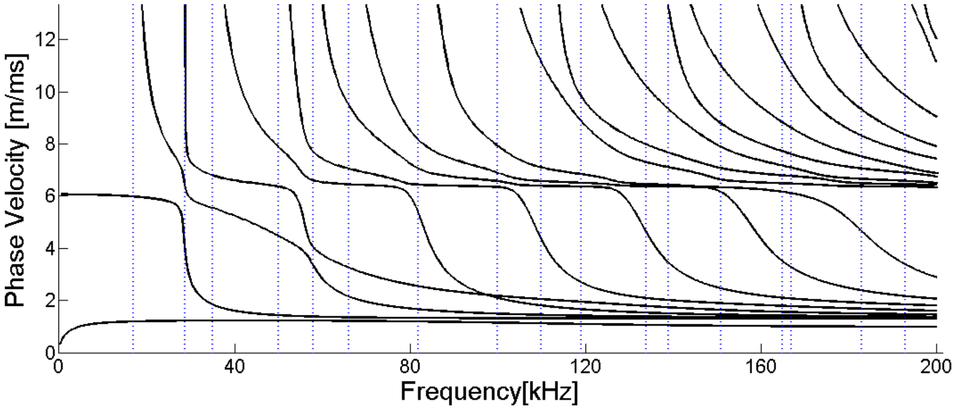

Figure 2.7: Cut-off frequencies for the 150 L tank

are evidently highly dispersive near their cut-off frequencies, then reach a range of relatively low dispersion and become highly dispersive again before finally leveling off. When choosing a frequency range, it is logical to try to choose a range that has a relatively low amount of dispersion for all propagating modes to limit wave-packet spreading. Nevertheless, inspection of figures 2.4 and 2.5 shows that this is not a feasible goal for each and every propagating mode given the complexity of the dispersion curves for these structures.

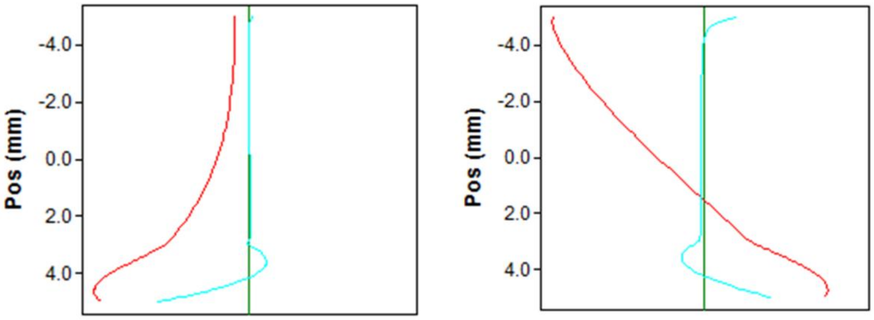

Figure 2.8: Theoretical modeshapes for Mode 1 (left) and Mode 2 (right) for the 2.5 L reservoir. red = displacement normal to surface. blue = displacement in direction of propagation. Recall that overall thickness is 10mm with a layer interface at 3 mm. Frequency = 200 kHz

2.5.2.2 Cut-off Frequencies

Cut-off frequencies refer to the frequency below which the mode in question cannot propagate. All modes of order higher than the first two have an associated cut-off frequency. In general, operating frequencies should not coincide with cut-off frequencies since modes are highly dispersive near their respective cut-off frequencies. Figure 2.6 and figure 2.7 show the phase velocity dispersion curves for the 2.5 L and 150 L COPV respectively with the relevant cut-off frequencies super-imposed for the ease of the reader. For the case of the 2.5 L tank, it is worth pointing out that there are two ranges of interest that lay between cut-off frequencies, namely from 150 to 190 kHz and from 230 to 280 kHz. These zones consist of low-enough frequencies to limit the number of propagating modes, and in zones where the majority of the propagating modes exhibit relatively low dispersion (as compared to regions near cut-off frequencies). However, it will be seen in chapters 3, 4 and 5 that other considerations need to be taken into account when selecting an operating frequency range, most notably the ‘visibility’ modes at that frequency have to defects.

2.5.2.3 Modeshapes

Modeshapes are a function of frequency. Since modeshapes are also strongly related to the ability to detect damage, they are an important characteristic to

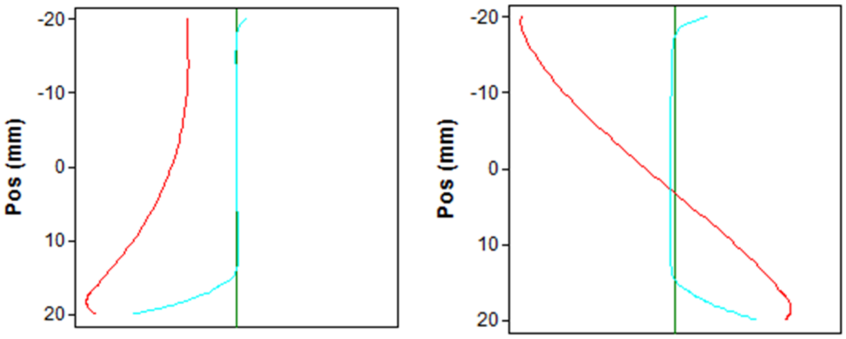

Figure 2.9: Theoretical modeshapes for Mode 1 (left) and Mode 2 (right) for the 150 L reservoir. red = displacement normal to surface. blue = displacement in direction of propagation. Recall that overall thickness is 40mm with a layer interface at 16 mm. Frequency = 100 kHz

consider when choosing an operating frequency range for an SHM system. The role of modeshapes for the purpose of excitation and reception will be further investigated in chapter 3, and their role in damage interaction will be the focus of chapters 4 and 5. As an example case of modeshapes, consider figure 2.8 and figure 2.9 where the first two modes are displayed in terms of out-of-plane and in-plane displacement for the 2.5 L and 150 L COPV respectively. The polyamide layer occurs between 2.5 and 4.5 mm for the 2.5 L COPV, and the remaining portion makes up the carbon-epoxy overwrap. For the 150 L COPV, the polyamide liner occurs between 16 and 20 mm, and the carbon-epoxy overwrap, again, makes up the rest. Both sets of modeshapes are displayed at frequencies in the non-dispersive region.

2.6 Study on Attenuation

The theoretical work presented up until this section assumes that all losses of wave energy can be ignored. In reality, the acoustic energy is converted into thermal energy or scattered in the environment. It is generally accepted that for UGW, there exists two forms of energy dissipation [20]

- Absorption in the media, including dissipation due to internal friction and internal scattering

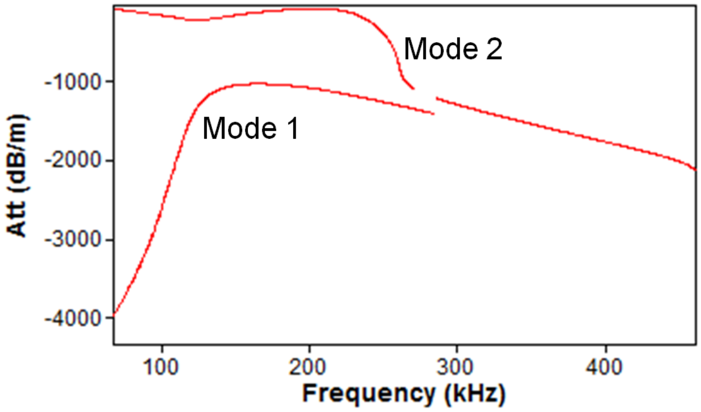

Figure 2.10: Attenuation of Modes 1 and 2 for the 2.5 L reservoir, using nominal thickness values, and $C=C_{given} + i * (0.25*C_{given})$

- Leakage into the surrounding material associated with the upper and lower boundaries of the waveguide

These two forms of energy dissipation, as well as geometrical spreading of the wave packet, are the three conventional causes of a decrease in amplitude at a distinct frequency as a function of propagation distance. It is assumed in this study that the main mechanism of attenuation in this study is the former, and that leakage contributes minimally to the overall energy loss simply because the internal medium is gas and the external one is air.

The general form for the displacement vector *u* is a three-dimensional real valued tensor. However, this form can be easily adapted to account for the energy loss due to the absorption in the media by introducing a negative exponential:

$$u = Ae^{i(k_{real}x-\omega t)}e^{-k_{imag}x} \tag{2.3}$$

where *x* is the Cartesian coordinate direction of propagation, *k* is the complex wavenumber, *t* is time, *A* is the amplitude of the wave, *ω* is temporal frequency, *i* is the imaginary number, and *u* is the displacement in the x-direction. The real portion of the wavenumber k_{real} describes the harmonic propagation of the waveform and the imaginary portion k_{imag} accounts for the natural decay due to absorption. It should be noted that with the inclusion of complex wavenumbers, there is no longer an analytical difference between propagating and evanescent modes.[5]

Recall that in an elastic waveguide the group velocity can be computed by taking the partial derivative of frequency with respect to wavenumber, as seen in equation 2.2. However, it was shown by Auld [21] that this definition is not valid for visco-elastic materials due to the complex nature of k. If differentiation is carried out only in terms of the real part of k, the calculation can give non-physical results, such as infinite velocities at finite frequencies. Auld defines a new quantity dubbed the energy velocity, V_e, which is more appropriate for visco-elastic materials, and is restated here for the ease of the reader:

$$V_e = \frac{P_{AV}}{u_{AV}} \tag{2.4}$$

where P_{AV} is the time-average Poynting vector and represents the average power flow density, and u_{AV} is the time-average stored energy density [21] (pg 222 vol. 1).

Using the commercial software Disperse [2], the attenuation of Mode 1 and Mode 2 are plotted and displayed in figure 2.10. Since no visco-elastic properties were given, it was assumed that the carbon epoxy-material stress tensor C had an imaginary component C_{imag} that was 25% of the pure elastic values given in table 2, as per the work of Cinquin [17]. It should be noted that the actual visco-elastic properties are unknown, and thus the y-axis is of arbitrary units. However, the overall shape should be indicative of the expected attenuation function for Mode 1 and Mode 2. Specifically, there exists a high level of attenuation below 125 kHz for Mode 1, and its overall attenuation is greater than that of Mode 2. Mode 2 suffers large energy loss at frequencies higher than 250 kHz. Optimally, a maximum amount of energy is conserved around 160-250 kHz for both modes. It can be noted that

Mode 1 in figure 2.10 is calculated only until 300 kHz. And Mode 2 has a discontinuity around 280 kHz. These are due to known limitations of the software and have no physical meaning.

2.7 Study on Anisotropy

The propagation of UGW in composite materials is further complicated by their anisotropic nature. Evidently, the analytical formulations are more complex, due to the coupling between particle displacement directions which are directionally dependent [5]. Previously, researchers have used models based on the transfer matrix, which allows for the analytical prediction of dispersion curves in an arbitrary direction [1], and commercial software, such as Disperse, is available that makes use of the Global transfer matrix method [2]. In general, dispersive relationships along different directions of an anisotropic material can be vastly different. Furthermore, in general, coupling can occur between SH and Lamb modes, which is not possible in isotropic media.

It is possible, however, to reduce analytical and numerical studies to two-dimensions, when working along planes of symmetry. In this case, the SH and Lamb waves are decoupled and can be studied individually [22]. In this work we will assume that the waves are propagating along the axial direction of the reservoir, which is in-line with one of the principal directions. Furthermore, we assume here that the Lamb waves and SH waves are weak functions of each other to the point that they can be considered to be uncoupled along propagation paths directly next to the principal directions (within ± 15°).

To investigate the effect of slight path changes on the dispersive qualities of the Lamb waves, consider figure 2.11. The dispersion curves for waves propagating along the axial direction are shown in black. The SH waves along the principal direction are shown in red. A change of 15 ° off the principal direction is shown in

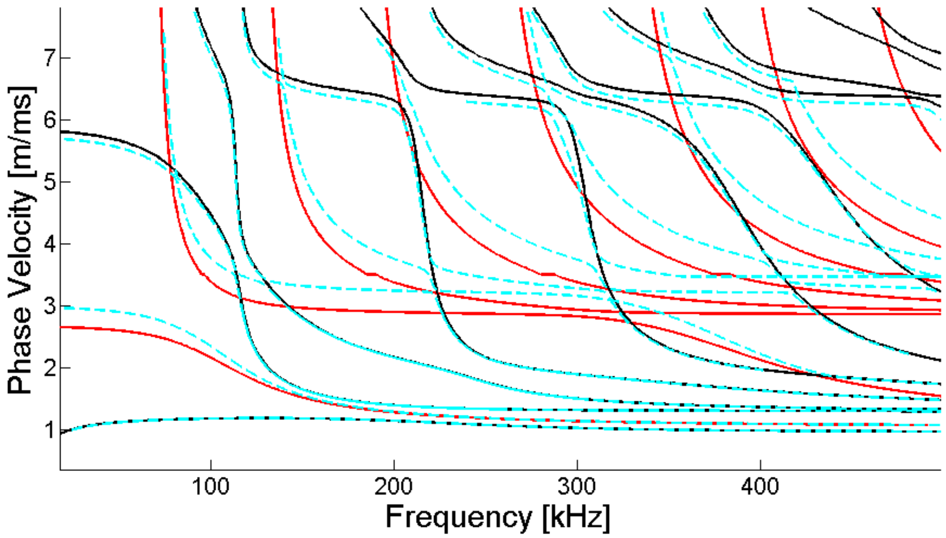

Figure 2.11: Comparison of Lamb waves (black) and SH waves (red) along the axial principal direction and the coupled UGW propagating 15° off the principal direction (blue dashed)

blue. Note that the changes are minimal for the Lamb waves, with a greater difference being observed for the SH waves.

2.8 Conclusion

Following the study presented in this chapter on modes, dispersion and attenuation, several important observations can be made:

- Dispersion curves can be plotted as functions of the product of frequency and thickness for two cases: monolayer structures and multi-layer structures when the thickness ratio between layers is kept constant
- The structures of interest in this work are multi-layer with variable thickness ratios and therefore dispersion curves are more logically plotted as functions of pure frequency
- Higher operating frequencies result in the possible propagation of more modes, complicating signal analysis

- Mode shapes are distinct and functions of frequency and should ideally be chosen based on their interaction with damage (see chapters 4 and 5).
- Although visco-elastic properties are unknown for the carbon-epoxy material, it is known that attenuation will be a limiting factor. Studies indicate that an operating frequency range between 125 kHz and 300 kHz will limit energy loss for Mode 1 and Mode 2.
- Phase velocity for Lamb modes does not fluctuate significantly in directions near the principal direction, and therefore is chosen over SH waves for the remainder of this study

2.9 References

[1] A. H. Nayfeh, Wave propagation in layered anisotropic media, The Netherlands: Elsevier Science B. V., 1995.

[2] M. Lowe, *Disperse (software),* London; Imperial College: http://www3.imperial.ac.uk/nde/products%20and%20services/disperse, 1997.

[3] I. Bartoli, A. Marzani, F. d. Scalea and E. Viola, "Modeling wave propagation in damped waveguides of arbitrary cross-section," *Journal of Sound and Vibration,* vol. 295, pp. 685-707, 2006.

[4] D. N. Alleyne and P. Cawley, "Optimization of lamb wave inspection techniques," *NDT&E International,* vol. 25, no. 1, pp. 11-22, 1992.

[5] I. Bartoli, Structural Health Monitoring by Ultrasonic Guided Waves, San Diego: University of California, 2007.

[6] H. Lamb, "On waves in an elastic plate," *Proc. R. Soc. London, Ser. A,* vol. 93, pp. 114-128, 1917.

[7] I. A. Viktorov, Rayleigh and Lamb Waves: Physical Theory and Applications, New York: Plenium Press, 1967.

[8] M. Castaings and B. Hosten, "Ultrasonic guided waves for health monitoring of high-pressure composite tanks," *NDT&E International,* no. 41, pp. 648-655, 2008.

[9] T. Hayashi, W. Song and J. L. Rose, "Guided wave dispersion curves for a bar with an arbitrary cross-section, a rod and rail example," *Ultrasonics,* vol. 41, pp.

175-183, 2003.

[10] J. Hall and J. Michaels, "Minimum variance ultrasonic imaging applied to an in situ sparse guided wave array," *IEEE Trans. Ultrason., Ferroelectr., Freq. Control,* 2010.

[11] J. Hall, P. McKeon, L. Satyanarayan, J. E. Michaels, N. F. Declercq and Y. Berthelot, "Minimum variance guided wave imaging in a quasi-isotropic composite plate," *Smart Materials and Structures,* vol. 20, 2011.

[12] P. Wilcox, M. Lowe and P. Cawley, "The effect of dispersion on long-range inspection using ultrasonic guided waves," *NDT&E,* vol. 34, pp. 1-9, 2001.

[13] P. D. Wilcox, "A rapid signal processing technique to remove the effect of dispersion from guided wave signals," *IEEE,* vol. 50, pp. 419-427, 2003.

[14] E. A. Birt and W. J. Percival, "A study of Lamb wave propagation in carbon-fibre composites," *INSIGHT,* vol. 39, no. 10, pp. 728-735, 1997.

[15] S. Kessler, S. Spearing and C. Soutis, "Damage detection in composite materials using Lamb wave methods," *Smart Materials and Structures,* vol. 11, pp. 269-278, 2002.

[16] D. N. Alleyne and P. Cawley, "A two-dimensional Fourier transform method for the meausrement of propagating multimode signals," *Journal of the Acoustical Society of America,* vol. 89, no. 3, pp. 1159-1168, 1991.

[17] M. Cinquin, "Suivi par Ondes Guidees de l'Etat de Sante de Reservoirs Composites," Universite de Bordeaux, Bordeaux, 2004.

[18] J. L. Rose, Ultrasonic Waves in Solid Media, Cambridge, U.K: Cambridge University Press, 1999.

[19] N. Newhouse, R. G.B., R. M.D., S. B.F. and G. M.R., "Development of ASME Section X Code Rules for High Pressure Composite Hydrogen Pressure Vessels With Nonload Sharing Liners," *Journal of Pressure Vessel Technology,* vol. 134, 2012.

[20] S. Huo, Estimation of Adhesive Bond Strength in Laminated Safety Glass Using Guided Mechanical Waves, Urbana, Illinois: University of Illinois at Urbana-Champaign, 2008.

[21] B. A. Auld, Acoustic Fields and Waves in Solids, Рипол Классик, 1990.

[22] M. Castaings and B. Hosten, "Guided waves propagating in sandwich structures made of anisotropic, viscoelastic, composite materials," *Journal of the Acoustical Society of America,* vol. 113, no. 5, p. 2622, 2003.

[23] Z. Su, L. Ye and Y. Lu, "Guided Lamb waves for identification of damage in composite structures: A Review," *J. of Sound and Vibration,* vol. 295, pp. 753-780, 2006.

[24] D. Alleyne and P. Cawley, "The Interaction of Lamb Waves with defects," *IEEE,* vol. 39, pp. 381-397, 1992.

[25] S. Valdes and C. Soutis, "Real-time nondestructive evaluation of fiber composite laminates using low-frequency Lamb waves," *Journal of the Acoustical Society of America,* vol. 111, pp. 2026-2033, 2002.

[26] H. J., S. K. H. and K. Y. Y., "Dispersion-based short-time Fourier transform

applied to dispersive wave analysis," *Journal of the Acoustical Society of America,* vol. 117, no. 5, pp. 2949-2960, 2005.

[27] R. D. Costley and Y. H. Berthelot, "Dispersion curve analysis of laser-generated Lamb waves," *Ultrasonics,* vol. 32, pp. 249-253, 1994.

[28] W. Gao, C. Glorieux and J. Thoen, "Laser ultrasonic study of Lamb waves: determination of the thickness and velocities of a thin plate," *International Journal of Engineering Science,* vol. 41, pp. 219-228, 2003.

[29] S. Grondel, J. Assaad, F. E. Youbi, E. Moulin and N. A. Leyla, "Experimental Lamb mode identification in a plate containing a hole using dual signal processing," *Measuring Science Technology,* vol. 19, pp. 1-6, 2008.

[30] J. S. Hall and J. E. Michaels, "A model-based approach to dispersion and parameter estimation for ultrasonic guided waves," *Journal of the Acoustical Society. America,* vol. 127, pp. 920-930, 2010.

[31] M. Niethammer, L. J. Jacobs, J. Qu and J. Jarzynski, "Time-frequency representations of Lamb waves," *Journal of the Acoustical Society of America,* vol. 109, pp. 1841-1847, 2001.

[32] M. Niethammer, L. J. Jacobs, J. Qu and J. Jarzynski, "Time-frequency representations of Lamb waves using the reassigned spectorgram," *Journal Acoustical Society America,* vol. 107, pp. L19-L24, 2000.

[33] J. Hong, K. H. Sun and Y. Y. Kim, "Dispersion-based short-time Fourier transform applied to dispersive wave analysis," *Journal of the Acoustical Society of America,* vol. 117, pp. 2949-2960, 2005.

[34] Y. Y. Kim and E. Kim, "Effectiveness of the continuous wavelet transform in the analysis of some dispersive elastic waves," *Journal of the Acoustical Society of America,* vol. 110, pp. 86-94, 2001.

[35] F. Li, G. Meng, L. Ye, Y. Lu and K. Kageyama, "Dispersion analysis of Lamb waves and damage detection for aluminum structures using ridge in the time-scale domain," *Measuring Science Technology,* vol. 20, pp. 1-10, 2009.

[36] Z. Su, L. Ye and X. Bu, "A damage identification technique for CF/EP composite laminates using distributed piezoelectric transducers," *Composite Structures,* vol. 57, pp. 465-471, 2002.

[37] L. Wang and F. Yuan, "Group velocity and characteristic wave curves of Lamb waves in composites: Modelingand experiments," *Composite Science Technology,* vol. 67, pp. 1370-1384, 2007.

[38] Lemistre, "Structural health monitoring system based on diffracted Lamb wave analysis by multiresolutional processing," *Smart Material Structures,* pp. 504-511, 2001.

[39] J. S. Hall, "Adaptive dispersion compensation and ultrasonic imaging for structural health monitoring," Georgia Institute of Technology, Atlanta, Georgia, 2011.

CHAPTER 3

FINITE ELEMENT METHOD, MODELS AND VALIDATIONS

3.1 Introduction

Modeling via the finite element method (FEM) has become a common practice, especially when analytical solutions are difficult or unattainable [1, 2, 3]. As stated in Chapter 1, FEM can offer insight into the nature of wave propagation and help explain experimental results. Although the goal in this present work is to optimize key parameters for the sake of damage detection, this chapter is devoted to the development of a healthy waveguide, which is considered an integral first step. Chapter 4 will then continue the work by introducing geometrical and parameter alterations in order to model the damage types.

The work detailed in this chapter concerns the numerical simulations of wave propagation in a healthy bilayer orthotropic structure. As a first step, wave propagation has been modeled via the FEM in a bulk medium, but is included in Appendix B to alleviate this document. This chapter is organized as follows: a very brief review of the finite element method will be followed by the governing equations in both the temporal domain and frequency domain. The chapter continues with the simulation of Lamb waves in traction-free plates. Conceptual validation in single layer plates is presented in Appendix C to alleviate this document. Since simulations are carried out in both the spatial and time domains, mesh size and time step are important; parameter choices impact the accuracy of the simulation and the computational effort required for solving the problem. Material symmetries are exploited to simplify the model from three to two dimensions [4], and if the FE model can be reduced geometrically, the resulting computational efforts are reduced as well. The size of the excitation will also be discussed, both for directivity of the source, and the efficiency of the source to radiate sound energy into the medium. Although reflections at upper and lower boundaries play a significant role for any plate-like waveguide, cross-sectional boundaries will leads to reflections which are not present in the theoretical problem. Absorbing boundary layers will need to be utilized to help limit the spatial length of the plate as well as to help simulate more accurate conditions for the propagation of bulk waves.

Concerning propagation in healthy waveguides, dispersion diagrams are calculated (see Chapter 2) and verified to have excellent agreement with dispersion curves attained from the finite element models. As it will be seen in chapter 6, the finite element model will be compared with experimental work to validate real-world behavior.

3.2 Background

Generally speaking, the finite element method supplies a numerical approximation to a given differential equation over a specified domain, subject to specified boundary conditions. The generalized governing equation is of the form [5][1]:

$$e_a \frac{\partial^2 u}{\partial t^2} + d_a \frac{\partial u}{\partial t} + \nabla \cdot (-c\nabla u - \alpha u + \gamma) + au + \beta \cdot \nabla u = f(t) \tag{3.1}$$

where the various coefficients are related to their function for the partial differenctial equation, namely e_a is the mass coefficient, d_a the damping coefficient, c the diffusion coefficient, a the absorption coefficient, γ the conservative flux source term, α the conservative flux convection coefficient and β the convection coefficient[5]. Note that, equation 3.1 allows for second order partial derivative equations. In addition, any of the

---

[1] As discussed in section 1.4.3.2, the commercially available FEM software COMSOL Multiphsyics will be employed in this project.

various coefficients may be made complex, or functions of time *t* or the vector ***u***. The coefficients may be simply set to zero if they do not come into play in the theoretical governing equation. The vector ***u*** has not necessarily been associated with any physical value, but in general can be chosen to be two or three dimensional. The domain can be divided into subdomains where each subdomain is subject to its own coefficients, and consequently different theoretical governing equations.

The subdomains are discretized in either triangular or quadrilateral sized element, and the interpolation function between nodes is a polynomial of a user-chosen degree. The speed of the FEM calculation is a strong function of the total number of nodes. Therefore, an important user-defined choice is the size of the elements, which needs to be small enough (large number of nodes) to enable an accurate solution. Conversely, too many nodes may be superfluous, and cause unnecessarily long computation times. Choosing a higher order polynomial interpolation function may allow for a larger element size, but it has been found that any order over 3 causes unwanted undulation[2], as the interpolation function is forced to pass through certain points.

The generalized boundary conditions can be chosen to be either:

$$n \cdot (c\nabla u + \alpha u - \gamma) + qu = g \tag{3.2}$$

or

$$hu = r \tag{3.3}$$

where *n* is the unit vector perpendicular to the surface, *q* the boundary absorption coefficient, *g* the boundary source coefficient, *h* the boundary dependent variable

---

[2] Information taken from class, curriculum number ME6758: Numerical Methods in ME, Dr. L. Capolungo, Fall 2011, and verified independently by the author

coefficient and finally *r* is the boundary dependent variable term. Regardless, as for equation 3.1, the terms in equations 3.2 and 3.3 can be reassigned to fit the governing equation for the given physical system, and can be set to zero if they do not come into play.

Note that equation 3.2 corresponds to a Dirichlet boundary condition, whereas equation 3.3 is a pure Neumann boundary condition. Only one of these boundary conditions may be applied to a single boundary segment at a time; however, the two may both be employed in a single model by dividing the boundary into a desired number of line segments.

3.3 FEM Equations

FEM can model wave propagation in complex wave guide geometries either in the time domain or the frequency domain [6]. The following subsections will address the relevant governing physical equations for both domains.

3.3.1 Time Domain

For generally anisotropic, visco-elastic materials, we can use this form of the wave equation:

$$C_{ijkl}\frac{\partial^2 u_l}{x_j x_k} = \rho\frac{\partial^2 u_i}{\partial t^2} \qquad i,j,k,l = 1,2,3 \tag{3.4}$$

where C_{ijkl} is the elasticity matrix and can be composed of complex moduli, *i, j, k*, and *l* are indices referring to one of the three Cartesian coordinates, u_i is the displacement in the direction given by its subscript, ρ is density and *t* is time. Note that, in this work the notation u_i (i = 1, 2, 3) and *u, v, w* and are used interchangeably to refer to the displacement in the three Cartesian coordinate directions, *x, y* and *z* respectively.

In general, a 4th order tensor has 3^4 = 81 elements, but physical limitations imposed by the symmetry of the stress and strain tensors place the following restrictions on the generally 81 element tensor:

$$C_{ijkl} = C_{jikl} = C_{ijlk} = C_{jilk} \tag{3.5}$$

thereby reducing the number of elements to 36. However, the generalized governing eq. 3.1 in Comsol allows for the solution of a general 81 element, 4th order tensor. The COMSOL software package organizes the 81 elements as 9 * 3x3 matrices (3 x 3 x 9 = 81), as shown in figure 3.1. This figure makes use of the Voigt notation, which uses the symmetry relations introduced in eq. 3.5.

Most of the other variables required for equation 3.1 are more apparent, such as the role of e_a as density in eq. 3.4. Although d_a in eq. 3.1 can be likened to a damping coefficient, the individual elements of C_{ijkl} can also be made complex to account for visco-elastic effects. All other coefficients are equated to zero.

Eq. 3.4, which operates in the temporal domain, has the advantage of having a direct correspondence with real-world experiments, and does not necessarily require the use of a Perfectly Matched Layer (PML) or Absorbing Boundary Regions (ABR) to deal with the problem of edge reflections. Note that edge reflections are an artifact of the necessity of simulating a finite geometry. Instead, time windowing can be used to ensure that only direct arrivals are taken into account. Furthermore, temporal domain simulations can excite a broad range of frequencies in a single simulation, as opposed to investigating the effects of a single frequency and relying on superposition to create a realistic waveform (see section 3.3.2).

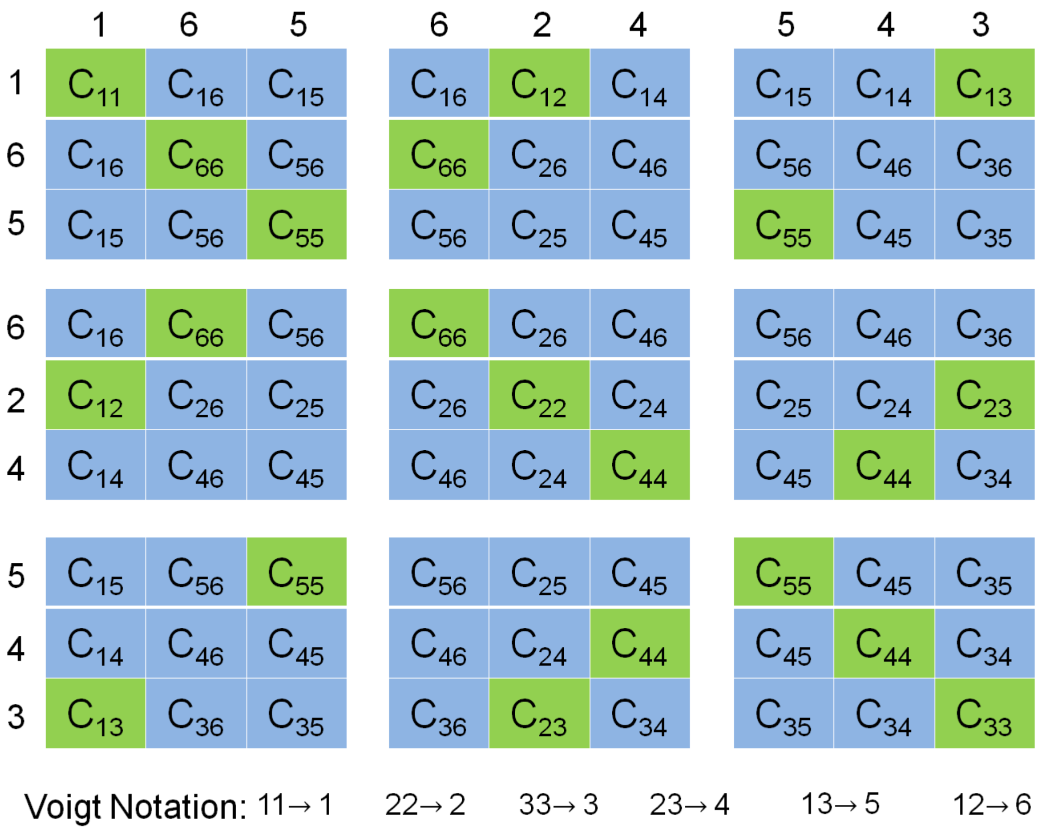

	1	6	5	6	2	4	5	4	3
1	C_{11}	C_{16}	C_{15}	C_{16}	C_{12}	C_{14}	C_{15}	C_{14}	C_{13}
6	C_{16}	C_{66}	C_{56}	C_{66}	C_{26}	C_{46}	C_{56}	C_{46}	C_{36}
5	C_{15}	C_{56}	C_{55}	C_{56}	C_{25}	C_{45}	C_{55}	C_{45}	C_{35}
6	C_{16}	C_{66}	C_{56}	C_{66}	C_{26}	C_{46}	C_{56}	C_{46}	C_{36}
2	C_{12}	C_{26}	C_{25}	C_{26}	C_{22}	C_{24}	C_{25}	C_{24}	C_{23}
4	C_{14}	C_{46}	C_{45}	C_{46}	C_{24}	C_{44}	C_{45}	C_{44}	C_{34}
5	C_{15}	C_{56}	C_{55}	C_{56}	C_{25}	C_{45}	C_{55}	C_{45}	C_{35}
4	C_{14}	C_{46}	C_{45}	C_{46}	C_{24}	C_{44}	C_{45}	C_{44}	C_{34}
3	C_{13}	C_{36}	C_{35}	C_{36}	C_{23}	C_{34}	C_{35}	C_{34}	C_{33}

Voigt Notation: 11→ 1   22→ 2   33→ 3   23→ 4   13→ 5   12→ 6

Figure 3.1: Organization of the 9x3x3 matrix used to describe the 4th order tensor *c* in equation 4.1. Each column corresponds to one of the three equations in terms of u, v and w respectively.

Concerning multi-layer structures, the boundary occurring between two layers *m* and *n* will be assumed to be perfectly adhesive, and consequently $u_m = u_n$, $v_m = v_n$ and $w_m = w_n$ at the boundary. Otherwise it will be assumed that the outer surfaces of the structure, which is to say those in contact with the air, adopt the traction-free requirement of the traditional Lamb wave definition. This means that the Dirichlet boundary condition described in equation 3.2 will be employed and q, α, γ and g are all set equal to zero.

Various boundary conditions are used throughout this work to act as the excitation source, both of the Dirichlet and the Neumann type. When the propagation and subsequent effects of just one incident mode are required, a Neumann boundary condition is employed along the boundary corresponding to the cross-section of the plate. Consider the two-dimensional depiction in figure 3.2. Two function, *G(z,t)* and *H(z,t)* are applied to the left boundary of the finite element structure. The displacement in both Cartesian coordinate directions is prescribed in the direction perpendicular to the surface via function *G* and in the direction of propagation via function *H*. Each of these functions can be thought of as a separable function. For example for function *G*, there exists two parts, *ZG(z)*, and *TG(t)*, and similarly for function *H* there exists *ZH(z)*, and *TH(t)*. *ZG* and *ZH* are given by the mode-shapes according to particle displacement in the *z* and *x* directions, respectively (see chapter 2.)

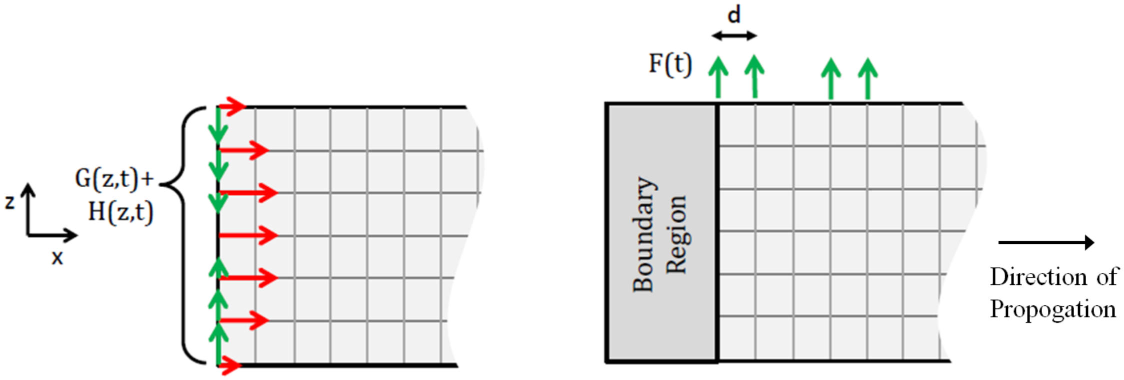

Figure 3.2: Excitation forms: (left) Modal shapes are used to excite one end of the plate to excite pure modes and (right) a series of half wavelengths are used on the free surface to favor the formation of a given mode

This type of excitation, which acts over the entire left edge, is very useful for limiting the size of the finite element geometry (thus reducing computational efforts), since it automatically forgoes any geometry to the left of the excitation, be it an absorbing boundary region or perfectly matched layer. Instead, the left boundary is itself the excitation source. All waves are necessarily initially right-traveling. Left-traveling waves only occur after interaction with some obstacle to the right of the excitation. The functions *ZG* and *ZH* describing particle displacement stem from the analytical descriptions of a given pure mode traveling in a healthy waveguide.

The success of this method of excitation lies essentially in two components. First and foremost, the analytical solution exists. For the case of UGW traveling along a principal direction of an orthogonal material, the analytical solutions do exist, although are admittedly complicated for multi-layer materials. In this work, commercially available software capable of calculating dispersion curves, Disperse, is used to numerically approximate the analytical solution for the mode-shape. (It is notable, however, that this technique would be vastly more complicated to employ along a non-principal direction. The model would necessarily have to be three-dimensional and the analytical solution for each plane wave would have to be computed and summed to approximate the elliptically spreading wave, based on the Huygens-Fresnel principle.) The second component to ensure the successful implementation of this excitation type concerns the position and number of nodes on the left-edge boundary of the finite element geometry. If the nodes are unfortunately placed on the left edge, they can occur at nodal points in the mode-shape, i.e. no motion will be prescribed. Likewise if there are not a sufficient number of nodes on the left-edge of the plate, unwanted modes can be excited. Of course, to a certain extent this phenomenon will almost always occur in a numerical environment. Although the motion of nodal points in the mesh can be described by means of an analytical function, the boundary of the element between the nodal points is approximated by means of some interpolation function, generally a low-order polynomial. The amount of numerical error approaches zero as the interpolation functions approach the behavior of the true mode profile.

Alternatively, to more closely simulate the effects of a contact PZT, a Dirichlet type (equation 3.2) can be employed, as depicted on the right hand side of figure 3.2. Here a forcing function is applied to an adjacent series of boundary elements. The forcing function, F(t), is a function of time only. The forcing function shown in the figure is in the z-direction and corresponds to a longitudinal type contact PZT. To simulate the effects of a shear contact transducer, this function could easily be altered to apply force in the x-direction. The relationship between the boundary condition and the propagating wave packet/modes is revisited in section 3.4.4.

The simulations carried out in the time domain mimic results obtainable in real-world experiments. The time step must also be adequately small so that it does not exceed the distance between two nodal points in an element divided by the wave speed of the fastest mode possible in the given frequency range. Consequently, this means using a time step Δt that follows the relation:

$$\frac{\delta}{c_{g,max}} \geq \Delta t \tag{3.6}$$

where δ is the smallest length between two adjacent nodes as shown in figure 3. 3, and $c_{g,max}$ is the wave speed of the fastest mode possible in the given frequency range. The waveforms are thus directly related to particle displacement. Note that equation 3.6 is not sufficient to ensure proper mesh size, but rather an appropriate time step after the mesh size has been ascertained. Convergence calculations will be further discussed in section 3.4.3.

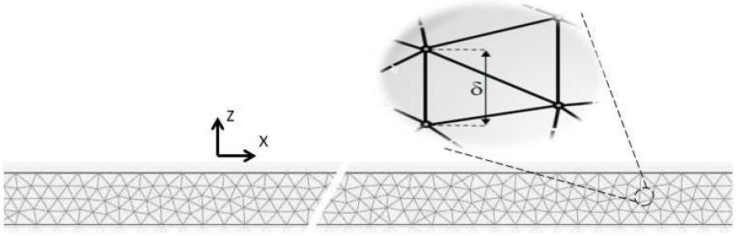

Figure 3.3: Schematic of mesh

3.3.2 Frequency Domain

Consider equation 3.4. In terms of an assumed harmonic solution via separation of variables, with a constant temporal frequency ω, equation 3.4 can be rewritten as:

$$C_{ijkl}\frac{\partial^2 u_l}{\partial x_j \partial x_k} - \rho\omega^2 u_i = 0 \qquad i,j,k,l = 1,2,3 \tag{3.7}$$

where we can see that *c* from eq. 3.1 has retained its meaning from the temporal formation (eq. 3.4), but d_a has effectively become -$\rho\omega^2$.

Both forms of the theoretical governing equations (3.4 and 3.7) have their merits. The Helmholtz formulation, i.e. eq. 3.7, is more computationally efficient for simulating the effect of a single frequency. However, proper use of PMLs or ABRs are necessary. Otherwise, the geometry becomes polluted with a high number of reflections. Specifically, in the purely elastic case, the number or internal reflections would be infinite, and set-up a standing wave pattern.

In order to suppress end reflections, a hybrid method of PML and ABR are applied to each end of the plate. For these regions, the components of the stiffness matrix are altered to the form

$$C_{ij}^{ABR} = C_{ij}\left(1 + iA\left(\frac{x_{ABR}^{3}}{L_a^{3}}\right)\right) \qquad i,j = 1,2 \tag{3.8}$$

where L_a is the length of the ABR, and A is a constant for optimization. The independent variable x_{ABR} is defined as being equal to zero at the ABR border and increasing in magnitude in the direction away from the propagation domain. A schematic of a waveguide with an ABR present can be seen in figure 3.4.

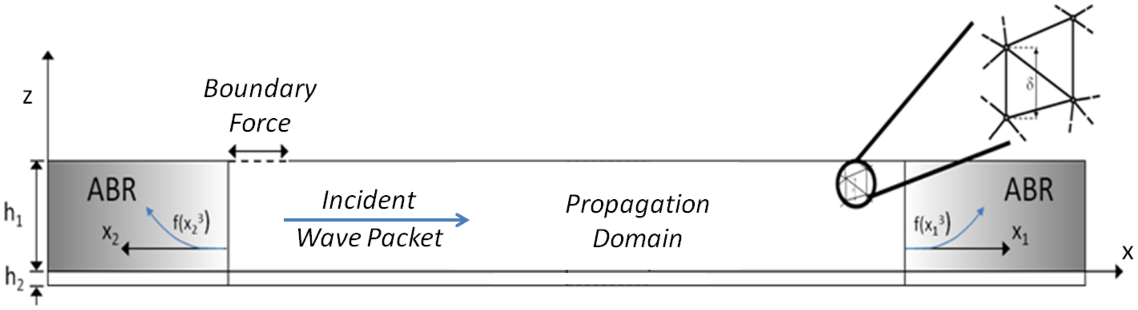

Figure 3.4: Schematic of healthy 2D waveguide with Absorbing Boundary Regions

3.4 2D Numerical Simulations

In general, three-dimensional (3D) simulations are necessary for studying anisotropic materials. The thin inner polyamide liner of the 2.5 L reservoir is isotropic, i.e. wave propagation behavior is expected to be directionally independent. More interestingly, the carbon-epoxy outer layer macroscopically exhibits orthotropic material properties, meaning that there are three axes of symmetry, namely the principal directions. Due to symmetry, wave propagation along these principal axes can be studied in two-dimensions, provided that particle motion is restricted to the plane of simulation. For the case of UGW, this means (assuming one of the principal axis is perpendicular to the surface of the structure) that there are two directions in which wave motion can be simulated two-dimensionally excluding shear horizontal modes. Mechanical disturbances involving particle motion perpendicular to the would-be plane of simulation, still require three dimensional analyses.

Two-dimensional (2D) studies can be very useful for several reasons, both generally speaking and also specifically to the geometry in question (see figure 1.2). The computational effort for FEM simulations is directly related to the number of elements, and the reduction in the number of elements in deleting one dimension is considerable. More specifically to this case, the principal axes for the tank in question are aligned in a very useful manner. Recall the Cartesian basis shown in figure 1.2 also denotes the principal directions of the orthotropic layer. Therefore the two-dimensional numerical studies will be carried out in the direction the most easily accessible for experimental verification, namely axially (x-direction).

3.4.1 Aim

The aim of this section is to investigate certain aspects of the 2D model. Convergence studies are carried out with respect to the propagating wavelengths and relevant parameters are explored to optimize computing time. The absorbing region is studied and optimized to save computing time and to suppress boundary reflections which consequently eases signal analysis. Finally, the Dirichlet boundary condition that models the excitation due to a contact piezo-electric transducer attached to the upper surface of the reservoir is examined. The excitation study investigates our ability to generate a desired mode, subsequently helping to optimize and/or explain experimental set-ups.

3.4.2 Validation of the Bilayer Model

The model's behavior can be verified to reflect analytical predictions, ensuring that the simulated waveguide supports modes with the expected amount of dispersion. This verification is carried out in the frequency-wavenumber space. Consequently, the concept of the two-dimensional fast Fourier transform (2DFFT) is introduced.

3.4.2.1 Material Property Substitution

During early phases of this work, material characteristics for the application of interest were unavailable. Consequently, large portions of the 2D study presented here are done using material properties of common isotropic materials (aluminum, steel, etc.) It is rationalized that due to the restriction of particle displacement along a principal direction, and thus ignoring shear horizontal wave generation, orthotropic materials will behave isotropically. Therefore, little value is lost by validating model response with the afore-mentioned substitution.

3.4.2.2 Separating Modes in the Frequency-Wavenumber Domain

Often it is found that geometrical restraints do not allow for the spatial separation of two modes. In these cases, Alleyne and Cawley [7] have shown that the 2DFFT is a useful tool for resolving individual modes traveling in the same wave packet. The two-dimensional discrete Fourier transform is given by [8]:

$$F(\mu,\nu) = M^{-1}N^{-1}\sum_{\sigma=0}^{M-1}\sum_{\tau=0}^{N=1} f(\sigma,\tau)e^{-i2\pi\left({}^{\mu\sigma}/_{M}+{}^{\nu\tau}/_{N}\right)} \tag{3.9}$$

where σ and τ are the independent variables of the function *f* being transformed and μ and ν are the respective variables in frequency space. Since the function *f* is discrete, M and *N* are the total number of points for σ and τ respectively. By recording the signal as a function of time at a series of regularly spaced intervals, space and time become the two independent variables. The 2DFFT can then be used to ascertain a complex three-dimensional representation of the amplitude of Lamb waves as a function of spatial frequency (i.e. wavenumber) and temporal frequency. After taking the absolute value of the complex array, the various modes, each propagating at different wavenumbers for a given temporal frequency, manifest themselves as areas of high magnitude in the two-dimensional frequency spectrum. It should be noted that this method is valid for real-world applications as well as numerical experiments as long as the same rigorous requirement for data collection is met, i.e. that the temporal waveform is recorded at evenly-spaced intervals along the surface of the plate, sufficiently close enough to avoid aliasing.

3.4.2.3 Window Selection

In reality, signals must be truncated before they can be treated in a post-processing environment. This truncation necessarily introduces error into the 2DFFT, whether it is a continuous transform, or some discrete version as in eq. 3.9. The effects of truncation can be categorized by two error types: smoothing error and leakage error. A trade-off of the extent of these two error types can be controlled by an intelligent choice of the window function in the temporal and/or spatial domain [8, 9, 10]. Consider figure 3.5 where three common window types (upper row) are compared with their respective Fourier transforms (bottom row) on an arbitrary scale. Here 100 point windows are used with non-zero values occurring between -1 and 1. The discrete Fourier transform of a signal of interest is convolved with the Fourier transforms of the window function, thus producing the two types of error (smoothing and leakage). One can note from figure 3.8 that the rectangular window, shown in the first column, has both the thinnest central lobe and the largest side lobes. This thin central lobe coincidentally means that it has the highest resolution (lowest smoothing error), but the side lobes are a manifestation of large amounts of spectral leakage (largest leakage error). Next consider the Gaussian window in the center column. This truncating window function has a very wide central spectral feature (large smoothing error) but no apparent side lobes (low leakage error). The Hanning window on the right hand side can be considered somewhat of a compromise between the two former columns, but its characteristics lean toward the Gaussian window. Therefore, loss of resolution can be leveraged to decrease side lobe appearance, but for the lowest leakage error, the manifestation of side lobes is inevitable.

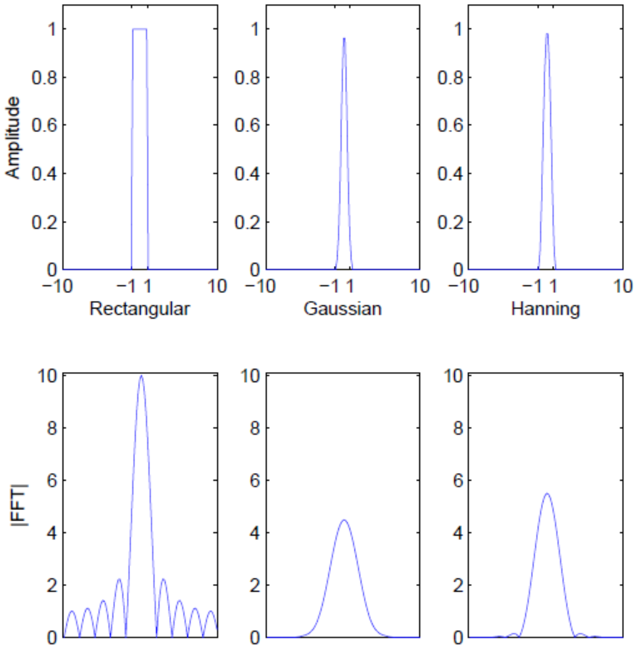

Figure 3.5: Three common window types (upper row) are compared with their respective Fourier transforms (bottom row)

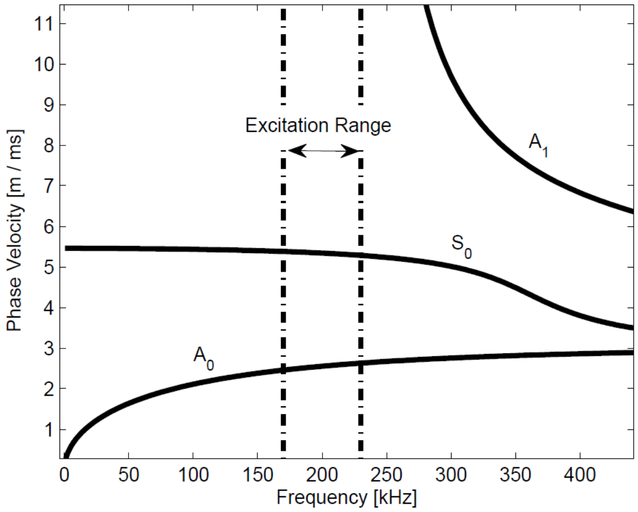

Figure 3.6: Phase velocity dispersion curves for a steel plate (see table 3.1). Operation below the cut-off frequency for the A_1 mode guarantees mode conversion occurs solely between the two fundamental modes.

Table 3.1: Bulk velocity and density values for steel

Density (ρ)	**8000 [kg/m^3]**
Longitudinal Bulk Velocity (c_{Long})	**5960 [m/s]**
Shear Bulk Velocity (c_{Shear})	**3250 [m/s]**

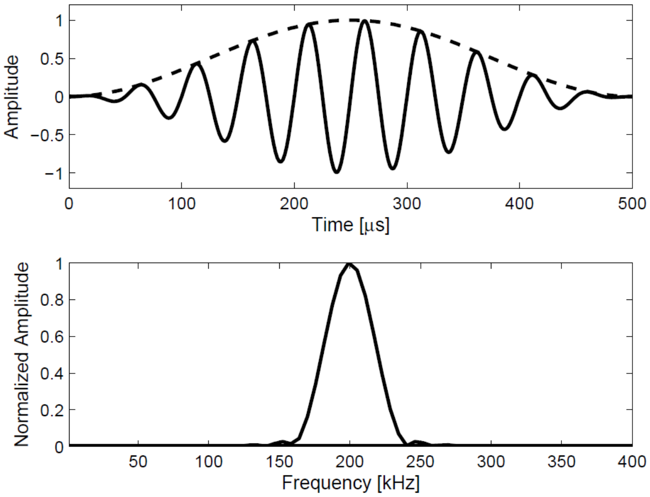

Figure 3.7: Top: Excitation signal used. A ten cycle, Hanning-windowed signal centered at 200 kHz. Bottom: The frequency spectrum of the excitation signal, which matches the frequency range of low dispersion indicated in figure 3.9.

As an example case, consider two modes propagating in the positive x direction according to the analytical expression:

$$F(x,t) = A_0 e^{2\pi i\left(ft - \frac{fx}{c_p^A(f)}\right)} + S_0 e^{2\pi i\left(ft - \frac{fx}{c_p^S(f)}\right)} \tag{3.10}$$

where F is the wave packet amplitude at a given position x and time t, f denotes frequency, $c_p(f)$ denotes phase velocity as a function of frequency for the appropriate mode, and A_0 and S_0 are the amplitudes for the A_0 and S_0 modes respectively. Consider these two fundamental modes traveling in a steel structure with a thickness h = 6.75 mm and with the material properties given in table 3.1. The corresponding dispersion curves for such a structure are given in figure 3.9. The problem is treated as a boundary value problem, where the wave shape at $x=0$ is defined at all times as a 10-cycle, Hanning-windowed sine wave shown in figure 3.10 for both fundamental modes, but with $S_0 = 1$ and $A_0 = 0.25$. The central frequency for the sine wave is 200 kHz, but due to the

Hanning-window in time, it has a frequency spectrum as depicted by the excitation range in figure 3.10 (bottom).

The function given by eq. 3.10 is evaluated numerically in Matlab, by discretizing the time and space dimensions. The time dimension was discretized via a 1.5 MHz sampling frequency. The x vector was discretized with a resolution of 0.5 mm. A 75 μs long time vector was found to be sufficient, and the x vector was limited to 2 cm to mimic a geometrically restrained problem, where additional scattering features necessitate a limited scanning length. The results of the numerically propagated wave packets are shown in figure 3.11.

On the left side of the figure, the wave packet is plotted in space and time subject to the various displayed window functions. The right side shows that the number of different windows in the spatial domain affects the frequency wavenumber space differently. In this manner the effects in the wavenumber-frequency plane can be compared qualitatively. Theoretical dispersion curves *k(f)* are super-imposed for the reader's convenience. It is also clear from this figure that due to the relative proximity of the two dispersion curves in question in the two-dimensional frequency plane, only the rectangular window offers the appropriate resolution to be able to distinguish between two separate modes at the given frequency. The spreading error caused by applying a smoothing window causes overlap, since smoothing via a window function inherently gives an erroneous large value for the width of a spectral feature [8]. This is one of the reasons that rectangular windows (i.e. truncated signals) are employed in this work; the need to resolve spectral features outweighs the need to suppress side lobes caused by spectral leakage. However, for the case of a rectangular window, special care must be taken that side lobes are not confused for true modes, and interference is problematic for the detection of low amplitude converted modes.

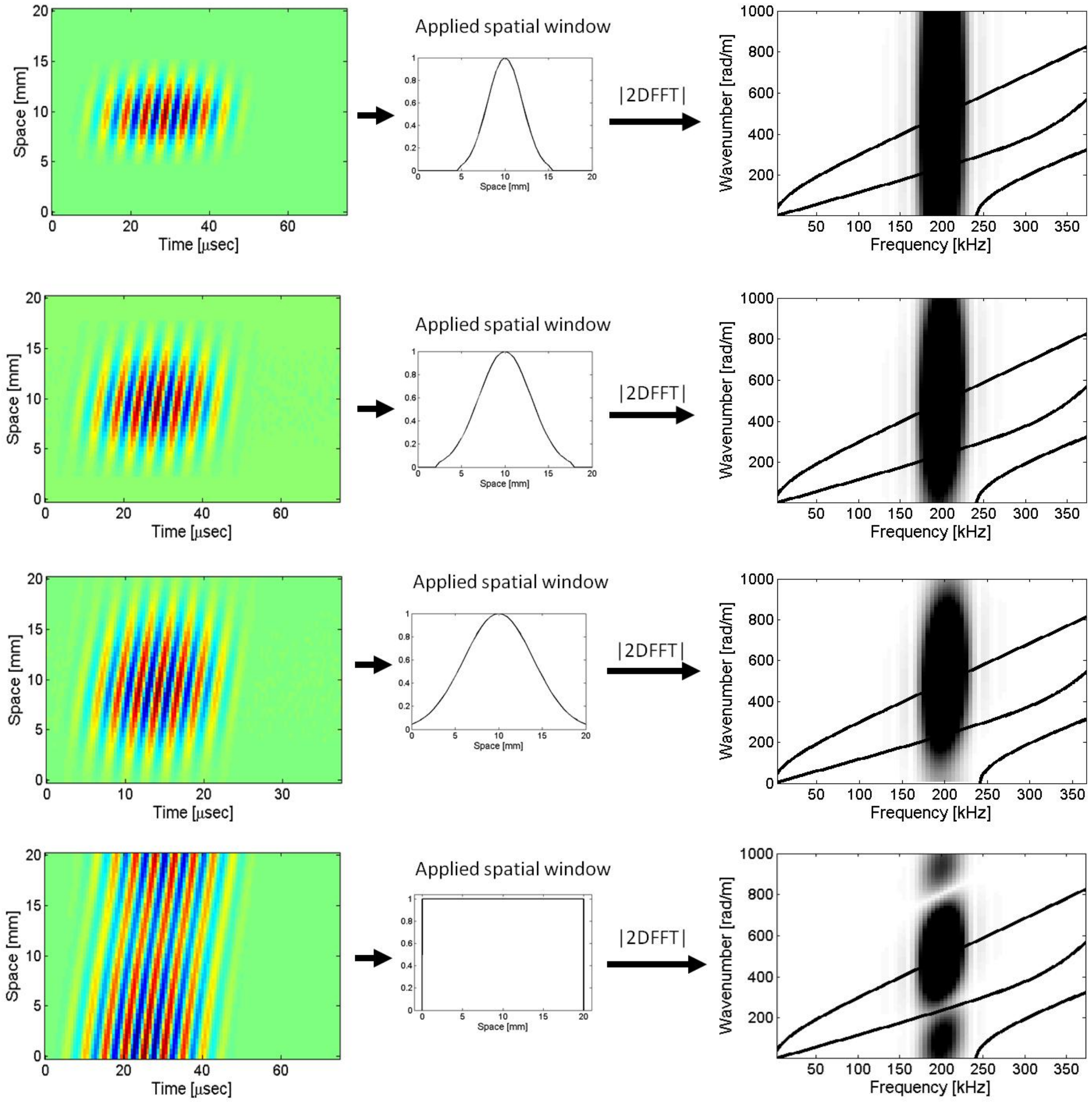

Figure 3.8: Three Gaussian windows (upper) with various widths and a rectangular window (bottom) are applied to the same set of data to show the trade-off between resolution and suppression of spectral leakage. Analytical dispersion curves are superimposed on the two-dimensional frequency plane to show agreement.

Secondly, rectangular windows offer a large benefit when attempting to detect low-amplitude frequency components in the presence of white noise. Noise bandwidth, B_{Noise} is given by:

$$B_{Noise} = \frac{1}{|H(f)|^2_{max}} \int_0^\infty |H(f)|^2 df \tag{3.11}$$

where *H(f)* is the window in question as a function of frequency. It is well documented [11] that rectangular windows offer the best possible bandwidth.

3.4.2.4 Results

Accordingly, regularly spaced points of investigation are made on one face of the plate, and the array of temporal waveforms is visualized in the frequency-wavenumber space. In figures 3.12 and 3.13 the solutions for dispersion curves found by DISPERSE are laid over top the output from COMSOL, for antisymmetric modes and symmetric modes respectively, to confirm that the dispersive relationship in the FEM model agrees with the analytically determined dispersion curves.

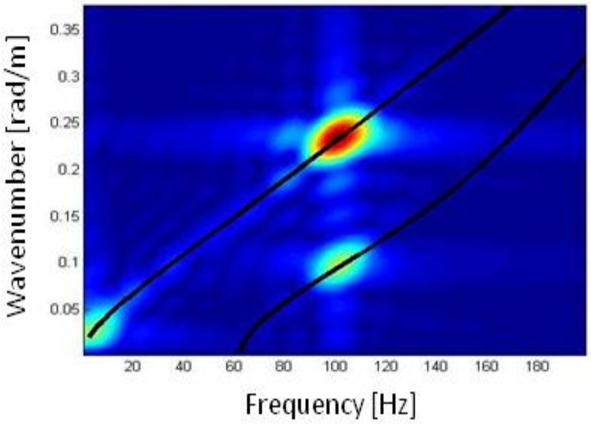

Figure 3.9: 2DFFT of the data from COMSOL when antisymmetric modes are excited at 100 Hz. Dispersion curves for the A_0 and A_1 modes are superimposed in black to show agreement.

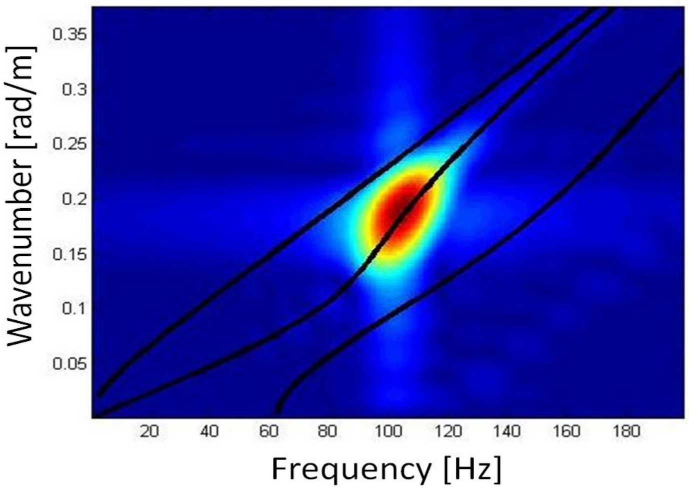

Figure 3.10: 2DFFT of the data from COMSOL when the S_0 mode is excited at 100Hz. Dispersion curves for the S_0, A_0 and A_1 modes are superimposed in black to show agreement. The excitation frequency is below the cut-off frequency, which is why only the fundamental mode is excited.

3.4.3 Computational Convergence Study for Multilayer Structure

There are several parameters that affect computational time and accuracy of the solution. For example, the degree of the interpolation polynomial, size of the mesh, element shape, tolerance, and solver method can all impact solution accuracy and computational efforts. Truncation convergence tests (as opposed to iteration convergence tests) can be an efficient method to ensure that the mesh is sufficiently dense, and the temporal step is sufficiently small, so as to supply an accurate result. Checking the convergence of a solution is a well-known technique to determine the error associated with the truncation and discretization of the given problem [5]. All numerical simulations have some associated numerical error, but that error should approach zero as mesh size and time step decrease. Unfortunately, a decrease in mesh size and time step also means an increase in computational effort. Monitoring certain values at certain points in the finite element geometry, and plotting them versus the computational time, is the most common way to ensure that the solution is appropriately converged, without over-compensating with valuable CPU time.

Several truncation issues exist when dealing with UGW in multi-layer structures. For instance, when simulations are carried out in the time domain, errors can accumulate with each time step. Therefore, the accuracy of the simulation can be a function of overall time. Furthermore, mesh constraints (for a given frequency bandwidth) that are applicable to a given layer when it is acting as a free standing plate may change when that layer is rigidly bound to a layer of a different material on one (or both sides), since this condition alters overall mode shape. This subsection shows the results of a convergence study concerning mesh size done both for single layer and bilayer media.

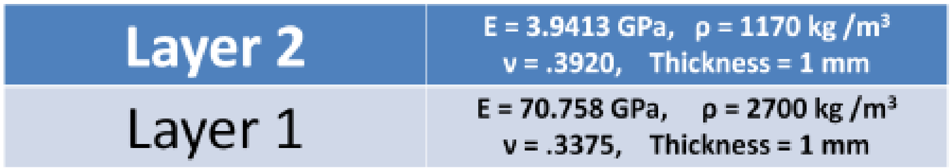

Layer 2	$E = 3.9413$ GPa, $\rho = 1170$ kg $/m^3$ $\nu = .3920$, Thickness = 1 mm
Layer 1	$E = 70.758$ GPa, $\rho = 2700$ kg $/m^3$ $\nu = .3375$, Thickness = 1 mm

Figure 3.11: Characteristics of the two layers.

As an example case, consider the FEM model described in figure 3.11[3]. Here the material properties and simulation geometry are displayed. The material properties were chosen specifically to disparage greatly, but to still be in the realm of common material properties, so as to highlight the importance of convergence tests. Two sets of dispersion curves are shown in figure 3.12, for the bilayer case (left), and also for one of

---

[3] The study presented here was carried out before the relevant material properties were supplied, hence the inconsistency in this section in regards to materlal properties, dimensions, and operating frequencies

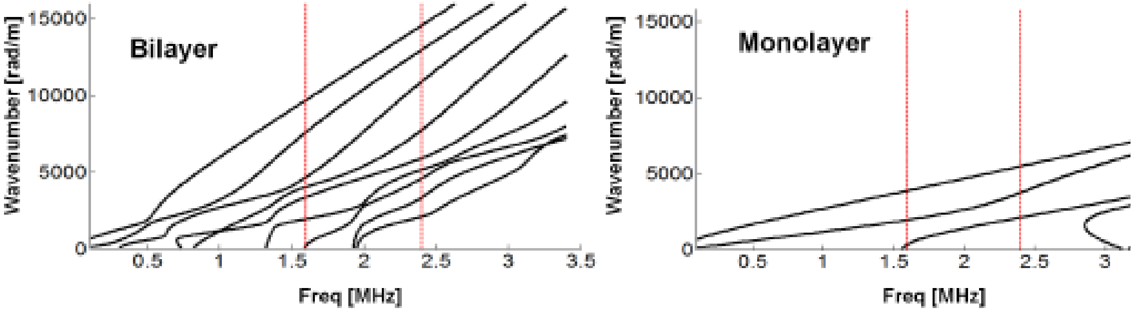

Figure 3.12: Wavenumber dispersion curves of bilayer (left) and monolayer (right) media. Characteristics of the two layers are given in figure 3.11.

the individual layers (right). Note that there is a significant difference between the two sets of curves, both in the overall number of modes and the maximum expected wavenumber.

It is assumed that simulations carried out in the temporal domain have more demanding convergence criteria since numerical errors attend to accumulate with each time step. Therefore the models in this section are carried out in the time domain, and it is assumed that the time domain parameter constraints will necessarily produce similar results in the frequency domain. Consequently, the monitor points are inspected near or at the intended final time step. Overall, superimposing analytical curves on the frequency-wavenumber space is a good method to verify that the mesh works for the wide range of possible modes, as opposed to a displacement convergence test which may monitor only the strongest mode, or the mode with the highest displacement at that particular depth. On that note, monitoring several points throughout the thickness of the waveguide is important, due to the varying stress and displacement fields possible for the various modes.

The excitations used are Hanning-windowed sinusoids, and thus exhibit gradual change with no sharp edges. Cubic interpolation functions work well for approximating sinusoidal type functions, since any higher order polynomial tends to lead to massive oscillations between interpolation points, as per Runge's phenomenon. Linear and quadratic functions may be applied, but do not offer the same flexibility as a cubic interpolation. Different time steps were used, but ultimately the time step was taken to be one tenth of the period of the central frequency, which was sufficient for approximating sinusoids.

It is logical that if a solution is expected to behave symmetrically, then the mesh should also be symmetric to most closely reflect that behavior. So naturally, square elements seem the natural choice to approximate the geometry of traditional Lamb waves in a mono-layer material that have symmetrical mode shapes with respect to the bisector. That being said, bilayer materials have non-symmetrical modeshapes, and it is possible that the best mesh is a variable one with elements having different characteristic lengths. With this in mind, triangular elements seem the more natural choice, since they are simpler to mesh between subdomains with variable mesh sizes. For the sake of continuity in the convergence tests, the two layers acting independently as mono-layers are also meshed with triangular elements.

Layer 1 was found to converge immediately using a characteristic mesh dimension equal to the layer thickness (1 mm). Figure 3.13 shows the triangular elements used to mesh the layer (top), and the solution in terms of z-displacement, perpendicular to the surface of the plate. One can note that with this relatively coarse triangular mesh, the symmetry of the problem is still respected by the mesh geometry. Layer 2, however, required more vigorous convergence tests, and due to the necessarily more fine mesh (smaller wavelengths couple with higher order modes with more drastically changing modeshapes), the triangular elements no longer respected the symmetry of the problem. Consequently monitor points were setup throughout the structure, both internally, and on the surface, to check for convergence.

Thus far, the identity of the quantity to be considered at the aforementioned monitoring points has been ignored. Time of flight seems like an important quantity to monitor, since it directly reflects the numerically simulated waves ability to propagate at the theoretical wave speeds. The generalized equation is truly solving for particle displacement, in both ‘x’ and ‘z’ directions, so both of those quantities also seem like viable candidates. Modal amplitude is also a commonly used quantity for identifying and sizing damage [3], and so the amplitude of certain modes at the central excitation frequency is also a logical choice to verify convergence. Exemplary convergence tests are shown in figures 3.14, 3.15, and 3.16 for the monlayer structure, monitoring time of flight, central frequency amplitude, and maximum displacement respectively. Convergence is determined when the percent difference of the monitored quantity between two successive mesh sizes is less than 2%. Notably, of these three, the convergence test concerning displacement measurements is the most demanding of characteristic mesh size.

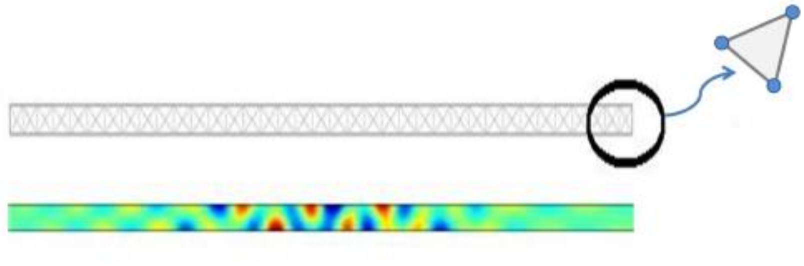

Figure 3.13: Mesh and out of plane displacement results for the first layer behaving as a mono-layer. The triangular mesh is able to describe the geometry in a symmetrical pattern, respecting the natural symmetry of the problem.

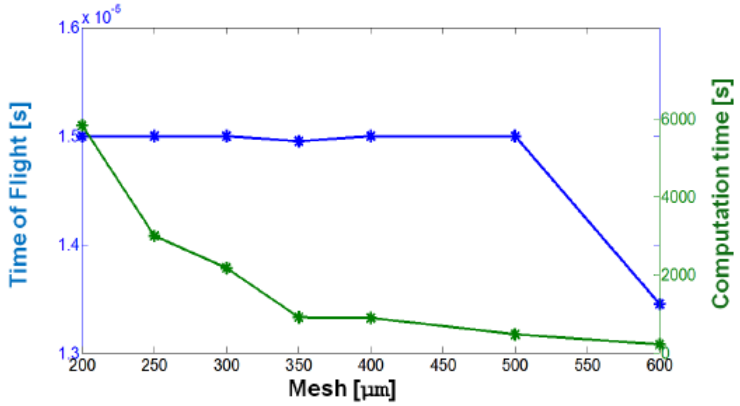

Figure 3.14: Convergence test concerning time of fight for the fastest mode for layer 2 acting as a monolayer. Convergence occurs with a characteristic mesh size of 0.5 mm.

The bilayer has many more modes and a wider range of wavelengths to take into account, i.e. 0.48 mm up to 4.5 mm, an order of magnitude difference. However, there is no symmetry to respect in the problem. Figure 3.17 shows an exemplary convergence test done when monitoring the maximum displacement at a certain monitoring point on the surface of the first layer. In this figure, the x-axis denotes the mesh size for layer 2, and layer 1 was unrestricted. Convergence is again reached near 0.5 mm. To demonstrate the success of the final mesh on properly propagating all the modes having such a wide range of wavelengths, the frequency-wavenumber space is show in figure 3.18, with analytical dispersion curves superimposed in black to show agreement.

In conclusion, the bilayer reached convergence the fastest when the characteristic mesh size was unrestricted, in the layer having the larger wavelengths when acting as a monolayer. The characteristic mesh size of 0.5 mm in the bilayer indicates that optimal convergence is of similar order of magnitude as in the layer with the smaller wavelength when acting as a monolayer. Overall, it was found that time-of-flight measurements were less effective and not satisfactory predictors of convergence rate.

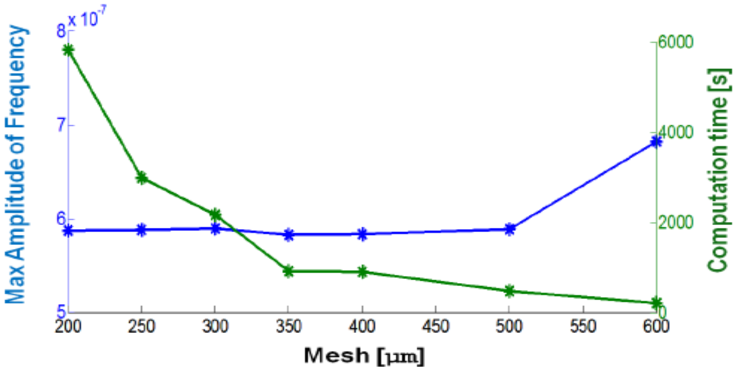

Figure 3.15: Convergence test concerning maximum amplitude of central frequency in the frequency-wavenumber space for the out of displacement of the plate. Convergence occurs with a characteristic mesh size of 0.5 mm

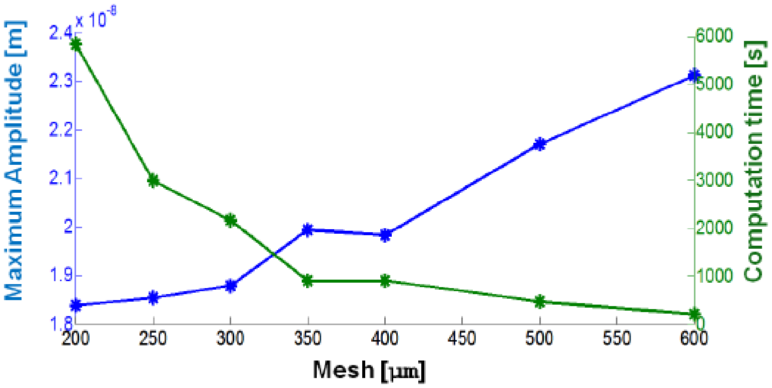

Figure 3.16: Convergence test concerning maximum displacement in the out-of-plane direction (z). Convergence occurs with a characteristic mesh size of 0.3 mm, differing from figures 3.14 and 3.15.

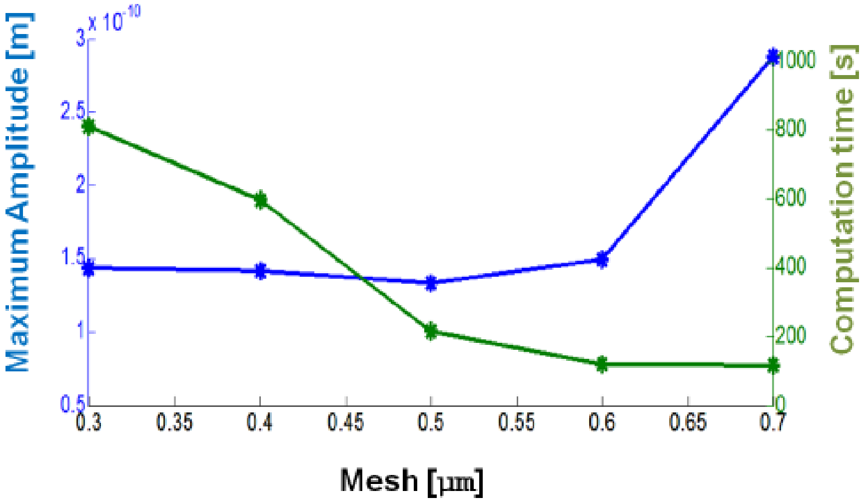

Figure 3.17: Convergence test concerning maximum displacement in the out-of-plane direction (z), for bilayer geometry. X-axis denotes characteristic mesh size of layer 2, while layer 1 was unrestricted.

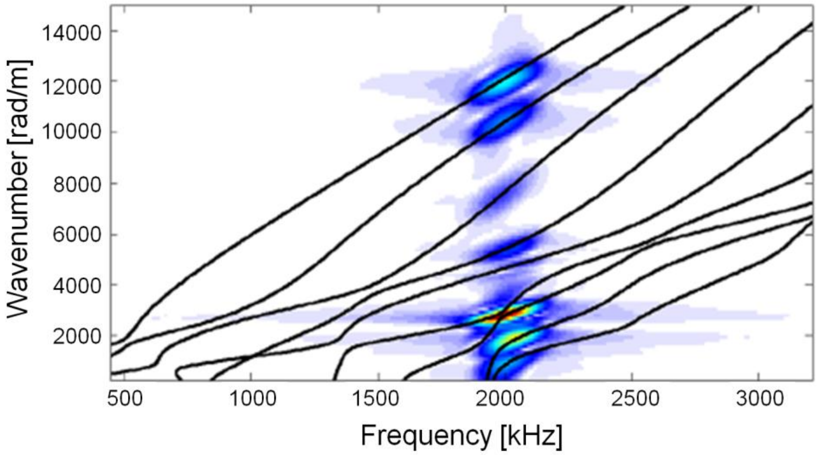

Figure 3.18: results from converged solution displayed in the frequency-wavenumber space to show that all modes were propagating at the correct frequency range, and at the correct wavenumber. Analytical dispersion curves are superimposed to show agreement

3.4.4 Excitation Study

As discussed in section 3.1, two forms of excitation are employed in this work. The Neumann boundary condition formulation has already been discussed at length and is used to generate a right-traveling wave-packet consisting of a pure mode. The Dirichlet boundary condition is used to more closely emulate the contact transducers that will eventually be used in the experimental investigations (see chapter 6). The excitation is modeled as a force on the upper side of the plate (see figure 3.2) which corresponds to the restriction of outer surface interrogation. Here, the Dirichlet boundary excitation is developed in more detail.

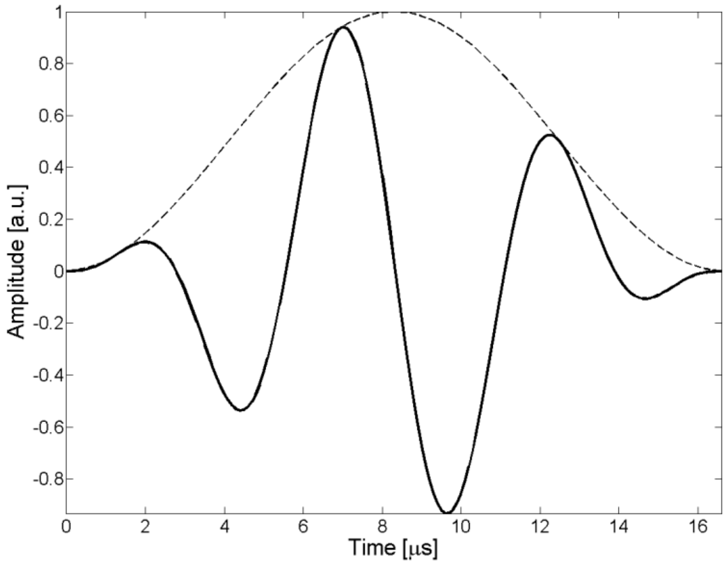

Figure 3.19: Temporal function used in excitation shown in solid line. Centered at 180 kHz, 3-cycle, Hanning- windowed (window used shown with dashed line).

Two studies are carried out to investigate the behavior of this excitation type[4]. Firstly, the parameter *d* as seen in figure 3.2 is varied according to wavelength of Mode 2 (1/4 λ; 1/2 λ; 3/4 λ; 1 λ). Coincidently, Mode 2 is chosen for this study since it is to detect and excite given its large modal displacement on the free surface of the carbon-epoxy layer. The temporal signal used is a 3-cycle, Hanning-windowed sinusoid, as shown in figure 3.19. The two-dimensional Fourier transforms for these four cases is shown in figure 3.20. Secondly, the effect of adding multiple, periodic, forcing-function boundary conditions to emulate the effects of a comb transducer are studied, as shown in figure 3.21.

Consider figure 3.19, which shows the results in frequency-wavenumber space of changing the element length with regard to the wavelength of Mode 2. Figure 3.20.A shows the frequency-wavenumber space for an emitter $d = \lambda$. One can note that there is almost no amount of mode detected at the center frequency of 180 kHz. The propagation frequency range is shifted towards the lower end of the overall excited frequency range. Figure 3.20.B shows the case for $d = 3/4\lambda$. Here one can see that the central frequency, although being excited for Mode 2, is not the center of the propagation frequency range. In figure 3.20.C, $d = 1/2\lambda$, and although it does not appear that 180 kHz is the dead center of the propagated frequency range, it is clear that it is near the center and very strong. Figure 3.20.D shows the case for an emitter length of just $d = 1/4\ \lambda$, and despite the fact that the frequency range and propagation range now seem to both be centered at 180 kHz, the overall signal strength has decreased by almost 33%.

---

[4] The work presented here uses the material properties supplied by our industrial partners (see Chapter 2).

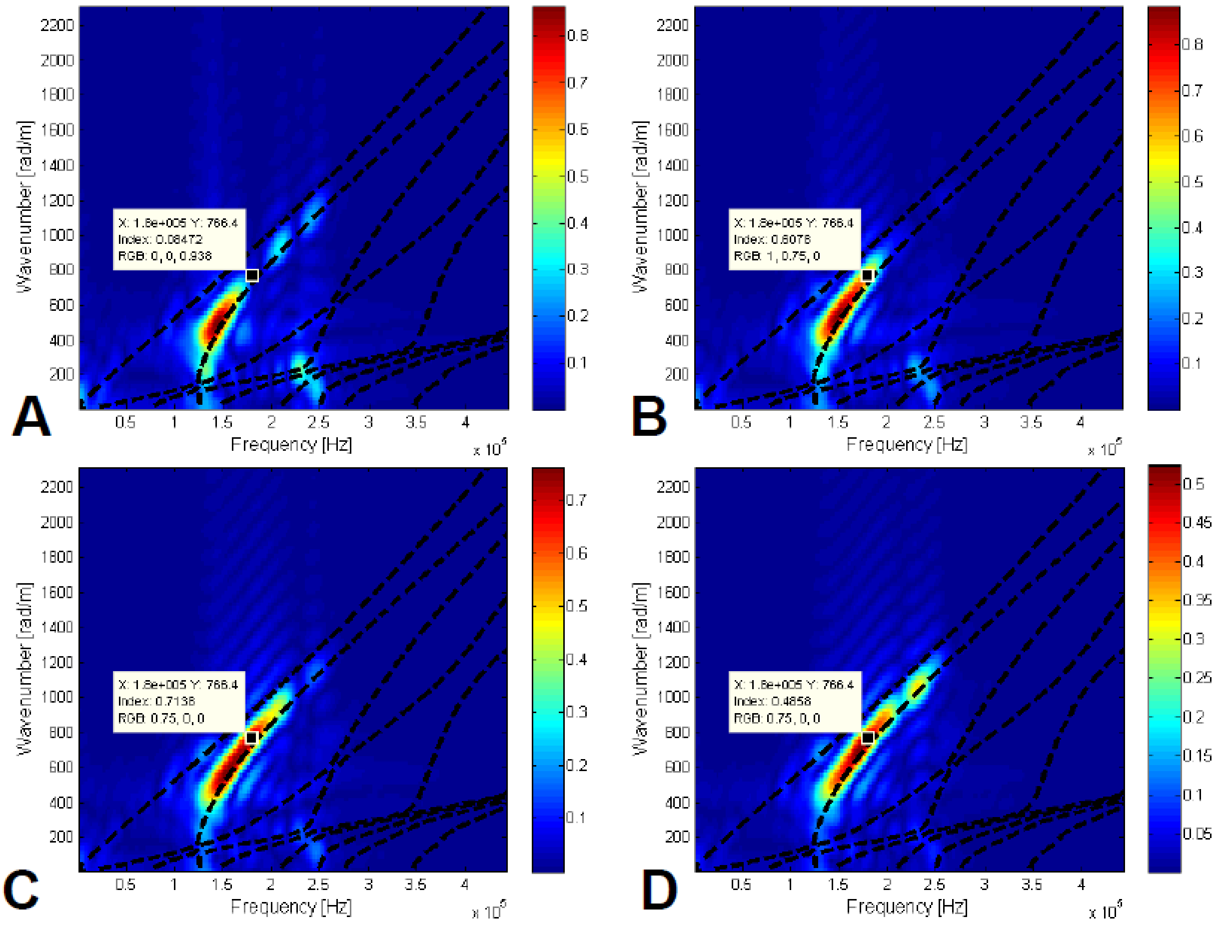

Figure 3.20: Frequency wavenumber domain representation for 4 cases. (A) emitter length = 1 λ, (B) emitter length = 3/4 λ. (C) emitter length = 1/2 λ. (D) Emitter length = 1/4 λ

Consequently, for the strongest signal in the desired frequency range, the emitter should be equal to one-half of the wavelength of the desired central frequency. Less than one-half will still excite the correct frequency range, but with less power. More than one-half causes destructive interference and shifts the propagated frequency range to the left of the intended range in this case.

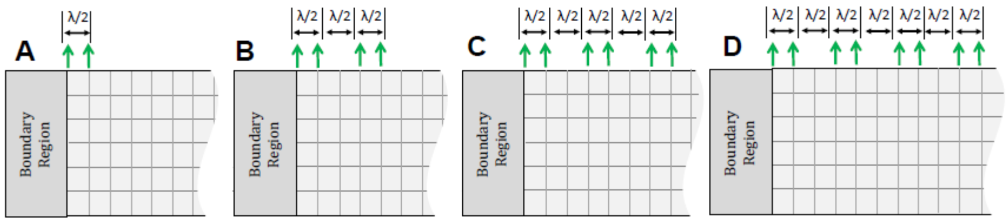

Figure 3.21: Schematic of 4 boundary conditions used to generate figure 3.25

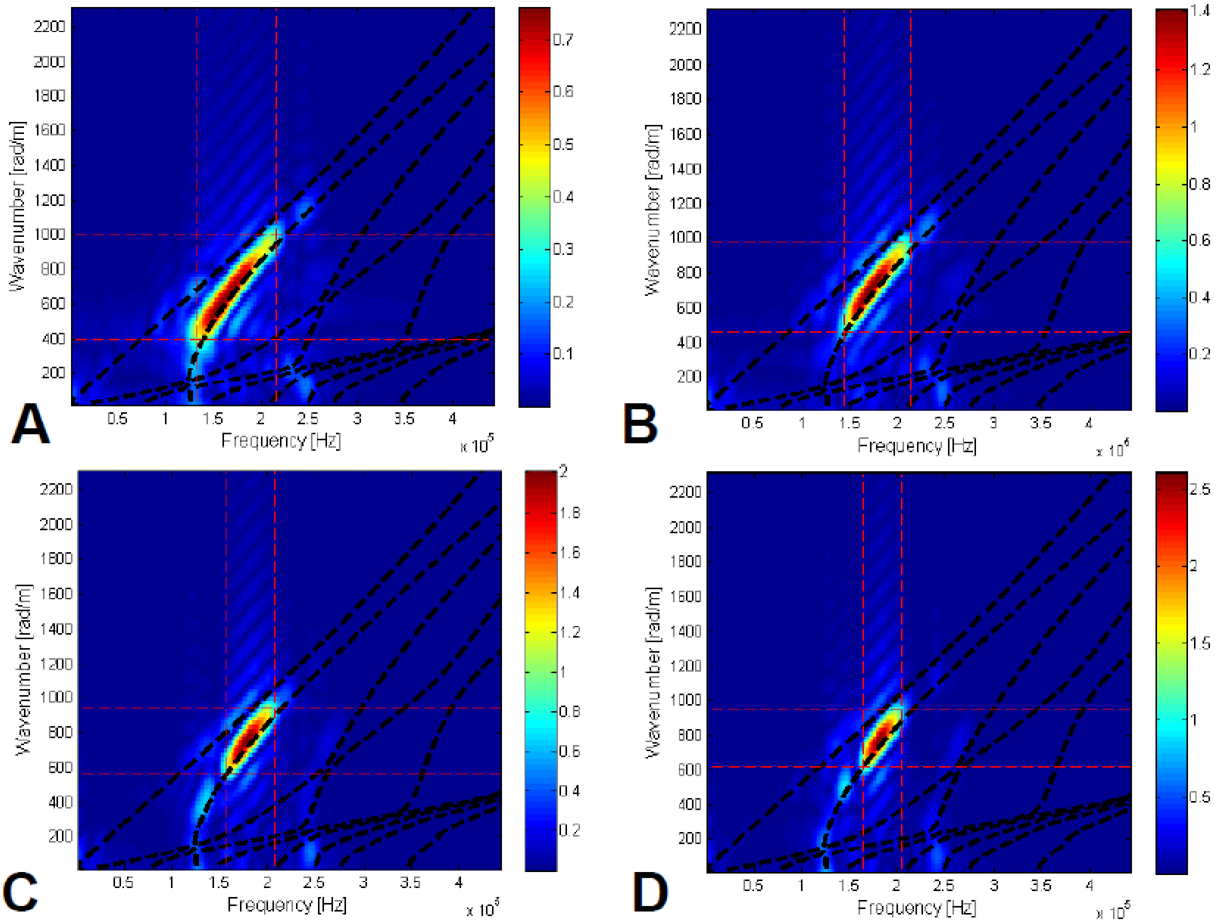

Figure 3.22: Frequency wavenumber domain representation for 4 comb-like boundary conditions when emitter length = 1/2 λ. (A) 1 element, (B) 2 elements, (C) 3 elements and (D) 4 elements.

Now consider the second excitation geometry investigation, as depicted in figure 3.21. A study was conducted on the effect of the propagated signal by increasing the number of elements, spaced one wavelength apart. The excitation zone is chosen to be 1 cm long, for two reasons: 1 cm corresponds to roughly 1.5 wavelengths of Mode 2 at 180 kHz, and 1 cm diameter contact transducers are readily available at Georgia Tech Lorraine. The force is applied in the in-plane direction (x-direction). Four cases were investigated, as depicted in figure 3.21. Figure 3.22.A is the frequency-wavenumber representation for an excitation with one element, figure 3.22.B is two elements, figure 3.22.C is three elements, and figure 3.22.D is four elements. One can note that the propagated frequency range and wavenumber range (boxed-in by thin dotted red lines) both become increasingly narrower with an increased number of elements. Amplitude at the central frequency for Mode 2 also increases proportionally with the energy being added by the increased boundary force, as can be attested to by the maximum amplitude shown by the amplitude color scheme on the right hand side of each figure.

3.4.5 2D Simulation Summary

The work detailed in this section regards the FEM simulation of UGW propagation in a 2D bilayer medium and the investigation of some key model parameters. Lamb modes are successfully simulated in bilayer orthotropic plates along one of the principal material axes which is aligned with the propagation direction. Moreover, the two dimensional fast Fourier transform (2DFFT) algorithm is presented and used both to identify the propagating modes in a given model, and to corroborate the degree of dispersion with analytical results.

A convergence study is performed to master the selection of key parameters such as element size (with respect to wavelength), time step, interpolation function, etc. This study is essential to ensure accurate numeric solutions and optimize computing time. It is shown that for a multi-layer structure, the element size for each layer should follow the same size restrictions as in the case when that layer is treated as a mono-layer.

Lastly, the Dirichlet boundary condition was investigated to help optimization studies (see Chapter 5) and/or explain experimental results (see chapter 6). It is found that if the boundary element is exactly one half the wavelength of a given mode, that mode will be more prominent in the resulting wave-packet. If frequency range is desired to be limited (for dispersion-limiting purposes for example) a comb transducer can be used to hone in on a certain wavenumber range [12].

3.5 3D Numerical Simulations

In general, three dimensional simulations are needed to simulate wave propagation in anisotropic media. It will be seen that computational demands will limit the practicality of these models. Nevertheless, this section is devoted to work done in a three-dimensional FEM environment.

3.5.1 Orthotropic Plate

Consider again eq. 3.3. In an orthotropic medium, as is the case for the carbon-epoxy layer, the material symmetry further simplifies the 6x6 Voigt notation elastic material matrix. The simplification leads to zeros for every blue field in figure 3.1, and non-zero values for the green fields only. The material properties for the carbon-epoxy layer (see Chapter 2) reflect this simplification. A square plate is simulated using these material properties, excited by a circular PZT-type Dirichlet boundary condition in the center. Other geometries can be used, but the circular boundary condition most closely imitates the cylindrical transducers in the L.U.N.E. facilities. The simulation is carried out in the time domain, and plate thickness is equal to the layer thickness of the carbon-epoxy overwrap for the 2.5 L pressure vessel. Three-dimensional triangular mesh elements

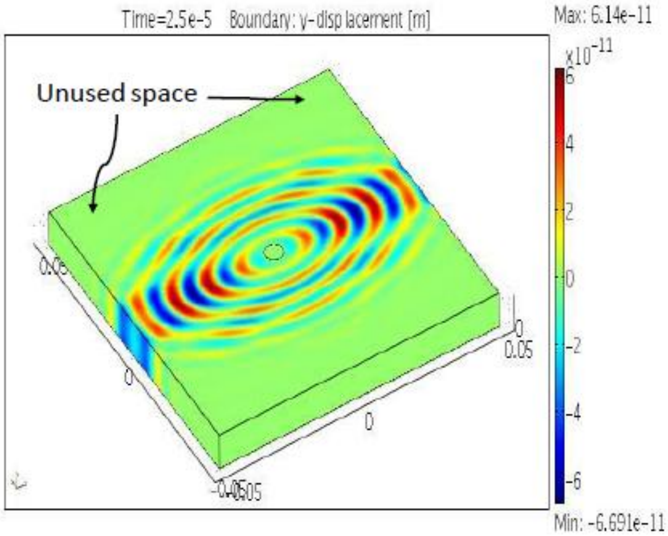

Figure 3.23: Example of 3D propagation in an orthotropic plate. Note the elliptical spreading pattern, and the consequent wasted space near the four edges of the plate.

are used. No ABR are used since they are ineffective in dampening reflections from oblique incident waves [13] and the last time step is chosen so as to avoid the effects of edge reflections. Figure 3.23 shows a simulation result from this 3D orthotropic plate example.

Analytical Rayleigh-Lamb wave equations exist for plane waves in orthotropic media. Since the elliptical spreading wave shows symmetry in the direction tangent to the wave front, and parallel to the surface of the plate in the principal directions, the numerical solution to these dispersion relationships can be compared with the frequency-wavenumber domain representation along the principal directions. The agreement between the UGW propagating along the principal directions in the model and the analytical dispersion curves is shown in figure 3.24 by displaying the solutions in the frequency-wavenumber space via the 2DFFT. It is clear that waves are propagating as expected along the two principal directions. However, computation time is

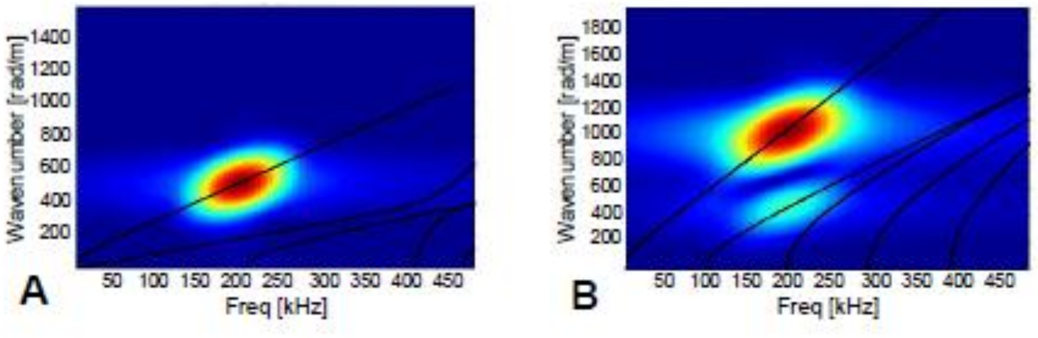

Figure 3.24: Frequency-wavenumber domain representation of waves propagating along the (A) z-direction and (B) x-direction. Analytical dispersion curves (in black) are superimposed to show agreement.

approximately 10 hours which is considerably higher than then the computational time of the 2D model (5 minutes). Furthermore, the propagation domain is shorter in the x-direction (0.05 m) than it is for the two-dimensional model (1 m) .

3.5.2 Geometrical Simplifications

As previously stated, computational time is a strong function of the number of elements used to approximate the finite element domain. Remarkably, the computational time cited in section 5.1 (10 hours for a single layer) is impractically high. Consequently, two methods for limiting the geometry of three-dimensional models are developed and discussed here.

The first method restricts the geomeotrical size of the propagation domain by assuming elliptically spreading wavefront. The method entails numerically solving the analytical solutions along the principal directions and calculating the expected propagation distance by the fastest mode at all ranges of frequency of the excitation signal. Then an elliptical type pattern is assumed, and the wave front is interpolated between the wave propagation extremes in the ‘x’ and ‘y’ directions (see figure 3.25). As an example to

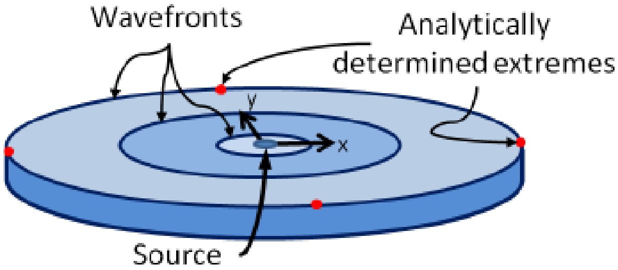

Figure 3.25: Diagram for method 1 for limiting the finite element geometry, and consequently reducing the number of meshed elements. The red points indicate the maximum wave propagation distance for the fastest mode in the frequency regime of the excitation

illustrate the usefulness of method 1, reconsider figure 3.23. Note the existence of space near the corners in the propagation domain that is unperturbed by the UGW due to the time-windowing of the FE model.

The second method used to decrease computational time involves taking advantage once again of the natural material symmetry that occurs along the principal directions.

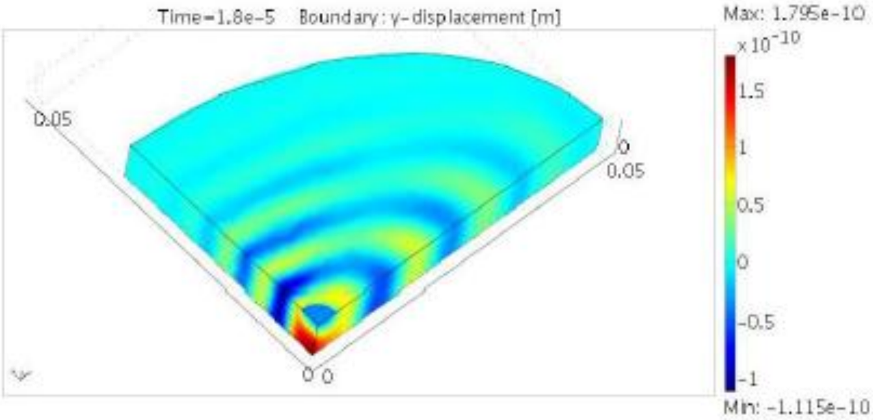

Figure 3.26: Quarter model: waves propagating in an orthotropic media.

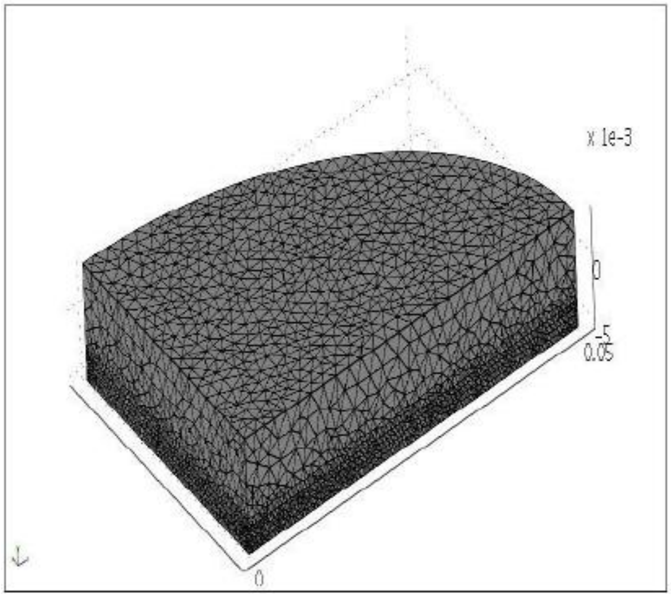

Figure 3.27: Triangular, non-even mesh for the quarter model. The more extreme changes in modeshape in the isotropic layer necessitate a tighter mesh.

This is the same principle that made two-dimensional models possible (see section 4). Since there is a natural symmetry along the ‘x’ and ‘y’ axes, one can imagine constructing a boundary condition which acts as if identical waves were approaching from the other side of the boundary. Indeed a pressure- release boundary condition does just that, and so enabling the creation of a model exactly one-fourth the size of the original. That is to say that if origin of the x-y planar basis is placed in the middle of the plate, only one quadrant of the Cartesian coordinate system needs to be modeled, as long as the boundary condition along each axis is ‘free’. The result displaying the elliptical wave spreading in the bilayer quarter model is shown in Figure 3.26. The computational time with this quarter mesh size is roughly 30 minutes, a reduction of about 95% computational time from a square bilayer plate having the same mesh size. This ‘quarter model’ is validated in the same manner as the square model, but due to the similarity of the results with figure 3.24, the validation is omitted here.

Three dimensional models presented in this section up until this point are single layer, orthotropic plates. A bilayer model is also created taking advantage of the geometrical simplifications described in section 5.2. Figure 3.27 shows the mesh used for the 3D model. This mesh is found to be sufficient for convergence requirements. The tighter mesh in the lower isotropic layer is similar to that of the 2D case (see section 4.3). Unfortunately, the addition of this high density mesh layer, increased computational time significantly to 13 hours, despite the geometrical simplifications.

3.5.3 3D Simulation Summary

This section treats the modelization of Lamb wave propagation in the orthotropic carbon epoxy layer in three dimensions. Theoretical dispersion curves, which dependent on the direction of propagation, are plotted for several cases. The results obtained in different direction of propagation are validated and have a very good agreement with theoretical results. After the monolayer orthotropic plate model is corroborated with analytical results, two geometrical simplifications are developed. Taking advantage of the orthotropic nature of the material and the elliptical spreading pattern of waves, a sizable improvement of 95% is gained in the CPU time. Despite this improvement, the addition of the second material layer subsequently increases computational time due to its high density nodal point requirement.

3.6 Closing Remarks

This chapter deals with the development of finite element models both in two and three dimensions for a healthy waveguide. The 2D model supports wave propagation along principal directions for the orthotropic layer. The two dimensional fast Fourier transform algorithm is used for both model types to corroborate the FEM simulations with expected analytically determined dispersion curves.

The 2D model is used to investigate parameters such as time step, mesh size, and excitation type and geometry. It is found that the parameters used in the 2D study translate to the 3D study easily, and that both show a high level of agreement with the analytically determined dispersion curves. It is shown that for a multi-layer structure, the element size for each layer should follow the same size restrictions as in the case when that layer is treated as a mono-layer.

Although the 3D model is more general and can support wave propagation along non-principal directions, it was found that the associated computational efforts necessary render it impractical. Furthermore, the quarter model, which gives a significant gain in CPU time, will be useless when scatterers (damage sites) are present in the model. These scatterers will cause diffraction and modal conversion, which in turn will reflect off the artificial pressure release boundaries imposed in the quarter model, obviously giving false results. Also, as previously stated, the experimental setup will investigate wave propagation along the axis of the cylindrical reservoir, which lines up with the principal direction, making the 2D simulations an acceptable depiction of real world experimental results. For these reasons, the finite element damage investigation carried out in the following chapter is in a 2D environment.

3.7 References

[1] N. Terrien, D. Osmont, D. Royer, F. Lepoutre and A. Deom, "A combined finite element and modal decomposition method to study the interaction of Lamb modes with micro-defects," *Ultrasonics,* vol. 46, pp. 74-88, 2007.

[2] D. Singh, M. Castaings and C. Bacon, "Sizing strip-like defects in plates using guided waves," *NDT&E International,* vol. 44, pp. 394-404, 2011.

[3] P. Cawley and D. N. Alleyne, "The interaction of Lamb waves with defects," *IEEE Transaction on Ultrasonics, Ferroelectrics and Frequency Control,* vol. 39, no. 3, pp. 381-396, 1992.

[4] M. Castaings, C. Bacon, B. Hosten and M. V. Predoi, "Finite element predictions for the dynamic response of thermo-viscoelastic material structures," *Journal of the Acoustical Society of America,* vol. 115, no. 3, pp. 1125-1133, 2004.

[5] Comsol, "COMSOL Multiphysics User’s Guide," version 3.3, 2006.

[6] J. Mackerle, "Finite-element modelling of non-destructive material evaluation, an addendum: a bibliography," *Modelling Simul. Mater. Sci. Eng.,* vol. 12, pp. 799-834, 2004.

[7] P. Cawley and D. N. Alleyne, "A two-dimensional Fourier transform method for the meausrement of propagating multimode signals," *Journal of the Acoustical Society of America,* vol. 89, no. 3, pp. 1159-1168, 1991.

[8] R. N. Bracewell, The Fourier Transform and its Applications, USA: McGraw-Hill, 2000.

[9] F. Harris, "Use of windows for harmonic-analysis with discrete Fourier transform," *IEEE,* vol. 66, pp. 51-83, 1978.

[10] A. H. Nuttall, "Some windows with very good sidelobe behavior," *IEEE,* pp. 84-91, 1981.

[11] L. W. Couch, Modern Communication Systems: Principles and Applications, Prentice Hall, 1995.

[12] J. Philtron and J. Rose, "Mode perturbation method for optimal guided wave mode and frequency selection," *Ultrasonics,* vol. 54, pp. 1817-1824, 2014.

[13] W. Ke, "Simulations 3D de la Generation et de la Reception d'Ondes Guidees - Application a la Detection de Defauts dans des Structures Composites," University of Bordeaux, Bordeaux, 2009.

[14] T. E. Michaels, J. E. Michaels and M. Ruzzene, "Frequency-wavenumber domain analysis of guided wavefields," *Ultrasonics,* vol. 51, pp. 452-466, 2011.

[15] N. Declercq, J. Degrieck and O. Leroy, "On the influence of fatigue on ultrasonic polar scans of fiber reinforced composites," *Ultrasonics,* vol. 42, pp. 173-177, 2004.

[16] M. E.-C. El-Kettani, F. Luppe and A. Guillet, "Guided waves in a plate with linearly varying thickness: experimental and numerical results," *Ultrasonics,* vol. 42, pp. 807-

812, 2004.

[17] A. H. Nayfeh, Wave propagation in layered anisotropic media, The Netherlands: Elsevier Science B. V., 1995.

CHAPTER 4

SIMULATION OF SELECT DAMAGE TYPES IN THE FINITE ELEMENT ENVIRONMENT

4.1 Introduction

The preceding chapter established a working model of the environment in question, which was verified to agree with theoretical dispersion curve calculations in both 2D (where the UGW propagated along the axial direction) and 3D along principal directions. This chapter continues in the same vein, and investigates the interaction of UGW with select defect types. The defects are modeled in an FEM environment. In order to simulate the presence of damage, alterations to the “healthy” waveguide model are made, such as geometrical, material properties (i.e. coefficients in the governing equation) and/or boundary conditions.

Various analytical models exist (ray models for bulk wave problems [1] and Global Matrix methods for guided wave problems [2]) to predict the properties of wave in continuous uniform structures. However, a discrete approach offers the flexibility to look at wave interaction with discontinuities [3]. Furthermore, the use of Finite Element Modeling (FEM) is highly beneficial for the optimization of SHM systems. In the past, FEM results have been used to help select the most efficient methods of excitation and reception so as to identify which UGW modes are sensitive to various damage types and orientations as demonstrated by the seminal work of Alleyne and Cawley [4]. Frequency range and receiver placement also influence damage detection capability. It is noteworthy that frequency range also influences modeshapes since, in general, UGW modeshapes are a function of frequency. The stress and displacement across the thickness of the material inform which modes are capable of being excited / detected from the top surface, and with which kind of damage they will most strongly interact. Occasionally, the same damage type can be modeled in a few ways. It is often appropriate to compare different FEM damage modelization approaches with experimental data to select the method that best predicts realistic behavior.

The chapter is organized as follows: a brief literature review is presented highlighting previous work done concerning the numerical simulation of UGW interaction with damage types. This section not only provides a precedent for the modelization carried out in this present work, but also provides results in simpler structures that are used to benchmark the current model. Then, a general methodology that is applicable to all localized damage types is described, and certain key variables are defined. The subsequent sections investigate the following defect types:

1. Surface originating cracks or cut-type defects caused either from the further propagation of micro-cracking (due to surface impacts) or gauges / cuts
2. Abrasions (defined as the decrease in carbon-epoxy layer thickness due to rubbing or grinding against external structures). However, since these will be modeled as removing geometry in the FE model, this damage type has been extended to “voids” including internal gaps.
3. Disbonding or ‘collapse defect’ (defined specifically as the detachment of the polyamide liner from the overwrapped carbon epoxy matrix. As thus defined, disbonding is specifically and explicitly different from delaminations, which are defined rather as the separation of fibers within the carbon epoxy matrix.)

Since cut type defects (or surface-originating cracks) have been documented by several groups for simpler structures, this defect type is used as a benchmarking tool in its corresponding section. It will be seen that in the process of verifying our numerical results for simpler structures, that some issues detecting low-amplitude modes without information provided by theoretical dispersion curves is encountered. Thus, a novel algorithm that leverages the concept of baseline subtraction applied in the frequency-wavenumber domain has been developed to detect low-amplitude converted modes with minimal *a priori* information [5]. The algorithm is presented in section 4.4.

4.2 Short Review

Finite element analysis (FEA) is a common tool for investigating Lamb wave interaction with various damage types. Notably, several authors [4, 6, 7, 8, 9, 10, 11, 12] have proposed taking advantage of the mode conversion and transmission loss that occurs when one of the pure fundamental modes encounters a crack in a plate as a means of identifying and sizing damage. It has been shown that it is possible to use transducers in two configurations, i.e. pulse echo or pitch-catch [13], which monitors the reflection and transmission fields, respectively. In general, interactions with symmetrical features cause reflection and transmission patterns differently than features that are not symmetrical. In both pipe-like and plate-like structures, symmetrical features are often permanent components of the system, e.g. welds between two sections. Non-symmetrical features often indicate damage. Values akin to transmission and conversion coefficients for various crack depths (modeled as notches) in plates have been calculated, and have been shown to be a good indicator of crack depth, especially for the case when the S_0 mode is incident in a frequency range below the A_1 mode cut-off frequency [4]. Separation of modes in time is not always possible due to geometrical constraints. If so, the amplitudes of different modes propagating in the same wave packet are often determined by means of a 2DFFT (see Chapter 3, section 4.2.2).

Kessler *et al*. used numerical simulations as a means to optimize experimental setups, and to study the effects that various parameters have on the sensitivity of damage detection [14]. They deduced that more energy signifies a stronger Lamb wave and would lead to a more accurate wave speed calculation. Material properties and geometry of the composite plate being investigated in their work were adjusted and the Lamb solution for the wave equation was used to plot dispersion curves for each of the altered configurations. Tensile modulus, Poisson ratio, density and thickness were all varied independently and the effects on the dispersion curves were documented. Lastly, actuator and sensor geometry were explored albeit admittedly unexhaustively to see if different propagation patterns could be generated. Kessler *et al*. compared their numerical predictions with two sets of experiments, one on narrow strips of composite structures, and the other on sandwich structures.

Their results showed that low frequencies generally meant a clearer signal since fewer modes were present to confuse the response, however if the A_0 mode is desired for the particular type of damage detection, then it is advisable to use a frequency high enough to avoid the dispersive (steeper) section of the dispersion curve, and instead use frequencies along the less dispersive (flatter) section of the curve directly before the formation of higher antisymmetric modes. Choosing the optimal number of cycles is tagged as the most complicated decision in choosing the pulse signal, since more cycles means a thinner frequency response and correspondingly less dispersion effects, but too many cycles means less time between an incident pulse and a reflected signal, which may be difficult to interpret if reflectors (possibly damage if the stress is concentrated enough) are too close together, or too close to the emitter or receiver. It was found that using a Hanning-windowed signal in intervals of a half sine helped to limit the bandwidth. Concerning the dispersion curve effects from changes in material properties, an increase in tensile modulus or a decrease in density both caused an increase in wave speed, whereas small changes in the Poisson ratio appeared to have negligible effects. Expectedly, changing the thickness shifted the dispersion curves to the left (lower frequency) or right (higher frequency) since the curves for a mono-layer plate are a function of the frequency-thickness product. Kessler also showed in the same study, that different types of signal analysis are more sensitive to different types of damage. For example, through hole damage, which causes a stress concentration, was most easily identifiable by wavelet decomposition since there was a very large energy drop of the primary driving frequency.

The work of Valdes *et al*. [15] inspected delaminations, which is a common and serious problem in composite structures that is obviously not a concern in previous isotropic studies. Artificially induced damage of increasing size was created with a scalpel knife blade in the mid-section of the experimental beams used during the resonance spectrum studies, and the exact dimensions of each stage of damage was documented using a traditional ultrasonic C-scan. Then, using a simple arithmetic difference method, the original "healthy" signal was compared with each stage of increasing damage, with the interesting result that the back wall difference amplitude was the most noticeable change in the signal. With each increasing size of delamination, the back wall reflection amplitude difference signal continued to grow, which was attributed to being partly due to a change in amplitude, but mostly due to a shift in time. The authors concluded that in the area of delamination, the wave must travel separately along two regions, top and bottom, and therefore for a limited period of time has a lower frequency-thickness product which means for the A_0 mode, a lower wave speed. This discovery shows that even though delaminations may not produce a reflection of significant amplitude, that a change in time-of-flight can indicate damage when measured from a surface that is present both in the healthy and damaged received signal. Valdes used this finding to help simulate the effects of other damage in finite element calculations, but decreasing a section's elastic properties by 50% and therefore mimicking the effects and changing the wave speed temporarily through a damaged region.

4.3 General Methodology

As illustrated in Chapter 1 (section 4, figure 1.3), isolated incidences of the defects in question are investigated. The goal of the numeric simulations is to predict the modal “fingerprint” caused by reflection, transmission and conversion when the UGW interacts with the unique damage site. The inverse problem can be used to detect, identify and size a given defect. To this end, modal amplitude ratios are used as the means of determining the quantity of modal conversion, transmission and reflection when a UGW is incident on a defect zone.

Here, a two-dimensional model is used (see Chapter 3, section 4). Consider a pure, plane UGW mode that eventually interacts with a damage site. When the pure mode interacts with the damage site, there will be diffraction and mode conversion. Therefore, any modes present other than the incident mode are necessarily caused by interaction with a damaged structure. Since the assumption was made that the problem is restricted to two dimensions, the diffraction is limited to reflection or through transmission.

Thus, the propagating domain can largely be thought of as having three fields, namely the incident, reflected, and transmitted wave fields. Geometrically, the incident wave and the reflected wave fields occupy the same space. However, the wave packets will be traveling in opposite directions and can be identified thusly. The transmitted wave field shares no geometrical domain.

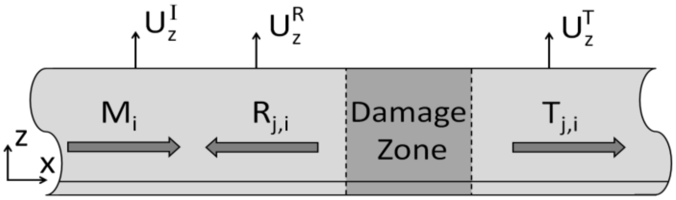

Figure 4.1: Schematic of general case where an incident mode M_i interacts with an isolated defect, and results in a summation of reflection modes $R_{j,i}$ and transmitted modes $T_{j,i}$. All displacement quantities are measured at, and perpendicular to, the upper surface of the plate.

Consequently, we define here two coefficients which can be thought of as ratios of the modal amplitude in either the reflected or transmitted wave fields to the amplitude of the original pure incident mode.

$$\mathrm{T_{j,i}} = \frac{\mathrm{U_{z,j}^T}}{\mathrm{U_z^I}} \tag{4.1}$$

$$\mathrm{R_{j,i}} = \frac{\mathrm{U_{z,j}^R}}{\mathrm{U_z^I}} \tag{4.2}$$

where U_z refers to displacement at the upper surface of the plate, perpendicular to the surface as shown in figure 4.1. $U_{z,j}^T$ is therefore the surface displacement in the transmission zone, attributed to mode *j.* $U_{z,j}^R$ is likewise the surface displacement in the reflected zone, attributed to mode *j.* Note that in general, in each of these zones, several modes can be present. Therefore the overall wave packet may be considered to be a superposition of modes $j = 1 \dots \infty$. Although an infinite number of Lamb modes are possible, the number will be practically restricted by the frequency range (see chapter 2). U_z^I refers to the out-of-plane, surface displacement of the incident mode *i,* and is often assumed to be the only mode propagating in the incident field. $T_{j,i}$ is thus anagolous to a transmission coefficient that is measuring the amount of mode *j* in the transmission field due to the interaction of mode *i* with a certain defect. $R_{j,i}$ is anagolous to a reflection coefficient quantifying the amount of mode *j* in the reflection field due to the interaction of mode *i* with said defect.

To illustrate, consider the example case of a simple isotropic, single-layer plate. The S_0 mode (Mode 2) is excited at a frequency below the A_1 (Mode 3) cut-off frequency. As the pure S_0 mode propagates it encounters a notch, and therefore some conversion due to the interaction of the UGW mode with the defect zone occurs. This conversion results in the propagation of the A_0 mode (Mode 1) in the transmission and reflection fields. Additionally, some of the S_0 mode is reflected and transmitted as well. However, due to the frequency range, no other modes are possible. The ratio of the S_0 modal amplitudes in the transmission and incident fields are used to compute $T_{2,2}$. The ratio of the A_0 modal amplitude in the transmitted field to the original S0 mode in the incident wave field is used to calculate $T_{1,2}$. If the modes are not easily separated by time-windowing, a method such as the 2DFFT can be used.

It should be noted that the coefficients defined here are similar to those used in previous related work to measure transmission ratios of modes, and only take into account motion perpendicular to the surface of the plate [7]. These definitions are practical, since out of plane motion on the surface of the plate is not only accessible, but a common parameter monitored by already existing SHM methods [16]. Additionally, the defect sites are assumed to be isolated, i.e. that the given damage site is the sole source of UGW modal conversion. The studies in the subsequent 3 sections are carried out in a 2D modeling environment. As in Chapter 3, the direction of wave propagation is restricted to the axial direction. Accordingly, the defect sites are assumed to be independent of the circumferential direction.

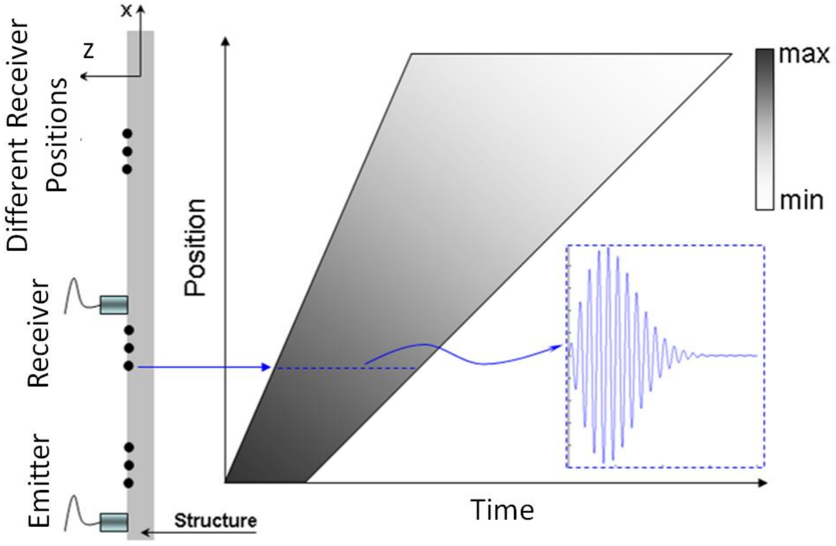

Figure 4.2: Time-space diagram: Amplitude of the signal acquired on the basis of propagation time for different positions of the receiver.

Supplementary information can be gleaned from a spatial-temporal representation. This representation is also known as (time, position) which means the position of the receiver vis-à-vis the emitter. This representation shows the amplitude wave displacement as a function of propagation time and distance. (This representation is described schematically in the figure 4.2). One can note that when the distance separating the receiver and the transmitter increases:

1. Time of flight increases;
2. The amplitude of the received signal decrease (in real cases);
3. The duration of the received signal increases.

To extract the signals required to construct this kind of images, the nodes on the boundary of the plate should be equidistant. In traditional ultrasonic testing, when the x-position being investigated is recorded at regularly spaced intervals, and temporal

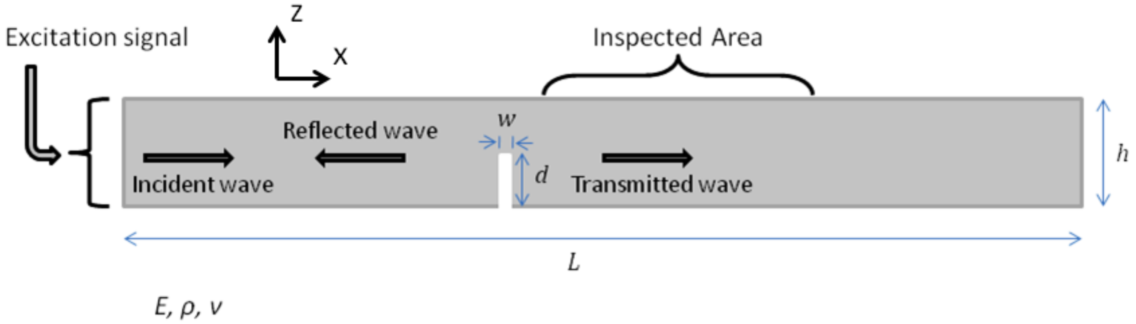

Figure 4.3: Notch schematic

waveforms are thus measured as a function of position, this is commonly referred to as a "B-scan". Consequently, since this plot is in the same vein, this representation is also identified as a "B-scan", despite that the emitter is stationary.

4.4 Study of 1st Damage Type: Cut-Type Defects

The 1st type of damage to be numerically investigated is a cut or surface-originating crack. As seen in chapter 1 (table 1.1), this type of defect can be caused either by sharp impacts, or by the cyclical loading of pressure causing the eventual propagation or expansion of micro-cracks. In either event, this damage type necessarily occurs on the outer surface, and therefore appears in the composite epoxy layer. Thus, a cut can be considered to be a collection of fiber ruptures which was seen in chapter 1 to be considered a critical damage type.

4.4.1 Model Description

A cut or surface-originating crack can be modeled in an FEM environment as a notch, as per the work of Cawley *et al*. [4]. Here, a steel (ρ = 8000 kg/m3, c_L = 5960 m/s and c_T = 3250 m/s) mono-layer plate is presented in order to benchmark the current work with

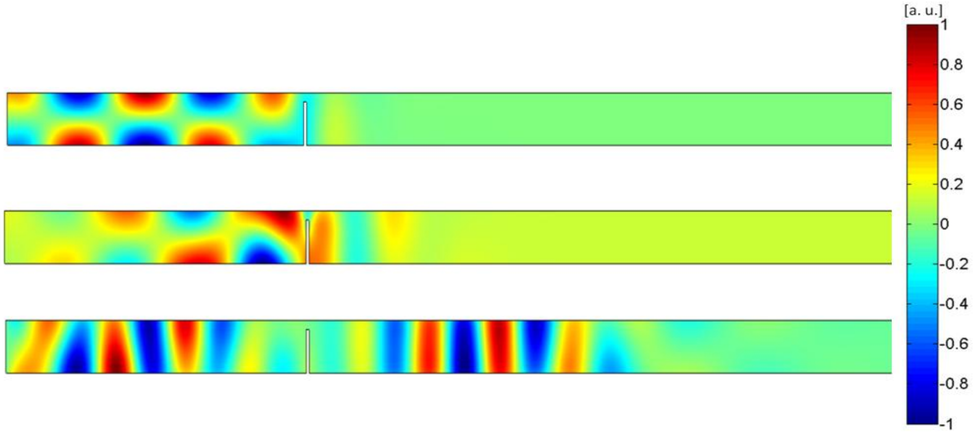

Figure 4.4: S_0 excitation signal after it interacts with crack at t=1.47e-5 s (top), at t=1.86e-5 s (middle) and t=3.12e-5 s (bottom). Z-displacement is shown.

that in the literature [4, 6]. As such, the geometry of the subdomain is altered as shown in figure 4.3. The boundary conditions on the sides of the notch remain traction free, as they are on the free surfaces of the structure. The notches investigated are perpendicular to the direction of propagation, and of a constant depth in the circumferential direction, as per section 3. The notch in question is isolated.

Since UGW interaction (modal conversion, reflection, transmission, etc) is well documented for isotropic single-layer cases, this damage type serves as a bench-marking tool for the FEM model. Pure modes are excited on the left hand side of the plate (see Chapter 3, section 3). Since pure modes are being excited, any amplitude attributed to other modes in the transmission zone is recognized as being due to modal conversion.

4.4.2 Results and discussions

Below three screen shots of waveguide numerical simulation are presented to show the different stages of the Lamb wave, excitation, interaction with the crack and transmission including mode conversion.

As we can see from figure 4.4, a very well formed S_0 mode is excited on the left hand side, but interaction with the notch causes a considerable amount of mode conversion. Some of the original S_0 mode remains, but much of the wave packet in both the reflection and transmission field is comprised of the A_0 mode. To understand the results, some post-processing is needed. In the next two subsections, we extract some information in time, space and frequency domains.

4.4.2.1 Time-Distance Representation

Recall that a B-scan is traditionally a time-space representation of a point-by-point scan. Here, the term B-scan will be used to signify a time-space representation of out-of-plane displacement on the surface of the structure. This definition differs from the traditional in that a single waveform can be represented as it propagates along the plate. This is in sharp contrast with the point-by-point scan which shows a different waveform at each position [17].

Example B-scans in the transmission field for 4 cases are shown in figures 4.5 and 4.6. Figure 4.5 depicts two cases for an incident S_0 mode, and similarly figure 4.6 depicts two cases for an incident A_0 mode. For these example B-scans, the incident wave packet was a ten-cycle Hanning-windowed mode with a center frequency of 200 kHz traveling in a steel plate, with a thickness of 6.75 mm. This gives a frequency-thickness product of 1.35 MHz-mm.

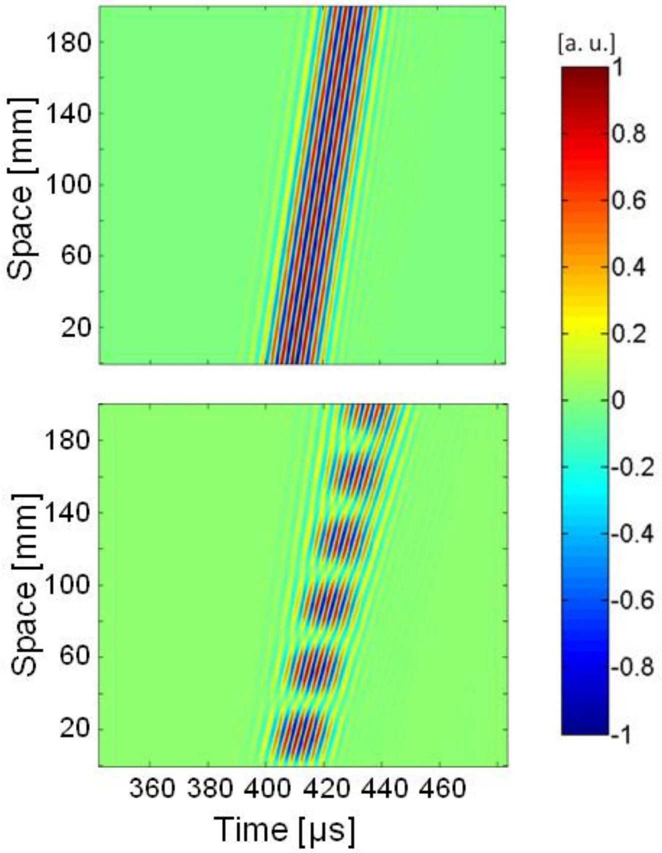

Figure 4.5: B-scan in transmission field for the case of an incident S_0 mode when (top) no notch is present and (bottom) a notch depth of 2.8 mm is present.

As can be seen in figure 4.5, the S_0 mode travels unmodified except for a small amount of spreading due to dispersion for the case when no defect is present. However, it is subject to mode conversion for the case when the incident S_0 mode interacts with a notch having a depth of 2.8 mm. Interestingly from figure 4.5, one can observe that for this inspection region (which is located shortly after the notch but in the far field to allow the waveform to fully develop) the wave packet does not have enough time for full mode separation despite the different wave velocities of the two fundamental modes present. The result is a “beat-like” waveform that oscillates due to constructive and destructive

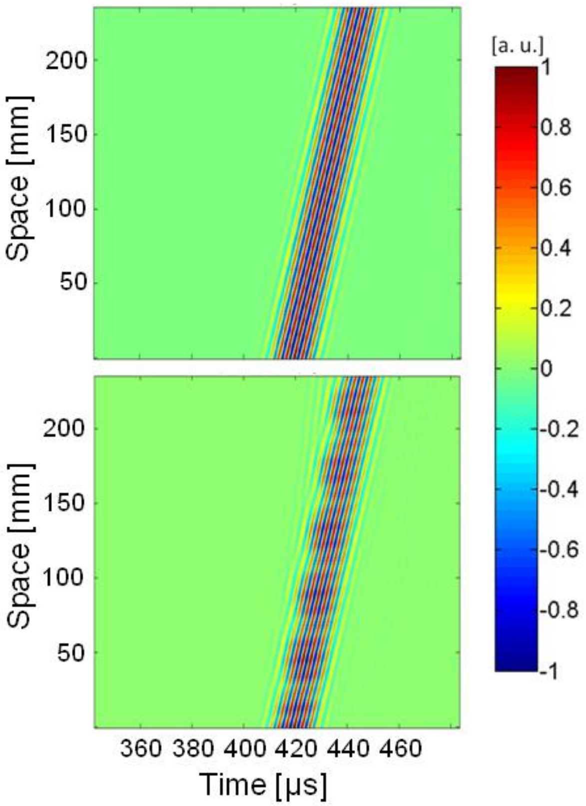

Figure 4.6: B-scan in transmission field for the case of an incident A_0 mode when (top) no notch is present and (bottom) a notch depth of 2.8 mm is present.

interference as the two waveforms begin to separate. The difference in group velocities can clearly be observed by the two distinct sloping wavefronts in figure 4.5 (bottom).

In figure 4.6, the A_0 mode is incident, and again two cases are depicted. The first is for baseline case when no notch is present, and for the second case the incident A_0 mode has interacted with a notch having a depth of 2.8 mm. Again, a “beat-like” wave motion can be observed, however in this example the oscillatory motion is not as evident since there was not as much mode conversion as in the previous case. The result is a slight

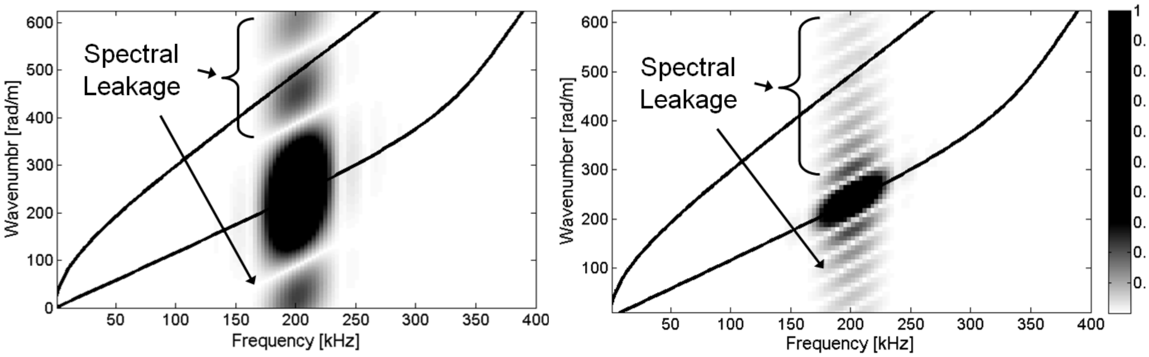

Figure 4.7: Frequency–wavenumber representation for a healthy plate of steel when only the S_0 mode is excited for case 1 (left) and case 2 (right).

amplitude change as the faster S_0 mode propagates more quickly causing the change between constructive and destructive interference.

Evidently, figure 4.5 and 4.6 are example cases. Wavespeed velocities and wavelengths are dependent on the frequencies present in the wavepacket. Furthermore, the amount of mode conversion is directly dependent on the geometry of the crack.

4.4.2.2 Frequency-Wavenumber Representation

The information extracted in the spatiotemporal domain can be complemented by that in the wavenumber-frequency domain. Consider a few of the 2DFFT images taken in the transmission field shown in figures 4.7, 4.8 and 4.9. Again, out-of-plane displacement on the surface of the steel plate is used as in section 4.2.1, and likewise a ten cycle, Hanning-windowed signal centered at 200 kHz is used as an excitation signal. The superimposed black curves are the dispersion curves calculated with Disperse.

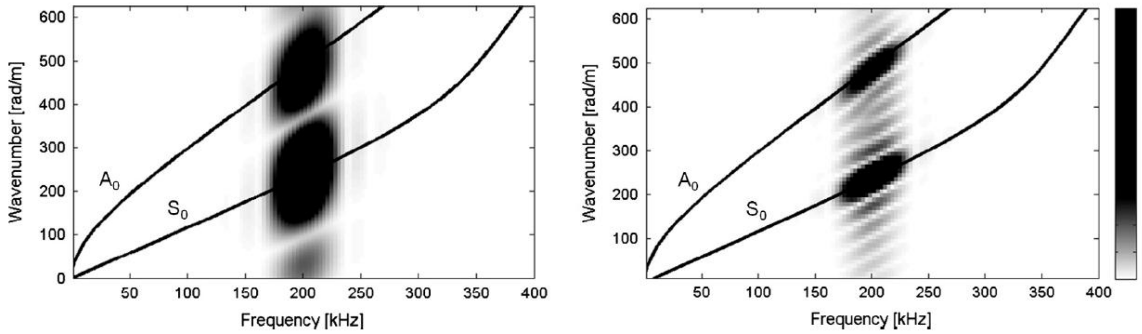

Figure 4.8: Frequency–wavenumber representation for S_0 incident on a notch with depth 1.6 mm (23% of the nominal plate thickness) for case 1 (left) and case 2 (right)

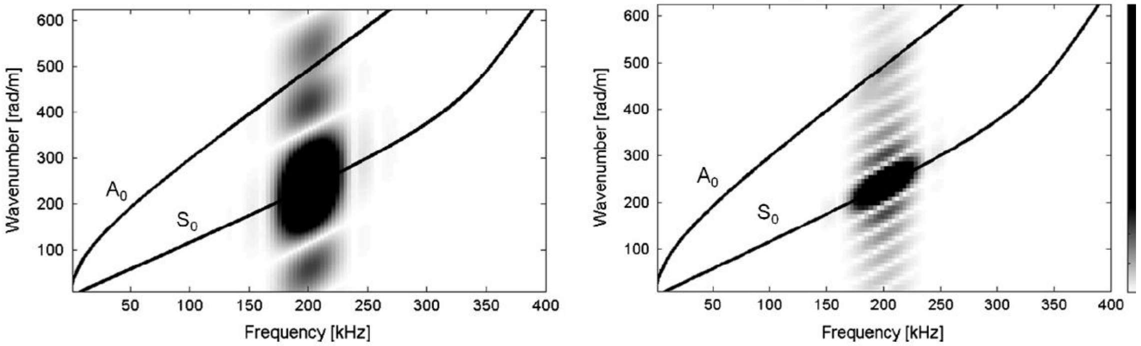

Figure 4.9: Frequency–wavenumber representation for S_0 incident on a notch with depth 0.6 mm (9% of the nominal plate thickness) for case 1 (left) and case 2 (right)

Two cases are considered:

- Case 1: A geometrically restrained problem is imitated. The number of points is limited to only twelve, spaced 4.2 mm apart. The resulting monitored area is 4.62 cm long.

- Case 2: No geometrical or scanning restrictions are assumed. The number of points is an impractical 200, spaced 0.5 mm. The resulting monitored area is 10 cm long.

The intended purpose of exhibiting both cases here is to demonstrate that increasing scanning resolution and length results in a clearer wavenumber–frequency space representation. However, the former case will end up giving transmission and conversion coefficients that closely agree with the latter. Notably, the rectangular window used in the spatial domain (see Chapter 3, section 4.2.3) results in observable leakage along the wavenumber axis, as shown in figure 4.7.

Quantitatively, the amplitude of a given mode can be determined from the frequency-wavenumber space, as was seen in Chapter 3, section 4.2.2. Figure 4.8 shows the frequency-wavenumber space in the transmission field after the incident S_0 mode interacts with a 1.6 mm notch. Mode conversion to the A_0 mode is clearly visible above the spectral leakage. However, figure 4.9 shows the frequency-wavenumber space in the transmission field after the incident S_0 mode interacts with a 0.6 mm notch. In this case the converted A0 mode is hidden by the presence of spectral leakage.

4.4.3 Comparison with Literature

The amount of mode conversion in the transmission field after a pure fundamental mode's interaction with a notch in an isotropic plate had been quantified previously by other researchers [4, 6]. Note that a steel, mono-layer plate is used for the sake of bench-marking. Here, the amplitude of each mode is measured to compare quantitatively with values reported in the literature [6]. The amplitude for each mode at the central frequency is determined via the 2DFFT. Recall that two cases are investigated (detailed in section 4.2.2). Figure 4.10 shows the amplitude of the modes

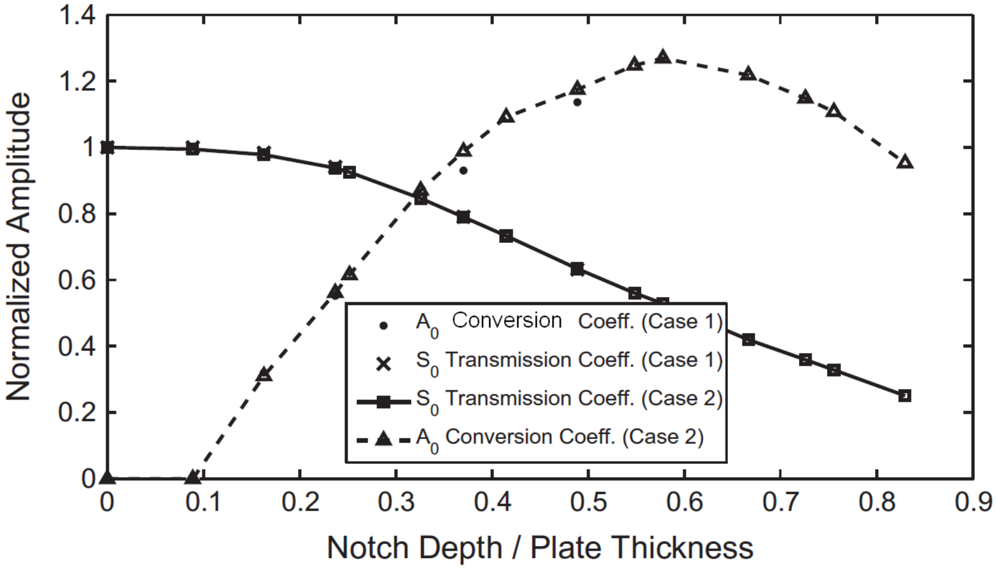

Figure 4.10: Amplitude of the transmitted A_0 mode and converted S_0 mode with an incident A_0 signal as a function of the ratio of notch depth/plate thickness

as a function of notch depth/plate thickness for a pure incident S_0 mode. Data concerning the transmitted and converted modes agrees very well with that which is reported in the literature [4] for notch depths higher than 15% of the plate thickness. Recall from figure 4.9 that this is due to the amplitude of the converted mode being hidden by the spectral leakage of the stronger transmitted mode. If *a priori* information concerning the expected location of the converted mode in the wavenumber-frequency space (i.e. the calculation of theoretical dispersion curves) is levied, the amplitude of the converted mode can be ascertained.

4.4.4 Baseline Subtraction Algorithm

This section proposes a novel technique the use of a baseline subtraction technique in the frequency-wavenumber domain to improve the lower limit of defect detection in a structure with limited *a priori* dispersion curve information. This technique is based on baseline subtraction in the frequency-wavenumber domain. Previous researchers have used transmission and mode conversion successfully for sizing the depth of straight-edged notches, but have relied on *a priori* dispersion curve information [4, 6]. The novel frequency-wavenumber domain baseline subtraction technique [5] shown here allows for the detection of small amounts of a converted mode, without making assumptions concerning plate thickness or nominal bulk wavespeeds needed to compute dispersion curves (see Chapter 2).

It was previously seen (figure 4.9) that spectral leakage may hide the appearance of small amplitude converted modes rendering them undetectable. However, if the healthy 2DFFT from figure 4.7 were to be subtracted from figure 4.9, the appearance of the mode conversion would no longer be hindered by spectral leakage. Therefore, a baseline subtraction technique was applied to the frequency-wavenumber domain according to the formula:

$$\Gamma(f,k) = \left|\left|2DFFT\left(u_D(t,x)\right)\right| - \left|2DFFT\left(u_B(t,x)\right)\right|\right| \tag{4.3}$$

where u_D is the signal with damage present, and u_B is the baseline signal. The absolute value is taken because the incident mode loses some amplitude due to transmission loss through the damage site, and therefore it would cause the region around the S_0 mode at 200 kHz to be negative. In figure 4.11, we can now clearly see the A_0 mode, which before was not visible above the spectral leakage. Since the transmission coefficient was near ‘1’, the S0 mode has almost entirely been deleted from the 2-D frequency space, along with the spectral leakage that accompanies it. The A0 mode is now highly visible.

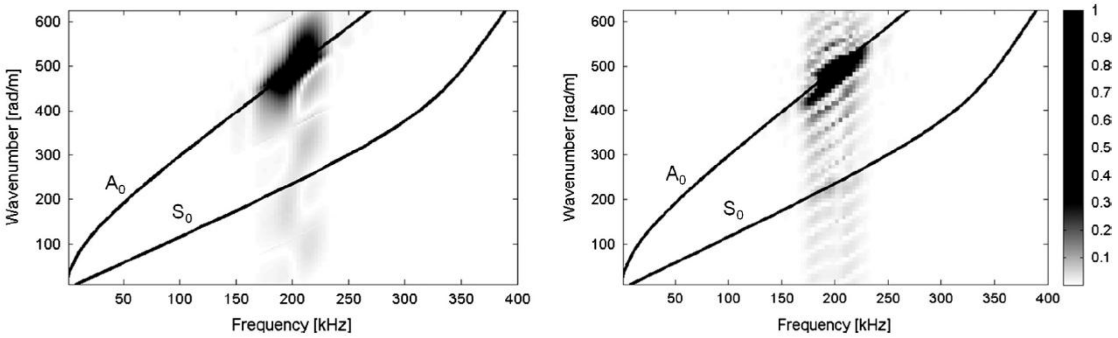

Figure 4.11: Results of the baseline subtraction technique for the case when the crack is 0.6 mm deep for case 1(left) and case 2 (right).

Equation 4.3 is necessary to extend the limits of work previously pursued by other authors [4, 6]. In cases when the 2DFFT is used to separate modes, spectral leakage due to the obligatory use of window functions may make small amplitude converted modes difficult to detect. If material properties are assumed for the plate in question, one can estimate the ordinate and abscissa of the location of the converted mode via analytically determined dispersion curves. However, in general, eliminating the need for *a priori* assumptions also eliminates error associated with discrepancies between the assumed values and the true values. By contrast, it is clear in figure 4.11 that there is a spectral feature pertaining to a mode occurring at 200 kHz that is not the original pure mode visible in the baseline 2DFFT (figure 4.7). This new converted mode (pertaining to the A_0 mode) is apparent without any *a priori* information specifying where it is expected to appear in the frequency-wavenumber plane. Furthermore, unlike a normal baseline subtraction method carried out in the time domain, this novel approach does not include differences in phase, and therefore is robust for any change in arrival time. It should be noted that both 2DFFT referenced in equation 4.3 must be of the same resolution and size.

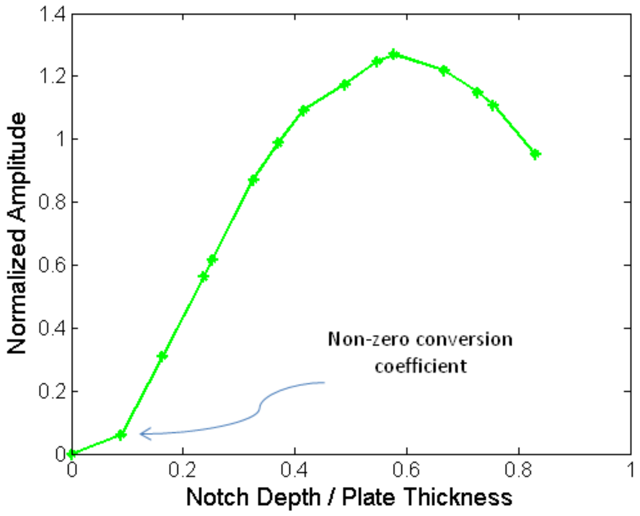

Figure 4.12: New point from baseline subtraction technique added to figure 4.10. Amplitudes were extracted from the 2DFFT at the center frequency of 200 kHz, and normalized by the incident S_0 mode.

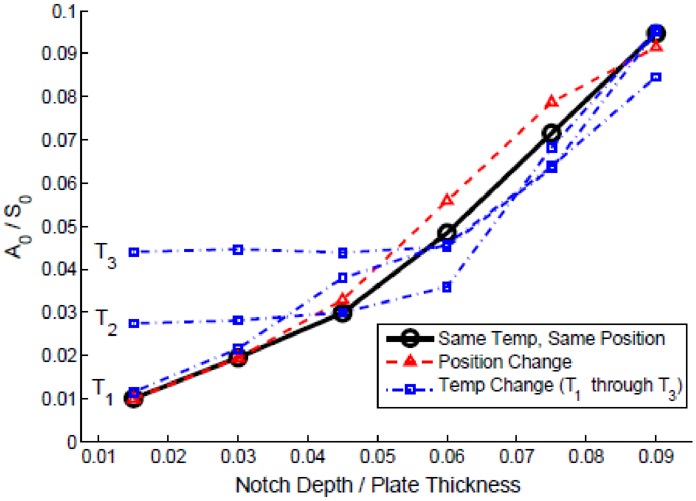

Figure 4.13: Conversion coefficients for a range of smaller notch depths. Amplitudes were extracted from the 2DFFT at the center frequency of 200 kHz, and normalized with respect to the incident S_0 mode. (Circle) Data collected at same temperature and inspection position. (Triangle) Data collected at same temperature with a 1 cm shift in inspection position. (Square) Data collected with shift in temperature via change in Young's modulus: T_1~ 50℃, T_2 ~100℃, T_3 ~150℃.

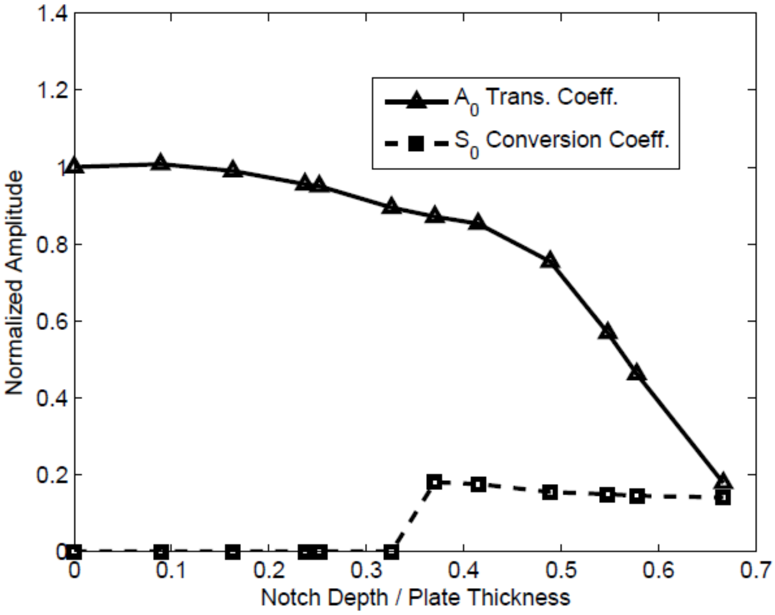

Figure 4.14: Conversion coefficients for the case when A_0 is incident without using the baseline subtraction method. Amplitudes were extracted from the 2DFFT at the center frequency of 200 kHz, and normalized with respect to the incident A_0 mode.

Now revisiting figure 4.10, it is possible to measure the amplitude of the converted A_0 mode for the case when notch depth is 0.6 mm, i.e. 10% of the thickness of the plate. The results are shown in figure 4.12. Carrying on in this manner, it is also possible to continue decreasing the depth of the crack and test the limits of detectability. Mode conversion coefficients for a smaller range of crack depths are shown in figure 4.13.

A similar study has been conducted for the case of A_0 incidence. Figure 4.14 shows the results of measuring the transmitted (A_0) and converted (S_0) modes, normalized with respect to the incident A_0 mode. One can note that overall, the converted mode has a relatively low amplitude, even with large notch depth. This means that when using a A_0 incident wave, even larger notches can go undetected due to the problematic

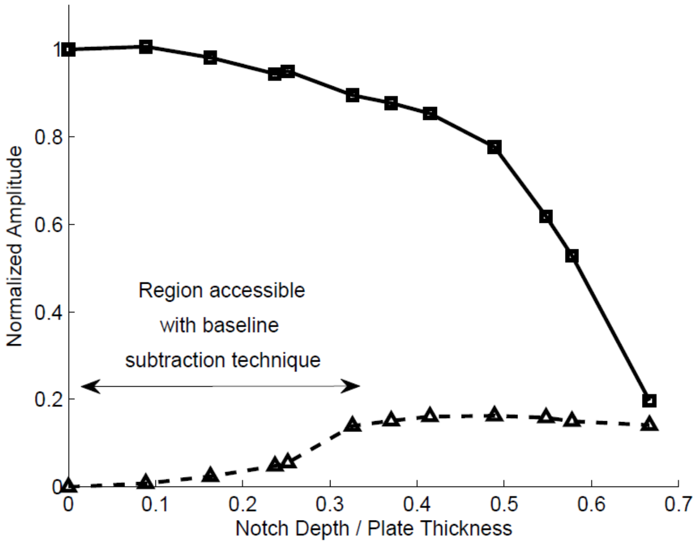

Figure 4.15: Conversion coefficients for the case when A_0 is incident, using baseline subtraction technique. Amplitudes were extracted from the 2DFFT at the center frequency of 200 kHz, and normalized with respect to the incident A_0 mode.

appearance of side lobes. Figure 4.15 shows the improvement possible when using the baseline subtraction technique.

Here the frequency domain baseline subtraction technique more emphatically changes the lower limit of detectability. Previously anything below 35% of the plate thickness was inaccessible without *a priori* knowledge of the expected location of the converted S_0 mode in the frequency-wavenumber domain. Using equation 4.3, no *a priori* assumptions need to be made, and the converted mode becomes apparent.

It is important to point out an assumption that the two-dimensional frequency baseline subtraction makes: the amplitudes of the side lobes do not vary between the baseline and damage-present signal. This of course is not fully true; the amplitudes of the side lobes are directly proportional to the amplitude of the spectral feature that they flank, i.e.

the central lobe. If this central lobe changes amplitude, so will the side lobes. Nevertheless we can make the assumption that the variation is negligible. This is because for every unit change in the central feature, the side lobes will not also experience a unit change but rather some percentage of the difference. For example, consider a spectral feature with unit amplitude, and with the largest side lobe having a maximum amplitude of 20% of the central lobe. Then a decrease in amplitude by 10%, for example, would result in only a decrease in 0.2(0.1) = 2% of the side lobe amplitude.

4.4.5 Robustness to Changes in Temperature and Sensor Placement

One of the advantages of the proposed wavenumber-frequency baseline subtraction method is its low vulnerability to changes in one of the most common environmental condition fluctuations, i.e. temperature. Fluctuations in temperature often affect the material in two specific ways namely changes in geometry due to thermal expansion, and changes in material properties. Croxford *et al.* [18] state that, most notably, the shear and longitudinal bulk velocities of a material change with temperature and consequently used the relation between bulk wave speed and Young's modulus to take into account the effects of temperature in numerical models. In a similar fashion, the Young's modulus in the current work is altered from its original value of 218.76 GPa to 216 GPa, 213 GPa and 210 GPa, to respectively simulate the effects of 50℃, 100℃, and 150℃ rises in temperature. The change in Young's modulus was determined thanks to literature provided by the National Institute of Standards and Technology [19]. However, it should be noted that the change in Young's modulus with temperature is approximate and has been cited in the literature for a specific structural steel sample. Furthermore, the steel sample cited in the literature started at 0℃ with a lower Young's modulus, and consequently the change in Young's modulus in the present work is relative to the starting value of 218.76 GPa. This range of temperatures is deemed to be an appropriate range to simulate many applications.

The results for the simulated temperature change with S_0 incidence are shown in figure 4.13 for the range of small notch depths found using the frequency wavenumber domain baseline subtraction technique. The smallest change in Young's modulus provided for little effect on the conversion coefficient, and any discrepancies found at higher temperatures occurred mainly for the smallest notch depths tested. An explanation for such robustness can be found by comparison of the proposed technique with traditional baseline subtraction methods, for example those performed by Michaels [20]. Since alterations in Young's modulus directly affect the arrival times, and only minutely affect the guided wave mode shapes for a given frequency-thickness, it follows that traditional baseline subtraction techniques fail due to changes in arrival time, and distortion of the signal to dispersive spreading. However, the conversion and transmission coefficients should remain the same, since the same basic wave shape is interacting with the same notch/depth ratio. Therefore, since the proposed method deletes phase information before comparing the healthy signal with the damage-present signal, arrival times do not affect the computation of the conversion coefficient. The error at lower notch depths is due to the shift of the incident wave spectral feature in the frequency-wavenumber domain, and consequently a misalignment of spectral leakage between the baseline and the current signal.

The same concept can be applied to account for robustness concerning sensor placement. In fact, for both the transmitter and receiver, exact location on the structure can vary between signal collection times. This is, again, thanks to the proposed method's deletion of phase information before comparing signals. Consider once more figure 4.13 where the inspection points for the damaged signal were first shifted to the

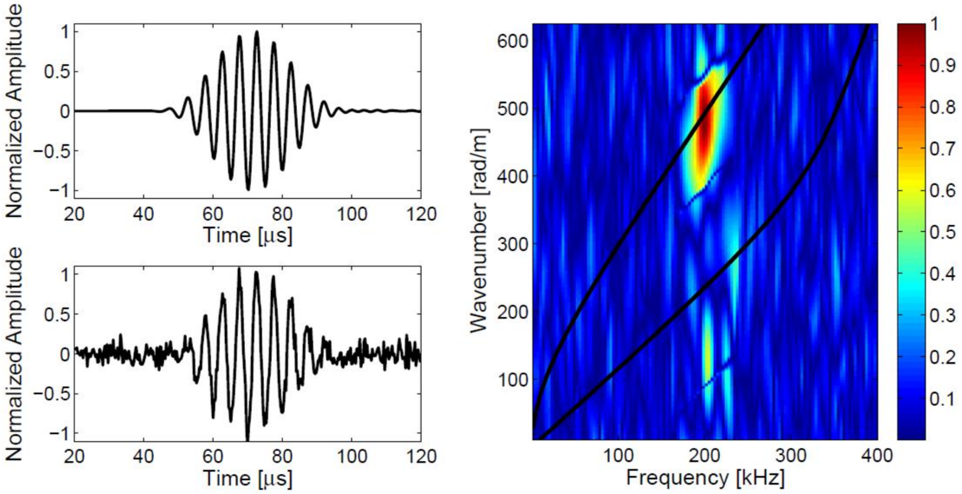

Figure 4.16: Results of the baseline subtraction technique for the case when the crack is 0.6 mm deep, with Gaussian white noise added, 10 dB SNR. Left Top: temporal waveform collected 2 mm after notch. Left bottom: Signal with 10 dB white Gaussian noise added. Right: Result of equation 4.3.

right by 1 cm, to simulate inexact sensor placement. Very similar results are found yet again, and any small differences can be accounted to numerical error in the FEM calculations.

4.4.6 Effects of Noise

This work is carried out via finite element analysis, and therefore provides a medium for inspecting the proposed post-processing methods limits of detectability. Up until this point the only noise present has been due to numerical error. In reality, signals acquired during experiments or *in situ* are not as clean, and contain some noise. In general, the higher the SNR, the easier the signals are to treat in post-processing.

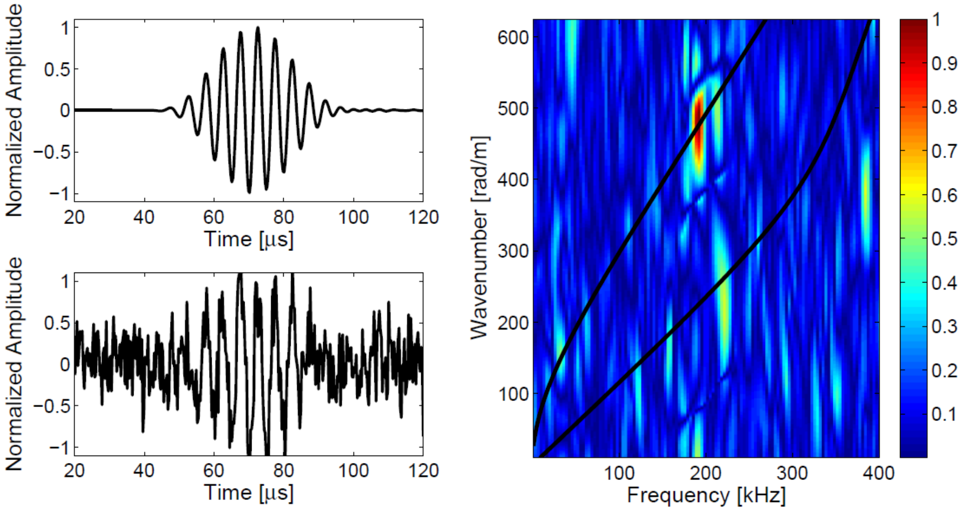

Figure 4.17: Results of the baseline subtraction technique for the case when the crack is 0.6 mm deep, with Gaussian white noise added, 1 dB SNR. Left Top: temporal waveform collected 2 mm after notch. Left bottom: Signal with 1 dB white Gaussian noise added. Right: Result of 4.3. The A_0 is still visible despite the addition of Gaussian white noise.

In order to test the reliability of the proposed method in a more realistic scenario, white noise was added to the signal before applying the baseline subtraction technique, according to the expression:

$$s(t) = s_0(t) + e(t) \tag{4.4}$$

where $s(t)$ denotes the signal as a function of time, $s_0(t)$ denotes the pure signal devoid of noise, $e(t)$ is the Gaussian white noise. The white noise was added to each waveform collected along the inspection area after FEA computation using MATLAB. The proposed baseline subtraction technique is carried out as usual, according to equation 4.3. The result for the case when the notch is 0.6 mm deep (9% of the plate thickness) is shown in figure 4.16, for the case when SNR is set to 10 dB. The A_0 converted mode is still easily visible despite the addition of noise. Figure 4.17 shows the

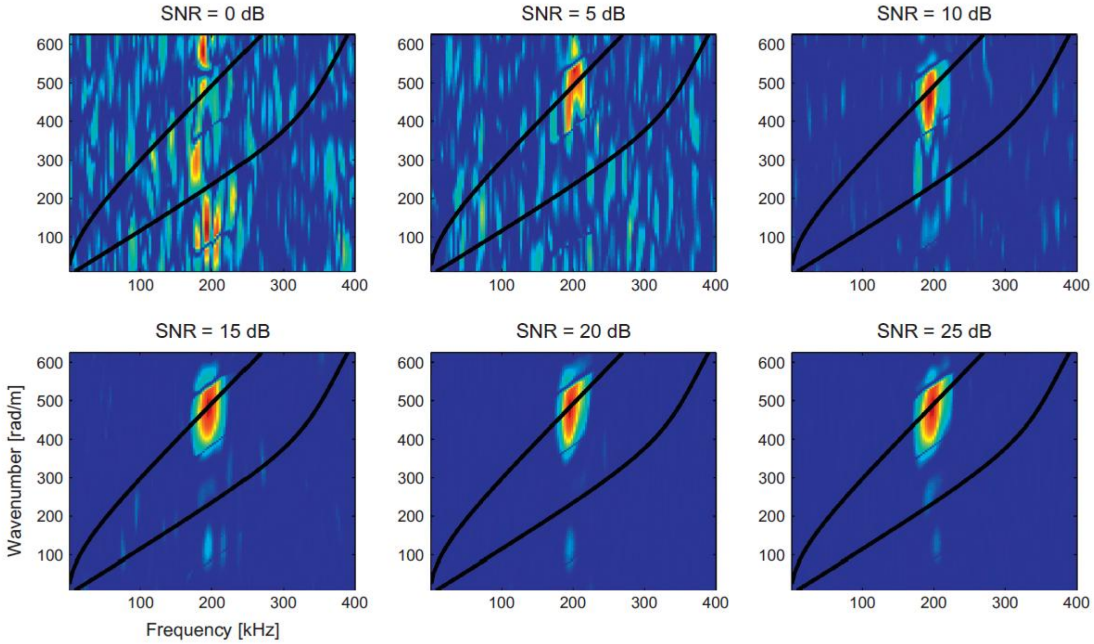

Figure 4.18: Comparison of the baseline subtraction technique with Gaussian white noise added from 0 to 25 dB SNR. Crack depth/thickness is 0.075, i.e. approximately 0.5 mm.

case when 1 dB SNR is added. Although there are some artifacts in the signal that have similar magnitudes, again the spectral feature corresponding to the converted mode is visible.

Figure 4.18 shows the baseline subtraction technique results for a notch depth-to-plate ratio of 0.075. In the present study this translates to a notch depth of 0.5 mm. Figure 4.17 compares side by side cases where the added noise ranges from 0 dB to 25 dB. The converted A_0 becomes apparent around 5 dB SNR. This figure indicates that there is a threshold of notch depth detectability based on SNR.

To identify the threshold, white Gaussian noise was added to a range of small notch depths. Due to the stochastic nature of noise, the numerical simulations were run 50

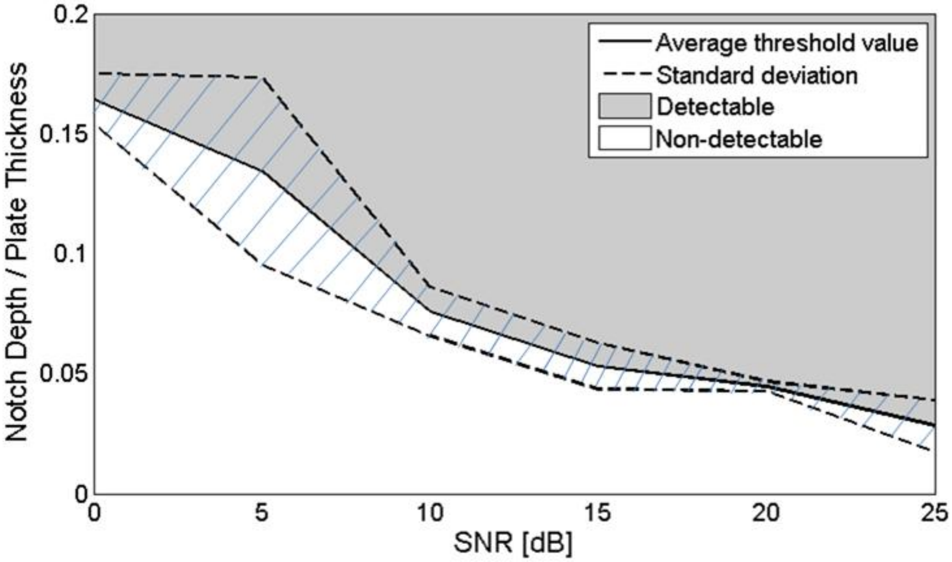

.

Figure 4.19: Notch detectability threshold as a function of SNR. The threshold is displayed with standard deviation.

times for each notch depth, with a white noise generator in Matlab. The converted mode was considered detected if its amplitude was twice that of any other spectral feature due to noise. Figure 4.19 depicts the results of these numerical simulations. This figure shows the threshold of detectability for small notch depths as a function of SNR.

Defects with a depth above the line for the given SNR should be detectable using the frequency-wavenumber baseline subtraction technique. Note that the work developed here is without the use of any denoising technique, and the use of such (for example the discrete wavelet transform) could help to further improve sensitivity.

4.4.7 Procedure of the Method

This method is useful in the context of SHM as well as periodical NDT. The method is applicable for the inspection/monitoring of zones characterized as being crucial to structural safety and vulnerable to damage. Whether within the framework of SHM or periodical NDT, the data to be processed should be collected in two periods (P_1 and P_2). In the following, the steps are summarized:

I. For period P_1

1. Fix one emitter (E) on one side of the zone to be tested/monitored and N receivers (R_i) on the other side of it. The receivers should be equidistant (distance between 2 successive receivers, R_i and R_{i+1} with i = (1,.., N-1), is constant), and aligned in the direction of propagation;

2. Measure the time domain out-of-plane displacement at the first point (i=1);

3. Apply a rectangular window in time, which is chosen with regard to the distance between the emitter E and the receiver R_i to eliminate unwanted reflections. This window can be constant when the excited mode is non-dispersive, since the duration of the wave packet does not change length as a function of propagated distance.

4. Redo steps 1 and 2 for all receivers (R_i with i = (2,.., N)). The obtained data can be formed into a matrix (S) having dimensions N*M, where M is the size of the temporal vector (length of the sampled signal).

5. Pad with zeros if necessary, and apply a 2DFFT to S.

II. For period P_2, ($P_2 = P_1 + \Delta P$), where ΔP is the time between the two periods P_1 and P_2

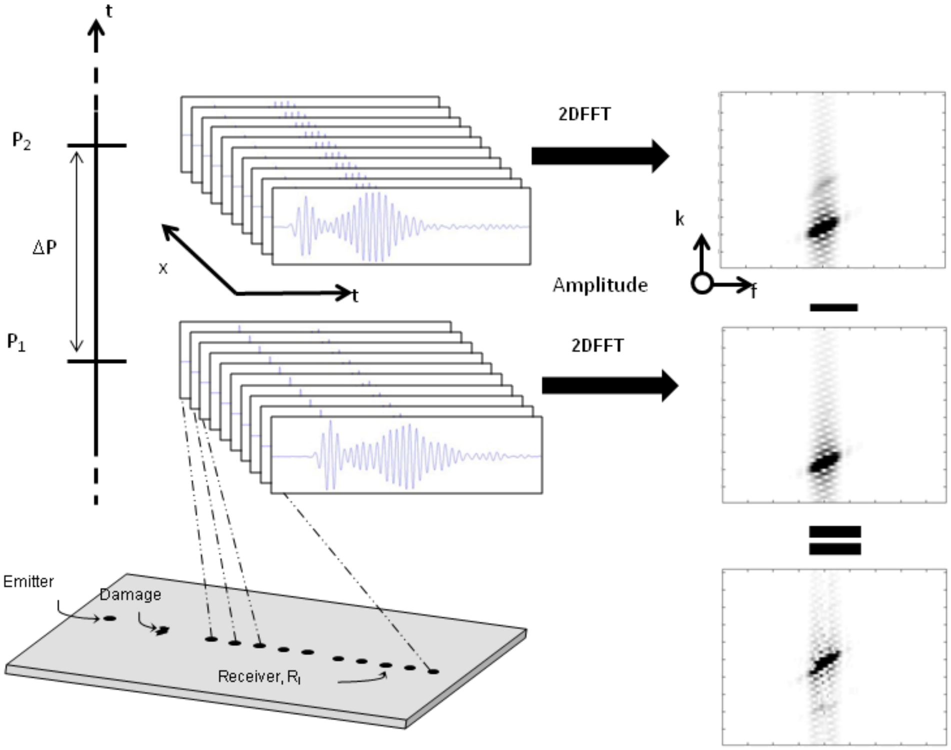

Figure 4.20: Diagram depicting the method based on the frequency-wavenumber domain baseline subtraction technique.

1. Redo steps 1 to 5 maintaining initial positions from P_1
2. Call an algorithm based on equation 4.3

Based on the signal-processing steps, a code within the Matlab programming environment was developed. The inputs of this code are the data matrices S_1 and S_2, obtained respectively in the periods P_1 and P_2. This procedure and the code are schematically illustrated in figure 4.20.

4.4.8 Baseline Subtraction Algorithm Advantages

The baseline subtraction technique has been applied to the frequency-wavenumber domain in order to increase the detectability of low amplitude modes. Such modes occur due to mode conversion when an incident wave interacts with damage such as a crack. Since the conversion coefficient is related to defect size, detectability of low amplitude modes is directly related to the lower limit of damage detection. Through finite element analysis, mode conversion coefficients have been calculated for notch depths of less than 10% of the total plate thickness. The smallest notch depth detected has a depth of around 1.5% of the total plate thickness.

Spectral leakage, which occurs as a direct result of the signal being truncated, i.e. finite, can hide low amplitude converted modes. If *a priori* assumptions are made concerning the material properties and thickness of the sample, the location of the converted mode can be predicted in the frequency-wavenumber space. A novel approach takes the difference between a damaged 2DFFT and a healthy one. This frequency-wavenumber baseline subtraction method makes limited *a priori* assumptions, and makes low amplitude converted modes apparent. Since the detection floor is no longer determined by spectral leakage, relatively small damage can be detected as long as the signal-to-noise ratio is not a determining factor.

To conclude, the method has the following advantages:

- It improves damage detectability (detection of smaller defects); it allows for the detection of damage in early stage;
- It is applicable in the field of SHM as well as in periodic NDT (data acquired for a ‘healthy' sample should be saved, since it is the input of this signal processing technique). The technique is very sensitive to small evolution in damage size;

- Experimentally speaking, the method is easy to apply and not exorbitant. In SHM, the actuators/sensors (which are relatively inexpensive) live permanently with the structure and the data is automatically saved. In periodical NDT, a multi-element receiver can be used to save testing time. Evidently, all acquisitions should be taken with the same environmental conditions (temperature, humidity, pressure,...);
- The amount of assumptions made with *a priori* knowledge concerning structural characteristics (bulk velocities and geometrical dimensions) is minimal.

4.5 Study on Internal Voids (Internal Cracks)

In the previous section, we studied the detection of type 1 damage. Another ideal damage type can be representative of more complex problems is that of a rectangular cavity within a plate. Cracks commonly form at boundaries of dislocations, (or disbondings in the case of multi-layer materials). So it is important to be able to numerically predict the interaction between incident Lamb waves and such interior crack formations. Lamb modes use the whole thickness of the plate to propagate. This is less true for the fundamental modes at high frequency-thickness products where the wave motion asymptotically approaches that of surface Rayleigh waves traveling in parallel on either surface of the plate. Additionally, mode shapes are functions of position, and therefore Lamb waves will interact differently with cracks that are enclosed within the material at different depths even if they have the same relative geometry and size as a surface-originating crack.

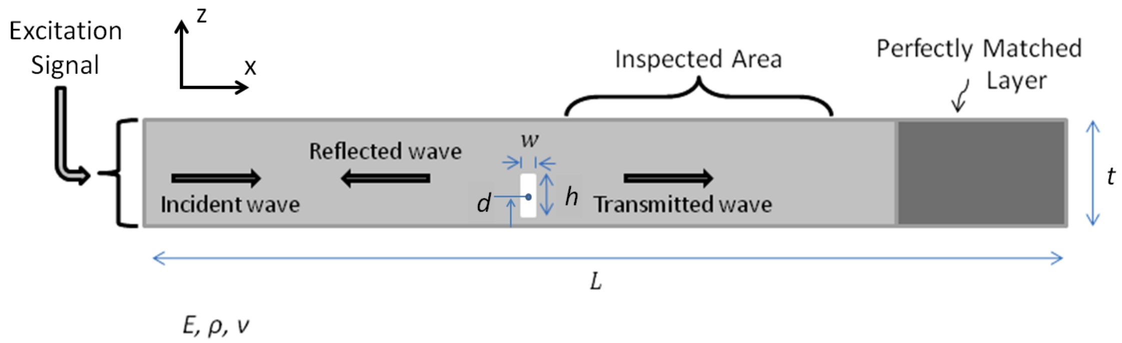

Figure 4.21: Schematic of the finite element model for an internal void.

4.5.1 Model Description

A steel (ρ = 8000 kg/m3, c_L = 5960 m/s and c_T = 3250 m/s) plate with constant 6.75 mm thickness is used, as in section 4. An internal void or interface-originating crack can be modeled in an FEM environment as a geometrical void in the defined geometry, i.e. the creation of an internal boundary. As such, the geometry of the subdomain is altered as shown in figure 4.21. The internal boundary conditions are traction free, as they are on the free surfaces of the structure. The internal voids used in this work are rectangular in nature, and any given void is assumed to be isolated as per chapter 1, figure 4.4. Thus a given void's geometry can be classified by its width *w*, height *h* and vertical position *d* in the material layer.

Pure modes are excited on the left hand side of the plate (see Chapter 3 section 3). Since pure modes are being excited, any amplitude attributed to other modes in the transmission zone is recognized as being due to modal conversion. Furthermore, this model made use of a PML as described in Chapter 3, section 3.2, in order to suppress edge reflections.

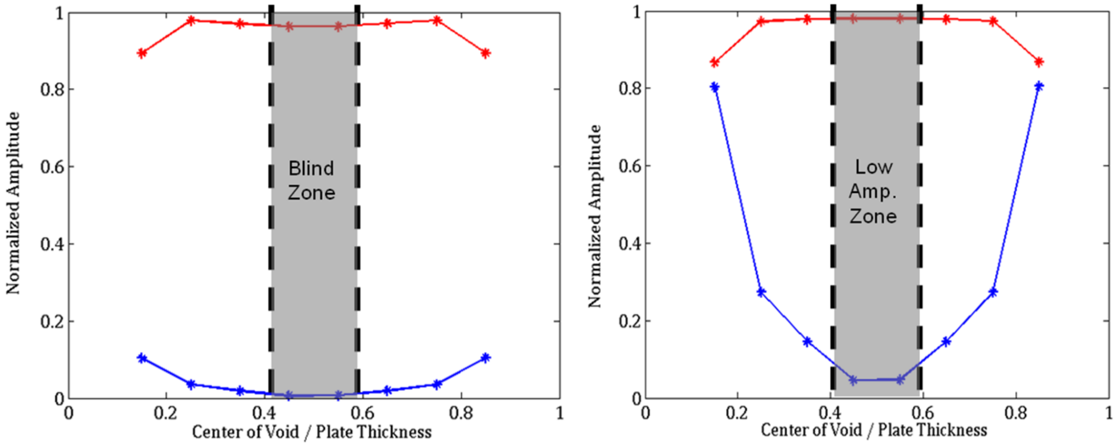

Figure 4.22: Transmission (red) and Conversion (blue) coefficients for the case when the (left) A_0 mode is incident and (right) the S_0 mode is incident. Void dimensions: d = 2mm, and w=0.5 mm.

4.5.2 Results

One of the notches that is used in the previous section 4 is used here and fixed at a constant height and width, but varied in vertical position *d* throughout the plate, as shown in figure 4.21. As in the previous study on surface-originating cracks, both an incident A_0 mode and S_0 mode are used in this study, and the relative strength of the transmitted and converted modes are measured and normalized to the incident mode. The goal is to observe how the ratio changes as a function of crack depth, when the relative crack geometry and size stayed constant.

The fixed height used for this numerical study was that of notch depth of 2 mm and the fixed notch width was identical to the one for the surface notch dimensions (i.e. 0.5 mm). Ten separate cases were investigated, and the vertical position *d* was varied linearly from the case where the crack was in contact with the bottom surface to the case where it was in contact with the upper one.

The results for the fixed-geometry, variable-depth numerical experiments are shown in figure 4.22. The central excitation frequency is 200 kHz. The figure shows both the case of pure A_0 mode incidence (left) and pure S_0 mode incidence (right). We can observe a dynamic but fairly symmetrical response, which is to be expected since the mode shapes changes with respect to cross-sectional position, *z*. Figure 4.22 suggests that it may be possible not only to predict the size of a defect, but also its vertical displacement from the surface of the plate. The region in the central of the figure, where the converted transmission coefficient drops to zero is troubling, in that it implies that there may be a central region of the plate to which the incident A_0 mode is completely blind, and the S_0 mode undergoes weak conversion.

It can be noted that the surface crack condition is the only one that leads to notable variation in the transmission coefficient for either incident mode. Furthermore, the transmission coefficient appears fairly constant (and fairly close to unity) for both incident mode cases. However, the conversion mode is much more variable. When the S_0 mode is incident, it can be seen that the resulting A_0 mode conversion varies from 0.8 for the surface crack, all the way to below 0.1 for the case when the void is located along the central axis (y=0). Therefore, the mode conversion coefficient, as opposed to the transmission coefficient is a better indicator of void locality in the plane perpendicular to wave propagation. It can also be seen that, relatively, the case when the S_0 mode is incident and the A_0 mode is the converted mode, the conversion coefficient varies on a greater scale, and can therefore be considered to more sensitive.

4.6 Study on 2nd Damage Type: Surface Abrasions

The second defect of interest is referred to as an abrasion, and amounts to the loss of upper layer thickness due to rubbing with the environment. The term ‘abrasion’ is

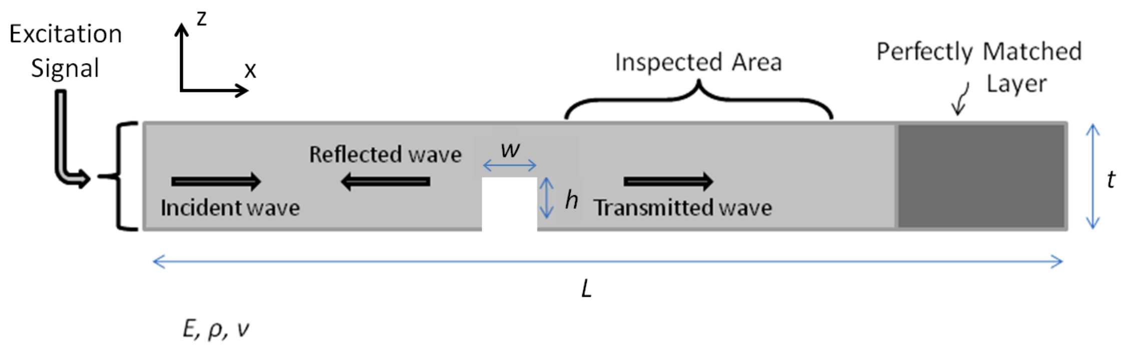

Figure 4.23: Abrasions are modeled as being a notch with variable width and depth.

therefore not applicable to impact damages which cause material compression, even though they may also cause thickness changes. Abrasions are caused by the loss of material on the carbon-epoxy surface, and are akin to corrosion in metals.

4.6.1 Model Description

FE models are carried out in the time domain for a steel (ρ = 8000 kg/m3, c_L = 5960 m/s and c_T = 3250 m/s) plate with constant 6.75 mm thickness, as in section 4. The defect site is modeled as being a surface notch with variable width *w* and depth *d* as seen in figure 4.23. Thus, it resembles the modeling of the surface-originating crack except that the width will be investigated as well. The boundary conditions on the sides of the notch remain traction free, as they are on the free surfaces of the structure.

As in the case of the surface-originating crack (section 4), the excitation is a pure mode excited on the left-hand side. Excitation is a 10-cycle Hanning windowed sine function centered at 200 kHz, which is below the A_1 cut-off frequency. The modal conversion coefficients for the case of S_0 incidence are shown in figure 4.24. Four defect widths are chosen: 0.85, 1.28, 2.13, and 2.84 mm.

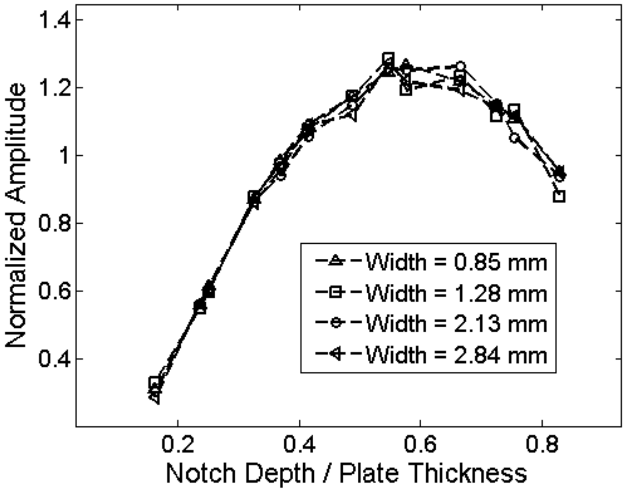

Figure 4.24: Amplitude of the converted S_0 mode with an incident A_0 signal as a function of the ratio of notch depth/plate thickness for various abrasion widths.

4.6.2 Discussion

The results for the abrasion type defect largely resembled the results discussed in section 4.2 for a surface-originating crack. It is therefore deduced that the modal conversion is fundamentally caused by the interaction and refraction off of the corner of the notch. Defect width has little to no effect on the FEM simulations as seen in figure 4.24.

4.7 Study of 3rd Damage Type: Collapse Defect

The final defect of interest is referred to as a ‘collapse defect’ and amounts to disbonding occurring between two layers. It is so-called because this type of defect commonly occurs due to rapid depressurization of the high-pressure reservoir, and thus the change in pressure may cause the inner isotropic layer to collapse from its usual cylindrical shape and become detached from the carbon-epoxy layer. This section is devoted to determining how UGW interact with this type of defect.

4.7.1 Model Description

Unlike the previous damage types, this one necessitates a two layer structure. Thus, the mono-layer steel plate used to benchmark the modeling of the previous defect types (sections 4, 5 and 6) is not employed. Instead, two layers are simulated, the lower one having thickness 1.39 mm and the upper one having thickness 7.85 mm, both of which are chosen as being representative of the real 2.5 L tank[1]. Carbon-epoxy material properties are thus used in the 7.85 mm thick layer and nylon material properties are used in the 1.39 mm thick layer.

The model makes use of excitation type 2, given in chapter 3 (section 3, figure 4.4). Although this excitation type does not necessarily excite a single mode, it is more deemed to be more realistic since it approximates excitations from top-surface contact transducers[2]. The excitation motion is prescribed in the x-direction, and is a 10-cycle, Hanning windowed sine function centered at 180 kHz. This central frequency was chosen based on the study of dispersion curves carried out in Chapter 2, section 5.2. The length of the excitation zone is chosen to coincide with a half wavelength of Mode 2 (see chapter 3, section 4.4). This excitation is chosen for this type of defect to ease comparison with experimental results, since the excitation type more closely approximates the real-world excitation.

---

[1] Thickness values were chosen based not on specifications provided, but rather by the time of flight experiments. See Chapter 6: Thickness Measurements

[2] Only top surface excitation is pragmatic. See Chapter 1: Pragmatic Restrictions

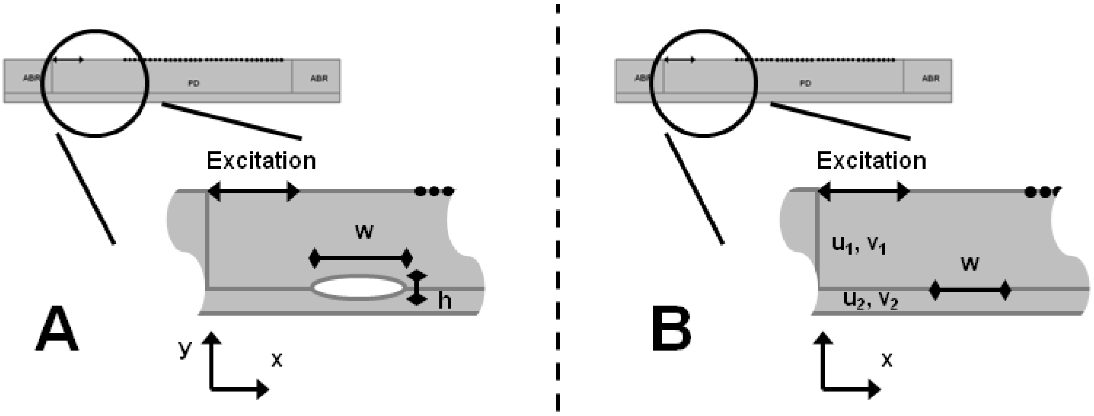

Figure 4.25: (A) Schematic of method 1, where the disbond is modeled as an elliptical void. (B) Schematic of method 2 where four independent variables are used and the disbond is modeled by altering the boundary conditions along *w*

In the following sections, two methods of modeling disbonds between layers are presented. The damage sites are between the excitation zone and the inspection points. Therefore, the inspection points are monitored in the transmitted field, after the incident wave has passed through and interacted with the damage site.

4.7.2 Geometrical Modeling Approach

A simple method for modeling disbonding is to create a geometrical void corresponding to the location of the disbond. A schematic of this model type is shown in figure 4.25 A. Thus, collapse defects are approximated by an elliptical-shaped void centered between the two layers. There exist two dimensions that can be chosen to determine an ellipsis: height *h* (z-direction) and width *w* (the x-direction) as seen in figure 4.25 A. The height *h* is kept constant here at 0.7 mm in order to compare the two modeling types, but will be investigated later in section 7.5 and again in Chapter 5. Since Mode 2 is the primary mode excited and detected in the healthy waveguide, the values for *w* are given in terms of actual length and percent wavelength of Mode 2 λ_2 in table 4.1.

Table 4.1: Width of elliptical void and corresponding percent of Mode 2 wavelength λ_2

w [mm]	**% λ_2**
0.85	10 %
1.28	15 %
2.13	25 %
2.84	30 %
4.27	50 %
6.40	75 %
8.53	100 %
12.80	150 %

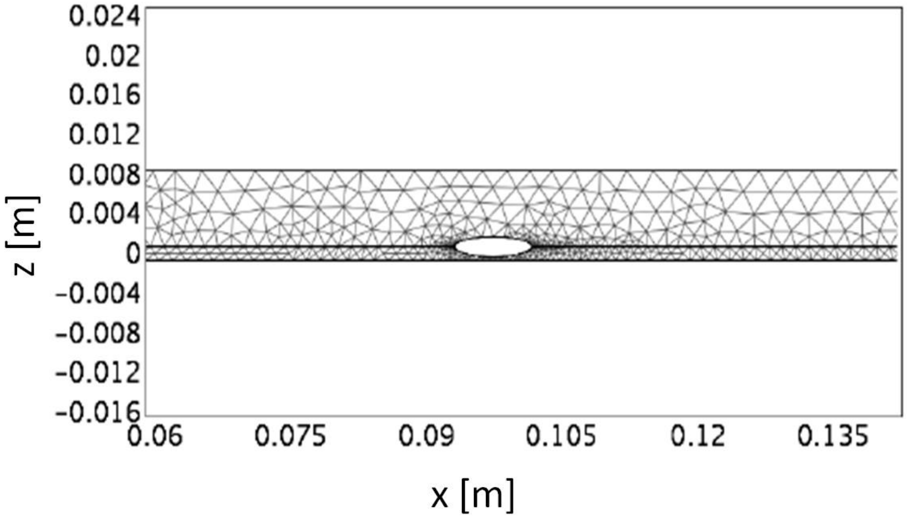

Figure 4.26: Example of mesh for the largest elliptical void (collapse defect).

Since this defect type occurs in a model pertaining to the novel bilayer COPV environment and not the steel plate used in previous examples, the model is described in further detail here: The mesh used consists of a 1.5 mm maximum element size in the thinner isotropic layer, and a larger 3 mm maximum element size in the orthotropic layer. Convergence tests show these mesh restrictions to be efficient, as long as a cubic interpolation function is used. A tighter mesh is used around the defect to properly approximate its more complex geometry, as shown in figure 4.26. A total of 2855 elements are used. The solution is solved in the time domain. The time steps taken by the solver are forced to be less than 3e-7 seconds, and the solution is recorded every 3e-7 seconds. A total of 667 time steps are recorded, i.e. from 0.0 to 20e-5 seconds.

4.7.3 Boundary Condition Modeling Approach

It is also possible to model disbonds by changing boundary conditions between the two layers. Consider figure 4.25 B. In this figure, four independent variables are used: u_1 and v_1 describe displacement in the upper layer, and u_2 and v_2 describe x and z displacement respectively in the lower layer. Accordingly the boundary conditions need to be established between the layers. Normally $u_1=u_2$ and $v_1=v_2$, but these relationships can be altered from their norm to model a disbond. In this work, each variable is treated as free in the defect zone. The length of the effected boundary line segments are equal to the values of w used in the previous section.

4.7.4 Comparison of Modeling Types

Each width is simulated and the results are analyzed based on the Fourier transform of the results collected from the inspection points, which allows for the separation of the modes via wavenumber. Although there are five guided wave modes present at this particular frequency, the highest two modes (Mode 4 and Mode 5) have similar

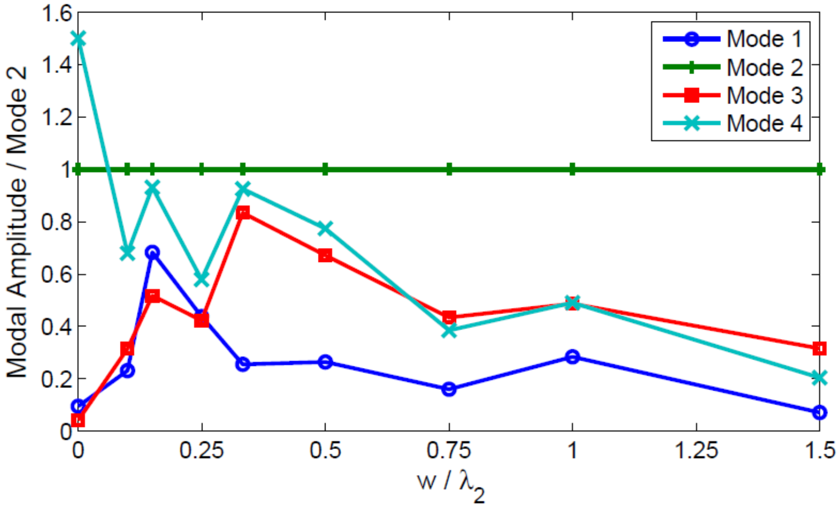

Figure 4.27: Normalized modal amplitude in the transmission field after interaction with the elliptical void as a function of defect width

wavenumbers and cannot be resolved. The modal amplitudes after interaction with the elliptical void disbond model are shown in figure 4.27, normalized by the amplitude of Mode 2 (the principal excited mode). The modal amplitudes after interaction with the defect modeled via the change in boundary conditions are shown in figure 4.28, again normalized by the amplitude of Mode 2.

It can be seen that the ratio of modal amplitudes vary significantly with defect width. Although the two models provide different modal amplitudes, the overall patterns are similar. Interestingly, despite the fact that Mode 2 the principal target for excitation, Mode 4 has a much higher amplitude for the case with no defect present. Despite this excitation problem, its amplitude decreases quickly with the defect in both models. Mode 3 apparently has an strong amplitude when the defect width is between 40% and 50% of $\lambda_{2,}$ and Mode 1 seems to have the highest amplitude when the defect site has a width between 15% and 30% *of* $\lambda_{2.}$.

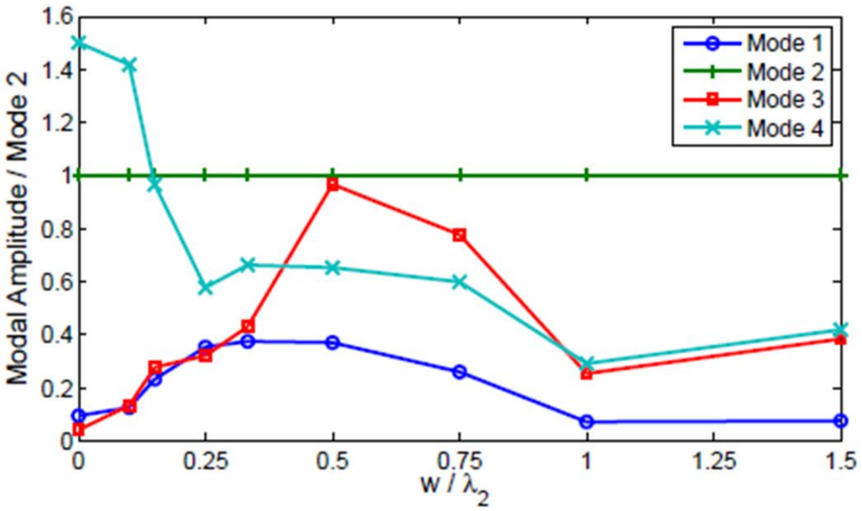

Figure 4.28: Normalized modal amplitude in the transmission field after interaction with the defect modeled via changing boundary conditions as a function of width

4.7.5 Spatio-Temporal Analysis

B-scans (spatio-temporal representations) are analyzed here concerning models with disbond-type defects of various sizes. A B-scan conducted along the top of the carbon-epoxy layer and measuring out-of-plane displacement is shown in figure 4.29 for a healthy (no defect present) model. The excitation type is the same as described in section 7.1. At least one strong mode corresponding to Mode 2 can be observed, but several other modes can also be detected before interaction with the right side of the plate at 25 cm, which is due to the fact that the excitation signal favors Mode 2, but does not excite it uniquely. Note that there are zones of constructive and destructive interference as was seen in figure 4.5 and figure 4.6. However, the number of propagating modes has increased, as well as the complexity of their dispersivity, so naturally the interference pattern is more complex.

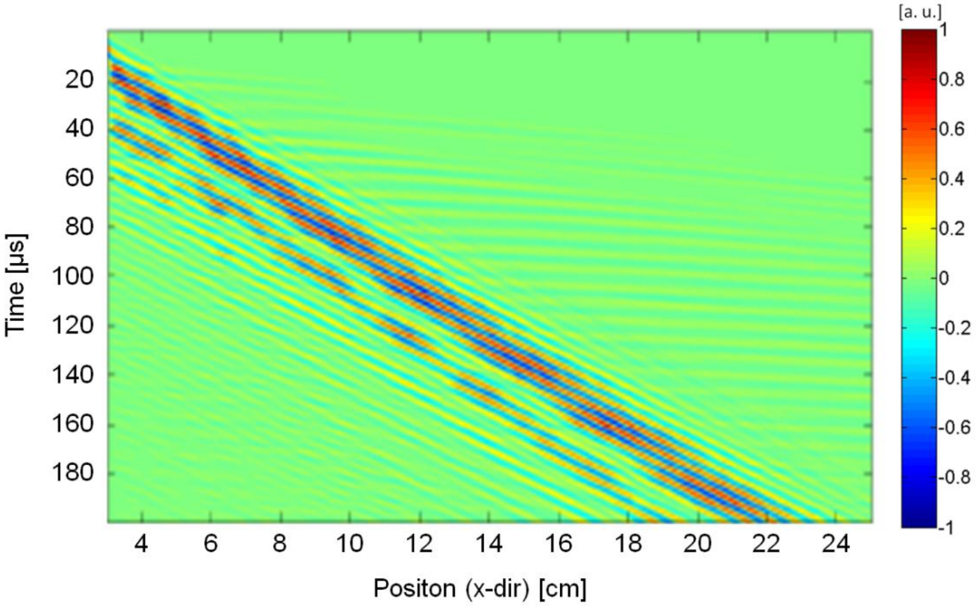

Figure 4.29: Healthy B-scan of 2D structure with top PZT-like excitation

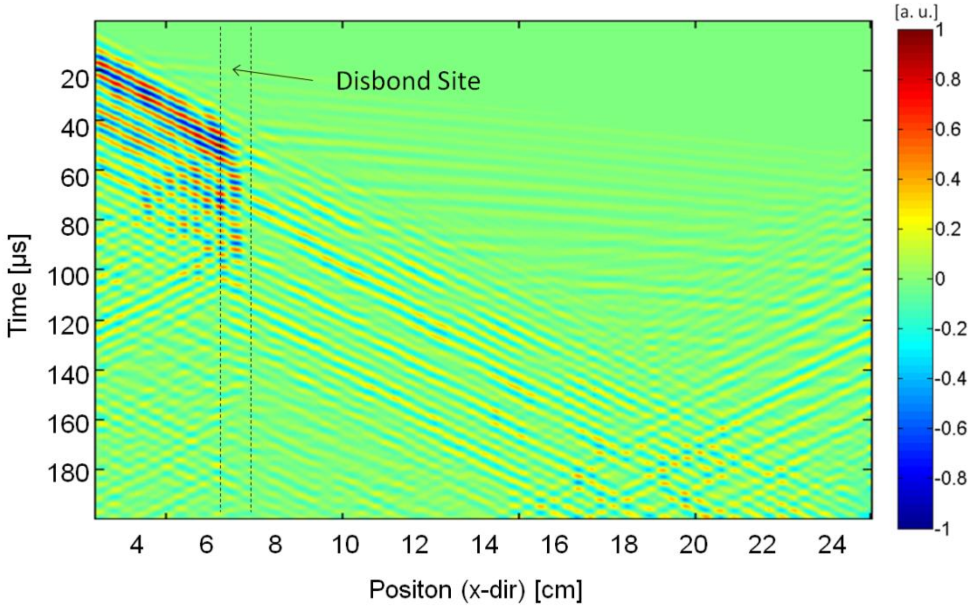

Figure 4.30: B-scan of the FEM model with largest disbond, w = 8.5mm, d = 1.043mm

Next, three disbond sizes modeled as elliptical voids are introduced to compare their respective effects on the incident wave packet. The largest defect has dimensions *w* = 8.5 mm, *d* = 1.043 mm, the intermediate defect, *w* = 2.8 mm, *d* = 0.92 mm and the smallest defect shown here has dimensions *w* = 0.85 mm, *d* = 0.56 mm. Compare the healthy B-scan from figure 4.29 with one for the largest defect shown in figure 4.30; the defect site is marked along the x-axis. There is clear reflection from wave interaction with the defect site, and the transmitted wave packet has a lower amplitude than the original healthy case. The B-scan for the intermediate sized damage is displayed in figure 4.31. Here, again, there is disruption in the UGW, although expectedly less severe. As one last defect example, consider figure 4.33, which corresponds to the smallest defect size considered. The damage site occurs slightly after 6 cm. Here it appears that the second wave packet interacts more strongly with the defect than the first. These series of figures demonstrates the use of UGW not only for defect detection, but also sizing.

Simulation results before, during and after interaction with the defect are shown in figures 4.33, 4.34, and 4.35 respectively for the largest defect type. Notice that a portion of energy is ‘trapped’ under the defect. This phenomena, which occurs as waves are continuously diffracted from the front edge and back edge of the defect, was also observed by other researchers [14]. However, the practicality of using this to localize defects in this case is limited since the majority of the energy is trapped on the lower layer, which will be inside the tank and consequently inaccessible.

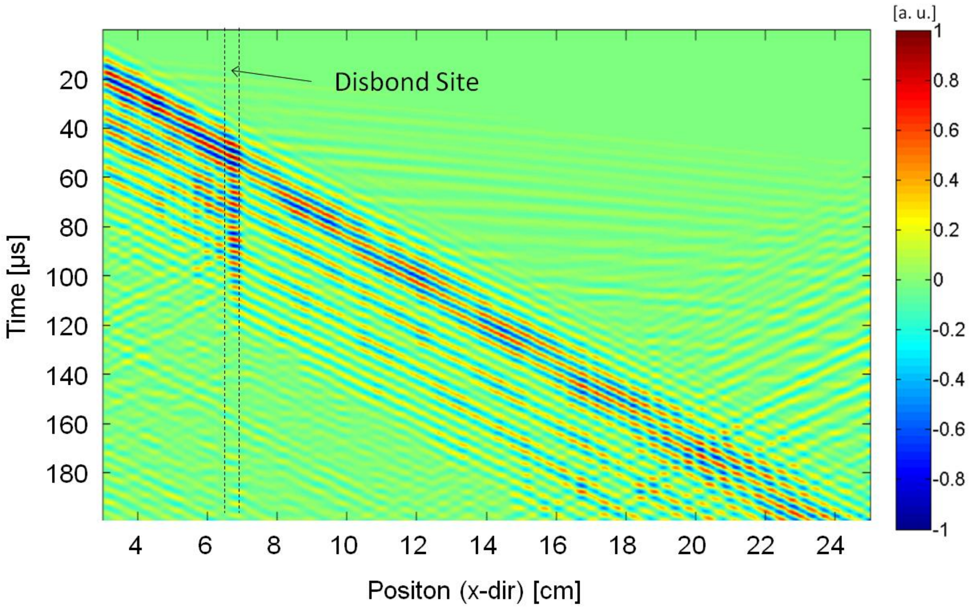

Figure 4.31: B-scan of FEM model with the intermediate disbond, d = 0.463 mm, w = 8.5 mm

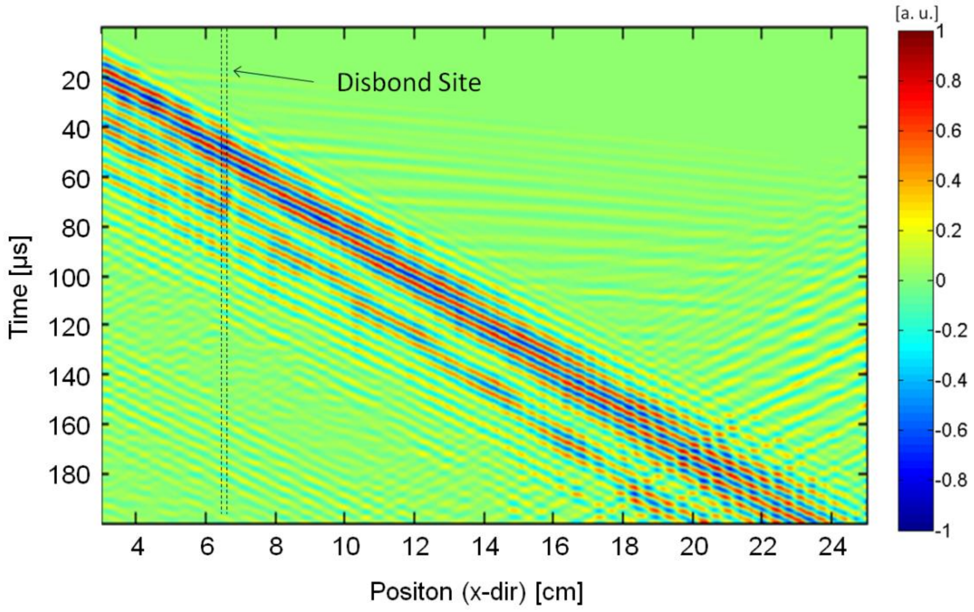

Figure 4.32: B-scan of model with smallest disbond, d = 0.56mm, w = 0.85 mm.

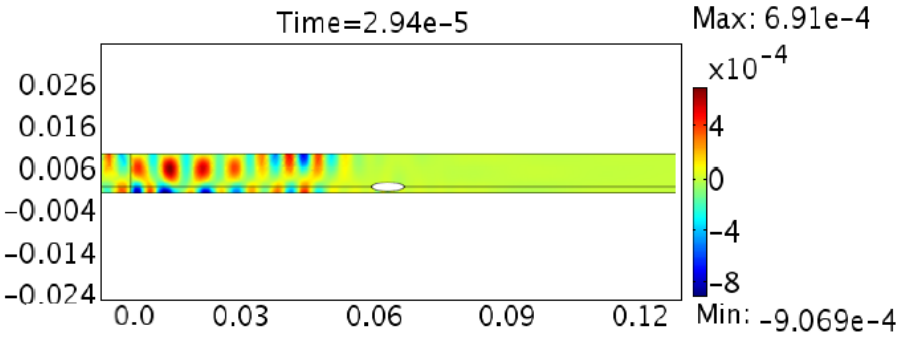

Figure 4.33: z-direction displacement at time step before interaction with the collapse defect

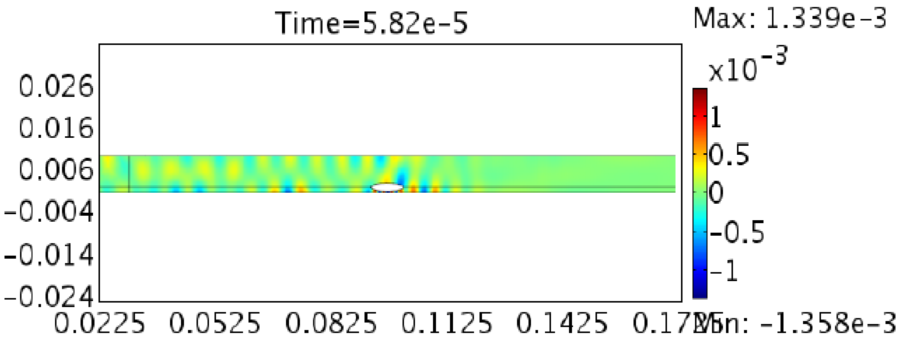

Figure 4.34 : z-direction displacement during interaction with the collapse defect

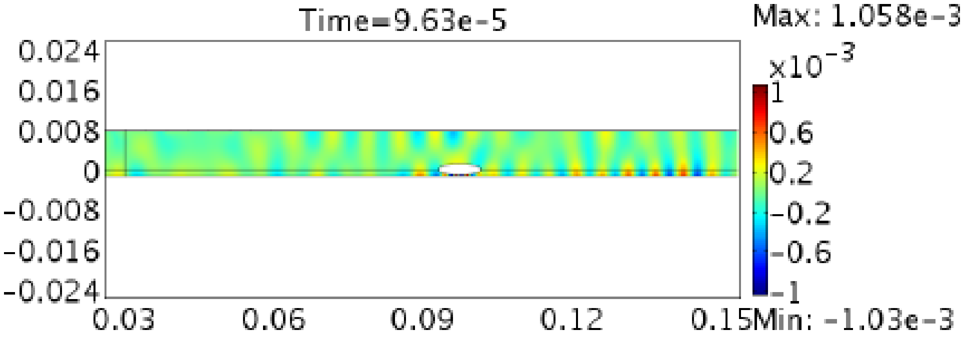

Figure 4.35: z-direction displacement after the largest wave packet has passed through the defect zone

4.7.6 Single Point Inspection

Single point inspections, or A-scans, give insight to the type of information that can be gleaned when stationary single element transducers are used as receivers. A-scans for three different inspection points are shown in figure 4.36. The three inspection points are located at 10 cm, 15 cm, and 20 cm from the emitter, all or which occur after the defect in the transmission field. The three damage sizes displayed here are the same as in section 7.3: small (w = 0.85 mm, d = 0.56 mm), medium (w = 2.8 mm, d = 0.92 mm) and large (w = 8.5mm, d = 1.043mm). In the A-scan grid it is evident that the principle wavepacket, corresponding mostly to Mode 2, loses amplitude after it interacts with the site of disbonding. The amount of amplitude loss appears to be proportional to defect size, with the highest attenuation occurring after interaction.

Obviously, due to multi-modal propagation, modal amplitudes are difficult to obtain without complete modal separation. If modal separation does not occur in the temporal domain due to geometry restrictions, this is possible in the frequency domain via such tools as the STFT [21].

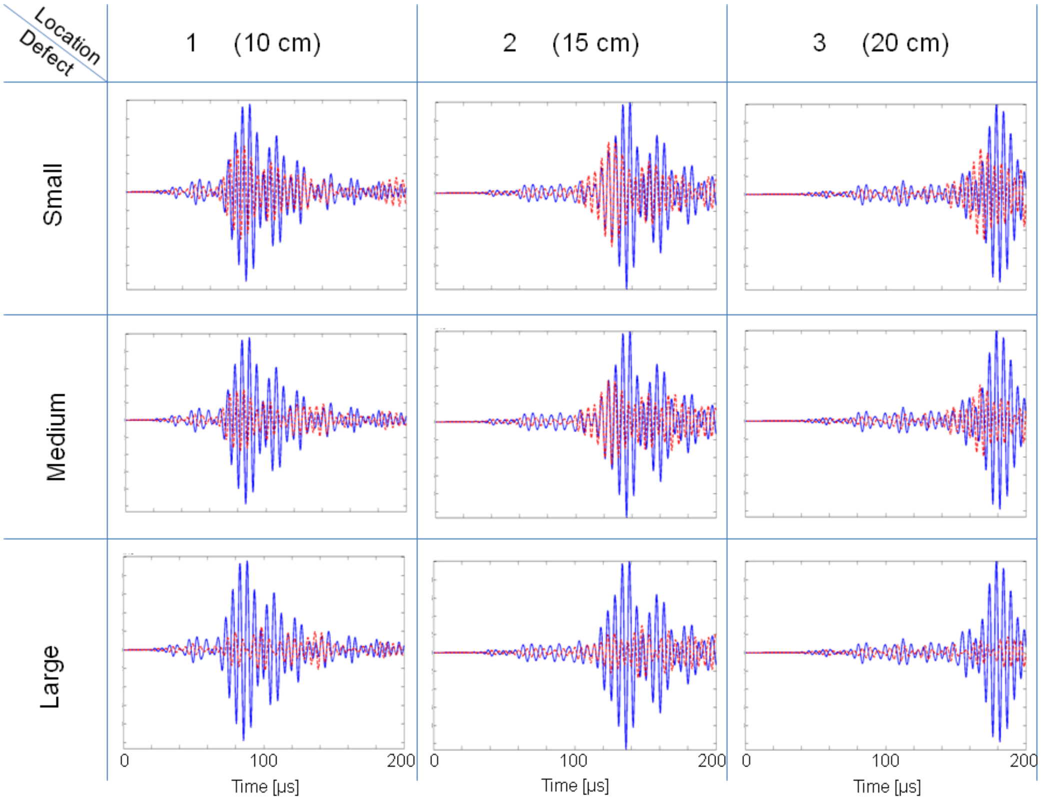

Figure 4.36: Waveforms for three inspection points occurring at Location 1 = 10 cm, Location 2 = 15 cm, and Location 3 = 20 cm. The waveforms for the baseline (healthy) case are plotted (solid blue) for each case as a reference. The waveforms for the signal after interaction with three defects (red dotted) are plotted for three cases: small (w = 0.85 mm, d = 0.56 mm), medium (w = 2.8 mm, d = 0.92 mm) and large (w = 8.5mm, d = 1.043mm).

4.8 Summary

A summary is provided here of the findings for the FEM for each defect type, i.e. surface-originating cracks/notches, internal voids, abrasions, and collapse defects *i.e.* disbonds.

4.8.1 Summary of Notch-Type Defect Study

The validation of the detection of defects has been accomplished. The simulated defect was a notch, which models a cut or surface-originating crack. This kind of defect can appear during the life of metallic structures as well as composite materials. Therefore previous work done in metal plates was used to benchmark the accuracy of the current work.

A spatiotemporal representation was used to demonstrate the beating behavior possible due to modal conversion. The spatiotemporal diagram showed that there are constructive and destructive interferences which generate some zones in which the displacements amplitude is very low. This demonstrates that in practical cases, a single element receiver cannot be placed anywhere, but must be intelligently placed, and that if a comb array transducer is used (as assumed in this work) that the inter-element spacing must also be intelligently chosen. The spatiotemporal representations were followed by frequency-wavenumber representations. This kind of representation offered the possibility to separate the wavepacket into the various propagating modes after interaction of the excited mode with the given defect. Ultimately, this can be used to size the notch. Finally, a novel baseline subtraction algorithm is developed, which improves the lower limits of defect detection with minimal *a priori* information.

4.8.2 Summary of Internal Void Study

A variation on the 1st type of damage is studied. A void of fixed dimensions is moved through the thickness in the z-direction, simulating surface and subsurface (internal) cracks. Modal conversion and transmission coefficients are symmetrical with respect to the mid-plane for single layer structures. Therefore a defect’s through-thickness position can only be determined with respect to the mid-plane for a mono-layer plate.

Furthermore, if the defect is localized in the middle of a monolayer plate, it may go undetected by the fundamental modes. An incident S_0 mode appears to be more sensitive to the through-thickness position of an internal void for a mono-layer plate.

4.8.3 Summary of Abrasions Study

A change in upper layer thickness is modeled as a notch having variable depth and width. Ultimately, the study shows that modal conversion is mainly due to refraction and seems to be largely independent of defect width. Therefore, the results resembled very closely that of a surface-originating crack. Therefore, conclusions concerning the detection of surface-originating cracks are assumed to be valid for the case of abrasions as well, as long as the abrasion has the same depth.

4.8.4 Summary of Collapse Defect Study

Two methods of modeling disbond-type defects are presented, i.e. elliptical voids and altered interface boundary conditions. The elliptical void allows for changes in two dimensions, i.e. defect length and the separation between the two layers, whereas the boundary condition approach is limited to defect length. Geometrical voids therefore offer greater flexibility in parameter manipulation. However both methods have drawbacks concerning their physical interpretation. Altering boundary conditions allows thicknesses to remain the same, but also allows for the two layers to occupy the same space, a physical impossibility. The geometrical void makes changes to layer thickness which may also not be representative of the physical case.

It is shown that amplitude measurements can indicate the presence and width dimension of collapse defects simply by exciting Mode 2 with a surface excitation. If modal amplitudes can be measured, modal reflection, transmission and conversion can also be used to determine the size of such collapse-type defects. Modal transmission as well as mode conversion to other low order modes, is evaluated for various collapse defect geometries. Spatio-temporal representations are presented as well for three select disbond sizes, which demonstrate the complexity of the propagation of a multi-modal signal. Modal separation is possible via spectral analysis.

4.9 References

[1] L. E. Kinsler, A. R. Frey, A. B. Coppens and J. V. Sanders, Fundamentals of Acoustics, U.S.A.: Wiley and Sons, 1999.

[2] A. H. Nayfeh, Wave propagation in layered anisotropic media, The Netherlands: Elsevier Science B. V., 1995.

[3] I. Bartoli, Structural Health Monitoring by Ultrasonic Guided Waves, San Diego: University of California, 2007.

[4] P. Cawley and D. N. Alleyne, "The interaction of Lamb waves with defects," *IEEE Transaction on Ultrasonics, Ferroelectrics and Frequency Control,* vol. 39, no. 3, pp. 381-396, 1992.

[5] P. McKeon, S. Yaacoubi, N. Declercq, S. Ramadan and W. K. Yaacoubi, "Baseline subtraction technique in the frequency–wavenumber domain for high sensitivity damage detection," *Ultrasonics,* vol. 54, pp. 592-603, 2014.

[6] N. Terrien, D. Osmont, D. Royer, F. Lepoutre and A. Deom, "A combined finite element and modal decomposition method to study the interaction of Lamb modes with micro-defects," *Ultrasonics,* vol. 46, pp. 74-88, 2007.

[7] N. Terrien, D. Royer, F. Lepoutre and A. Deom, "Numerical predictions and experiments for optimizing hidden corrosion detection in aircraft structures using Lamb modes," *Ultrasonics,* vol. 46, no. 3, pp. 251-265, 2007.

[8] M. Lowe, D. Alleyne and P. Cawely, "Defect detection in pipes using guided waves,"

Ultrasonics, pp. 147-154,, 1996.

[9] M. Lowe and O. Diligent, "Low-frequency reflection characteristics of the S0 Lamb wave from a rectangular notch in a plate," *Journal of the Acoustical Society of America,* vol. 111, no. 1, pp. 64-74, 2001.

[10] M. Lowe, P. Cawley, J.-Y. Kao and O. Diligent, "The low-frequency reflection characteristics of the fundamental antisymmetric Lamb wave a0 from a rectangular notch in a plate," *Journal of the Acoustical Society of America,* vol. 112, no. 6, pp. 2612-2622, 2002.

[11] F. Benmeddour, S. Grondel, J. Assaad and E. Moulin, "Experimental study of the A0 and S0 Lamb waves interaction with symmetrical notches," *Ultrasonics,* vol. 49, pp. 202-205, 2009.

[12] B. Kim and Y. Roh, "Simple expressions of the reflection and transmission coefficients of fundamental lamb waves by a rectangular notch," *Ultrasonics,* vol. 51, pp. 734-744, 2011.

[13] J. Rose, "Guided Wave Nuances for Ultrasonic Nondestructive Evaluation," *IEEE Transactions on Ultrasonics, Ferroelectrics, and Frequency Control,* vol. 47, no. 3, pp. 575-583, 2000.

[14] S. Kessler, S. Spearing and C. Soutis, "Damage detection in composite materials using Lamb wave methods," *Smart Materials and Structures,* vol. 11, pp. 269-278, 2002.

[15] S. Valdes and C. Soutis, "Real-time nondestructive evaluation of fiber composite

laminates using low-frequency Lamb waves," *Journal of the Acoustical Society of America,* vol. 111, pp. 2026-2033, 2002.

[16] T. E. Michaels, J. E. Michaels and M. Ruzzene, "Frequency-wavenumber domain analysis of guided wavefields," *Ultrasonics,* vol. 51, pp. 452-466, 2011.

[17] J. L. Rose, "Ultrasonic Guided Waves in Structural Health Monitoring," *Key Engineering Materials,* pp. 270-273, 2004.

[18] A. J. Croxford, P. D. Wilcox, B. W. Drinkwater and G. Konstantinidis, "Strategies for guided-wave structural health monitoring," *Proceedings of the Royal Society A,* vol. 463, pp. 2961-2981, 2007.

[19] W. E. Leucke, J. McColskey, C. McCowan, S. Banovic, R. Fields and T. Foecke, "Federal building and fire safety investigation of the world trade center disaster: mechanical properties of structural steels," U.S. Department of Commerce: National Institute of Standards and Technology, 2005.

[20] J. E. Michaels, "Detection, localization and characterization of damage in plates with an in situ array of spatially distributed ultrasonic sensors," *Smart Material Structures* , vol. 17, pp. 1-15, 2008.

[21] M. Niethammer, L. J. Jacobs, J. Qu and J. Jarzynski, "Time-frequency representations of Lamb waves," *Journal of the Acoustical Society of America,* vol. 109, pp. 1841-1847, 2001.

[22] E. A. Birt and W. J. Percival, "A study of Lamb wave propagation in carbon-fibre composites," *INSIGHT,* vol. 39, no. 10, pp. 728-735, 1997.

[23] D. N. Alleyne and P. Cawley, "Optimization of lamb wave inspection techniques," *NDT&E International,* vol. 25, no. 1, pp. 11-22, 1992.

CHAPTER 5

OPTIMIZATION STUDIES AND GUIDELINES

5.1 Introduction

Considering the work presented in the precedent chapters, it is clear that UGW inspection of the given structure is complicated by many factors, including defect size and form, excitation type, frequency range, etc. Due to the number of parameters at play, qualitative studies of conversion coefficients are difficult to perform, even when assumptions are made concerning the ideal nature of the waveguide [1]. Nevertheless, the finite element method can increase understanding of the physical phenomena, by providing a cross-sectional view of the effect of these parameters (as seen in Chapters 3 and 4). As the envisioned applications for UGW SHM systems become increasingly more complex, it has become increasingly necessary to begin with careful modeling studies. This ensures that the resulting developed procedures are optimized and robust [2]. Furthermore, the use of FEM as an optimization tool can overall save time and money, since expensive experimental setups need only to verify numerical results.

The aim of this chapter is to offer a generalization of the results obtained in previous chapters by analyzing patterns of modal conversion and identifying the most substantial changes to ease interpretation of results. In this manner, experimental setups or future SHM systems can be optimized to ensure the detection of damage appreciably prior to its critical stages. Some observations on the effect of certain parameters (especially defect dimensions) are presented so that trends can be used to establish experimental guidelines. Furthermore, some limitations are defined, in terms of defect identification and sizing.

Overall, the goal of this chapter is to provide a fundamental basis for the development of future SHM systems intended for thick-walled, multi-layer orthotropic structures. Decisions concerning controllable parameters are reviewed so as to minimize problems that may arise. This chapter is organized in two distinct sections: First optimization studies are carried out with the goal of identifying the easiest way to excite modes, and detect changes in transmission patterns. This section will be further divided for two damage types – notches and disbonds. Then a series of guidelines will be presented to inform SHM systems.

5.2 Optimization Studies

This section is organized as follows: Mode shapes first discussed in Chapter 2 will be investigated in more detail. Then, transducer vibrational mode will be discussed for the purpose of excitation. Subsequently, modal conversion will be optimized for select defect types, and guidelines will be presented to help the development of future SHM systems.

5.2.1 Mode Selection

As already seen in chapter 2, analytical solutions for the dispersion curves of multi-layer materials are complex, so semi-analytical or numerical solutions are preferred. The relevant dispersive relations are displayed in figure 5.2, determined semi-analytically for the frequency range of interest, i.e. 100-300 kHz. This frequency range is practical in that it helps limit the number of modes (the higher the frequency range, the more modes appear, indefinitely) and the wavelengths of the lower order modes (Modes 1 and 2) span an order of magnitude of wavelengths from 4 mm to 3 cm. The higher the frequency range, the more modes appear, indefinitely, as testified by the appearance of higher order modes at higher frequencies in figure 5.1. In another words, this range is

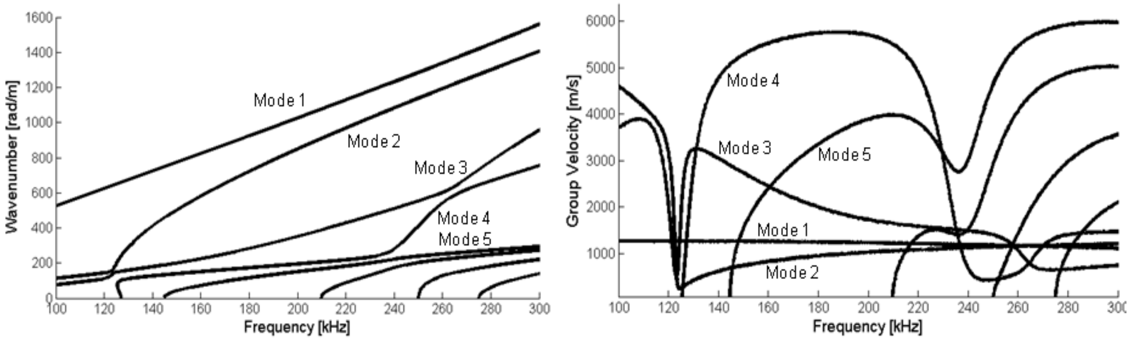

Figure 5.1 : Wavenumber (left) and group velocity (right) dispersion curves determined numerically from analytical expressions along the direction of propagation (x) for the two-layer structure.

favorable in order to have a relatively simple signal and satisfactory sensitivity, which is often found to be directly correlated to wavelength size [3].

Furthermore, modeshapes are functions of frequency. The optimization of mode selection is strongly related (though not limited) to the optimization of the operational frequency. Modeshapes can be predicted via semi-analytical methods with the commercially available software Disperse [4]. However, it will be seen in Chapter 6, section 3.6 that dispersion curves extracted from numerical simulations more closely emulate experimentally extracted dispersion curves for this particular waveguide. It follows that modeshapes determined via the FEM will also more closely emulate physical modeshapes than those calculated by Disperse.

Modeshapes can be determined via the FEM by evaluating points at regular intervals; the process is demonstrated in figures 5.2, 5.3 and 5.4. The modeshapes are more easily determined using the Helmholtz equation and solving wave propagation in the frequency domain to ensure that each mode only has one associated modeshape. First, the displacement is monitored in both the *z* and *x* directions as seen in figure 5.2. Note that this figure shows the graphical output from Comsol [5] of the top layer in both

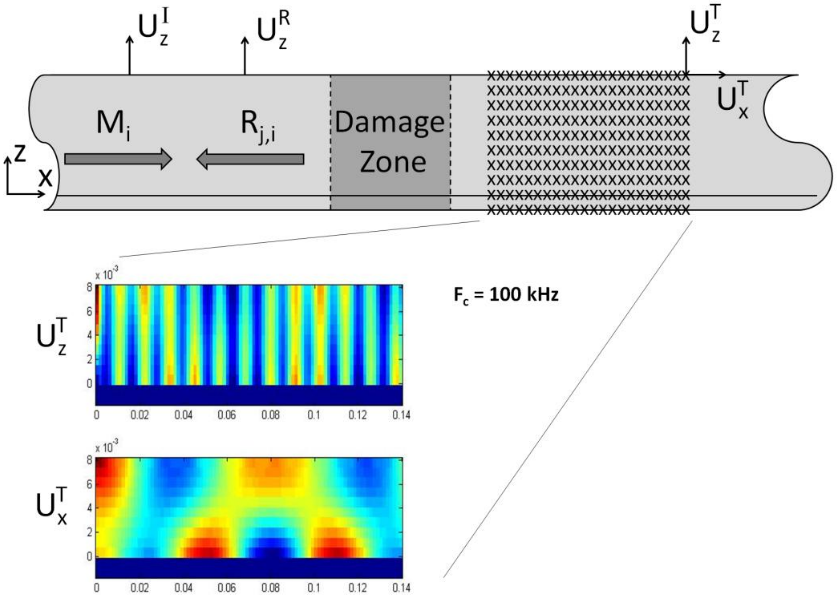

Figure 5.2: Displacement in the x and z directions for the transmission region for a center frequency of 100 kHz.

Cartesian coordinate directions. Since the two layers are separated into two solution domains, only one layer's displacement solution can be displayed at a time. This results in the second layer being displayed as having a uniform displacement (uniform color). However, in general, the displacement solutions for both layers are utilized.

Next, the wavenumber spectrum is ascertained as a function of depth z as depicted in figure 5.3. Since this solution is carried out in the temporal frequency domain, right traveling waves appear as "negative" wavenumbers and left traveling waves appear as "positive" wavenumbers. In the transmission field there exists only right traveling waves. However this method of separation enables the separation of the incident and reflective fields which physically occupy the same geometry.

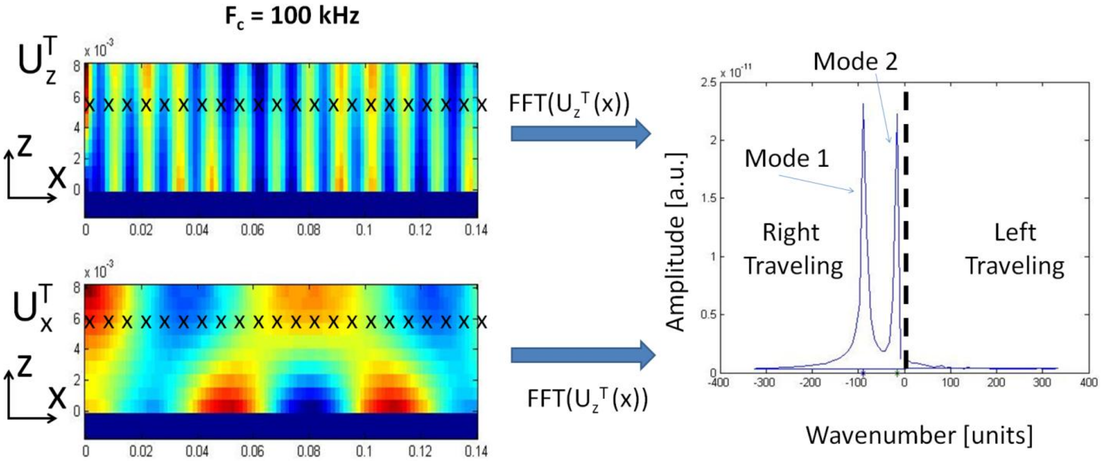

Figure 5.3: Finite Element models are evaluated at various through-thickness points. A Fourier transform can separate a multi-modal environment, where peaks represent modes at a certain wavenumber.

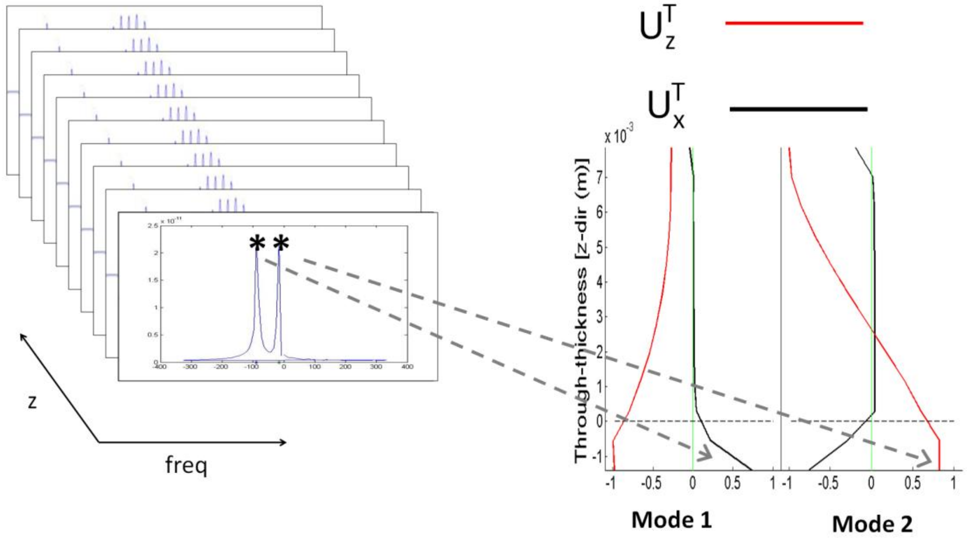

Figure 5.4: Taking peak values at each z position leads to modeshapes. Special consideration needs to be given to phase at each point.

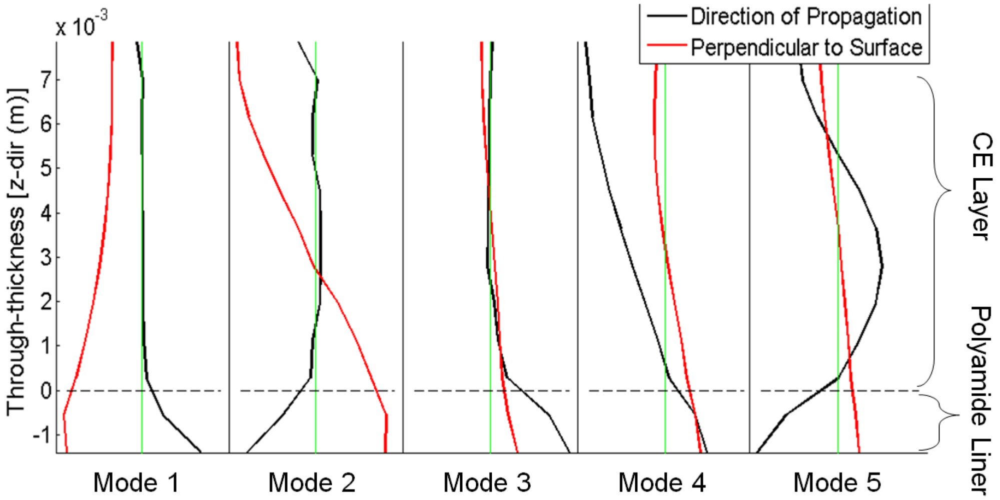

Figure 5.5: Mode shapes as determined via the FEM for the five propagating modes at 150 kHz.

Finally the peak values in the wavenumber spectrum correspond to the various propagating modes as shown in figure 5.4. Special attention must be paid to the phase to determine whether the modeshape is given a positive or negative value. Low amplitude portions of the modeshape, i.e. points near zero, may give false phase values due to numerical error. However, due to their relatively low amplitude, this error in phase can be considered trivial.

As an example case, modeshapes at 150 kHz are depicted in figure 5.5 for the first 5 modes[1]. It is possible to predict which modes will be most useful based on their modeshapes. Consider Modes 1 and 2, which will have the two shortest wavelengths and therefore have the potential to detect damage with small characteristic dimensions. If excitation is to be carried out in the direction of propagation, Mode 1 will be incredibly difficult to excite due to its lack of modal amplitude at the top surface.

---

[1] 150 kHz is chosen as an example case due to the presence of Mode 4 which proves difficult to excite at other frequencies.

Alternatively, Mode 2 displays modal displacement in both directions at the surface. Furthermore, Mode 2 only experiences a complete modal point near 2.5 mm, where both directions are near zero. It can be inferred therefore that Mode 2 should exhibit modal conversion and interaction with damages at any other through-thickness depths. Defects will only be invisible if they are found precisely at Mode 2's nodal point.

It can also be noted that Mode 3 is invisible to the top surface regardless of which direction is investigated. Indeed, Mode 3 remains difficult to detect and excite over the majority of the frequency range of interest. Its modal amplitude remains low except in the polyamide layer, which is inaccessible. However, when choosing an operating frequency to be used to detect a specific damage type, instead of looking at the evolution of each propagating mode from 100 to 300 kHz, it is instead more efficient to model the interaction of the modeshape as a function of frequency with a defect site. This is realized in section 2.3.

5.2.2 Transducer Vibrational Mode

One of the defining characteristics of transducers is their vibrational mode; commercial piezoelectric transducers, like the ones employed in this work, are available in both shear (parallel to the surface of the plate) and longitudinal (perpendicular to the surface of the plate) configurations, as displayed in figure 5.6. On the left hand side of the figure, a longitudinal transducer is displayed as well as its corresponding excited Lamb wave-front if put in contact with an orthotropic thin plate. On the right hand side, a shear transducer is shown, with its corresponding shear horizontal wave-front and Lamb wave-front for the same thin orthotropic plate. Additionally, the 2D plane used in the FEM simulations is shown for the ease of the reader. Note that the 2D plane is the x-z plane,

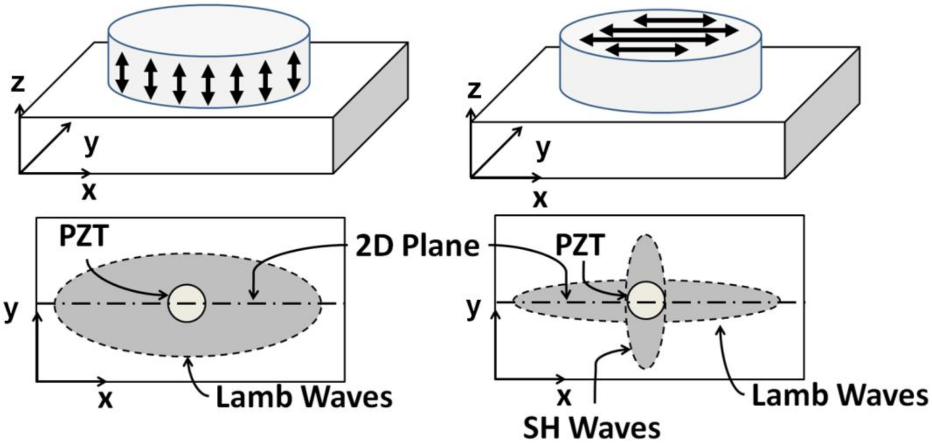

Figure 5.6: A longitudinal type transducer in contact with an orthotropic plate and its corresponding excited guided wave-front (left) and a shear type transducer in contact with an orthotropic plate with its corresponding excited guided wave-fronts (right).

and that it is a plane of symmetry, validating the use of a 2D model. It also occurs in a plane where it is safe to assume the absence of SH waves, for either transducer type.

Recall that the upper surface in the 2D FEM is analogous to the outer surface of the high pressure reservoir. Therefore the restriction to the upper surface is necessary for practical reasons as seen in section 2.1. In the FEM frequency domain simulations, these two excitation types can be modeled as a boundary force acting over the characteristic dimension of the transducer. The boundary force excitation is located between 0 cm and 1 cm on the top surface. Figure 5.7 shows the results of the FEM simulation in terms of out-of-plane displacement as a way of qualitatively comparing the two excitation types at 200 kHz, which is the center frequency of the range of interest and therefore deemed an appropriate example case.

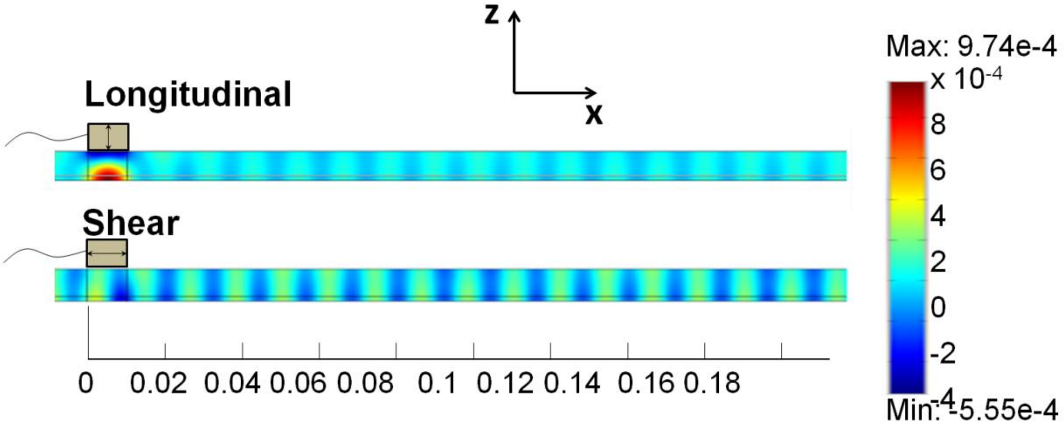

Figure 5.7: Vertical displacement, u_z, calculated via the FEM for longitudinal (top) and shear (bottom) mode transducer type excitation at 200 kHz.

A standing wave established between the top and bottom surface within the confines of the bounded beam profile of the contact transducers is expected. The excitation types mimic contact transducers (both shear and longitudinal) fixed flush to the surface of the waveguide, and therefore cannot take advantage of the phase matching effect that angular wedges or comb transducers may exploit. Accordingly, any UGW's that are propagated in the x-direction are a result of waves escaping the bounded beam profile of the transducer, due mainly to material stiffness. Although both methods succeed in propagating UGW, it is observed that the longitudinal transducer directs most of its energy in setting up a standing wave along the z-axis at the excitation site, whereas the shear transducer more efficiently propagates guided wave modes given the same input amplitude. Therefore, shear type excitation is chosen as being the optimal configuration and will be used for the remainder of the work.

5.2.3 Defect Detection

The purpose of optimization with regard to damage detection is to choose certain parameters so as to more easily ascertain the presence of said damage. To this end a representative case for two defect types are examined here. The goal is to identify the evidence of UGW interaction with the defect that is blatant, and therefore most likely to not be missed or cause false alarms.

In the following sections, the optimization of operational frequency is presented in terms of damage detection. Two damage types are presented; the surface-originating crack (notch) modeled in Chapter 4, section 4, and the collapse defect (disbond) modeled in Chapter 4, section 7. Furthermore, two excitation types are applied to the case of the notch: the first case models a single element PZT, and the second case models a multi-element PZT tuned to match Mode 2 at the given frequency.

Simulations are carried out in the frequency domain using the Helmholtz equation from 100 to 300 kHz in increments of 10 kHz. Excitation is achieved by shear vibration on the carbon-epoxy free surface as per section 2.2. Operational frequency (or frequency range) is chosen for a high level of damage interaction, and modal conversion that is visible at the top surface. This latter point is crucial since large modal conversions that are unobservable via the method of reception are ineffective.

5.2.3.1 Notch Defect with Single Element PZT

A single notch depth is examined for the purpose of optimizing its detection. The chosen notch depth is 50% of the carbon-epoxy layer, i.e. approximately 4 mm. The crack width is considered thin, so that the width of the notch in the FE model is one element.

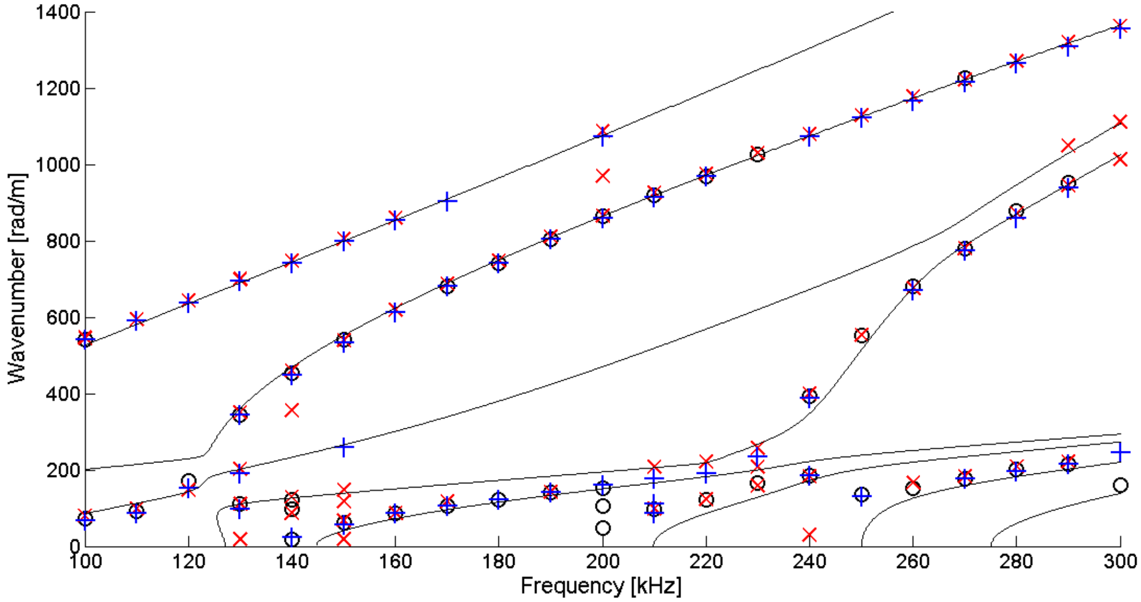

Figure 5.8: Locations of local maximums of the spatial Fourier transform of the incident (o), reflection (x) and transmission fields (+) for a surface-originating crack type defect.

The incident, reflection, and transmission fields are inspected as described by the process outlined in section 2.1; a series of evenly spaced points are monitored on the top surface, via a spatial Fourier transform. The locations of local maximums in the frequency wavenumber plane for the three fields (I, R and T) are shown in figure 5.8. Local maxima in a frequency-wavenumber space indicate the presence of a propagating mode [6]. Therefore figure 5.8 in essence shows which modes are propagating in each field (I, R and T), regardless of modal amplitude as long as that amplitude is above the numeric noise threshold. To this end, the threshold value is taken as 1.5 times that of the noise floor. Recall that the incident and reflection fields can be separated in the wavenumber spectrum (see section 2.1).

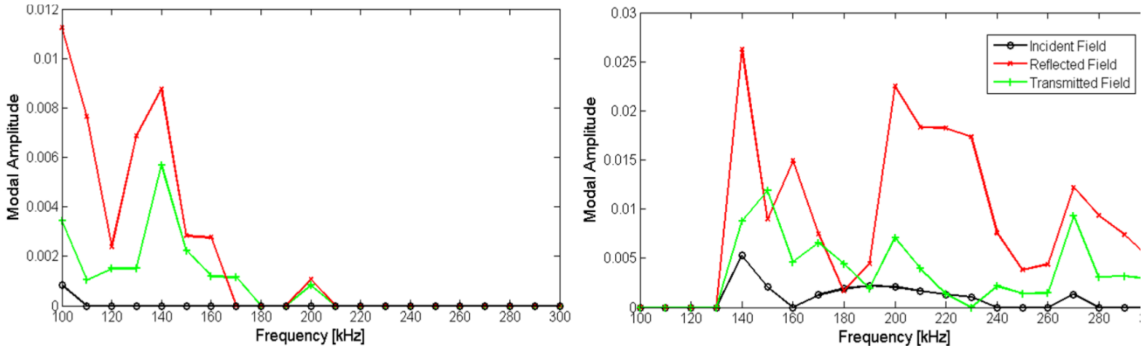

Figure 5.9: Mode 1 (left) and Mode 2 (right) amplitudes for the incident (o), reflection (x) and transmission fields (+) for a surface-originating crack type defect.

Figure 5.8 neatly displays which modes propagate in the incident, reflection and transmission fields as a function of frequency. However, the optimal frequency for detection of a given mode is directly related to its amplitude. The amplitudes corresponding to the maxima of the two lowest order modes (Mode 1 and Mode 2) are shown in figure 5.9.

Figure 5.9 shows that highest changes in modal amplitude occur in the reflective field between 140 and 170 kHz and between 200 and 240 kHz for Mode 2. Not only does this give information concerning the optimal frequency range, but also hints that the receiving transducer should be placed in the reflective field if possible to detect a notch with depth = 4 mm. However, the extent of the effect of phase of the incident wave remains unclear since the distance between the emitter and damage site has remained fixed. The effect of incident phase is further investigated in section 3.1.

5.2.3.2 Notch Defect with Multi-Element PZT

The same notch-type defect is investigated, but with a different excitation function. Excitation is still achieved by shear vibration on the carbon-epoxy free surface. The excitation function is altered to apply a forcing function in a sinusoidal shape with a spatial frequency corresponding to that of Mode 2 at the given operating frequency. This

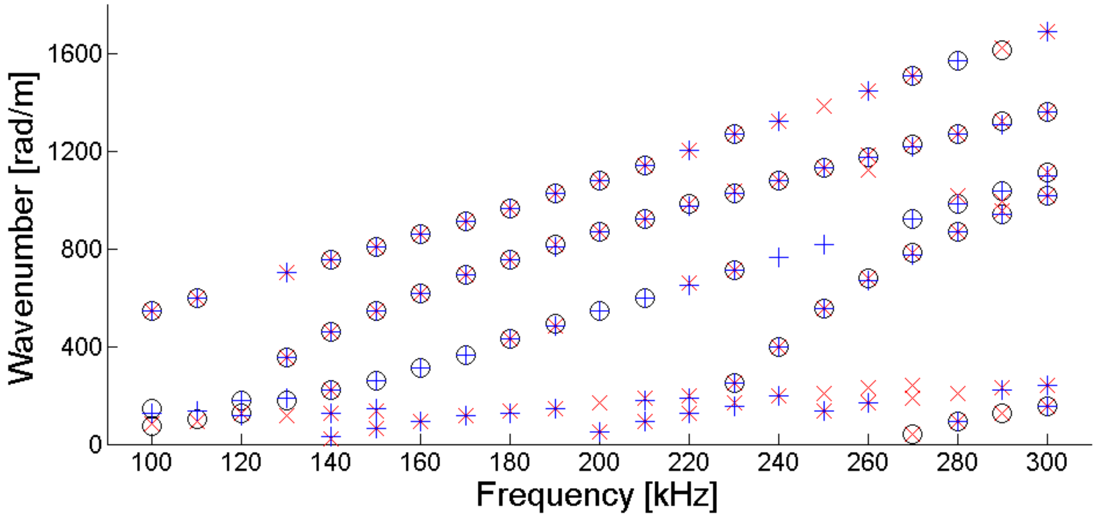

Figure 5.10: Local maximums above the numerical noise floor in the (o) Incident field, (x) reflection field, and (+) transmission field.

approximates a multi-element type transducer that can be tuned to excite Mode 2. Despite the strong formation of Mode 2, other modes still appear in the incident field, due to the finite length of the excitation boundary which is taken as 1.5 cm.

Modal amplitudes are again found by taking local maximums that occur above the numerical noise floor of the spatial spectrum, i.e. the wavenumber domain. Figure 5.10 shows which modes propagate in which domain; this is a qualitative assessment of which modes may be possible to detect, but gives no qualitative evaluation of modal amplitude. For example, one can note that Modes 1, 2 and 3 are present in all fields (incident, reflection, and transmission) at 180 kHz, but the amplitude of any given mode in any given field is not given by this figure.

In light of the mode shapes presented in section 2.1, displacement normal to the surface is monitored, so as to include Mode 1 which has little to no displacement in the direction of propagation. To qualitatively assess the modes, consider figure 5.11 which shows Modes 1, 2, 3 and 5 on a decibel scale, with the reference value taken to be the

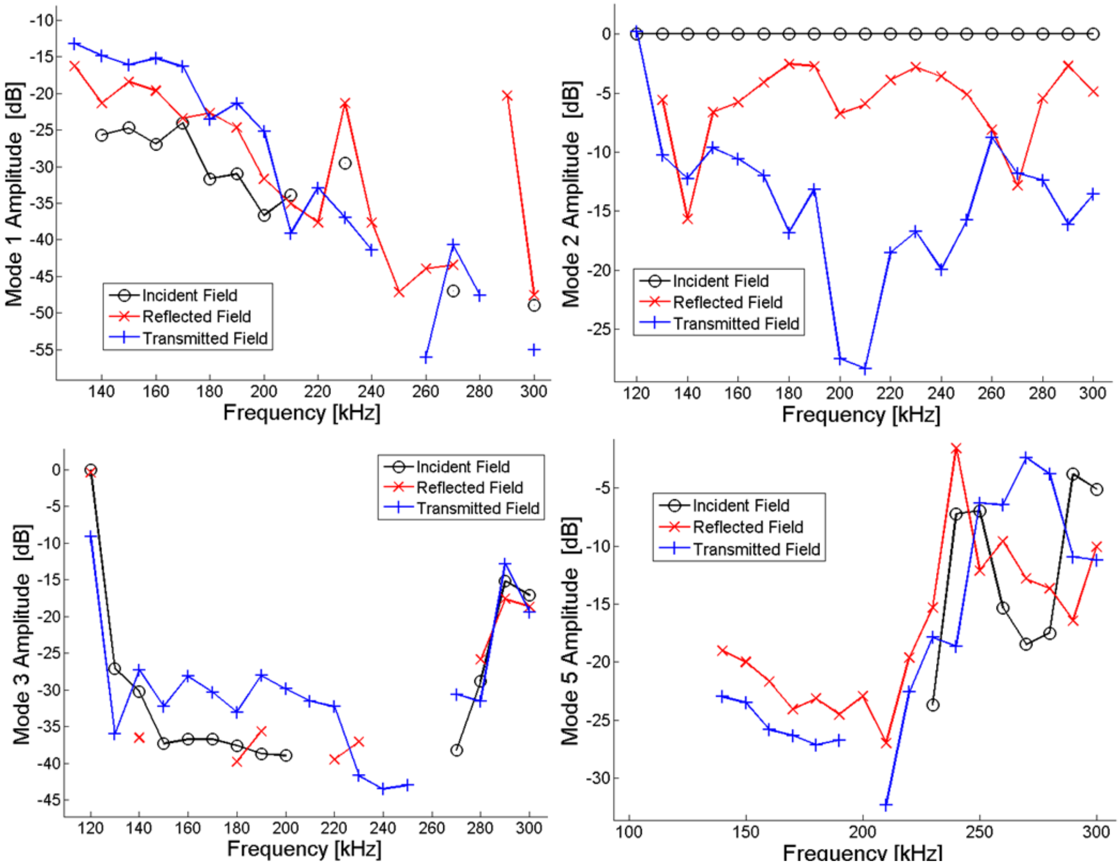

Figure 5.11: Modal amplitudes for Modes 1 (top left), Mode 2 (top right), Mode 3 (bottom left) and Mode 5 (bottom right) after interaction with a Notch (depth = 50 % of CE layer thickness)

amplitude of Mode 2 in the incident field, i.e. the principal mode excited. Consequently, Mode 2 has a constant amplitude of 0 dB in the incident field. Mode 4 is excluded due to its low manifestation (only in the reflection and transmission field near 150 kHz.)

It is apparent from figure 5.11 that the majority of the energy after interaction with the crack goes into reflecting Mode 2 and conversion to Mode 1 in the transmission field for frequencies inferior to 200 kHz. Mode 2 is most strongly reflected around 180 and 190 kHz. Mode 1 appears in the transmission field with a strong modal amplitude from 150 kHz to 170 kHz. Some of Mode 2 also gets transmitted through the defect zone, but with

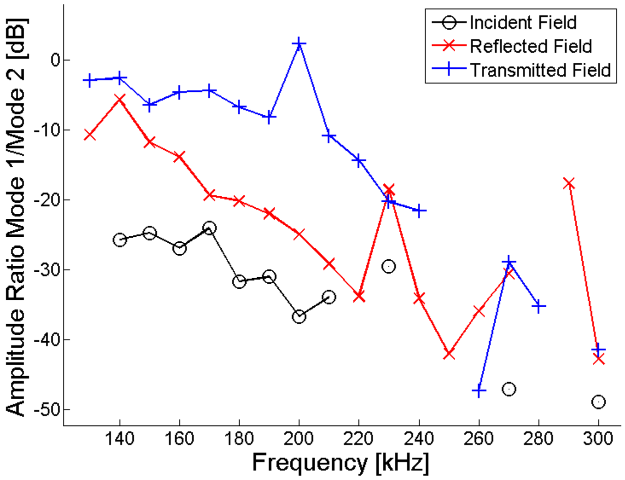

Figure 5.12: Modal amplitude ratio between Modes 1 and 2 after interaction with a notch having 50% of CE layer depth

an amplitude on the same order or magnitude as Mode 1. For higher frequencies (230 kHz - 300 kHz), Mode 5 is present in all fields, including the incident field. Mode 2 continues to be strongly reflected, but the presence of Mode 1 in the transmission field steadily decreases with increasing frequency in the inspected range.

Comparison of two modal amplitudes traveling in the same wave packet are necessarily not subject to certain measurement errors such as transducer functions, since both can be assumed to be affected equally. Therefore, figure 5.12 considers the ratio of Mode 1 to Mode 2 in each field, i.e. the amplitude of Mode 1 in the transmission field to the amplitude of Mode 2 in the transmission field and the amplitude of Mode 1 in the reflection field to the amplitude of Mode 2 in the reflection field. This figure demonstrates that, in the transmission field, the two modes have almost the same amplitude. At 200 kHz, the amplitude of Mode 1 surpasses that of Mode 2.

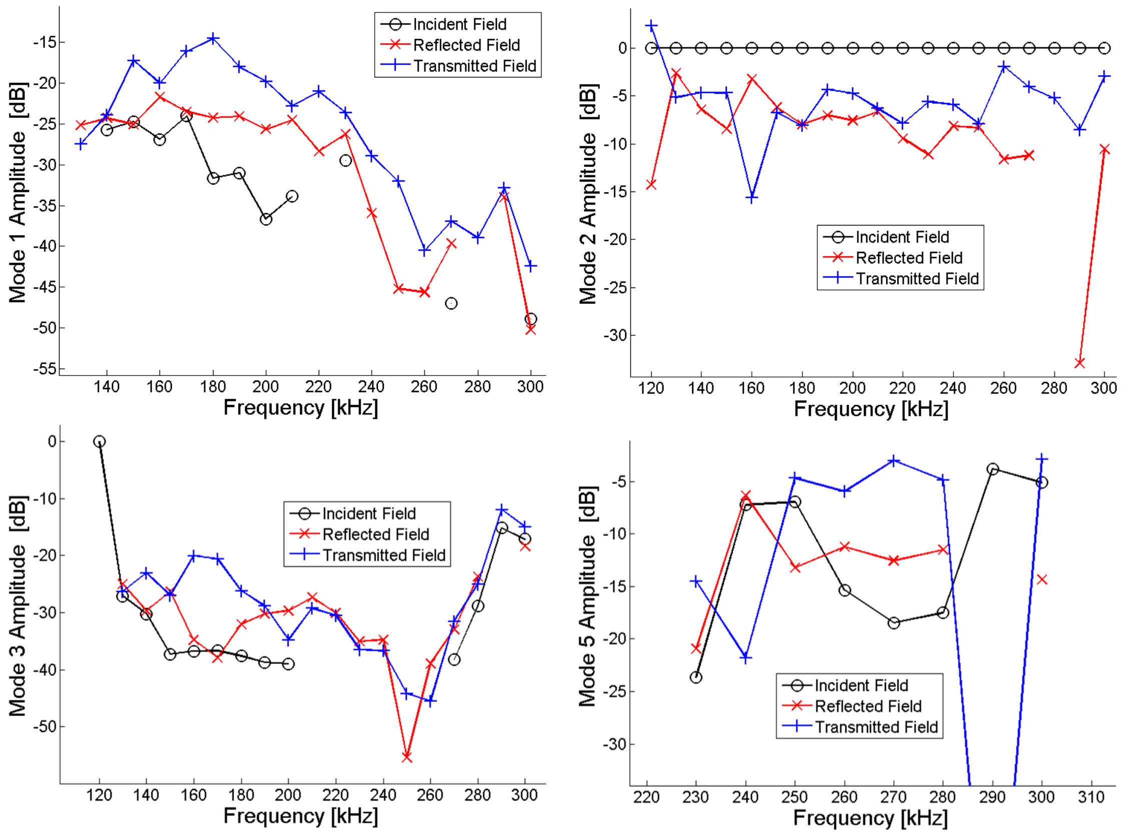

Figure 5.13: Modal amplitudes for Modes 1 (top left), Mode 2 (top right), Mode 3 (bottom left) and Mode 5 (bottom right) for all fields in the presence of a disbond type defect (1 cm)

5.2.3.3 Disbond Type Defect with Multi Element Excitation

FE models of disbond-type defects are presented in chapter 4. Here, a disbond with fixed length is examined for the purpose of optimizing its detection. The representative disbond length is chosen as 1 cm. The excitation applies a forcing function in a sinusoidal shape with a spatial frequency equal to Mode 2 at the given operating temporal frequency, as in section 2.3.2. Again, despite the strong formation of Mode 2, other modes also appear in the incident field, due to the finite length of the excitation boundary (1.5 cm).

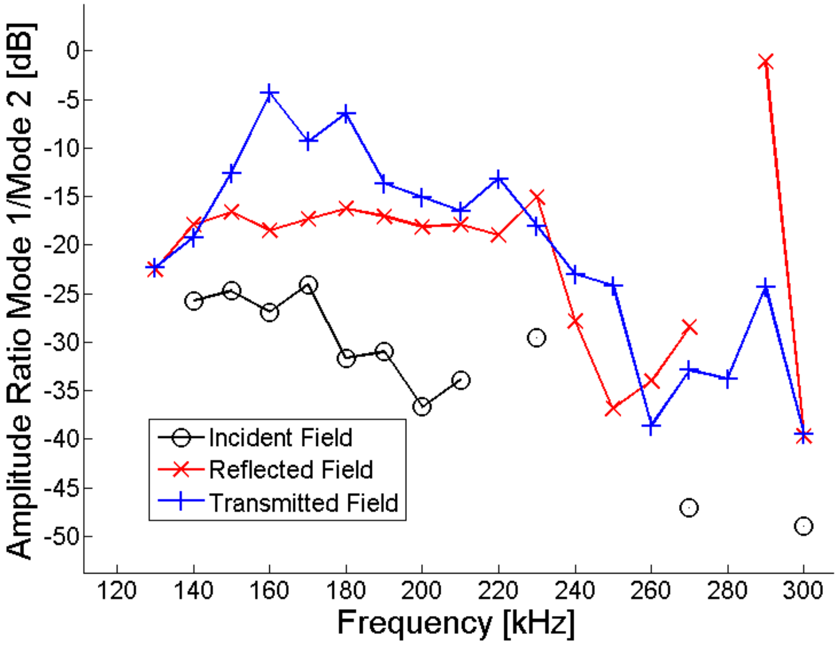

Figure 5.14: Modal amplitude ratio between Modes 1 and 2 after interaction with a disbond-type defect (1 cm)

Once again, modal amplitudes are found by taking local maximums that occur above the numerical noise floor of the wavenumber spectrum. The modal amplitudes are shown for the incident, reflection and transmission fields in figure 5.13. Amplitudes are shown on the decibel scale using the amplitude of Mode 2 in the incident field as a reference. Mode 4 is not shown due to its low amplitude across the entire frequency range of interest.

Comparison of two modal amplitudes traveling in the same wave packet are necessarily not subject to certain measurement errors such as transducer functions, since both can be assumed to be affected equally. Therefore, figure 5.14 considers the ratio of Mode 1 to Mode 2 in each field, i.e. the amplitude of Mode 1 in the transmission field to the amplitude of Mode 2 in the transmission field and the amplitude of Mode 1 in the reflection field to the amplitude of Mode 2 in the reflection field.

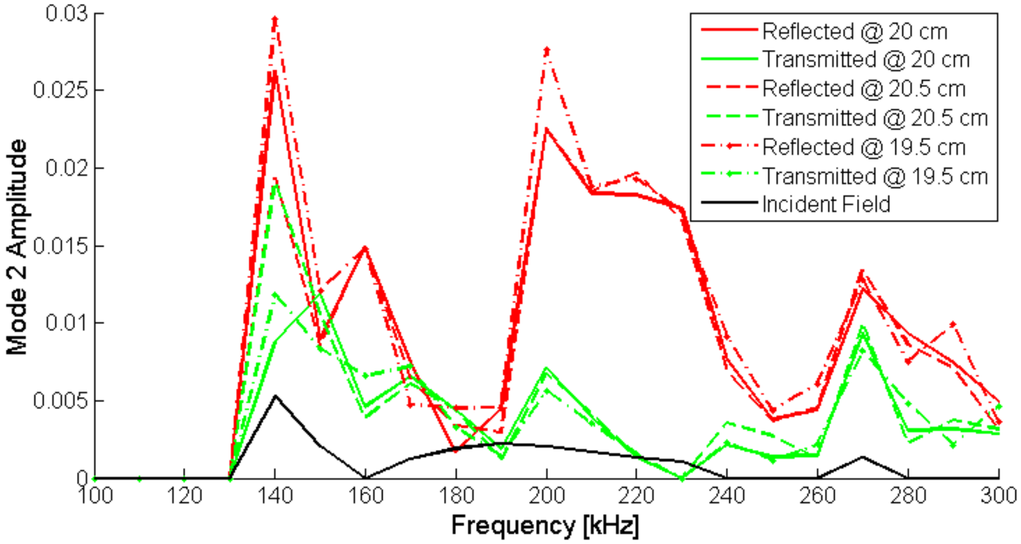

Figure 5.15: Influence of the phase of incident wavefield by comparison of three locations of a surface-originating crack modeled as a straight-edged notch.

5.3 Additional Guidelines

Observations made after FEM analysis led to questions concerning sensor placement and the relationship between time of flight and defect interaction. Therefore the following two sections are devoted to sensor placement and time of flight, respectively. Traditionally, time-of-flight measurements can be used to localize the damage location [7].

5.3.1 Sensor Placement

To investigate the robustness of our optimal frequency choice, other damage locations are simulated, so as to alter the phase of the incident wave. In a true experimental setup, the damage location would be fixed and the transducers could move, thus changing the phase of the incoming wave. However in a numerical environment the important aspect is the phase of the incident wavepacket at the moment of contact with the defect, and therefore can be realized by changing the location of the damage site.

Many damage sites were simulated, but figure 5.15 shows the resulting Mode 2 amplitude for the cases where the notch is located at 19.5, 20.0 and 20.5 cm as an example case. These three locations correspond to the case where Mode 2 changes phase by roughly a quarter wavelengths at 140 kHz and half wavelength at 200 kHz. One can note qualitatively, that despite some minimal changes, it is clear that the damage detection method is more or less robust to changes in the distance between the emitter and damage site.

The greatest amplitude change between the three methods is observable at the two frequencies that have the highest reflection coefficients, i.e. 140 kHz and 200 kHz. At 200 kHz, when the defect site is at 19.5 cm and 20.5 cm (and the incident wave is 360° out-of-phase) the result is the same, which is to be expected. However, when the incident wave is 180 degrees out of phase, the overall amplitude drops by 16%.

At 140 kHz, all three cases are roughly a quarter wavelength out of phase. The amplitude differences of 30% of these three cases is decidedly larger than at 200 kHz. However, despite these differences, one can note that the Mode 2 amplitudes as a function of frequency have similar trends, and this justly indicates a certain level of robustness in terms of changes in incident frequency. Furthermore, the observable amplitude differences that do occur may have potential in precise damage localization with respect to transducer position, especially since the reflection and transmission fields' changes are not directly proportional. For example, the reflection and transmission amplitudes are equal for the 20.5 cm case in figure 5.9 whereas the reflection amplitude is more than double that of the transmission amplitude at 20 cm.

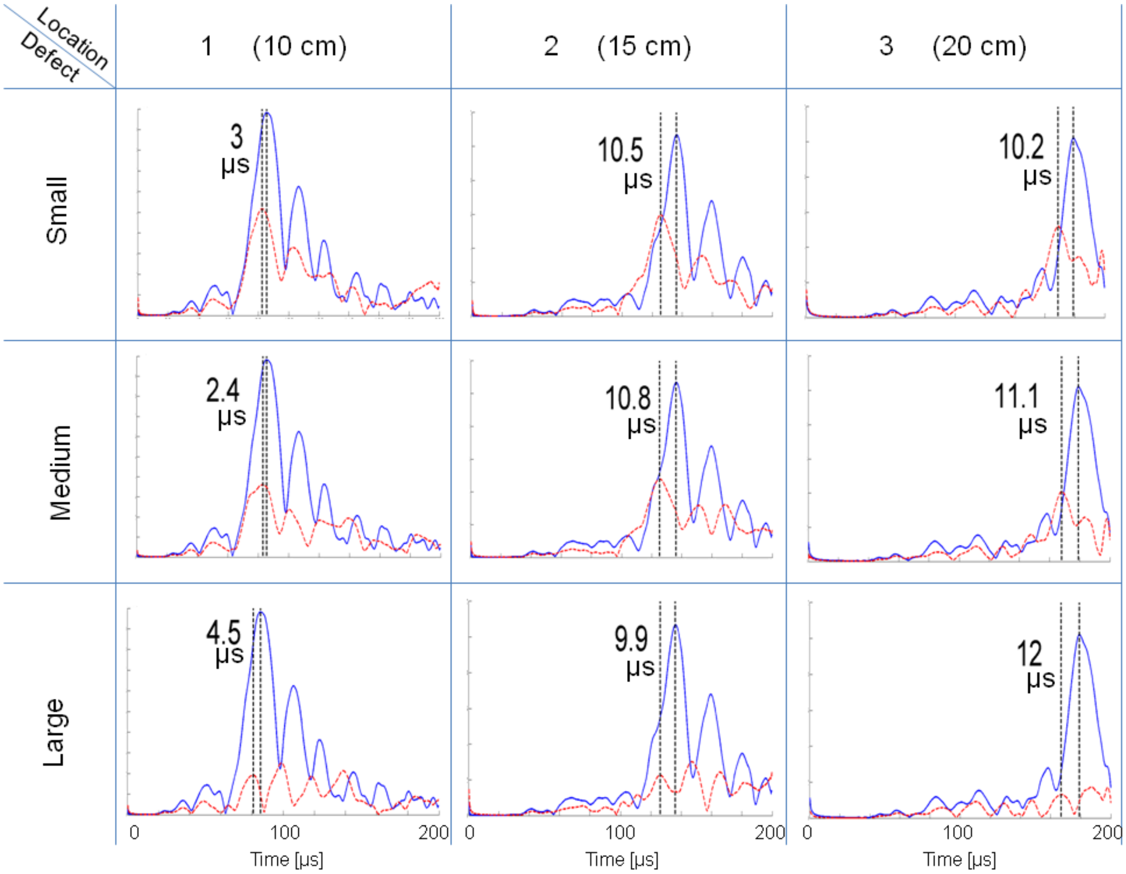

Figure 5.16: Envelope of waveform collected at three inspection points for three damage sizes. Time-of-flight measurements relative to the baseline are displayed.

5.3.2 Time of Flight

Time of flight measurements offer a method of localizing defects. It is even possible to locate damage sites within a 2D plane based on triangulation principles [8]. Although this study is not predominantly concerned with localizing defects, some work is presented here on the effect of modal conversion on time of flight measurements.

In general, time-of-flight (TOF) measurements are very difficult to make for UGW signals due to their dispersive nature. Dispersive signals tend to not only spread out in time and space, but also change phase within the wave packet, rendering wavefronts ambiguous. Consequently the TOF is defined here as being the time till the first local maximum of the principal wave packet reaches the inspection point. To illustrate, temporal domain FEM simulations were carried out for three abrasion sizes. (For a description of temporal domain FEM, see Chapter 3. For a description of the subsequent modeling of abrasions in the FEM environment, see Chapter 4.) The TOF for 3 damage sizes of abrasions [small (w = 0.85 mm, d = 0.56 mm), medium (w = 2.8 mm, d = 0.92 mm) and large (w = 8.5mm, d = 1.043mm)] are shown in figure 5.16. Three inspection points after interaction with the defect are shown [Location 1 = 10 cm, location 2 = 15 cm, location 3 = 20 cm]. Although no pattern is discernible from figure 5.16, the difficulty in measuring time of flight is apparent, since the envelopes each have several local maxima. Interaction in damage appears to give a faster time-of-flight than propagation in a healthy waveguide. In general, TOF measurements may give a general idea of location, but cannot give a precise location without further post-processing due to the fact that constructive and destructive interference is difficult to predict for multi-modal dispersive wave packets.

5.4 Summary

Optimization is necessary to find the best means of excitation and reception, frequency range, and modal selection to identify the presence of a given damage type. In this chapter, the optimization of certain parameters to detect surface originating cracks and disbonds is presented, however the procedure presented here has relevance beyond the example damage type simulated. It is shown that a single element shear contact transducer is more efficient at propagating UGW in the given thick composite plate-like structure than a single element longitudinal transducer.

Due to the large modal displacement at the surface, and its relatively smaller wavelength, it is suggested by this work that Mode 2 is the best choice for investigating mode. A drastic change in the amplitude of Mode 2 was identified in the transmission field at around 170 kHz - 220 kHz for interaction with notch type defects. This change, although slightly dependent on the incident phase, was more or less robust to the distance between the emitter and damage site. Furthermore it was seen that Mode 1 has an amplitude considerable to that of Mode 2 in the direction perpendicular to the surface of the structure in the transmission field. Therefore modal amplitude comparison is recommended to be used as a means of damage identification. However, it was also seen that time of flight measurements may not give accurate localization information without rigorous post-processing dispersion compensation.

5.5 References

[1] A. Demma, P. Cawley, M. Lowe, A. Roosenbrand and B. Pavlakovic, "The reflection of guided waves form notches in pipes: a guide for interpreting corrosion measurements"," *NDT&E International,* vol. 37, pp. 167-180, 2004.

[2] M. B. Drozdz, "Efficient Finite Element Modelling of Ultrasound Waves in Elastic Media," Imperial College, London, 2008.

[3] D. Alleyne and P. Cawley, "The Interaction of Lamb Waves with defects," *IEEE,* vol. 39, pp. 381-397, 1992.

[4] M. Lowe, *Disperse (software),* London; Imperial College: http://www3.imperial.ac.uk/nde/products%20and%20services/disperse, 1997.

[5] Comsol, "COMSOL Multiphysics User’s Guide," version 3.3, 2006.

[6] D. N. Alleyne and P. Cawley, "A two-dimensional Fourier transform method for the measurement of propagating multimode signals," *Journal of the Acoustical Society of America,* vol. 89, no. 3, pp. 1159-1168, 1991.

[7] J. L. Rose, Ultrasonic Waves in Solid Media, Cambridge, U.K: Cambridge University Press, 1999.

[8] J. S. Hall, "Adaptive dispersion compensation and ultrasonic imaging for structural health monitoring," Georgia Institute of Technology, Atlanta, Georgia, 2011.

[9] M. Drozdz, L. Moreau, M. Castaings, M. Lowe and P. Cawley, "Efficient numerical modelling of absorbing regions for boundaries of guided waves problems," *Review*

of Qualitative Nondestructive Evaluation, vol. 25, pp. 126-133, 2006.

[10] T. E. Michaels, J. E. Michaels and M. Ruzzene, "Frequency-wavenumber domain analysis of guided wavefields," *Ultrasonics,* vol. 51, pp. 452-466, 2011.

[11] D. Worlton, "Experimental confirmation of Lamb waves at megacycle frequencies," *Journal of Applied Physics,* vol. 32, no. 6, pp. 967-971, 1961.

[12] L. J. Jacobs and M. Niethammer, "Time-frequency representation of Lamb waves using the reassigned spectrogram," *Journal of the Acoustical Society of America,* vol. 107, no. 5, pp. 19-24, 2000.

CHAPTER 6

EXPERIMENTAL STUDIES

6.1 Introduction

The focus of this work has been to investigate the propagation of UGW in a thick-walled COPV intended for hydrogen storage, for the purpose of SHM. Chapters 3, 4 and 5 have carried out this investigation by means of the FEM. This aforementioned work was verified to agree with analytical predictions based on material properties supplied by our industrial partners. The developed models exploited simplifications based on assumptions that were either made in accordance with previous work (see Chapter 1) or investigated and verified theoretically (see Chapter 2).

The experimental work presented here has three main objectives, namely to:

- Inform modeling work by providing sample specific measurements (see Chapters 3, 4 and 5)
- Validate modeling work (see Chapters 3, 4 and 5)
- Provide future researchers (e.g. industrial partners) with an experimental set-up and procedure

It should be noted that this experimental work is not necessarily presented chronologically in the context of the rest of this thesis work. The first point was carried out before modeling work commenced, and validation was mainly performed after.

6.2 Determination of Layer Thicknesses

The thickness values used in the FEM models of the COPV (see chapters 3, 4 and 5) are chosen based on time of flight measurements, rather than nominal values supplied

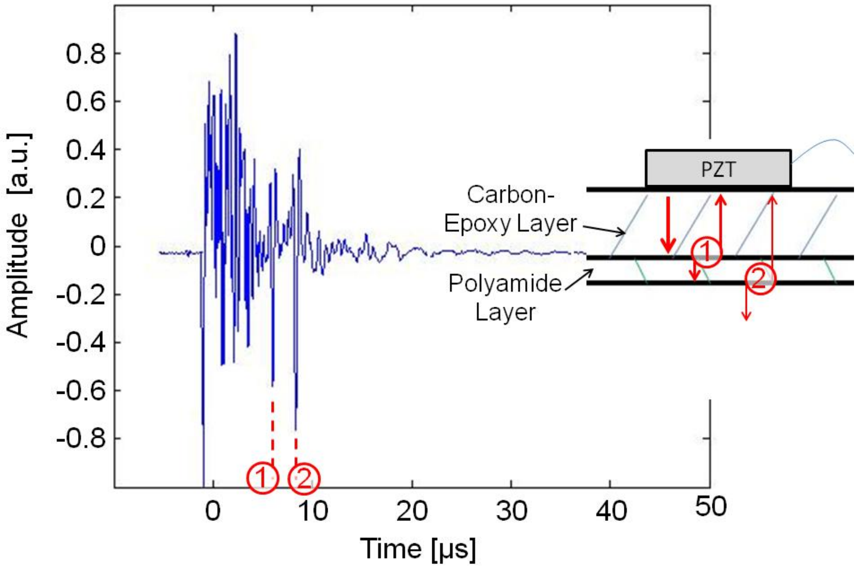

Figure 6.1: Schematic demonstrating the thickness tests. Waveform 1 is the result of the reflection from the first interface, and waveform 2, from the second.

by industrial partners. Thickness values for the two layers can be calculated knowing the material properties and the pertinent time of flight measurements [1].

6.2.1 Experimental Setup

Bulk waves are excited via a contact transducer in pulse-echo mode. A bulk longitudinal mode is excited that reflects first off the interface between the orthotropic and isotropic liner and then off the inner surface of the tank (see figure 6.1). A short pulse is necessary in order to cleanly distinguish different wave packets and consequently different arrival times. Since the modes resemble classic bulk waves, dispersion is minimal. Higher frequencies correspond to smaller wavelengths, and coincidently higher resolution for time-of-flight measurements. Therefore, a contact transducer with the highest frequency available in the L.U.N.E. facilities is used. The transducer is a

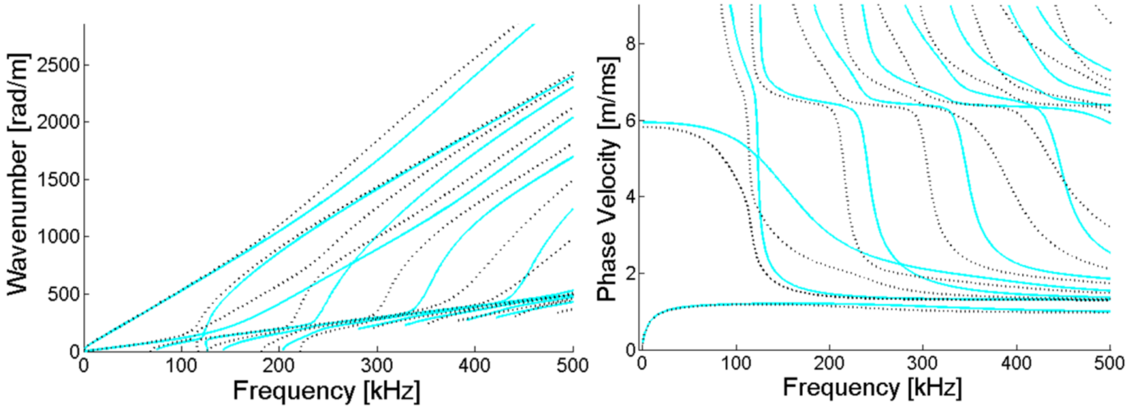

Figure 6.2: Comparison of dispersion curves calculated with nominative thickness values (blue solid) and values calculated from time of flight measurements (black dotted)

commercially-available model (Panametrics model V103) and is rated as having a central frequency of 15 MHz.

6.2.2 Time of Flight Results

Figure 6.1 shows the waveform received with a 15 MHz rated transducer in pulse-echo mode on the surface of the bilayer vessel, where the two wavepackets identified are resultant from interaction with the two interfaces. The carbon-epoxy layer thickness is calculated to be 7.85 mm and the isotropic polyamide layer thickness is 1.39 mm based on material properties reported in Chapter 2. These thickness values are more sample specific, and therefore more valid for the 2.5 L tank available for this work.

The analytical dispersion curves based on the new thicknesses (calculated via Disperse) are shown in figure 6.2. Two sets of curves are shown in the figure. The black dashed line denotes the theoretical dispersion curves calculated with the nominal thicknesses, and the solid blue line denotes the dispersion curves for the lay-up with the thicknesses calculated via time-of-flight measurements. The curves are notably different (for every mode), supporting the decision to use sample-specific thickness values.

6.3 Experimental Extraction of Dispersion Curves

6.3.1 Background

Dispersion curves obtained *in situ* at the time of testing can be more accurate than curves that are calculated numerically or analytically with assumed or measured parameters since they are sample specific. Several methods have been developed to extract dispersion curves from experimental data. Specifically, three methods, i.e. the Two-Dimensional Fourier Transform (2DFFT), the Model Based Parameter Estimation (MBPE) method, and Time-Frequency Representations (TFR) such as the Short-Time Fourier Transform (STFT) [2] have all been shown in previous work to provide dispersion curves with varying amounts of input information and computational efforts [3, 4, 5].

Alleyne *et al*. have shown in previous work that the 2DFFT is a method of measuring Lamb wave velocities [3]. In this approach, a Fourier transform is applied to data recorded in regular spatial and temporal intervals to simultaneously determine temporal and spatial frequency content. This technique gives a two-dimensional graphical output that allows for the visualization of all propagating modes at discrete wavenumber-frequency bins. It has previously been used not only on experimental received data to resolve various modes that may or may not have separated in time [6, 7], but also in numerical simulations, for example to determine the amplitude of mode conversions caused by damage [8]. The 2DFFT is discussed in further mathematical detail in chapter 3, section 4.2.2.

TFR's are capable of investigating frequency content as a function of time. Within the classification of TFR's, there exist many variations which boast different strengths and weaknesses, many of which deal with the manner that the specific TFR method resolves time and frequency. The Heisenberg uncertainty principle disallows the ability for perfect resolution in both the time and frequency domains simultaneously [2]. Instead the time-frequency tiling, i.e. the format of the resolution relationship between the two complimentary parameters, often determines how effective each TFR method is at extracting dispersion curves. Hong *et al*. [9] discuss how the rigidity in time-frequency tiling imposed by the conventional STFT is not always as effective in determining the wave velocity of dispersive signals as a TFR method that allows for a flexible time-frequency tiling such as the Continuous Wavelet Transform (CWT), since CWT time-frequency tiling can be modified based on the dispersive characteristics of the wave. Furthermore, within the CWT, different mother wavelet series can be used [10]. Li *et al*. [11] describe a process that determines the most effective mother wavelet series by comparing the Shannon entropy of wavelet coefficients. Niethammer *et al*. [12] have a very good discussion of the strengths and weaknesses of four different TFR extraction methods, in which they find that a method based on the STFT is extremely effective in cases where more than one Lamb mode is present in the signal. Many authors have reported using various TFR in the past with promising results [13, 14, 15]. Grondel *et al*. even used a relationship between the 2DFFT and STFT to identify modes in signals [16]. However, to the author's knowledge, TFR techniques can only give dispersion curves with respect to c_g (for further information, see Chapter 2, section 2.2).

Hall and Michaels developed the MPBE method in order to simultaneously estimate many different parameters of a signal, namely dispersion curves, propagation loss, propagation distances, transmitted signal and mode weighting coefficients [4]. The algorithm can operate with limited *a priori* information, and is based on an assumed model of wave propagation and the differences in phase between three or more received signals.

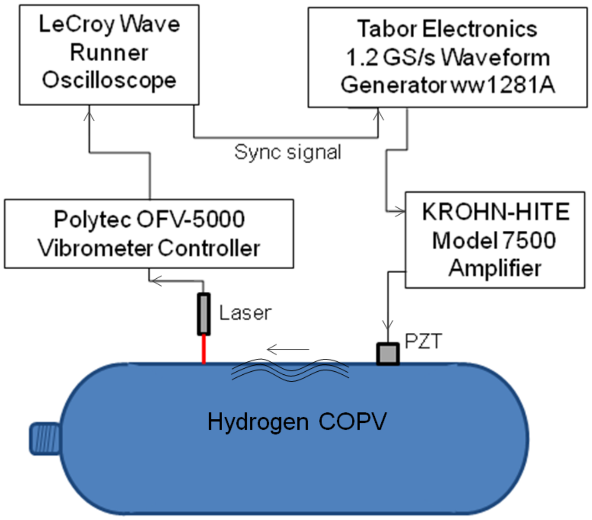

Figure 6.3: Schematic of the electronic equipment for the experimental setup

6.3.2 Application to COPV

Experimental tests are performed on two specific samples: an aluminum plate and a bilayer composite tank (see Chapter 1, figure 6.1). The aluminum plate is simpler, structurally speaking, and can be used to bench-mark the technique and equipment performance. Some results will be shown for the aluminum plate to help clarify the experimental procedure. However, the following section will detail the experimental setup for the bilayer hydrogen reservoir, being the more interesting of the two cases. The experimental setup for the aluminum plate is similar, and therefore omitted for brevity.

6.3.3 Experimental Set-up

A general schematic of the electronic equipment used is shown in figure 6.3. A function generator is used to supply the excitation function, so as to have a sinusoidal type excitation at frequencies besides the characteristic frequency of the transducer. The excitation transducers employed in this work are single component (non-array), contact transducers, due to availability. Commercially available contact transducers complete with internal electronic connections and dampening backing material with a central frequency of 1MHz are primarily used in this work. This is due to their high signal-to-noise ratio (SNR), and flexibility and breadth in terms of frequency range. As per section 3.2, shear mode transducers are employed, with the surface displacement parallel to the axis of the hydrogen reservoir.

The transducers have the possibility to be glued to the vessel with a permanent adhesive. This has two specific advantages: not only will the PZTs be permanently and rigorously attached, but the adhesive itself can act as a coupling medium. However, in the experimental setup presented here, the transducer is attached by means of electrical tape and/or rubber bands, so that the transducers can be easily detached. The couplant is a water-based gel commonly used in medical ultrasound applications.

In order to resolve various modal components from a single received wave packet, temporal waveforms can be detected at spatial intervals, known commonly in NDT as a B-scan. A 2DFFT can be performed on a B-scan to display the square root of the spectrum (on a linear scale) in the dual wavenumber-frequency space (see Chapter 3, section 4.2.2), essentially separating the modal components. Most electronic equipment offers a very high level of accuracy in the temporal domain. However, the stringent necessity for precision and accuracy in the spatial domain requires the use of either a multi-element transducer array or a robotic scanning system. Although the multi-element transducer is much more attractive option for SHM, a robotic scanning system is used in this work due to its flexibility in scanning parameters and availability.

Whereas the robot C-scanner itself offers a high level of precision, the difficulty in performing such a scan lies in the obligatory non-contact methods. Air-coupled

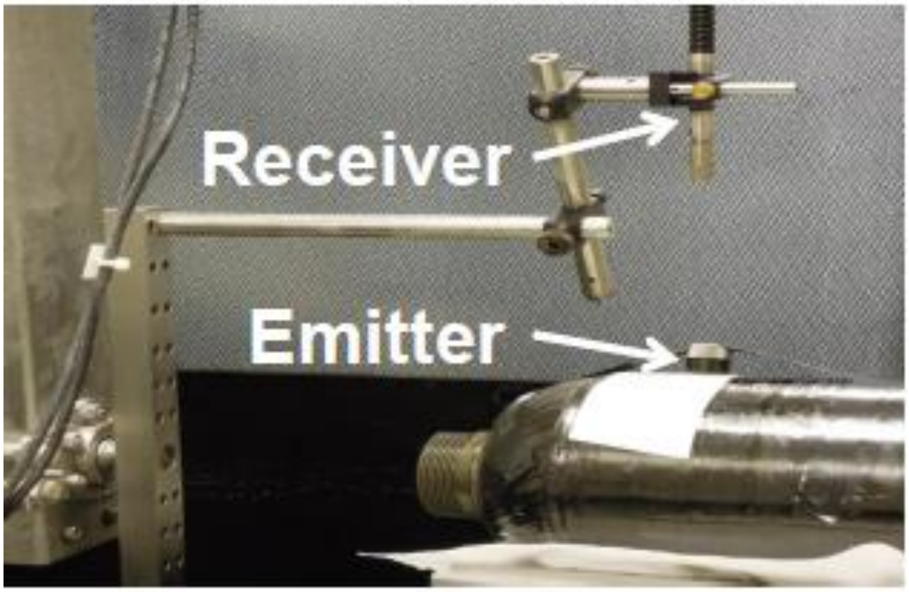

Figure 6.4: Photograph showing the experimental arrangement: the piezoelectric transducer acts as the emitter, and the laser vibrometer is the non-contact receiver.

transducers do not offer a satisfactory SNR. Instead, a laser vibrometer, measuring out-of-plane surface velocity, is employed. Reflective tape is used to increase the amount of light scatter from the surface of the reservoir, and accordingly boost the SNR. The laser head acting as a receiver attached to the robotic arm can be seen in figure 6.4.

6.3.4 Experimental Procedure and Validation of the Process

An aluminum plate was chosen as a test specimen for its simplicity. Aluminum material properties are well-documented, and it has the benefit of being isotropic. Furthermore, metals tend to support wave propagation very well, and not much energy is lost due to material dampening. The plate used in the experimental setting is 300 mm x 210 mm, and is 0.8 mm thick. B-scans are performed on the aluminum plate, which demonstrate not only the ability to excite and detect waves at various propagation distances, but also

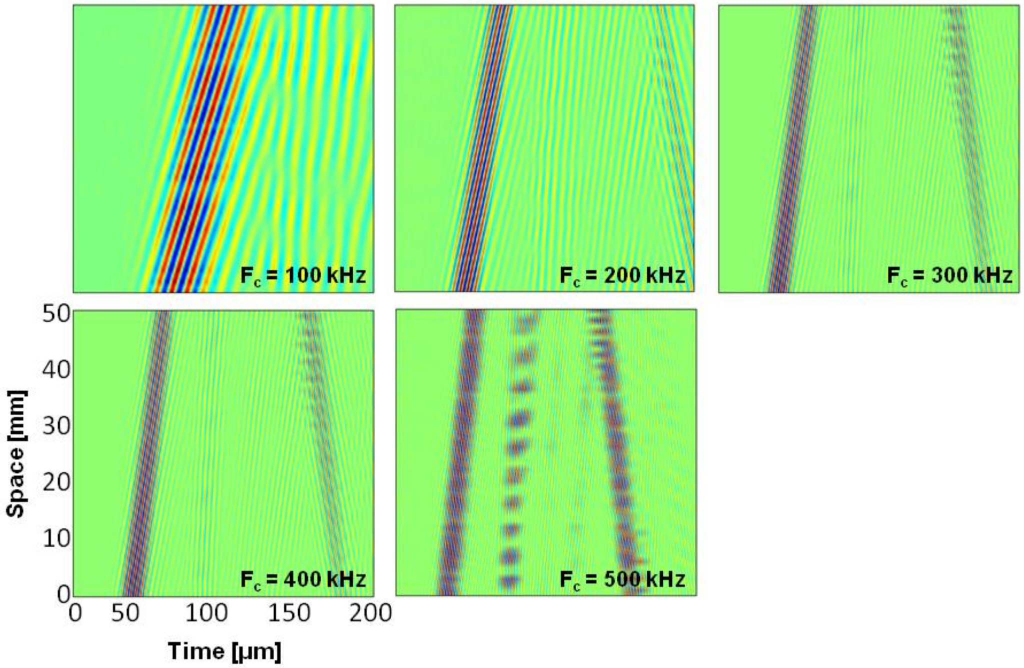

Figure 6.5: Experimental data collected from the aluminum plate for the five central frequencies used: 100 kHz, 200 kHz, 300 kHz, 400 kHz, and 500 kHz.

verifies correct equipment setup for the purpose of experimental dispersion curve extraction.

The B-scans were collected by attaching the laser-vibrometer to the robotic arm of the polar C-scanner. Excitation was achieved by use of commercially available contact Panametrics transducers, model type V153. The central frequency for the transducer used is 1 MHz and the diameter is 0.5 inches. This specific model of transducer is known for being broad-band, and able to excite (or detect in reception mode) shear waves, which means that viscous coupling gel that can support shear wave motion must be used. The couplant gel used is a thixotropic, water soluble gel produced by Sofranel. Five trials are carried out, each consisting of a three-cycle sine wave centered at five different center frequencies, namely 100 kHz, 200 kHz, 300 kHz, 400 kHz and 500 kHz.

Modeling clay is used to support the plate at the four corners, as well as attached to the borders of the aluminum plate in an attempt to dampen unwanted reflections from edges.

The starting point for the B-scan is 80 mm away from the center of the PZT, which is more than ample space for the Lamb waves to become fully formed, *i.e.* all measurements are carried out in the far-field. Each scan collects 51 points, traveling from the starting point of ‘0’ to an end point 5 cm away, with waveforms being collected every 1 mm. Averaging was set to 256 to decrease equipment electrical noise. It is worth noting that this satisfies the sampling frequency theorem resolution requirements, which in practical terms means using a resolution with a corresponding Nyquist frequency higher than any expected wavenumber in the analyzed signal [17].

The raw data collected from all five B-scans are shown in figure 6.5. The signals were treated afterward by applying a narrow band pass filter that was selected as a function of the central excited frequency f_c (not to be confused with the central frequency response of the transducer). The high pass portion has a cut-off at f_c - *75 kHz* and the low pass portion has a cut-off at f_c + *75 kHz*. The forward propagating, direct arrival waves are Hanning-windowed in time. The signals are also Hanning-windowed in space to limit the amount of spectral leakage in the wavenumber domain. The algorithm of signal post-processing is depicted in figure 6.6.

Next, the treated signals are converted into the wavenumber-frequency space via a 2DFFT; the results are displayed in figure 6.7. Theoretical dispersion curves computed with Disperse ® are superimposed in black to show agreement. One can note that there is an excellent level of agreement between the stronger mode with a higher wavenumber, corresponding to the fundamental antisymmetric mode. The agreement is still good but somewhat less satisfying for the fundamental symmetric mode, which

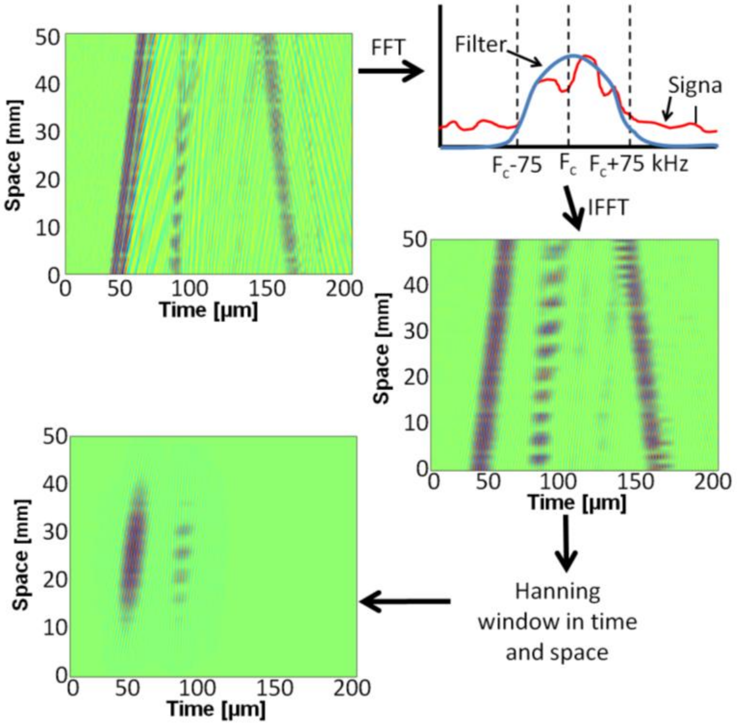

Figure 6.6: Depiction of the algorithm for post processing experimental data. Data from the case where F_c = 500 kHz is taken as an example.

propagates at lower wavenumbers, and appears with lower amplitude in the signal. The discrepancy becomes noticeable below 300 kHz, when the mode has a wavelength of $\lambda = {}^{2\pi}/_{k} \sim 1.5\ cm$. Several factors could play into the difference, including the material properties used to calculate the theoretical dispersion curves or slight changes in plate thickness. Despite this, the experimental results are considered to validate the experimental procedure to extract dispersion curves. All five wavenumber-frequency domain representations are displayed on the same figure for the ease of the reader in figure 6.7 (bottom right-hand corner).

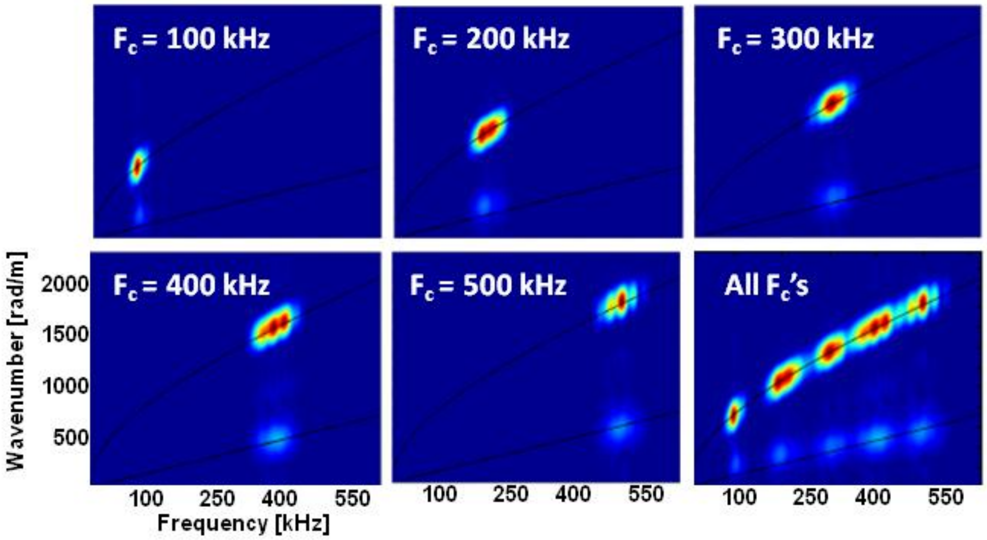

Figure 6.7: Bscans from figure 6.5 displayed in the frequency-wavenumber space. Analytical dispersion curves are superimposed to show agreement. All five wavenumber-frequency domain representations are superimposed on the same plot (bottom right).

6.3.5 Analysis of Aluminium Plate Results

Two phenomena are worthy of note from the UGW excitation and reception in the aluminum plate. First, modes traveling at different speeds are sometimes resolvable in the time domain because they may separate into different wave packets. However, if evenly spaced waveforms are collected at intervals that respect the sampling frequency theorem requirements, modes are always separable in the wavenumber-frequency domain. To illustrate, the difference in wavespeeds for different modes, one can note that the second wave-front appearing in figure 6.14 corresponds to the S_0 mode, and appears to move faster than the first wave front corresponding to the A_0 mode (despite having a later arrival time). In fact the later arrival time of the S_0 mode is attributed to it not being a direct arrival from the transducer, but rather due to modal conversion occuring at the edge of the plate.

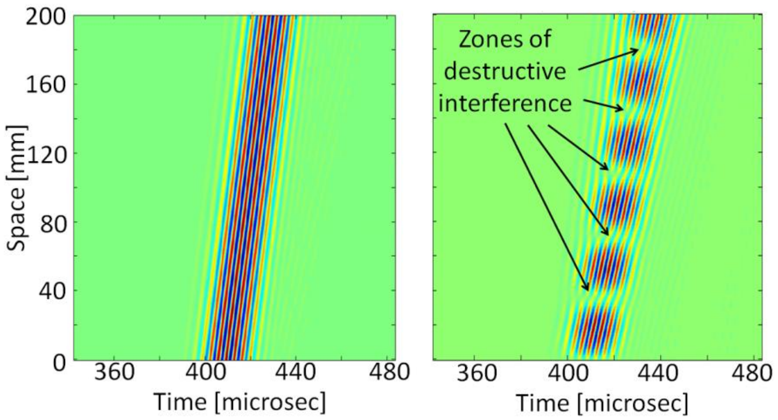

Figure 6.8: B-scan images (waveform in time and space) for an incident S_0 mode for the transmission field after the notch location for the case when (left) no notch is present and the S_0 mode continues propagating undisturbed through the region, and (right) a notch depth of 40% plate thickness was encountered and subsequently the incident S_0 mode was subject to transmission loss and mode conversion into the slower traveling A_0 mode.

The second phenomenon is most visible when f_c = 500 kHz. At this frequency, one can note alternating regions of constructive and destructive interference as two modes pass through each other. This phenomenon has also been observed in FEM simulations as illustrated in figure 6.8, which represents two B-scans obtained in an aluminum plate. The left hand side corresponds to the case of a healthy plate, and the right-hand side is the transmission field after interaction with a notch with a depth equal to 40% of the plate thickness. The incident Lamb mode used is an S_0 mode. After interaction with the notch, mode conversion occurs, and the A_0 mode and S_0 mode travel in the same wave packet. However, their difference in wavespeeds results in zones of destructive and constructive interference.

Interference phenomena can significantly impact the results of damage detection. In the FEM result presented here, if the sensor was in a destructive zone, the acquired amplitude would be near zero. This may cause technicians to assume that there is

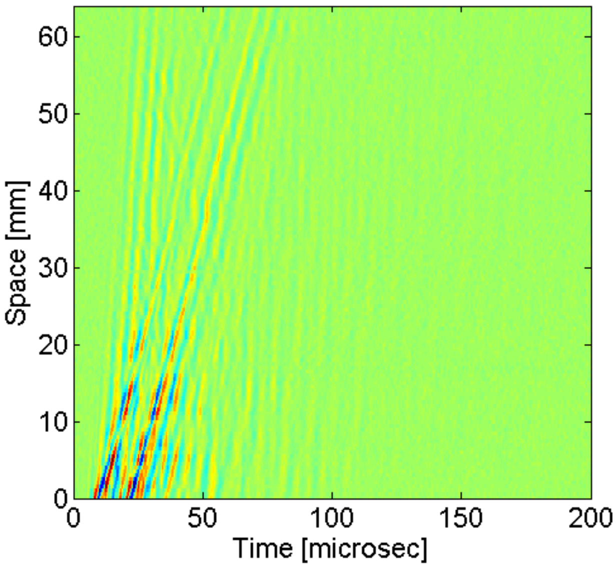

Figure 6.9: Experimental results for bilayer reservoir displayed in time-space domain. Samples were recorded along the axial (x) direction at 0.5 mm increments.

either a 100% rupture in the tank preventing the signal from reaching the sensor, or that the sensor is broken. Likewise, if the sensor is placed in a zone of constructive interference, the defect may go unnoticed, despite it being 40% of the original wall-thickness. To overcome this problem, it is important to have enough sensors so as to be able to properly resolve the present modal amplitudes. Even relatively small defects can be detected if proper post-processing techniques are employed [18].

Note that this interference phenomenon due to waves / defect interaction depends on various parameters such as wavelength (frequency), incident wave mode, defect shape and size, etc. The case where A_0 is the incident mode has also been modeled; the interference phenomenon exists, but is much less significant than the case of S_0 incidence, and is so omitted here. These experimental and numerical examples highlight the benefits of employing the FEM to help understand propagation physics, and optimizing NDT and SHM processes by guided waves.

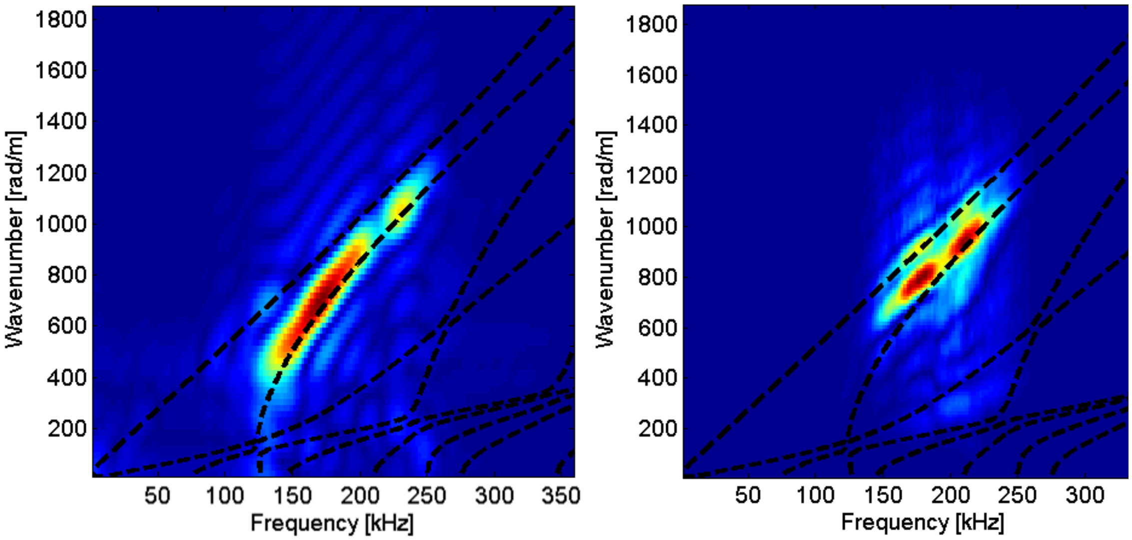

Figure 6.10: Theoretical dispersion curves (dashed lines) superimposed to frequency-wavenumber representations: numerical results (left), and experimental results (right).

6.3.6 Application to a Composite Vessel

Having successfully benchmarked the procedure and equipment used in the previous section, the same procedure was applied along the axial direction of the bilayer hydrogen reservoir. Using the contact transducers as a means of excitation, and the laser vibrometer attached to the arm of the polar C-scanner as a receiver, a series of evenly spaced waveforms was collected along the axial direction. The spacing used is 0.5 mm, again sufficient to satisfy the sampling frequency theorem resolution requirements. B-scan results are presented in figure 6.9.

The frequency-wavenumber representation of the waveform collected along the axial direction is displayed in figure 6.10 (right) as well as the frequency-waveform representation of the healthy finite element results from Chapter 3, (left) for comparison. Theoretical dispersion curves calculated using Disperse match reasonably well with the

Figure 6.11: Impact defects I1 (top), I2 (bottom left) and I3 (bottom right) on the three layer 2.5 L reservoir.

excited and received wave modes both in the numerical FEM environment (left), and the experimental setup (right). As predicted with the finite element model, Mode 2 is the principally propagating mode. The error in predicted wavelength at the central excitation frequency (200 kHz) between the two numerical methods is less than 5%. However, the error in wavelength between the FEM results and the experimental work at 200 kHz is less than 1%.

6.4 Damage Detection

Experiments concerning damage detection are carried out in a 2.5 L reservoir similar to that used in the previous section. However, this hydrogen reservoir has three layers instead of two due to the limited supply of damaged samples available. The third layer consists of a macroscopically orthotropic glass-epoxy layer. Its thickness is approximately 2 mm. The principal directions of the glass-epoxy layer are aligned with

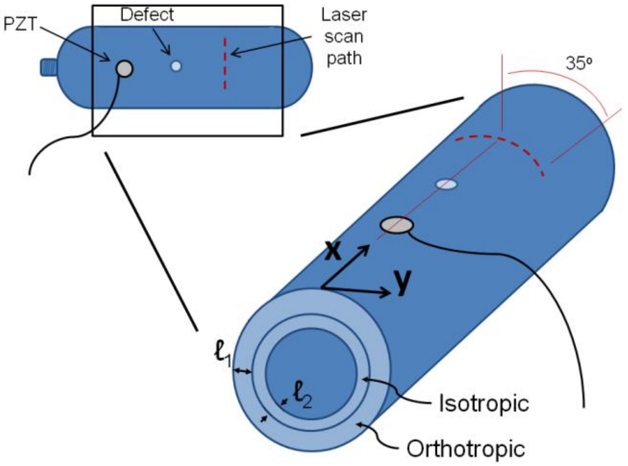

Figure 6.12: Schematic showing the sensor and the defect placements, and the laser scan path.

those of the carbon epoxy layer, so the overall layup remained macroscopically orthotropic. Three damage sites, labeled I1, I2 and I3 were created by a third party and can be seen in figure 6.11. All three damage sites were induced by means of controlled impact tests.

Excitation is achieved similarly to the previous tests for dispersion curve extraction in the 2-layer reservoir. A contact piezo-electric transducer is attached to the outer surface of the glass-epoxy layer by means of rubber bands. This transducer is rated for use from 50 kHz to 400 kHz, but has the highest frequency response between 100 kHz and 150 kHz. The coupling medium is a water-based gel commonly used for medical ultrasounds. The receiving mechanism was a laser vibrometer measuring out-of-plane velocity. The laser head was attached to the polar C-scanner. The excitation function was a 5-cycle sinusoidal burst. Five operating frequencies were tested, i.e. 100 kHz, 150 kHz, 200 kHz, 250 kHz and 300 kHz.

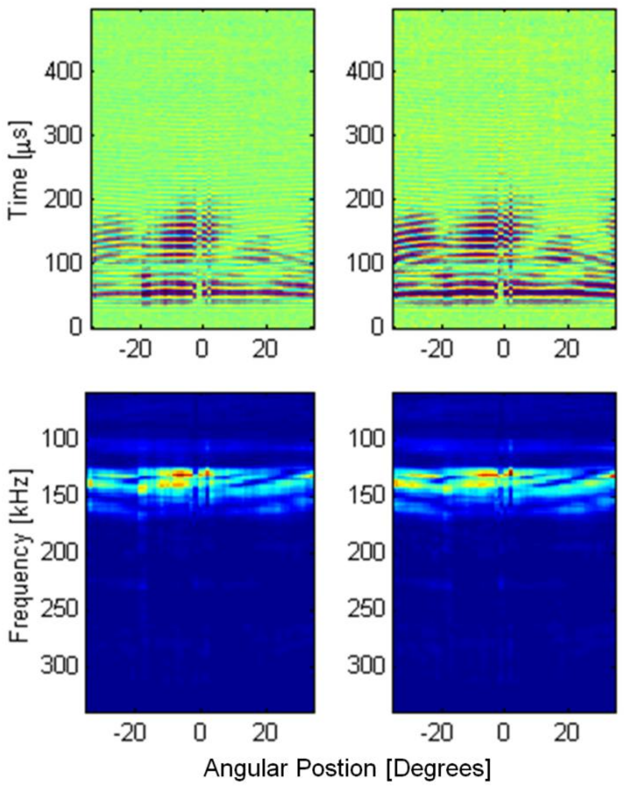

Figure 6.13: Transmission field data after interaction with damage site 'I3' with an operating frequency of 150 kHz. Top left: raw circumferential B-scan data. Bottom left: Spectrums of raw data. Top right: Circumferential B-scan data normalized with respect to the maximum position in each temporal waveform. Bottom right: Spectrums of normalized data.

All three damage sites are investigated, as well as a stretch of tank that had been deemed "healthy". B-scans were performed circumferentially along an arc length path 70^o long, centered on the x-axis as shown in figure 6.12. The x-axis also intersected the center position of the excitation transducer and the center of the defect site.

The results for the B-scan performed on the I3 damage site (i.e. the smallest one) are shown in figure 6.13. The upper left-hand image is the collection of temporal waveforms displayed as a function of circumferential position. Again, the center position, 0 degrees, corresponds to position in line with the defect so any direct arrival must pass through the damage site. The lower left hand image is the spectrum as a function of circumferential position. Note that the operating frequency was 150 kHz, but the spectrum has shown the strongest results slightly below this value in correlation with the frequency response function of the excitation transducer. Upon first inspection, it appears that there are at least two separate wave packets corresponding to two UGW modes. The first seems to have an arrival time around 50 microseconds and appears relatively independent of theta. The second however, appearing just after 100 kHz, arrives earlier along the edges of the scanned area, with the latest arrival time appearing at the central 0 degree position. This time of flight anomaly, although impossible in isotropic materials, can be attributed to the anisotropic material properties. That is to say that wave speed is a function of propagation direction.

One can note in the top left circumferential B-scan that there is an amplitude drop occurring near 0^o. Upon first inspection, it is unclear if this is caused by the presence of the defect, or is caused by a lowering in the signal strength of the laser vibrometer that is a function of reflectivity and therefore is prone to change with position. Therefore, each temporal waveform S_θ is normalized with respect to its highest amplitude, as described in the following equation:

$$\mathrm{S}_\theta^{\mathrm{n}}(\mathrm{t}) = \frac{\mathrm{S}_\theta(\mathrm{t})}{\max\left[\mathrm{S}_\theta(\mathrm{t})\right]}, \tag{6.1}$$

where *t* and *θ* are respectively the time and the angle of acquisition.

Although this post-processing technique cancels out the effect of transmission loss through the defect, it should highlight changes in the waveform arrival time and/or mode conversion that may occur at a given position. The results are displayed in the top right hand corner of figure 6.13. From this figure, it is clear that there is definite mode

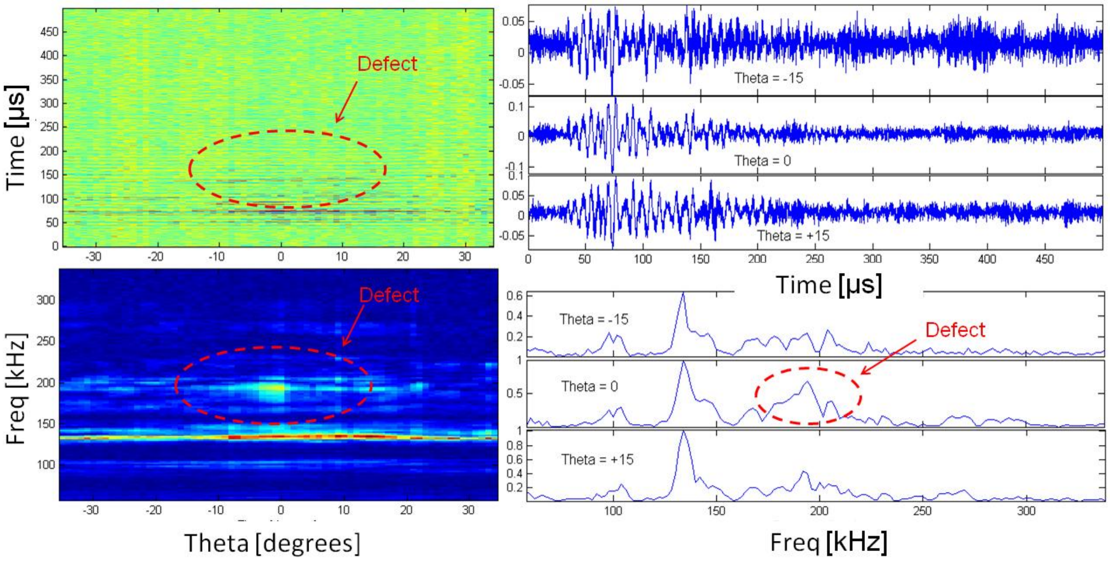

Figure 6.14: B-scan image (top left) and its correspondent FFT amplitudes (down left). A-scan waveforms (top right), and their correspondent spectrum, at three different angles, θ = -15, 0 and 15 degrees.

conversion occurring, as well as an overall time of flight delay, since the faster mode amplitude is still significantly lower, and the second arrival packet is present but not in phase. Although it is difficult to ascertain the exact modal amplitudes without more information in the axial direction to perform a 2DFFT, it is clear that this damage site could potentially be identified via through-transmission modal conversion.

Figure 6.14 shows a polar B-scan image (i. e. signal amplitude versus radial position) (top left) and its corresponding temporal Fourier transform (lower left), as well as three A-scan waveforms (top right) at three different angles, and their corresponding spectra (lower right). On the B-scan image, a wave packet can be seen at a time of flight equal to 150 µs. This wave packet may be due to the interaction of propagating waves with the defect site, and the generation of a specific mode. The width of the wave packet extends from -10 degrees to 10 degrees where the center of the defect is localized at 0 degree. This can be explained by the interaction between the defect and the transducer beam. Three waveforms, collected at -15 degrees, 0 degree, and 15 degrees, are plotted separately.

From figure 6.14, it can be deduced that some modal conversion is occuring, resulting in the second wave packet in the direct transmission zone after the defect. For further analysis, the FFT of the B-scan is plotted as well (lower left). In the frequency domain it appears that the modal amplitude is linked to modal conversion occuring at slightly less than 200 kHz. However, overall amplitude increases as well for the wave packet at 140 kHz after interaction with the damage site.

6.5 Summary

Experimental work was presented that corroborates and utilizes the optimization findings (which was the primordial aim of this work), first on an aluminum plate to justify the experimental setup and then on a multi-layer vessel intended for housing hydrogen at high pressures. Impact defects have been used to verify the ability to detect damage via modal conversion. This experimental example argues that a SHM method utilizing UGW is a good candidate for testing and / or monitoring composite vessels, and thus contributes to the safety of hydrogen storage.

6.6 References

[1] D. T. Blackstock, Fundamentals of Physical Acoustics, Canada: John Wiley and Sons, 2000.

[2] M. Niethammer, L. J. Jacobs, J. Qu and J. Jarzynski, "Time-frequency representations of Lamb waves using the reassigned spectorgram," *Journal Acoustical Society America,* vol. 107, pp. L19-L24, 2000.

[3] P. Cawley and D. N. Alleyne, "A two-dimensional Fourier transform method for the meausrement of propagating multimode signals," *Journal of the Acoustical Society of America,* vol. 89, no. 3, pp. 1159-1168, 1991.

[4] J. S. Hall and J. E. Michaels, "A model-based approach to dispersion and parameter estimation for ultrasonic guided waves," *Journal of the Acoustical Society. America,* vol. 127, pp. 920-930, 2010.

[5] H. J., S. K. H. and K. Y. Y., "Dispersion-based short-time Fourier transform applied to dispersive wave analysis," *Journal of the Acoustical Society of America,* vol. 117, no. 5, pp. 2949-2960, 2005.

[6] R. D. Costley and Y. H. Berthelot, "Dispersion curve analysis of laser-generated Lamb waves," *Ultrasonics,* vol. 32, pp. 249-253, 1994.

[7] W. Gao, C. Glorieux and J. Thoen, "Laser ultrasonic study of Lamb waves: determination of the thickness and velocities of a thin plate," *International Journal of Engineering Science,* vol. 41, pp. 219-228, 2003.

[8] D. Alleyne and P. Cawley, "The Interaction of Lamb Waves with defects," *IEEE,* vol. 39, pp. 381-397, 1992.

[9] J. Hong, K. H. Sun and Y. Y. Kim, "Dispersion-based short-time Fourier transform applied to dispersive wave analysis," *Journal of the Acoustical Society of America,* vol. 117, pp. 2949-2960, 2005.

[10] Y. Y. Kim and E. Kim, "Effectiveness of the continuous wavelet transform in the analysis of some dispersive elastic waves," *Journal of the Acoustical Society of America,* vol. 110, pp. 86-94, 2001.

[11] F. Li, G. Meng, L. Ye, Y. Lu and K. Kageyama, "Dispersion analysis of Lamb waves and damage detection for aluminum structures using ridge in the time-scale domain," *Measuring Science Technology,* vol. 20, pp. 1-10, 2009.

[12] M. Niethammer, L. J. Jacobs, J. Qu and J. Jarzynski, "Time-frequency representations of Lamb waves," *Journal of the Acoustical Society of America,* vol. 109, pp. 1841-1847, 2001.

[13] Z. Su, L. Ye and X. Bu, "A damage identification technique for CF/EP composite laminates using distributed piezoelectric transducers," *Composite Structures,* vol. 57, pp. 465-471, 2002.

[14] Lemistre, "Structural health monitoring system based on diffracted Lamb wave analysis by multiresolutional processing," *Smart Material Structures,* pp. 504-511, 2001.

[15] L. Wang and F. Yuan, "Group velocity and characteristic wave curves of Lamb waves in composites: Modelingand experiments," *Composite Science Technology,* vol. 67, pp. 1370-1384, 2007.

[16] S. Grondel, J. Assaad, F. E. Youbi, E. Moulin and N. A. Leyla, "Experimental Lamb mode identification in a plate containing a hole using dual signal processing," *Measuring Science Technology,* vol. 19, pp. 1-6, 2008.

[17] R. N. Bracewell, The Fourier Transform and its Applications, USA: McGraw-Hill, 2000.

[18] P. McKeon, S. Yaacoubi, N. Declercq, S. Ramadan and W. Y. Yaacoubi, "Baseline subtraction technique in the frequency–wavenumber domain for high sensitivity damage detection," *Ultrasonics,* vol. 54, pp. 592-603, 2014.

[19] D. N. Alleyne and P. Cawley, "A two-dimensional Fourier transform method for the meausrement of propagating multimode signals," *Journal of the Acoustical Society of America,* vol. 89, no. 3, pp. 1159-1168, 1991.

CHAPTER 7

CONCLUSION

7.1 Summary

The work presented here investigated the propagation of ultrasonic guided waves in a thick-walled composite over-wrapped pressure vessel intended for hydrogen storage and transporation. It is considered to be a fundamental study that will inform the eventual creation of a Structural Health Monitoring system. Most notably, this study used experimental, analytical and numerical modeling techniques to consider the modal shapes and dispersive properties in this novel environment in order to make key decisions concerning frequency range, modal selection and emitter/receiver type and placement.

Despite lower displacement amplitude in the thick carbon-epoxy layer as opposed to the the thinner isotropic liner, chapters 4, 5 and 6 showed that a system based on UGW is capable of identifying isolated occurrences of defects occuring at various through-thickness depths, including on the surface. Furthermore, the numerical study suggested that modal amplitudes could be used to size these defects as long as modal separation is possible either in the frequency or temporal domain. Three key defect types were identified by the industrial partners and were subsequently modeled: surface-originating cracks (or cuts), abrasions, and disbonds.

An analytical study of the dispersive relationships of propagating modes in the thick multi-layer structure revealed that sample-specific measurements are important for these structures. Dispersion relationships can no longer logically be displayed as function of the product of frequency-thickness unless the layer thickness ratio is kept constant. The analytical study also suggested that amplitude loss due to visco-elasticity will be lowest below 300 kHz. Despite the anistropic nature of the materials, UGW should have constant dispersive relations when traveling in the near vicinity of the axial direction.

Excitation was investigated numerically. It was seen that since contact transducers will be used (for non-invasive SHM), ultimately multi-element array transducers in shear mode will be most efficient. The proposed mode of excitation is Mode 2 due to its relatively larger surface displacement and relatively small wavelength (as compared to higher order modes at the same frequency). The finite element modeling of wave interaction with defects suggests that modal conversion can be an indicator not just for damage presence but also for damage sizing.

To this end, a post-processing technique was developed that proposes a method of identifying small amplitude converted modes with minimal *a priori* information. The baseline subtraction technique has been applied to the frequency–wavenumber domain in order to increase the detectability of low amplitude modes. Since the conversion coefficient is related to defect size, detectability of low amplitude modes is directly related to the lower limit of damage detection. Through finite element analysis, mode conversion coefficients have been calculated for notch depths of less than 10% of total plate thickness. The smallest notch depth detected has a depth of around 1.5% of the total plate thickness. Notably, the proposed signal processing method uses limited *a priori* information making it less susceptible to incorrect theoretical dispersion curve calculation.

The optimization study in Chapter 5 demonstrates that the most drastic change in modal conversion occurs from Mode 2 to Mode 1 in the reflective and transmitted fields at around 150 kHz - 210 kHz. This change, although slightly dependent on the incident phase, was more or less robust to the distance between the emitter and damage site.

Finally, some experimental work was presented that corroborates and utilizes the optimization findings (which was the primordial aim of this work), first on an aluminum plate to justify the experimental setup and then on a multi-layer vessel intended for housing hydrogen at high pressures. Intentional impact defects have been detected successfully via the developed procedure. This example argues that UGW techniques are a good candidate for testing and / or monitoring composite vessels, and thus contributes to the safety of hydrogen storage. Since UGW can be generated and detected through different physical effects such as piezoelectrity and magnetostrictivity, some other kind of sensors and actuators may be used to make the application of UGW on composite vessels easier and accelerate its deployment.

7.2 Limitations

Due to resource constraints, the damage types simulated in the finite element model section of this work were not able to be tested experimentally. Instead, the damaged sample supplied by industrial partners was subject to impact testing. Therefore, it was to be expected that the modal conversion coefficients caclulated in Chapters 4 and 5 could not be validated in this work. However, Chapter 4 validates the approach with a simple single layer isotropic model by comparison with results found in the literature. The experimental work presented in Chapter 6 validates that the dispersive properties and modal propagation behavior was correctly modeled by the finite element models used in this work.

Regardless, it is worth revisiting the assumptions that were made in Chapters 1 and 2 to assess their validity. Most notably, the model assumed propagation in a plate instead of the axial direction of an annular cylinder, and that the material is assumed to be perfectly elastic. Comparison of numerical and experimental work show that the planar approximation was a valid approach – modes appear in the wavenumber-frequency domain in the experimental setup with less than 1% error with respect to the numerical work. However, preliminary experimental work also suggest that the viscoelastic effects of the carbon-epoxy layer may have a large effect on the amplitude of modes with respect to distance. Attenuation due to visco-elasticity is not taken into account in this work and should be considered when comparing modal amplitudes. Furthermore, this study is valid only for the cylindrical portion of the reservoir and excludes the spherical endcaps on either end of the vessel. This study also excludes the possiblity of multiple damage sites occuring at once, or damage sites occuring in the near field of the emitting or receiving transducers.

7.3 Recommendations for Continued Research

This fundamental study intended to evaluate key parameters to aid in the development of a future SHM system for the inspection of a COPV. However, a significant amount of research remains if UGW will ultimately be used for damage detection in this system. Due to the reservoir’s intended use, the eventual system must be able to detect critical damages with zero margin for error.

First, although UGW have been predicted to be sensitive to critical damage types, and one such case has been evaluated experimentally, other damaged samples should be used in a controlled environment to validate numerical models. It is crucial that the interaction of UGW with each and every critical damage type be evaluated experimentally. The work presented here was limited in scope to three damage types deemed critical by our industrial partners. However, the entirety of table 1.1 should be investigated to ensure public safety. Finally, a post-processing method was proposed referred to as ‘the wavenumer-frequency baseline subtraction algorithm’ (Chapter 4). Although this method has been verified to improve the lower limits of damage detection in a numerical environment, the algorithm’s use should be evaluated for the COPV with experimental data.

APPENDIX A

DEVELOPMENT OF ANALYTICAL DISPERSION CURVES FOR A SINGLE LAYER PLATE

Guided waves are fundamentally governed by the same governing equations as bulk wave, but must satisfy a set of boundary conditions which leads to modes propagating along the structure. The additional boundary condition constraints makes finding an analytical solution much more complicated than that of the bulk wave case.

Since there are several different boundary conditions possible, they are correspondingly several different types of guided waves which have been investigated over the past 150 years. For the case of waves traveling along a thin plate, however, the most pertinent type are Lamb waves, so called after the man credited with having investigate them first, Sir Horace Lamb. This type of guided wave travels parallel to the surfaces of the plate, with displacements in both the direction of wave propagation and perpendicular to the plane of the plate [1]. Again, the stipulation for this particular type of guided wave is that there must be two free boundaries flanking the propagation direction of the wave packet.

Lamb waves are a particularly interesting type of guided wave due to their dispersive characteristics. The phase velocity of Lamb waves is dependent on the product of frequency and thickness. Furthermore, it has been shown that the modes of Lamb waves can be broken into two categories: antisymmetric and symmetric, each of which can exist independently of the other. Given a plane that bisects the plate into an upper and lower half, symmetric modes describe motion that is symmetric with respect to this plane, whereas antisymmetric modes accordingly describe motion that is antisymmetric with respect to this plane. Rose [2] notes that the Lamb frequency equations can be separated into these two modes as follows:

$$\frac{\tan(qh)}{\tan(ph)} = -\frac{4k^2pq}{(q^2-k^2)^2} \tag{A.1}$$

For symmetric modes, and

$$\frac{\tan(qh)}{\tan(ph)} = -\frac{(q^2-k^2)^2}{4k^2pq} \tag{A.2}$$

For antisymmetric modes.

The variables *p* and *q* are denoted as

$$p^2 = \left(\frac{\omega}{c_L}\right)^2 - \left(\frac{\omega}{c_p}\right)^2 \tag{A.3}$$

and,

$$q^2 = \left(\frac{\omega}{c_T}\right)^2 - \left(\frac{\omega}{c_p}\right)^2 \tag{A.4}$$

However, *k*, which in general is complex, has an imaginary component that can either be negative, positive or equal to zero. In the case where k_{im} is equal to zero, this signifies that the waves propagate without any damping. The other two cases are of little or no interest, since $k_{im} < 0$ signifies waves that grow with distance, which exist only mathematically and not in the physical world, and $k_{im} > 0$ signifies waves that decay exponentially with distance. This latter type denotes waves that are called “evanescent” and although they can exist, they are of little importance since they will in effect disappear rapidly.

Since the case when k_{im}=0 is of the most interest, the Lamb Frequency equation for the symmetric mode can be rewritten as:

$$\frac{\tan(qh)}{q} + \frac{4k^2p\tan(ph)}{(q^2-k^2)^2} = 0 \tag{A.5}$$

Note: since the development of the antisymmetric mode is analogous to that of the symmetric, its evolution will be excluded from the remainder of this paper in the interest of *ω.*

Taking the positive square root of the variables *p* and *q* and consequently inputting them into the symmetric mode equation yields:

$$\frac{\tan\left(\omega h\sqrt{\frac{1}{{c_T}^2}+\frac{1}{{c_P}^2}}\right)}{\omega\sqrt{\frac{1}{{c_T}^2}+\frac{1}{{c_P}^2}}}+\frac{4\left(\frac{\omega}{c_P}\right)^2\omega\sqrt{\frac{1}{{c_L}^2}+\frac{1}{{c_P}^2}}\tan\left(\omega h\sqrt{\frac{1}{{c_L}^2}+\frac{1}{{c_P}^2}}\right)}{\left(\left(\omega\sqrt{\frac{1}{{c_T}^2}+\frac{1}{{c_P}^2}}\right)^2-\left(\frac{\omega}{c_P}\right)^2\right)^2}=0 \tag{A.6}$$

Expanding the denominator in the second term makes it clear that there is a common ω^4 term that can be extracted. Canceling out similar terms, and multiplying both sides of the equation by ω leaves,

$$\frac{\tan\left(\omega h\sqrt{\frac{1}{{c_T}^2}+\frac{1}{{c_P}^2}}\right)}{\sqrt{\frac{1}{{c_T}^2}+\frac{1}{{c_P}^2}}}+\frac{4\left(\frac{1}{c_P}\right)^2\sqrt{\frac{1}{{c_L}^2}+\frac{1}{{c_P}^2}}\tan\left(\omega h\sqrt{\frac{1}{{c_L}^2}+\frac{1}{{c_P}^2}}\right)}{\left(\frac{4}{{c_P}^2}+\frac{1}{{c_T}^2}-\frac{4}{{c_T}^2{c_P}^2}\right)}=0$$

It is important to note that frequency, *ω*, is never present in the above expression without being multiplied by thickness, *h.* It is for this reason that we can find phase velocities that satisfy this equation as a function of the product of thickness multiplied by frequency. In this manner it is possible to find the dispersion curves for a given material, i.e. for a given c_T and c_L.

However, this problem is still not easily solved analytically, and so numerical methods presents itself as the most viable option. Choosing a single frequency-thickness, values for the left-side of the equation are incrementally investigated until the left-side switches signs, from positive to negative, or vice versa. This implies that a root has been found, or more explicitly a solution to the symmetrical frequency equation. However, it is important to note that for any given frequency-thickness several modes could be possible. It is therefore necessary to continue to search for a change in signs even if one has already been previously found for a given frequency-thickness. Continuing in this manner, it is possible to extract all of the roots possible over a certain frequency-thickness range, and subsequently plot the roots to display the dispersion curves for the given material.

Note: There are three different regions possible, namely when $c_P < c_T < c_{L,}$ when $c_T < c_P < c_L$ and finally when $c_T < c_L < c_P$ and these three regions complicate the procedure of finding possible roots for the Lamb frequency equation. In the first region, both *p* and *q* are imaginary, and therefore it is possible for both terms on the left-hand side of the equation to be complex. Accordingly only *p* is imaginary, and for the third region the entire expression is necessarily completely real. This introduction of imaginary components complicates the procedure of finding sign changes, i.e. roots. Pragmatically, one can assume that there are three cases that any numerical method code should take into account. First, when all terms are necessarily real, then it is a simple question of sign change. The second case deals with a real part equal to zero and looks for a sign change in the imaginary component. The third case is decidedly more difficult, and deals with the case of when both change sign for the same value of c_P. It is unknown as of yet if the third case can occur, and for all intents and purposes can most likely be ignored.

References

[1] I. A. Viktorov, Rayleigh and Lamb Waves: Physical Theory and Applications, New York: Plenium Press, 1967.

[2] J. L. Rose, Ultrasonic Waves in Solid Media, Cambridge, U.K: Cambridge University Press, 1999.

APPENDIX B

VALIDATION OF BULK WAVE PROPAGATION IN A FEM ENVIRONMENT

Bulk waves and guided waves are governed by the same set of partial differential equations [1]. Therefore, the success of correctly simulating guided waves in plates ultimately lies in the ability to propagate bulk waves at the correct (theoretically accepted) wavespeed. Unlike fluids, two bulk modes are possible in isotropic solids, namely longitudinal (pressure) waves and transverse (shear) waves. In the FEM software and DISPERSE, the material properties of the structure were specified, and the bulk wave velocities were calculated as follows:

$$c_L = \sqrt{\frac{\lambda + 2\mu}{\rho}} = \sqrt{\frac{E}{\rho}\frac{(1-\nu)}{(1+\nu)(1-2\nu)}} \tag{B.1}$$

where E is Young's modulus, λ is Lame's constant, ρ is density, μ is shear modulus, and ν is Poisson’s ratio. In table B.1 can be found the various values used in this study for three different materials, aluminium, brass and titanium.

Table B.1: Material properties used in this study

	Aluminum	Brass	Titanium
Young’s Modulus [Gpa]	69	108.41	123.37
Density [kg/m^3]	2700	8400	4440
Shear Modulus [Gpa]	25.94	40.65	47.47

$$c_T = \sqrt{\frac{\mu}{\rho}} \tag{B.2}$$

COMSOL offers the capability to create expressions as a function of time in the time-solver mode. A simple sinusoid was chosen to ease interpretation. The propagation of bulk waves was started at 100Hz, since lower frequency (larger wavelengths) is decidedly simpler to manage [2]. It was determined that at least six elements per wavelength were necessary to correctly propagate a real wave forward in space, and at least ten elements give better resolution. However, too fine a mesh size increases computational time, or even worse creates an error in the residual computation and causes COMSOL to abort the solver.

There is a synonymous idea in the time domain. Time steps taken by the solver can be completely independent from the solution set that COMSOL delivers at its output (however, it should be noted that it is possible to record all of the internal time steps for trouble-shooting analysis). The time solver also offers several options to control the basic nature of how COMSOL chooses its internal time steps. The 'strict' option necessarily takes a time step at each previously determined output time, and adds entries in between as COMSOL sees fit, whereas the 'intermediate' option necessarily takes time steps somewhere between each output time step. It was determined that the 'strict' option consistently gave the best results. Quite analogous to the spatial domain, a choice between six and ten output time steps per wavelength seemed to be able to solve and propagate the wave quite nicely, with six obviously leading to a more efficient solution, and ten giving better resolution. It was noted that too many internal time steps in the solver per wavelength not only increased computational time, but also lead to spurious frequencies present in the signal.

The concept of using matched absorbing layers is one method of resolving these spurious reflections, which contaminate the otherwise pure longitudinal mode [3]. Figure B.1 shows the results of a longitudinal mode when an absorbing boundary layer is used to dampen any unwanted reflections. This same idea can be translated to waveguides at the two extremities of the plate, i.e. the two boundaries that are supposedly infinite in the theoretical problem.

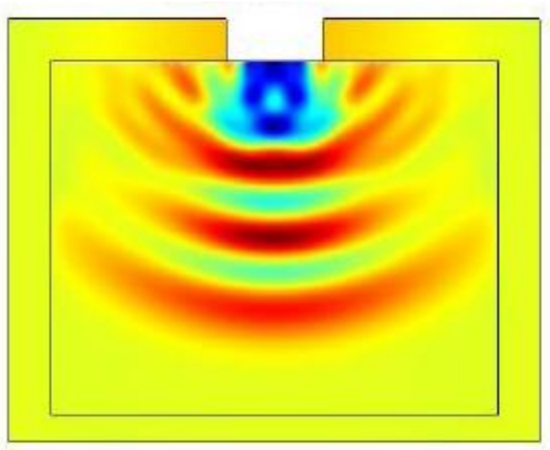

Figure B.1: A longitudinal wave with an absorbing boundary layer. Although by the fourth trough, some effects of the diffraction at the edges of the source can be observed

To validate that the bulk mode wavespeeds are correct, displacement at points inside the plate at regular intervals were recorded for each solution. Then Fourier transforms in both the time and space domains could determine the frequency and wavenumber present in every recorded waveform. Figure 8 shows that the longitudinal mode that was being excited at 100 Hz, had a measured wavenumber of 0.101 1/m, which agrees quite well with the theoretical value of 0.102 1/m for aluminum. This is an error of less than 1% and is well within the expected error due to discretization. The shear wave example can be seen in figure 9. For a shear wave in aluminium, the theoretical wavenumber at 100 Hz is 0.203 1/m, which is not as close to the 'measured' value of 0.196. But it is still leads to a percent error of around 3%, and is still totally acceptable within our expected error. Similar exercises were made with titanium and brass, and for the sake of brevity are not reproduced here. However, all bulk mode wavenumbers found with COMSOL were within a percent error of only 3%.

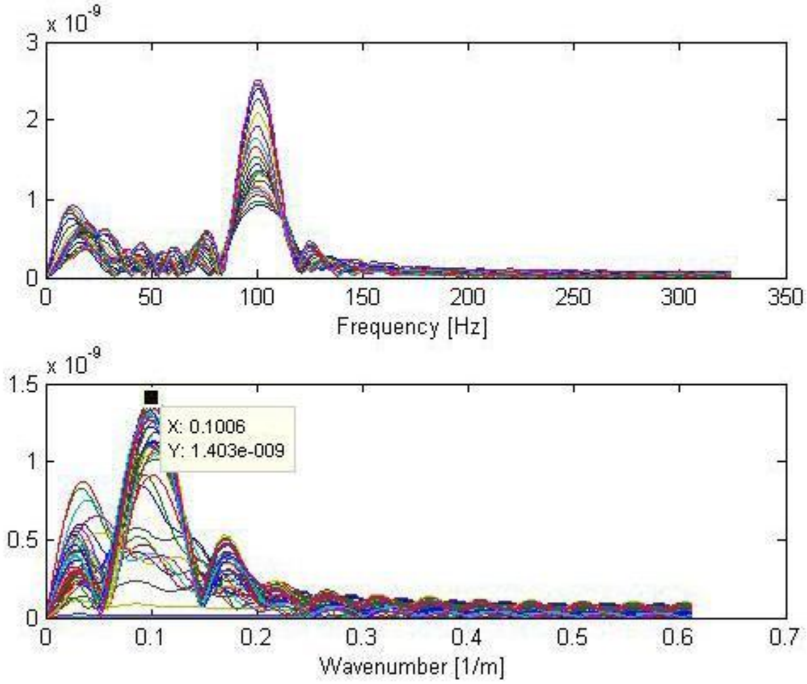

Figure B.2. : Fast Fourier transform of a 100 Hz longitudinal wave in aluminum in the time (top) and spatial (bottom) domains. The theoretical wavenumber is 0.102 1/m.

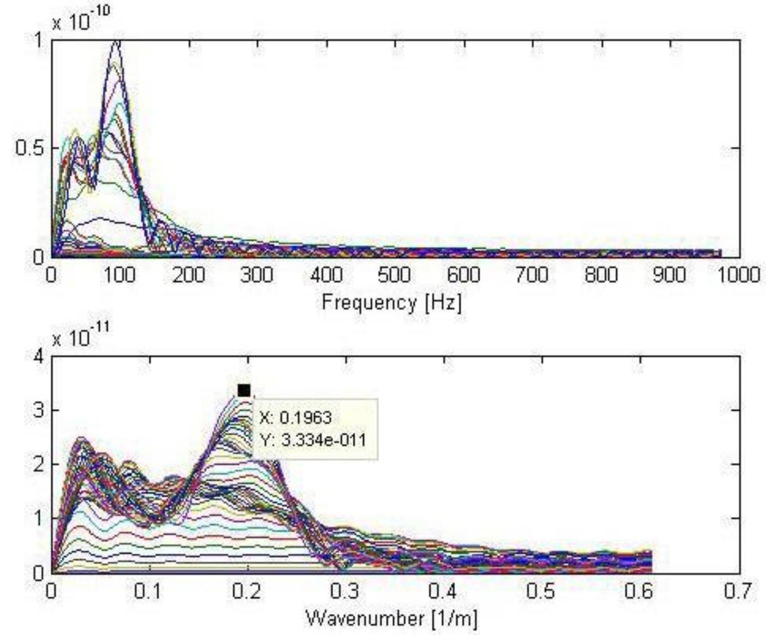

Figure B.2 : Fast Fourier transform of a 100 Hz shear wave in aluminium in the time (top) and spatial (bottom) domains. The theoretical wavenumber is 0.203 1/m.

References

[1] J. L. Rose, Ultrasonic Waves in Solid Media, Cambridge, U.K: Cambridge University Press, 1999.

[2] O. Zienkiewicz, "Achievements and some unsolved problems of the finite element method," *Intl J of Num Meth Engr,* vol. 47, pp. 9-28, 2000.

[3] L. Thompson, "A review of finite-element methods for time-harmonic acoustics," *JASA,* vol. 119, pp. 1315-1330, 2006.

APPENDIX C

VALIDATION OF GUIDED WAVE PROPAGATION IN A FEM ENVIRONMENT

For single layer geometries, the problem can be scaled without consequence, as long as the frequency-thickness product remains constant. Thus, operating at 100 Hz, a plate of aluminum was simulated with a width of 25m, which is slightly less than the wavelength of the bulk shear mode. Using two subdomains on either end of the plate that had the same material properties as aluminum, but unphysically high damping parameters, Lamb waves could be simulated in an environment similar to that of an infinite plate. Figures C.1 and C.2 show qualitatively the success of the Lamb wave propagation for symmetric and asymmetric modes respectively. Two Dirichlet sources were used in conjunction to generate either purely symmetric or purely asymmetric modes. The two sources were excited either in phase to excite asymmetric modes, or 180 degrees out of phase to excite symmetric modes. The regions of excitation are directly opposite each other and are located at the bottom or the two figures. The direction of excitation is marked for the ease of the reader.

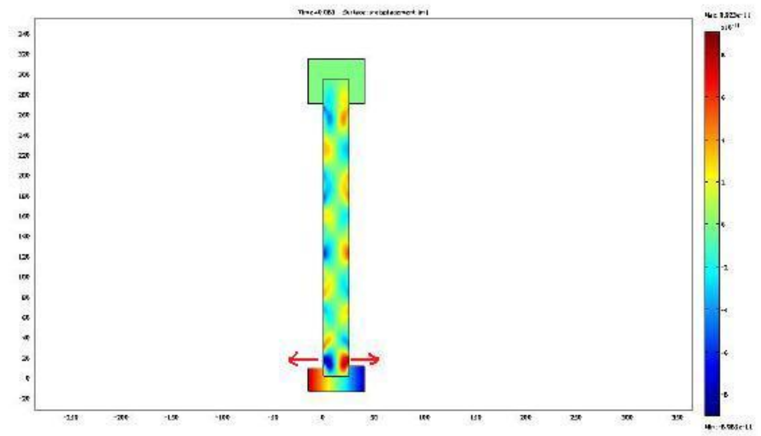

Figure C.1: COMSOL screenshot for symmetric Lamb waves being excited at 100 Hz in a 25m aluminum bar

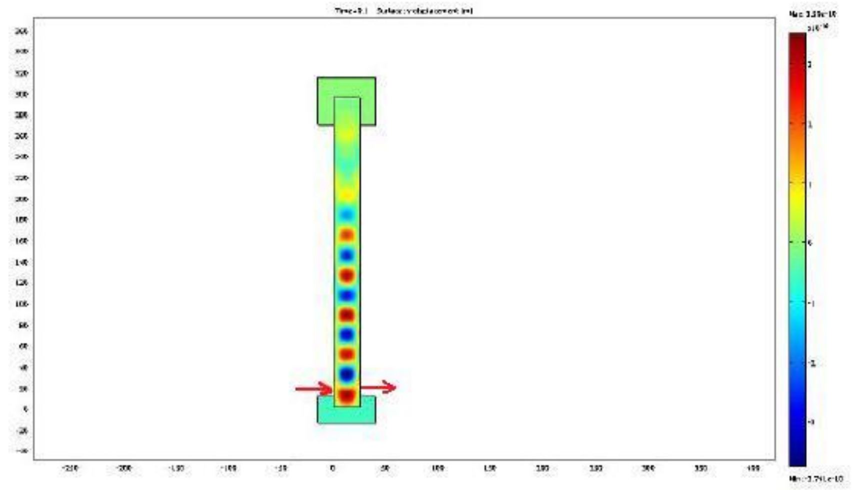

Figure C.2: COMSOL screenshot for asymmetric Lamb waves being excited at 100 Hz in a 25m aluminum bar